Probing and controlling coherent-phonon and spin-charge conversion in nanostructures with ultrafast visible and THz light pulses

Artem Levchuk

DOCTORAT MATIERE BRETAGNE MOLECULES LOIRE ET MATERIAUX

Le Mans Université

THÈSE DE DOCTORAT DE

LE MANS UNIVERSITÉ

ÉCOLE DOCTORALE N° 596
Matière, Molécules, Matériaux
Spécialité : *Physique, Ondes et Matériaux*

Par
Artem LEVCHUK

"Probing and controlling coherent-phonon and spin-charge conversion in nanostructures with ultrafast visible and THz light pulses"

Thèse présentée et soutenue à Le Mans, le 10 mars 2022
Unité de recherche : Institut des Molécules et Matériaux du Mans, UMR CNRS 6283
Thèse N° : 2022LEMA1002

Rapporteurs avant soutenance :

Steven JOHNSON Professeur, ETH Zurich
Luca PERFETTI Professeur, Laboratoire des Solides Irradiés École polytechnique

Composition du Jury :

Président :	Arnaud ARBOUET	Directeur de Recherche CNRS, CEMES-Toulouse
Examinateur :	Christine BOEGLIN	Directrice de Recherche CNRS, IPCMS-Univ Strasbourg
Dir. de thèse :	Pascal RUELLO	Professeur, IMMM-Le Mans Université
Co-dir. de thèse :	Vincent JUVÉ	Chargé de Recherche CNRS, IMMM-Le Mans Université

Acknowledgments

This long-short four-year journey was not possible without the help of many people. This brief letter is to express my most profound gratitude for their contributions to this work.

First and foremost, I sincerely thank my supervisors, Dr. Vincent Juvé and Prof. Dr. Pascal Ruello, for giving me the possibility to carry out this work. Furthermore, I sincerely appreciate their constant scientific, experimental, and personal guidance, which made the completion of this Ph.D. project possible. Moreover, I am immensely thankful for their availability, patience and encouragement, especially during the final steps of the manuscript and defense preparation. I could not have hoped for better supervisors and mentors.

I sincerely thank Prof. Dr. Steven Johnson, Prof. Dr. Luca Perfetti, Dr. Arnaud Arbouet, and Dr. Christine Boeglin for being the jury members. I highly appreciate their effort to come to Le Mans, time spent reading the manuscript, profound questions, and valuable suggestions about the work.

In addition, I want to acknowledge the enormous technical help and support provided by Dr. Gwenaëlle Vaudel. She was the one who has kept the main laser system running in a stable condition, allowing me to carry out the experiments on a daily basis. In addition, her reactivity and responsivity have simplified and accelerated the resolution of numerous problems.

Essentially, the experimental work carried out in the past four years was impossible without the high-quality samples. I thank Dr. Mathieu Edely for the in-lab growth of the thin metallic films of Aluminum and Chromium. In addition, I want to acknowledge our colleagues from the University of Silesia in Katowice for supplying us with beautiful nanofilms of Bismuth Telluride: Dr. Bartosz Wilk, Dr. Mateusz Weis, Dr. Katarzyna Balin, and Pof. Dr. Jacek Szade.

Ultimately, our fruitful collaboration with CEA SPEC in the frame of the ANR SANTA project has allowed us to investigate and understand the complex physics in a multitude of thin magnetic heterostructures. Given this opportunity, I want to acknowledge Dr. Michel Viret, Dr. Jean-Yves Chauleau, Dr. Aurélie

Solignac, and Dr. Jean-Baptiste Moussy.

Furthermore, I would like to thank all members of the Institut des Molécules et Matériaux du Mans, and especially the past and present NoVA team researchers, for their help and assistance. I can not factor out the vital theoretical contribution of Prof. Dr. Brice Arnaud and Dr. Rémi Busselez. Their valuable academic inputs and suggestions have stimulated some experiments and setup developments. A special thank goes to the Dr. Mads Weber for his constant encouragement and selfless help. Besides, I am thankful to Christiane Berne, Maxime Geoffroy, and Danielle Choplin for their assistance in the administrative part of this work.

My deep gratitude goes to my fellow labmates Yevheniia Chernukha, Thomas Perrault, Alexandr Alekhin, and Tadele Otomalo for the long, fruitful discussions, sometimes a necessary distraction from work, and invaluable help. Additionally, I appreciate the endless support of my friends Danylo Babich, Rostyslav Danylo, Pavel Leshuk, Anton Pylypenko, Artem Husiev, and Vadym Voytsekhovsky.

Last but not least, all of this would not have been possible without the constant encouragement and moral support of my beloved family: Irina, Andriy, Anton, Irina, Alexandr, Anatoliy, and Ludmila. In addition, I express my gratitude to Noémie, Sylvain, Marie, and Emilen, that have been by my side all along this journey.

I am grateful for the financial support of the French Ministry of Higher Education, Research and Innovation.

Contents

List of Figures

Introduction

Solid-state physics at the nanoscale has attracted considerable scientific and industrial interest over the past century. Today, we see an exponential increase in the amount of data generated, stored, and transmitted both locally and all around the web. However, in addition to the ever-increasing computational complexity, the question of the most powerful, robust, and energy-efficient core for future electronics remains unanswered. As chipmakers relentlessly pursue Moore's Law, advances in pulsed femtosecond lasers have allowed scientists to study physical processes six times faster than the clock speed of the best processors on the market. Ultimately, the rapid development in ultrashort lasers has defined new research directions in nanophotonics, solid-state physics, and spintronics. Therefore, understanding the ultrafast coupling between electrons, phonons, and spins in nanostructures is vital for new promising solutions to the numerous technological challenges.

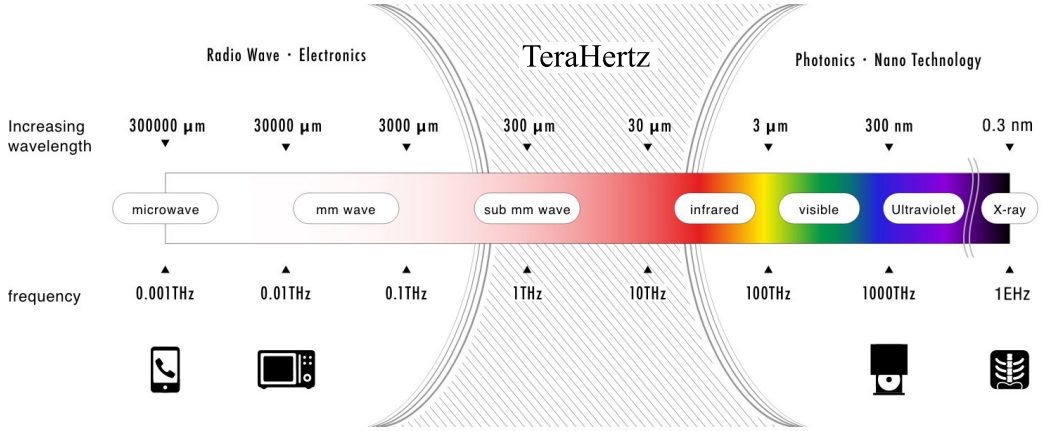

Figure 1 – *Shades of the electromagnetic spectrum. From nict.go.jp website.*

Today, we routinely use the microwave part of the spectrum (up to 300 GHz) for communication, remote control, and radar technology. In addition, we have mastered the production of electromagnetic waves in the infrared, visible, ultraviolet, and radiographic range, widely used for security, optical imaging, memory, and cancer treatment, to name a few. However, until recently, it was challenging to generate light in the so-called terahertz (THz) range (300 GHz-40 THz), which is very promising for the fundamental research and industrial applications. In particular, the THz frequency range is fascinating for scientific applications, as these frequencies resonate with collective modes of matter, such as the vibrations of molecules or crystals, collective spin excitation (magnons), or the motion of the free electrons [1]. For instance, the large amplitude THz transients generated by intense mid-infrared femtosecond pulses can be tuned in resonance with the infrared active vibrational modes inaccessible by thermal, mechanical, or optical excitation [2]. To explore

such intricate THz-matter interaction, developing the efficient, broadband, and tunable source of the pulsed THz radiation is a priority task. For example, it has been shown that femtosecond laser illumination of nm-thick magnetic heterostructures with strong spin-orbit interaction can lead to broadband THz emission with a tunable polarization state [3]. Furthermore, the selective control over subtle modulations of the matter's vibrational, electric, and magnetic properties, possibly achievable with the THz, is of particular interest for high-performance and low-power electronics. This thesis will contribute to both aspects of THz physics: the excitation of vibrational modes of a solid with THz pulses and the characterization of the promising spintronic THz emitters.

The first part of this thesis will be devoted to the experimental study of the coherent generation of acoustic phonons with picosecond pulsed THz radiation. Using ultrafast nonlinear spectroscopy in a pump-probe geometry, we will study the transient response of metal films (Cr, Al) and a narrow bandgap, n-doped topological insulator (Bi_2Te_3) at the picosecond time scale. Through a quantitative comparison between terahertz (4 meV) and near-infrared (1.5 eV) excitation, we will show that the acoustic phonon generation process in thin metal films with THz is mainly driven by thermoelastic stress caused by the ultrafast Joule heating of the lattice. To the best of our knowledge, it is the first demonstration of the THz-driven coherent acoustic phonons in metals and narrow-band semiconductors.

The following discussion will focus on the rich lattice dynamics when the terahertz pulse excites the Bi_2Te_3 nanofilm. We will demonstrate the non-resonant generation of coherent Raman active phonons, with frequencies up to five times higher than the center frequency of the driving THz pulse. Thus, this work contributes to the description of emerging nonlinear solid-state phononics and discusses different physical mechanisms of the selective control of the lattice vibrations with THz light.

The third cornerstone of this thesis aims to detect the ultrafast signature of the spin-charge interconversion due to the spin transport in the bulk of CoFeB combined with the injection-based spin-to-charge conversion mechanisms. In particular, the study will be focused on the sub-picosecond dynamics of the recently discovered Rashba-split band structure at the CoFeB/MgO interface [4]. Therefore, this thesis will try to probe the THz emission due to the ultrafast inverse Rashba-Edelstein conversion within the CoFeB/MgO bilayers. Among the results, we will show that the inverse Rashba Edelstein effect is sensitive to the pump photon energy, which opens exciting perspectives for ultrafast spintronic emitters.

The manuscript is constructed as follows. Chapter 1 will touch on the fundamentals of solid-state physics, including electron, phonon, and spin properties, basics of electromagnetism, and nonlinear optics. Chapter 2 is dedicated to the presentation of the experimental methods and techniques. Finally, the Chapters 3 and 4 present the results about coherent phonon excitation with pulsed THz radiation and ultrafast spin-to-charge conversion, respectively. We will then conclude this manuscript with a general summary of this thesis's main achievements and prospects for future work.

Chapter 1

Theoretical background

Contents

1.1 Introduction

Back in 1912, M. Laue proposed a rather simple experiment (Fig.1.1a) and observed the X-Ray interference due to the crystalline nature of a sample, for which he was awarded the Nobel Prize in 1914. One hundred years later, thanks to the progressively increasing knowledge and scientific interest in the condensed matter physics, we developed some remarkable solid-state devices such as transistors, semiconductor lasers, optical fibers, lithium batteries, liquid crystal display, and many others.

Here, we introduce the baseline theory necessary for discussion of the following chapters. This chapter will start with the notions about the arrangements and properties of atoms, electrons, and spins in solid matter. Next, the basics of the light-matter are explained with the definition of the electromagnetic wave, optical properties of the material, and second-order nonlinear processes in crystals. At the end, a brief description of the temporal coupling of light with the electrons, atoms, and spins will be given.

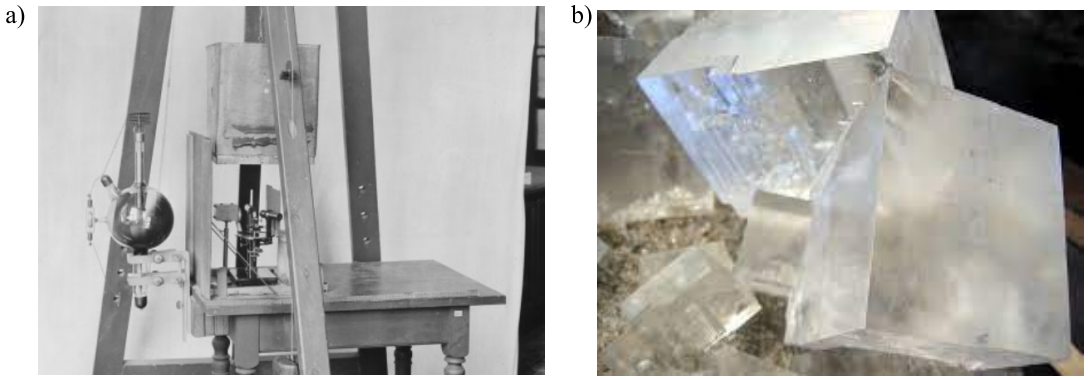

a) Famous x-Ray diffraction experiment that was proposed by Max von Laue and performed by Walter Friedrich and Paul Knipping, exhibit at Deutsches Museum in Munich [5]. b) Rock salt crystal. The periodical arrangement of the Na and Cl atoms on the lattice is responsible for the electronic, phononic and magnetic properties of the NaCl. From Wikipedia.

Figure 1.1 – *Experimental setup proposed by Max von Laue and NaCl crystal (rock salt).*

1.2 Atoms, electrons, and spins in condensed matter

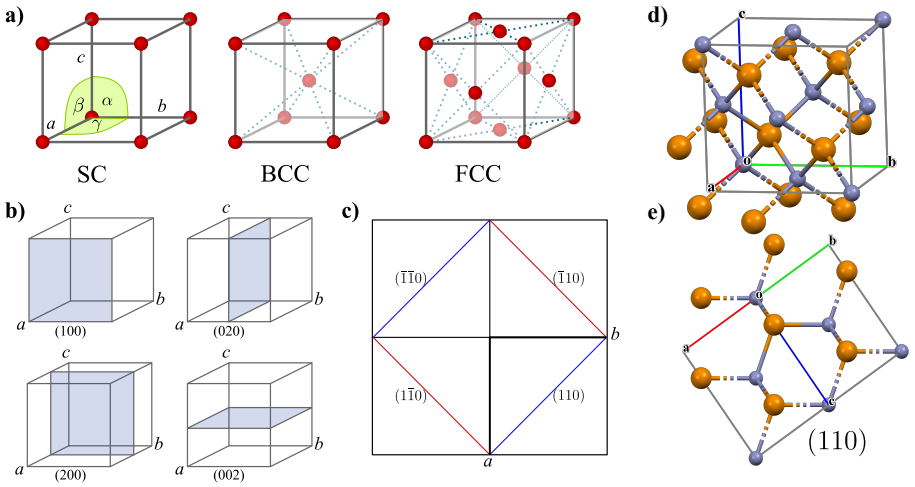

a) Bravais lattices with cubic symmetry: simple cubic (SC), body centered cubic (BCC) and face centered cubic (FCC). Redrawn from "Physics in a nutshell". **b)** Miller indices for different crystal planes. **c)** Projection down the **c**-axis, showing all four equivalent 110 planes. Adapted from [6]. **d)** Bravais lattice of the *Zinc-Blende* ZnTe crystal. **e)** (110) oriented ZnTe crystal plane.

Figure 1.2 – *Three cubic Bravais lattices, Miller indices for different crystal planes and Bravais lattice of ZnTe crystal.*

First, we will define what the ideal crystal is. The ideal three-dimensional (3D) crystal can be imagined as a periodic array of elementary building blocks, i.e., atoms or a group of atoms, that is called the basis (red circles on Fig.1.2a). The set of mathematical points (coordinates) to which the basis is attached is called the lattice [7].

3D lattices, due to the point symmetry, form 14 different lattice types in total: in addition to general triclinic, there are 13 other lattices named by the corresponding unit cell type. These 14 lattices are called Bravais or direct lattices. For example, 3 possible configurations of the cubic lattice are shown in Fig.1.2 (a).

The next important notation is the crystal plane orientation. The set of parallel planes that intercept the crystal unit-cell can be noted as (hkl), where Miller's indices $h, k,$ and l define the point of intercept on the given crystal axes a, b, c at position $1/h$, $1/k$ and $1/l$ respectively. The example of the crystal plane notation using Miller indices is shown in the Fig.1.2b. Usually, the reciprocal values of h, k, l are reduced to the set of integers with the least common multiplier. If plane cuts the axis on the negative side, the corresponding negative index is then noted as $\bar{h}, \bar{k}, \bar{l}$, as seen from Fig.1.2c. The type of Bravais lattice combined with the crystal plane orientation can affect the combination of the solid matter's elastic, electronic, magnetic, and optical properties.

1.2.1 Ionic subsystem

Phonon dispersion relation

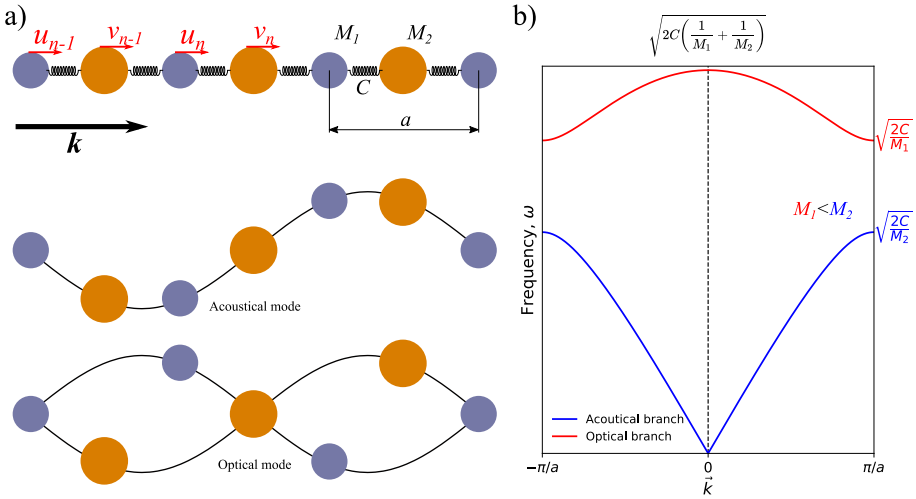

a) Diatomic crystal chain and transverse optical and acoustical waves. Vectors v_n, u_n denote the atomic displacement along the acoustic wavevector $\boldsymbol{k}$ of ions with masses M_1 and M_2 respectively. C is the spring constant, a is the lattice repetition rate. b) Phonon dispersion relation for the diatomic crystal chain. So called phononic bandgap, defined as $\sqrt{\frac{2C}{M_1}} - \sqrt{\frac{2C}{M_2}}$, defines the region with no solutions to the atomic equation of motion.

Figure 1.3 – *Diatomic crystal chain with respective transverse acoustical and optical waves and its dispersion relation.*

The 3D crystal is built with an ever-repeating pattern of atoms. For simplicity, within the harmonic potential approximation let us consider an infinite 2D diatomic chain, where two atoms with masses M_1 and M_2 lie on the plane, tied together with the elastic force constant C. This two-atom basis has the repeat distance a as shown in Fig.1.3a. We assume that each atom interacts only with its nearest neighbors. Therefore, the simple equations of motion for the ions in the chain reads:

$$\begin{cases} M_1 \dfrac{d^2 u_n}{dt^2} = C(v_n + v_{n-1} - 2u_n); \\ M_2 \dfrac{d^2 v_n}{dt^2} = C(u_{n+1} + u_n - 2v_n) \end{cases}, \tag{1.1}$$

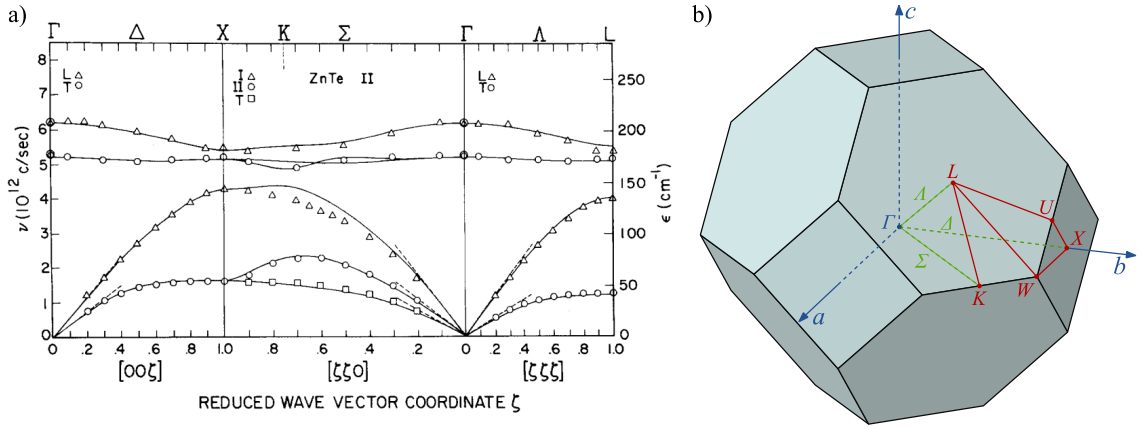

a) Phonon dispersion relation of a ZnTe crystal. Hollow symbols are experimental points, and lines are theoretical calculations. From [8]. b) First Brillouin zone of the FCC lattice, with high-symmetry points. From Wikipedia.

Figure 1.4 – *ZnTe phonon dispersion curve and first Brillouin zone of the FCC lattice.*

and we will look for the nontrivial solutions in the form of the wave with respective amplitudes v and u:

$$u_n = ue^{in\boldsymbol{k}a}e^{-i\omega t}; \qquad v_n = ve^{in\boldsymbol{k}a}e^{-i\omega t}. \tag{1.2}$$

Given the periodicity of this classical diatomic chain, we can apply the periodic boundary condition (Born-von Karman):

$$e^{i\boldsymbol{k}Na} = 1, \tag{1.3}$$

where N is the number of lattice repetitions, that defines the total chain length as $L = Na$. Solution of this boundary condition for $\boldsymbol{k}$ returns the value for the edges of the first Brillouin zone, containing all unique values of atomic vibrational frequency ω. If we substitute Eq.1.2 in Eq.1.1 we find solutions for ω^2:

$$\begin{aligned} \omega_{ac}^2 &= \frac{C}{M_1M_2}\left(M_1 + M_2 - \sqrt{M_1^2 + M_2^2 + 2M_1M_2\cos\left(\boldsymbol{k}a\right)}\right); \\ \omega_{opt}^2 &= \frac{C}{M_1M_2}\left(M_1 + M_2 + \sqrt{M_1^2 + M_2^2 + 2M_1M_2\cos\left(\boldsymbol{k}a\right)}\right). \end{aligned} \tag{1.4}$$

These solutions tell us about the frequency range of the permitted oscillations of the crystal within the first Brillouin zone, called phonon dispersion curves are referred to as an acoustical and optical branch, and are shown in the Fig.1.3b. Within the acoustical branches, two atoms oscillate in the same phase, following the similar pattern of the sound wave. For the optical branch, two ions oscillate out of phase. Such vibration can be imagined as the action of electromagnetic (EM) waves on the two dipoles with opposite charges [7], hence the optical branch name. Optical and acoustical branches are split by the amount of $\sqrt{\frac{2C}{M_1}} - \sqrt{\frac{2C}{M_2}}$ at the edge of the Brillouin zone, defining the range of forbidden vibrational frequencies within the crystal, named phononic bandgap.

The example of the phonon dispersion curve of a ZnTe crystal is shown in Fig.1.4a. ZnTe has fcc lattice and is from $F\bar{4}3m$ [216] space group (Hermann–Mauguin notation), also known as Zincblende. The 3 degrees of freedom (x, y, z) of each atom allow for $3p$ vibrational modes in total, where p is the number of atoms per unit cell. ZnTe phonon dispersion curves have 3 (1 Longitudinal (LA) and 2 Transverse (TA)) acoustical modes, where the remaining $3p - 3$ will be reserved for Longitudinal (LO) and Transverse (TO) optical phonon branches. Along the strong symmetry axes (ΓX, ΓL, see Fig.1.4b), due to the degeneracy of transverse branches, we can observe only 4 modes: TA, TO, LA and LO. If we move perpendicularly to the (110) crystallographic plane, i.e., along [110] direction, TO and two TA branches lose that degeneracy, resulting in $3 \times 2 = 6$ predicted vibrational modes in total.

Lattice heat capacity

The quanta of lattice vibrational energy is called a phonon. Energy of a given elastic mode, occupied by n_s phonons (n phonons within the branch s) with frequency ω_s and wave vector $\boldsymbol{k}$ defined as:

$$\epsilon_s = (n_s + 1/2)\hbar\omega_s(\boldsymbol{k}). \tag{1.5}$$

Therefore, the total vibrational energy of the crystal could be simply expressed as the sum over all discrete energy values for all existing phonon normal modes:

$$E_{ph} = \sum_{s,\boldsymbol{k}} \left(n_s + \frac{1}{2} \right) \hbar\omega_s(\boldsymbol{k}). \tag{1.6}$$

Phonons are bosons. The mean number of phonons that occupy $n_s(k)$ energy state at given temperature T can be approximated with Planck distribution:

$$\langle n_s(\boldsymbol{k}) \rangle = \frac{1}{\exp\left[\frac{\hbar\omega_s(\boldsymbol{k})}{k_B T} \right] - 1}, \tag{1.7}$$

where k_B is the Boltzmann constant. This distribution tells us that high-$\boldsymbol{k}$ states are more likely to be occupied at higher temperatures. Knowing the thermal distribution of the phonon modes, we can write the generalized expression for the crystal vibrational energy density [9]:

$$U_{ph} = U_{eq} + \frac{1}{2V} \sum_{\boldsymbol{k},s} \hbar\omega_s(\boldsymbol{k}) + \frac{1}{V} \sum_{\boldsymbol{k},s} \langle n_s(\boldsymbol{k}) \rangle \, \hbar\omega_s(\boldsymbol{k}), \tag{1.8}$$

where U_{eq} is the lattice energy at equilibrium ($T = 0$), and the second term corresponds to the zero-point vibration of the lattice mode s. The third term introduces the temperature dependence of U_{ph}. Finally, we can define the lattice heat capacity c_L, at constant volume as:

$$c_L = \left(\frac{\partial U_{ph}}{\partial T} \right)_V = \frac{1}{V} \sum_{\boldsymbol{k},s} \frac{\partial}{\partial T} \langle n_s(\boldsymbol{k}) \rangle \, \hbar\omega_s(\boldsymbol{k}), \tag{1.9}$$

showing the temperature dependence of c_L. For given temperature range, there are different approximations for c_L. For the majority of crystals at $T > 300\,\mathrm{K}$, one can use the law of Dulong and Petit ($c_L \propto 3k_B n_s/V$). At low temperatures Debye approximation ($c_L \propto T^3$) assumes that only low-ω acoustical modes are excited. This makes phonon frequency ω_s directly proportional to the wavevector $\boldsymbol{k}$, resulting in a constant sound velocity. While Debye approximation works for acoustical branches, Einstein approximation is usually chosen as a first approximation to describe the energy contribution of optical phonons to c_L. Both Debye and Einstein laws are designed to work within specific temperature range, and still, they both converge to the classic law of Dulong and Petit at high temperatures [7]. For the considerable number of the phonon modes, one can replace the sum over k in the Eq.1.9 by an integral, saying that crystal has $D_s(\omega)d\omega$ modes in the frequency interval $[\omega, \omega + d\omega]$ and in the branch s:

$$c_L = \frac{1}{V}\sum_s \int D_s(\omega)d\omega \frac{\partial}{\partial T}\langle n_s(\boldsymbol{k})\rangle \hbar\omega_s((\boldsymbol{k}), \tag{1.10}$$

where $D_s(\omega)$ is the phonon density of states. In its general form, $D_s(\omega) \propto \dfrac{1}{v_g}$ where v_g is the phonon group velocity, also known as the speed of sound.

1.2.2 Electronic subsystem

When considering the electronic Hamiltonian with a constant potential (even zero by selecting a specific energy scale), the electron wave function becomes that of a free electrons' Sommerfeld model with parabolic electron dispersion relation:

$$\epsilon = \frac{\hbar^2 \boldsymbol{k}^2}{2m}, \tag{1.11}$$

where m is the mass of the electron in vacuum. Adding some periodic boundary Born von Karman condition, we obtain the quantization of the wave vector and the associated energy. The surface at a constant energy, plotted in the $\boldsymbol{k}$ space, defines the Fermi sphere.

In reality, the periodic arrangement of the lattice and its translational symmetry invariance highly impact how the electron behaves inside the crystal. The electrons are indeed affected by the periodic potential generated by neighboring electrons and lattice ions that leads to specific electron-ions interaction, creating some "gaps" in the electronic band structure. The eigenfunction of the electron, or Bloch wave, is written as the plane wave having periodicity defined by the Bravais vectors $\boldsymbol{R}$ [9]. The electron wave functions become:

$$\psi_{n_b,\boldsymbol{k}}(\boldsymbol{r}) = e^{i\boldsymbol{k}\cdot\boldsymbol{r}} u_{n_b,\boldsymbol{k}}(\boldsymbol{r}), \tag{1.12}$$

where $\boldsymbol{k}$ is the electron wave-vector, and n_b is the so-called band index. The lattice periodicity is represented by the term $u_{n_b,\boldsymbol{k}}(\boldsymbol{r})$ with the symmetry invariance:

$$u_{n_b,\boldsymbol{k}}(\boldsymbol{r} + \boldsymbol{R}) = u_{n_b,\boldsymbol{k}}(\boldsymbol{r}), \tag{1.13}$$

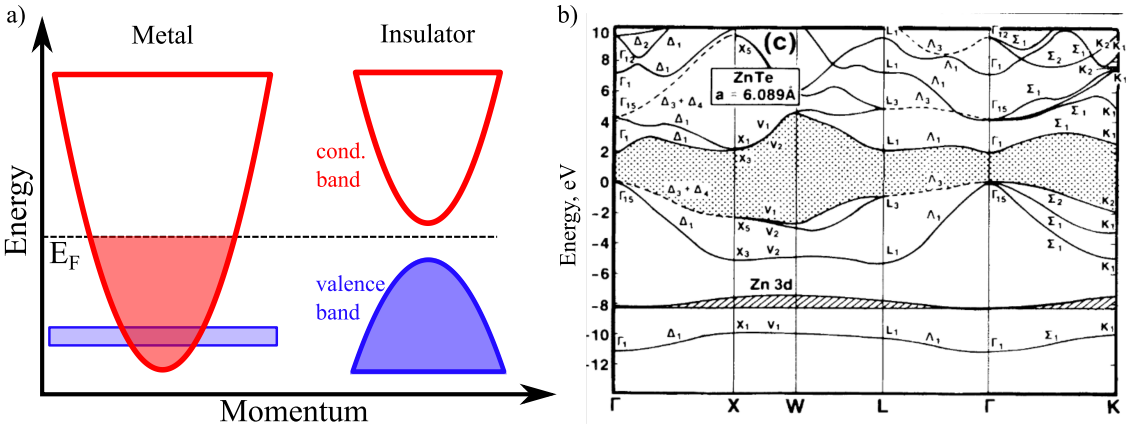

a) Schematic band structure of metal and insulator. Metal shows free-electron-like parabolic dispersion relation at T=0 K, with partially filled conduction band. Insulator has a band structure with Fermi energy E_F inside the band-gap. This results in a non-conducting behavior at T=0 K. b) Electronic band structure of ZnTe, calculated with "nonrelativistic Ceperley-Alder exchange-correlation." Dashed lines show doubly-degenerate bands; Shaded areas denote the fundamental band-gap region. From [10]

Figure 1.5 – *Schematic electron band structure of Metal and Insulator and ZnTe electron dispersion curve.*

and the periodic potential

$$U_{n_b,\boldsymbol{k}}(\boldsymbol{r}) = U_{n_b,\boldsymbol{k}}(\boldsymbol{r}+\boldsymbol{R}). \tag{1.14}$$

This impinges the same periodicity on the electron wave function with $\psi_{n_b,\boldsymbol{k}}(\boldsymbol{r}+\boldsymbol{R}) = e^{i\boldsymbol{k}\boldsymbol{R}}\psi_{n_b,\boldsymbol{k}}(\boldsymbol{r})$. The time-independent Schrodinger equation for the electron in a periodic potential reads [9]:

$$H\psi_{n_b,\boldsymbol{k}}(\boldsymbol{r}) = \left(-\frac{\hbar^2}{2m}\nabla^2 + U_{n_b,\boldsymbol{k}}(\mathbf{r})\right)\psi_{n_b,\boldsymbol{k}}(\boldsymbol{r}) = \epsilon_{n,\boldsymbol{k}}\psi_{n_b,\boldsymbol{k}}(\boldsymbol{r}), \tag{1.15}$$

where the set of eigenenergies $\epsilon_{n,\boldsymbol{k}}$ associated with the basis of the Bloch wave functions establish the electronic band structure of the crystal (see Fig.1.5a). In the case of metal at $T = 0\,\mathrm{K}$, some electron bands are partially filled up to a specific energy level, so-called Fermi energy E_F.

In another possible configuration, electrons completely fill a certain number of bands (valence bands), leaving others empty (conduction bands), with E_F positioned in between. Material with such an electronic configuration is called an insulator. The difference between highest occupied and lowest unoccupied electron levels is defined as band-gap energy E_g. At some specific points of the Brillouin zone (called valleys), the approximation of parabolic dispersion also usually works for semiconductors [9], with:

$$\epsilon(\boldsymbol{k}) = \frac{\hbar^2\boldsymbol{k}^2}{2m_e^*}, \tag{1.16}$$

where m_e^* is the effective mass that is defined by the curvature of the electron band. m_e^* is related to the change of electron group velocity along the wave vector $\boldsymbol{k}$ with $m_e^* = 1/\frac{\partial^2\epsilon(k)}{\partial k^2}$ and can be positive (electron) or negative (holes) at the Brillouin zone center of GaAs for instance. In

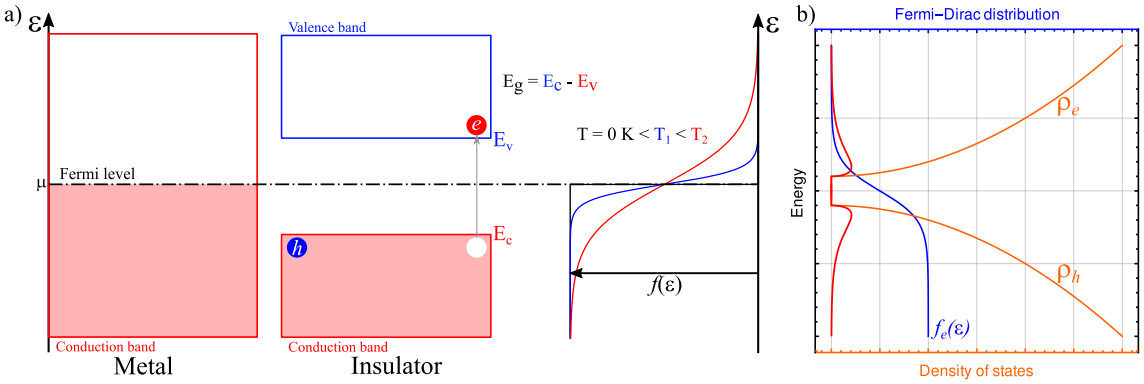

a) Fermi-Dirac distribution of metal for the different temperatures. Here, the chemical potential μ is equaled to E_F, which is usually true for $T = 0\,\mathrm{K}$. For an insulator, μ is chosen to lie equidistantly from the bottom of the valence and top of the conduction band. For an intrinsic semiconductor, if $\epsilon = \mu$, $f(\epsilon) = \frac{1}{2}$ [7]. At $k_B T_2 > E_g$, the electron is promoted from the valence to conduction band, creating an electron-hole pair, resulting in conducting behavior. b) Electron and hole density of states (orange), Fermi-Dirac distribution $f_e(\epsilon)$ for the electrons (blue). Hole distribution $f_h(\epsilon)$ is inverse to the one of electrons. The product of the electron-hole density of states and Fermi-Dirac distribution for an insulator, in the parabolic band approximation, is shown in red. Adapted from Wikipedia.

Figure 1.6 – *Fermi-Dirac distribution of the metal and insulator, and density of states for an insulator.*

that case the free-electron "picture" is then useful. However, such parabolic approximation does not hold for the whole Brillouin zone [9]. The electron dispersion relation, accounting for the lattice periodicity, generally leads to a rather complicated electronic band structure, with Fig.1.5b showing the electron dispersion relation of a ZnTe crystal.

Statistics. Fermi-Dirac distribution

Electrons are Fermions, so they obey the Pauli exclusion principle. At $T = 0\,\mathrm{K}$ electrons will fill the energy bands up to the E_F. For $T > 0\,\mathrm{K}$, the distribution of thermally activated electron can be described by the Bose statistics [9]:

$$f(\epsilon, \mu, T) = \frac{1}{1 + \exp[(\epsilon(\boldsymbol{k}) - \mu)/k_B T]}, \tag{1.17}$$

where μ is the chemical potential, and at $T = 0\,\mathrm{K}$, μ approaches the value of the Fermi energy E_F. This distribution show that thermally activated electrons will gradually occupy higher energy states with a discrete interval of $\approx k_B T$, as shown in Fig.1.6a.

Electron density of states. Heat Capacity

If we assume the parabolic shape of the electron dispersion relation (Sommerfeld model), we can write a rather simple expression for the electronic density of states (DOS). For the metal, it will take form:

$$\rho^{met}(\epsilon) = \frac{dn}{d\epsilon} = \frac{1}{\pi^2}\left(\frac{m_e^*}{\hbar^2}\right)^{\frac{3}{2}}\sqrt{2\epsilon}, \tag{1.18}$$

when for the semiconductor it will be:

$$\begin{aligned}\rho_e^{sc}(\epsilon) &= \frac{dn}{d\epsilon} = \frac{1}{2\pi^2}\left(\frac{2m_e^*}{\hbar^2}\right)^{\frac{3}{2}}\sqrt{\epsilon - E_c};\\ \rho_h^{sc}(\epsilon) &= \frac{dn}{d\epsilon} = \frac{1}{2\pi^2}\left(\frac{2m_h^*}{\hbar^2}\right)^{\frac{3}{2}}\sqrt{E_v - \epsilon};,\end{aligned} \tag{1.19}$$

where m_e^* and m_h^* are the effective mass of electron and hole, respectively; E_c is the energy of the top of conduction band, and E_v corresponds to energy at the top of the valence band. In metals, knowing the electron density of states, one can express the total electronic energy per unit of volume:

$$U_e = \int_0^\infty \epsilon \rho^{met}(\epsilon) f(\epsilon) d\epsilon. \tag{1.20}$$

To get the electron energy density for an insulator, one needs to account for the electron and hole density of states and adjust the integration boundaries for these two contributions. The temperature dependent Fermi-Dirac distribution implies the temperature-dependent electron heat capacity, defined as:

$$c_e = \left(\frac{\partial U_e}{\partial T}\right)_V. \tag{1.21}$$

The electron heat capacity c_e dominates the lattice heat capacity c_L for metals at low temperatures only when $E_F \gg k_B T$. A derivative of Eq.1.21 leads to the linear relation $c_e(T_e) = \lambda_e T$ with electron thermal conductivity $\lambda_e = 96.6$ J.mol^{-1}.K^{-2} for copper for instance. For semiconductors, c_e contribution to the heat capacity of the crystal dominates c_L only in the high-temperature regime, when $E_F \ll k_B T$, although not many materials can support that.

Electrical conductivity in the semi-classical approach

Let us picture the Fermi surface of a crystal centered at the origin of $\boldsymbol{k}$ space, as shown in Fig1.7a. In the ground state, the net electron momentum ($m_e \boldsymbol{v} = \hbar \boldsymbol{k}$) is zero, since for every electron orbital at $\boldsymbol{k}_{x,y}$ there is an occupied opposite electron state at $-\boldsymbol{k}_{x,y}$. In the presence of an external electric force $\mathbf{F} = -e\mathbf{E}$ acting on these electrons, the second law of motion reads:

$$-e\mathbf{E}_x = \hbar \frac{d\boldsymbol{k}_x}{dt} = m_e \frac{d\boldsymbol{v}_x}{dt}. \tag{1.22}$$

Over time t, each electron will experience the equivalent displacement in $\boldsymbol{k}$-space, as shown in Fig.1.7b, and the total shift of the Fermi surface could be written as:

$$\delta \boldsymbol{k}_x = \frac{-e\boldsymbol{E}_x t}{\hbar}. \tag{1.23}$$

After the electric field is lifted, the electrons will return to equilibrium. The electron momentum, gained in the presence of $\boldsymbol{E}_x$ can be dissipated via collisions with phonons, lattice imperfections and impurities. We can define the characteristic time $t = \tau_e$ during which the electrons will maintain

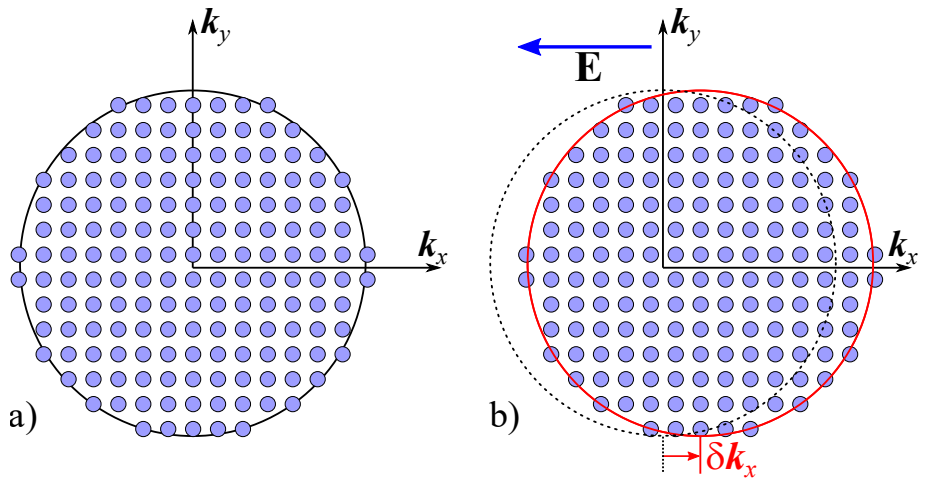

Circular Fermi surface of a 2D metal, with dots being the occupied free-electron states. **a)** Without applied field $\boldsymbol{E}$ the net momentum zero, since for each electron state (k_x, k_y) there is an electron at $(-k_x, -k_y)$. **b)**With $-e\boldsymbol{E}_x$ force applied on the electrons, Fermi surface will be shifted (red circle) from its initial position (dotted circle), gaining the increase of electron momentum $\delta p_x = \delta \boldsymbol{k}_x$

Figure 1.7 – *Shift of the circular Fermi surface under the presence of the electric field.*

the $\delta \boldsymbol{k}_x$ shift of the Fermi surface. Therefore, the density of electric current generated under the action of $\boldsymbol{E}_x$ is [7]:

$$\boldsymbol{j} = -en\boldsymbol{v}_x = \frac{e^2 n \tau_e}{m_e} \boldsymbol{E}_x = \sigma \boldsymbol{E}_x, \tag{1.24}$$

which is the definition of microscopic Ohm's law, with σ being the conductivity of the metal and τ_e is electron scattering time. For the conductivity of the semiconductor, one needs to account for the contribution of both electrons and holes:

$$\sigma^{sc} = \frac{e^2 n \tau_e}{m_e} + \frac{e^2 h \tau_h}{m_h}, \tag{1.25}$$

where τ_e and τ_h are the electron and hole collision time, respectively.

We then can explore the total amount of kinetic energy gained by the conduction electrons. With change of electron momentum $\hbar \delta \boldsymbol{k}_x$, change in kinetic energy per unit volume is:

$$\delta U_k = n \frac{(\hbar \delta \boldsymbol{k}_x)^2}{2m_e} = \frac{1}{2} \frac{m_e}{e^2 n} \boldsymbol{j}^2 = \frac{1}{2} \tau_e \frac{\boldsymbol{j}^2}{\sigma}. \tag{1.26}$$

The total density of absorbed energy by the electron subsystem will then read as:

$$W_k = \frac{\partial U_k}{\partial t} = \frac{1}{2} \boldsymbol{j}^2 \sigma^{-1} = \frac{1}{2} \boldsymbol{j}^2 \rho, \tag{1.27}$$

with resistivity $\rho = \sigma^{-1}$. This is a microscopic analogy of the well-known Joule heating process, saying that the electrical current generated by the motion of the charge, and it will contribute to the increase of the internal energy of the crystal.

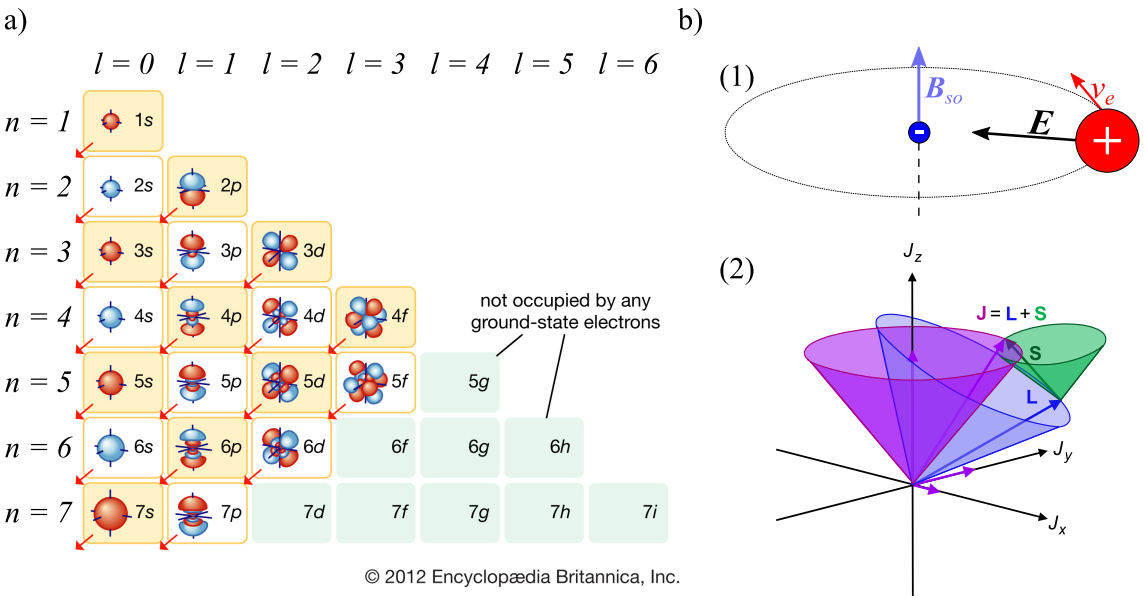

a) Depiction of atomic orbitals in molecules and solids. The principal quantum number n identifies electron shell when electrons with the identical orbital quantum number l from the subshell. The way electrons fill in shell and subshell levels is indicated by the arrows above. For example, because of the lower energy state, the 4s orbital fills before the 3d. Image is taken from Encyclopedia Britannica. b) **(1)** Classical view of the spin-orbit interaction. $\boldsymbol{E}$ generated by the nucleus in the rest frame of moving electron will transform into magnetic field $\boldsymbol{B}_{so}$, interacting with electron spin. **(2)** LS coupling of orbital and spin angular momenta for atoms with $Z < 10$.

Figure 1.8 – *Sketch of electronic states in an atom and electron spin-orbit interaction.*

Another important value related to the electron scattering time τ_e is the distance electrons traveled between the collisions, namely the electron mean-free path:

$$\Lambda = v_x \tau_e. \tag{1.28}$$

Usually, the electron velocity v_x is defined in terms of Fermi velocity v_F, which accounts for the curvature of the electron dispersion band. However, in the case of free-electron gas approximation, the average thermal electron velocity $\langle v_{th}^2 \rangle$ is proportional to the increase of system kinetic energy by amount $\frac{3}{2} k_B T / m_e$.

1.2.3 Spin subsystem

The electron state in an atom can be described with 4 quantum numbers: principal quantum number n, orbital quantum number l, magnetic quantum number m_l, and spin quantum number m_s. Electrons with the same n form an electron shell, and the principal quantum number can take integer values from 1 to 7. Orbital quantum number l defines an electron subshell within electron shell n, having n possible values from 0 to $(n-1)$, as shown in Fig.1.8a. Hund's rules describe the population of electron shells and subshells. l defines electron orbital within a subshell, and m_l gives a projection of the orbital angular momentum $\boldsymbol{l}$ on the given axis. Values of m_l are integers in the range $[-l; l]$. m_s gives the axis projection of intrinsic electron angular momentum, called spin $\boldsymbol{s}$. For an electron, m_s can take the fixed values of $\pm 1/2$, when two orientations of $\boldsymbol{s}$ along the

given axis are referred to as spin-up and spin-down. In quantum mechanics, components of spin angular momentum operator $\hat{\boldsymbol{s}}$ obey the following commutation relation [11]:

$$[\hat{s}_i, \hat{s}_j] = i\hbar\epsilon_{ijk}\hat{s}_k, \tag{1.29}$$

with ϵ_{ijk} being Levi-Civita permutation symbol. This permutation relation holds for orbital angular momentum operator $\hat{\boldsymbol{l}}$ as well. The eigenvalues of $\hat{\boldsymbol{s}}$ are $\pm\hbar/2$. Two commuting operators $\hat{s}_z$ and $\hat{\boldsymbol{s}}^2$ have respective eigenvalues of $\pm\hbar s$ and $\hbar^2 s(s+1)$. Electrons' orbital motion and spin associated with respective orbital $\hat{\boldsymbol{\mu}}_{orb}$ and spin $\hat{\boldsymbol{\mu}}_s$ magnetic moment operators as:

$$\hat{\boldsymbol{\mu}}_{orb} = -\frac{\mu_B}{\hbar}\hat{\boldsymbol{l}}; \qquad \hat{\boldsymbol{\mu}}_s = -\frac{\mu_B g_s}{\hbar}\hat{\boldsymbol{s}}, \tag{1.30}$$

where $\mu_B = |e|\hbar/2m_e$ is Bohr magneton with e being elementary charge and g_s is the Landé's g-factor. The electron total angular momentum operator $\hat{\boldsymbol{j}}$ (Fig.1.8b2), and hence the total magnetic moment operator are defined as:

$$\hat{\boldsymbol{j}} = \hat{\boldsymbol{s}} + \hat{\boldsymbol{l}}; \qquad \hat{\boldsymbol{\mu}}_{\boldsymbol{e}} = \hat{\boldsymbol{\mu}}_{\boldsymbol{s}} + \hat{\boldsymbol{\mu}}_{\boldsymbol{l}}. \tag{1.31}$$

The first existence of the electron spin was confirmed experimentally by Stern and Gerlach [12] in 1922, although the result of their experiment was misinterpreted. Researchers theoretically introduced the intrinsic magnetic moment of the electron 6 years after Stern's experiment as the consequence of the relativistic corrections [13].

Spin-orbit interaction

In 1928 Dirac published the paper on the quantum mechanics, where he derived the relativistic version of the Schrödinger equation, and introduced the spin-operators [14]. The relativistic single-electron Dirac Hamiltonian in the symmetric potential, under the static magnetic field $\hat{\boldsymbol{B}}^{tot}$, was derived as [13]:

$$\hat{H} = \hat{T} + \hat{T}_{rel} + \hat{H}_C + \hat{H}_D + \hat{H}_{SO} + \hat{H}_Z, \tag{1.32}$$

The first two terms in Eq.1.32 are non-relativistic $\hat{T}$ and relativistic $\hat{T}_{rel}$ corrections to the electron's kinetic energy. The next two terms are the potential energy of the electron in the nucleus potential, i.e., Coulomb force $\hat{H}_C$, and the so-called Darwin term $\hat{H}_D$, arising from the relativistic fluctuations of the electron's potential energy. Interestingly, in the Dirac representation, the wave functions associated with $\hat{H}$ are called spinors, and compared to vectors, they transform differently under rotation in 3D space [13].

The fifth term, $\hat{H}_{SO}$, describes the electron spin-orbit interaction, which helped explain the doublets in the hydrogen spectrum observed by Michelson back in 1892 [15]. One can approach the spin-orbit coupling term from the rest frame of the moving electron. The orbital motion of the nucleus around the stationary electron is equivalent to the current loop that will generate magnetic field $\boldsymbol{B}_{SO} \propto \boldsymbol{E} \times \boldsymbol{v}_e/c^2$ (Fig.1.8b1). This magnetic field will affect the electron spin

magnetic moment $\hat{\boldsymbol{\mu}}_{\boldsymbol{s}}$, introducing the coupling between the orbital and spin angular momenta of a single electron. Generally, the spin-orbit Hamiltonian can be written as:

$$\hat{H}_{SO} = \frac{e\hbar}{2mc}\hat{\boldsymbol{s}} \cdot (\boldsymbol{E}(\hat{\boldsymbol{r}}) \times \frac{\hat{\boldsymbol{v}}_e}{c}) = \lambda_{SO}\hat{\boldsymbol{l}} \cdot \hat{\boldsymbol{s}}, \tag{1.33}$$

with the speed of light c, electron band velocity $\hat{\boldsymbol{v}}_e$, and total electric field $\boldsymbol{E}$ experienced by the electron. Here, $\lambda_{SO} = e\hbar E(r)/(2mc^2 r)$ is the spin-orbit parameter (in classical notation), and it decreases rapidly with increasing nuclear distance [16].

There are two edge cases of angular and spin-orbital-momentum interactions. First one is known as Russell–Saunders (LS) coupling, saying that the total spin angular momentum $\hat{\boldsymbol{S}} = \sum_i \hat{\boldsymbol{s}}_i$ will be coupled to the total orbital angular momentum $\hat{\boldsymbol{L}} = \sum_i \hat{\boldsymbol{l}}_i$, as shown in Fig.1.8b2. LS coupling is true for the atoms with a small nuclear charge Z, resulting in a weak spin-orbit interaction. For heavy atoms, the individual coupling between the electron total angular momentum (JJ) $\hat{\boldsymbol{J}} = \sum_i \hat{\boldsymbol{j}}_i = \sum_i (\boldsymbol{s}_i + \boldsymbol{l}_i)$ is stronger than the electrostatic (LS) interaction between them. Pure JJ and LS interactions are rare, and spin-orbit coupling in atoms is regarded as the intermediate case between the two.

The last term in the Eq.1.32 is the Zeeman interaction operator $\hat{H}_Z$:

$$\hat{H}_Z = -\hat{\boldsymbol{\mu}}_{\boldsymbol{e}} \cdot \hat{\boldsymbol{B}}^{tot}. \tag{1.34}$$

It describes the interaction between the total electron magnetic moment and the static magnetic field. All magnetic moments in a solid will align parallel to the external magnetic field only when Zeeman interaction will compensate for the spin-orbit interaction. Therefore, the magnitude of the external magnetic field used to align the magnetic moments may vary depending on the crystallographic plane direction it is applied along. For example, to saturate the magnetization of bcc Fe, the magnitude of the magnetic field applied along the $\langle 111 \rangle$ direction (hard axis) will be significantly higher than the one applied along the $\langle 100 \rangle$ direction (easy axis).

Since the Zeeman and spin operators do not commute ($[\hat{H}_Z, \hat{\boldsymbol{s}}] \neq 0$), electron dispersion bands in solids may exhibit spin-dependent behavior in the presence of intrinsic or external magnetic field [17]. The latter will lead to the two derivatives of the Zeeman effect, known as Dresselhaus and Rashba effects, that describe the creation of the spin-polarized electron dispersion curves in solids [18]. The Rashba Hamiltonian, and its relation to the spin-to-charge conversion is discussed in the Chapter 4.

Direct exchange interaction

Let us now consider the system with two electrons, namely a and b, interacting with positively charged nucleus Ze. For simplicity, we will not account for the relativistic corrections. The eigenenergies associated with single electron Hamiltonian $\hat{H}_a$ and $\hat{H}_b$ are assumed to be known, and are E_a and E_b respectively. The total Hamiltonian of a two-electron system can be expressed

in a simple form:

$$\hat{H}_{ab} = \hat{H}_a(\hat{\boldsymbol{r}}_1) + \hat{H}_b(\hat{\boldsymbol{r}}_2) + \frac{e^2}{4\pi\epsilon_0|\hat{\boldsymbol{r}}_1 - \hat{\boldsymbol{r}}_2|}, \tag{1.35}$$

where the third term is the perturbation due to electron-electron interaction. Since we neglected spin-orbit interaction, the electron wave function can be factorized in orbital $\Phi_i(\hat{\boldsymbol{r}}_j)$ and spin $\Omega_i(\hat{\boldsymbol{s}}_j)$ parts [17]. For such a system of two fermions, due to the Pauli exclusion principle, each particle can be either spin up or down, resulting a total combination of four basis states of the spin-part wave function $\Omega_i(\hat{\boldsymbol{s}}_j)$: three Symmetric triplets:

$$\left.\begin{array}{l} |\uparrow,\uparrow\rangle \\ (|\uparrow,\downarrow\rangle + |\uparrow,\downarrow\rangle)/\sqrt{2} \\ |\downarrow,\downarrow\rangle \end{array}\right\} \; S = 1\hbar\,; \tag{1.36}$$

and one Asymmetric singlet:

$$(|\uparrow,\downarrow\rangle - |\uparrow,\downarrow\rangle)/\sqrt{2}\,; \;\; S = 0, \tag{1.37}$$

where S denotes the total spin of the basis state. When the electron-electron interaction is small compared to the E_a and E_b, it is assumed that there is no coupling of the orbital states. If a set of orbital-part electron wave functions form an orthonormal basis, it is possible to derive the eigenenergies of a singlet E_s and triplet E_t states [13]

$$\begin{aligned} E_s &= E_a + E_b + K_{ab} + J_{ab}; \\ E_t &= E_a + E_b + K_{ab} - J_{ab}, \end{aligned} \tag{1.38}$$

that are split by the amount of $2J_{ab}$. Here, the

$$K_{ab} = \int\int d\hat{\boldsymbol{r}}_1 d\hat{\boldsymbol{r}}_2 |\Phi_a(\hat{\boldsymbol{r}}_1)|^2 |\Phi_b(\hat{\boldsymbol{r}}_2)|^2 \tag{1.39}$$

is the quantitative measure of the overlap between two electron orbitals and is called the overlap integral. J_{ab} is an analogy of two-site Coulomb interaction and is called the interaction integral:

$$J_{ab} = \int\int d\hat{\boldsymbol{r}}_1 d\hat{\boldsymbol{r}}_2 \Phi_a^*(\hat{\boldsymbol{r}}_1)\Phi_b^*(\hat{\boldsymbol{r}}_2)\frac{e^2}{4\pi\epsilon_0 r_{12}}\Phi_b(\hat{\boldsymbol{r}}_1)\Phi_a(\hat{\boldsymbol{r}}_2). \tag{1.40}$$

Paul Dirac derived the eigenenergies from Eq.1.38 by introducing the spin-dependent term in the Hamiltonian instead of two-electron Coulomb exchange, as demonstrated above. The so-called Dirac exchange Hamiltonian $\hat{H}_{ex}$ for the two-electron system is:

$$\hat{H}_{ex} = \frac{1}{4}(E_s + E_t) - \frac{1}{4}(E_s - E_t)\hat{\boldsymbol{s}}_1 \cdot \hat{\boldsymbol{s}}_2/\hbar^2, \tag{1.41}$$

where the terms in parenthesis correspond to the energy of bonding $2(E_s - E_t)$ and antibonding $(E_s + E_t)$ orbitals. This equation says that the exchange interaction is a purely electrostatic effect that arises from the spin-spin interaction and Pauli exclusion principle. For N-electron system, the exchange interaction Hamiltonian is known as the Heisenberg Hamiltonian:

$$\hat{H}_{ex} = -2 \sum_{i<j}^{N} J_{ij}^{ex} \hat{\boldsymbol{s}}_i \cdot \hat{\boldsymbol{s}}_j / \hbar^2, \tag{1.42}$$

where the exchange integral J_{ij}^{ex} has the same form as J_{ab}. When the exchange integral J_{ij}^{ex} is positive, according to Eq.1.38, adjacent spins point in the same direction, i.e., aligned in parallel, which is the sign of ferromagnetic coupling. Inversely, if J_{ij}^{ex} is negative, consecutive spins point in the opposite direction, resulting in antiferromagnetic interaction. If more than one magnetic substrate with an antiparallel spin orientation do not cancel each other, ferrimagnetic ordering can occur [16].

The magnitude of the exchange integral J_{ij}^{ex} is determined by the overlap integral K_{ij} (see K_{ab} in Eq.1.39). If the wave functions of the participating electrons do not overlap, there will be no spontaneous spin ordering. When the distance between two magnetic ions is large, meaning that the direct exchange not possible, the spin-spin exchange mechanism can be mediated by superexchange (via oxygen orbitals in oxides, for instance) [17].

Ferromagnetism. Stoner model

The direct exchange interaction in solids can result in spontaneous spin ordering, giving rise to the macroscopic magnetization $\boldsymbol{M}$ defined as:

$$\boldsymbol{M} = \frac{1}{V} \sum_{i} \langle \hat{\boldsymbol{\mu}}_{\boldsymbol{i}} \rangle, \tag{1.43}$$

where $\langle \hat{\boldsymbol{\mu}}_{\boldsymbol{i}} \rangle$ is the expected value of the total magnetic moment operator (see Eq.1.31).

Measurement of the spontaneous magnetization in Fe, Co, and Ni revealed that the magnetic moment per atom is not indeed an integer multiple of Bohr magneton, contradicting the existing at that time theory. This problem was solved by Mott [19], Slater [20], and Stoner [21] around the 1940s. As an example, the Stoner band model was developed to explain broken μ_B numbers as a result of ferromagnetism .

The classical Stoner model is used to predict spontaneous ferromagnetic ordering in solids, and it assumes separate band structures for spin-up and spin-down electron states. Since it is always hard to keep track of the true sample magnetization, we can apply a static external magnetic field ($\boldsymbol{B}^{ext}$) to align the magnetization of the sample parallel to the applied field, as shown in Fig.1.9a. Since spin magnetic moment and electron spin have opposite directions (see Eq.1.30), the states with larger electron population (majority band) will be aligned in the opposite direction to $\boldsymbol{B}^{ext}$, while ones having a smaller population (minority band) will be parallel to the applied magnetic field. Hence, the magnetization and the spin minority will always point in the direction of $\boldsymbol{B}^{ext}$.

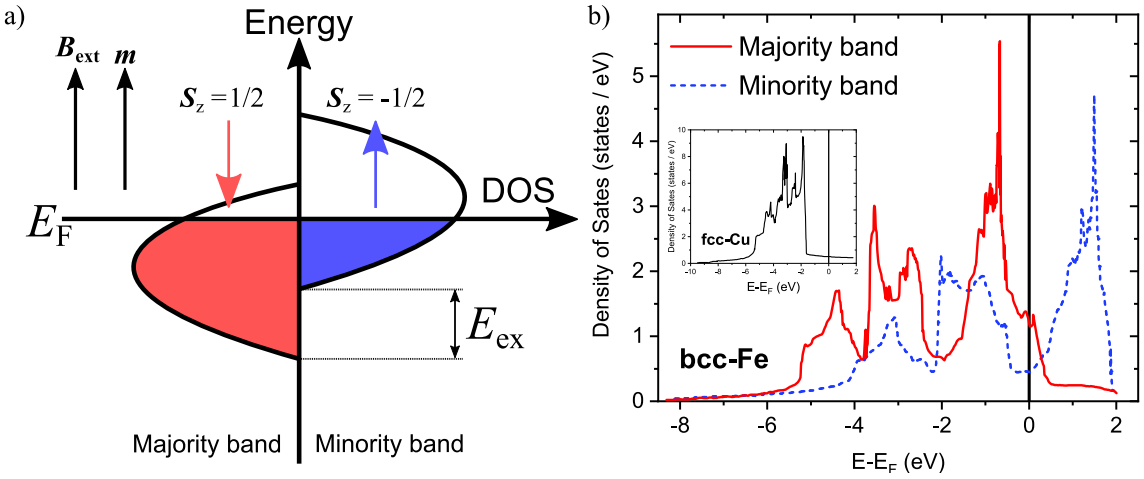

a) Schematic representation of the d-band spin-dependent electron density of states for a ferromagnet, under the external B^{ext} static magnetic field applied along the z direction. Since electron spin magnetic moment is opposite to the spin direction, the spin of minority band electrons will be aligned along B^{ext}. The minority and majority bands are split by the amount of E_{ex}. b) Density of states of bcc-Fe, with the majority and minority bands in colors. Inset is the DOS of fcc-Cu, with the absence of the exchange splitting. The figure is redrawn from [22]

Figure 1.9 – *Stoner model of ferromagnet and calculated density of states of bcc-Fe.*

We can define the difference in the number of electrons in the minority and majority bands as [17]:

$$N_e^{maj} - N_e^{min} = N_e^{\downarrow} - N_e^{\uparrow} = \int_{-\infty}^{E_F} \rho^{\downarrow}(\epsilon)d\epsilon - \int_{-\infty}^{E_F} \rho^{\uparrow}(\epsilon)d\epsilon, \tag{1.44}$$

with $\rho^{\uparrow\downarrow}(\epsilon)$ being minority or majority electron DOS. The magnetic moment of a solid ($\boldsymbol{m}$ in classical notation) will be proportional to the difference of electrons (or holes) between these two bands:

$$|\boldsymbol{m}| = \mu_B(N_e^{maj} - N_e^{min}) = \mu_B(N_h^{maj} - N_h^{min}). \tag{1.45}$$

The difference in the electron density of states at the Fermi level E_F and exchange interaction field B_{ex} (generated by exchange interaction Hamiltonian (see Eq.1.42)) will result in the majority and minority bands split by the amount of E_{ex} [17]:

$$E_{ex} \propto 2\boldsymbol{m} \cdot B^{ex}. \tag{1.46}$$

The Stoner model, assumes the parabolic shape of electron DOS, while "real" electron DOS has far more complex shape. The spin-polarized density of states of bcc-Fe is shown in Fig.1.9b, with $E_{ex} \approx 2.2\,\text{eV}$. Generally, the exchange interaction competes with other energies in solid [11]. As an example , one can expect that the thermal atomic disorder may overcome the exchange interaction contribution, resulting in a random alignment of magnetic moments. Indeed, the magnetization

$\boldsymbol{M}$ is proportional to [17]:

$$\boldsymbol{M} \propto (T_{crit} - T)^{\alpha}, \tag{1.47}$$

where T_{crit} is the critical temperature (Curie or Neel temperature for ferro- and antiferromagnets, respectively) above which the magnetic order vanishes, and α is the critical exponent that differs with the material.

Magnons

Ferromagnetic metal in the ground state at $T = 0\,\mathrm{K}$, according to Eq.1.38, prefers to have its spins aligned in parallel, which leads to the lowest possible energy state. If we treat spins as classical vectors, the total exchange energy in this ground state will be equal to $-2NJ^{ex}s^2$ with N being the number of neighbors. Thus, we can estimate the thermal energy (Eq.1.47) required to eliminate the spontaneous ground-state magnetization as [11]:

$$k_B T_C = \frac{-2NJ^{ex}\hat{\boldsymbol{s}}^2}{\hbar^2}. \tag{1.48}$$

Let us imagine an electron spin-chain with two nearest neighbors, i.e., $N = 2$. The magnetic order will vanish at critical temperature T_C, with corresponding thermal energy of $k_B T_C = J^{ex}$. In the mean time, the energy required to flip the spin of a single electron is equal to $2J^{ex}$ ($-4J^{ex}s^2 \rightarrow 4J^{ex}s^2$), i.e., two times the $k_B T_C$. Clearly, the single-electron spin-flip is not the best "energy-efficient" solution, and can not occur at low temperatures. Instead, all adjacent electrons will share the spin-reversal, which will form an excitation with a much lower energy cost per electron [7]. Such oscillation of the relative orientation of spins on the lattice, depicted in Fig.1.10, is called magnons, or spin-waves.

The exchange interaction Hamiltonian for the two nearest neighbours in the 1D electron chain can be rewritten in terms of:

$$\hat{H}_{ex}^{N=2} = \hat{\boldsymbol{s}}_j \hat{\boldsymbol{B}}_j^{ex}, \tag{1.49}$$

with the exchange field $\hat{\boldsymbol{B}}_j^{ex} = -2J^{ex}(\hat{\boldsymbol{s}}_{j-1} + \hat{\boldsymbol{s}}_{j+1})/\hbar^2$ generated by the neighbours at lattice sites $j \pm 1$. According to the Ehrenfest equation (in the absence of damping), this exchange field $\hat{\boldsymbol{B}}_j^{ex}$ will act as a source term of the spin precession [11]:

$$\frac{d}{dt}\langle \hat{\boldsymbol{s}}_j \rangle = \frac{g_s \mu_B}{\hbar} \Big\langle \hat{\boldsymbol{s}}_j \times \hat{\boldsymbol{B}}_j^{ex} \Big\rangle. \tag{1.50}$$

In Cartesian coordinates, the precession of the $\langle \hat{\boldsymbol{s}}_j \rangle$ components along the given axis could be expressed as the system of three coupled differential equations. We can neglect the products of x

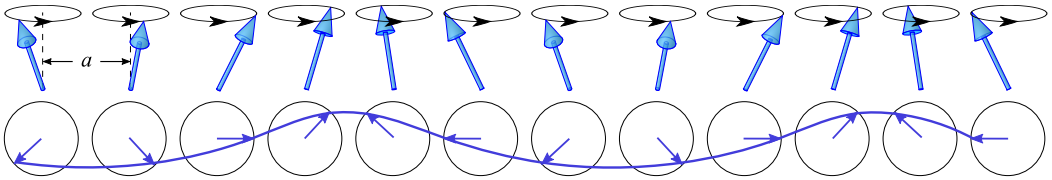

Perspective and an aerial view of spins on a lattice with lattice constant a. Spin wave in aerial view is drawn through the end of the spin vectors. The image was redrawn from [7]

Figure 1.10 – *Spin wave on the 1D chain of spins.*

and y components, since the expected values of $s_j^{x,y} \ll s_j^z$ [16]:

$$\begin{cases} \frac{d}{dt}s_j^x = -\frac{J^{ex}g\mu_B}{\hbar}\left(2s_j^y - s_{j-1}^y - s_{j+1}^y\right) \\ \frac{d}{dt}s_j^y = -\frac{J^{ex}g\mu_B}{\hbar}\left(2s_j^x - s_{j-1}^x - s_{j+1}^x\right) \\ \frac{d}{dt}s_j^z = 0 \end{cases} \tag{1.51}$$

We will look for the solutions in the form of traveling wave $\propto \exp[i\boldsymbol{k}_j a - \omega_m t]$, with lattice constant a. The solution for the precession with a frequency ω_m defines the magnon dispersion relation [7]:

$$\hbar\omega_m = -4J^{ex}S(1 - cos(\boldsymbol{k}a)). \tag{1.52}$$

The magnon dispersion relation for $\boldsymbol{k}a \ll 1$ has the form $\hbar\omega_m = D_{SW}\boldsymbol{k}^2$, with stiffness parameter $D_{SW} = 2J^{ex}Sa^2$. Magnons are bosons, and the quantized energy of a magnon is defined as:

$$\epsilon_m = \left(n_m + \frac{1}{2}\right)\hbar\omega_m, \tag{1.53}$$

where n_m is the number of magnons in the mode with frequency ω_m at the zone center [11]. For $T < T_{crit}$ magnons behave like bosons, so they follow the Bose statistics. Interestingly, the magnons are in some way similar to phonons. Instead of the relative precession of an atomic position on a lattice, spin waves are oscillations of the relative orientation of the lattice spin magnetic moments.

The magnon contribution to the heat capacity of the solid can be expressed in terms of the spin-correlation function $\langle \hat{\boldsymbol{s}}_i \cdot \hat{\boldsymbol{s}}_j \rangle$ (see Eq.1.42) [11]:

$$c_m = -2NZJ^{ex}\frac{\partial\langle \hat{\boldsymbol{s}}_i \cdot \hat{\boldsymbol{s}}_j \rangle}{\partial T} \tag{1.54}$$

1.3 Light-matter interaction

1.3.1 Optical properties and dielectric function

Most optical phenomena can be explained with the classical electromagnetic (EM) approach, from the perspective of the physical interaction between charged particles. The light propagation

inside the material can be described by Maxwell's equations:

$$\nabla \cdot \boldsymbol{D} = \rho, \qquad \nabla \cdot \boldsymbol{B} = 0, \qquad \nabla \times \boldsymbol{E} = -\frac{\partial \boldsymbol{B}}{\partial t}, \qquad \nabla \times \boldsymbol{H} = \boldsymbol{j} + \frac{\partial \boldsymbol{D}}{\partial t}, \tag{1.55}$$

where $\boldsymbol{D}$ is electric flux density, $\boldsymbol{E}$ is electric field strength, $\boldsymbol{B}$ and $\boldsymbol{H}$ are magnetic flux and magnetic field respectively, ρ is charge density and $\boldsymbol{j}$ is electric current density (free carriers). In the linear regime, when the material is not charged, homogeneous, and isotropic the following set of equations can be established:

$$\rho = 0, \qquad \boldsymbol{j} = \sigma \boldsymbol{E}, \qquad \boldsymbol{D} = \varepsilon_0 \varepsilon \boldsymbol{E}, \qquad \boldsymbol{B} = \mu_0 \boldsymbol{H}, \tag{1.56}$$

where σ is conductivity, ε_0 is electric constant, μ_0 is magnetic constant and ε is the medium permittivity. Therefore, using Eq.1.55 one can derive the generalized wave equation for the dielectric system:

$$\begin{aligned} \nabla^2 \mathbf{E} - \frac{\varepsilon}{\mu_0 \varepsilon_0} \frac{\partial^2 \mathbf{E}}{\partial t^2} = \mu_0 \frac{\partial \boldsymbol{j}}{\partial t}, \text{ which gives:} \\ k^2 \boldsymbol{E} = \omega^2 \mu_0 \varepsilon \boldsymbol{E} + i \mu_0 \omega \sigma \boldsymbol{E}. \end{aligned} \tag{1.57}$$

By noting that speed of light is $c = \frac{1}{\sqrt{\varepsilon_0 \mu_0}}$ and dielectric constant of the material is $\varepsilon = \varepsilon_0 \varepsilon_b$, the wave vector expressed in terms of light frequency ω as:

$$\boldsymbol{k} = \frac{\omega}{c} \sqrt{\varepsilon_b + \frac{i\sigma}{\varepsilon_0 \omega}} = k' + ik'', \tag{1.58}$$

with ε_b and $i\sigma/\varepsilon_0\omega$ are the bound and free electron contributions to the relative dielectric constant, with k' and k'' being the real and imaginary parts of the complex wavevector, respectively. We then can rewrite $\boldsymbol{k}$ as:

$$\boldsymbol{k} = \frac{\omega}{c} \tilde{n}(\omega) \tag{1.59}$$

where $\tilde{n}(\omega) = n(\omega) + iK(\omega)$ is complex index of refraction, with refractive index $n(\omega)$ and extinction coefficient $K(\omega)$. With the extinction coefficient $K(\omega)$ one can estimate the EM wave intensity $I(z)$ [1] attenuation in medium along the z-direction. From the Beer-Lambert law we obtain:

$$I(z) = I_0 \exp(-\alpha z), \tag{1.60}$$

with $\alpha = 2\omega K/c = 4\pi K/\lambda$ is the absorption coefficient (λ is the light wavelength). The absorption of EM has an exponential profile for $K \neq 0$, while $K = 0$ defines lossless transmission.

1. $I(z) \propto |E_0 \exp(Kz)|^2$

The well-known relation between $\tilde{n}(\omega)$, electric susceptibility $\chi(\omega)$ and complex permittivity $\tilde{\varepsilon}(\omega)$ of the material written as:

$$\tilde{\varepsilon}(\omega) = 1 + \chi(\omega) = \tilde{n}^2(\omega) = \varepsilon_1(\omega) + i\varepsilon_2(\omega), \tag{1.61}$$

where $\varepsilon_1(\omega)$ is real and $\varepsilon_2(\omega)$ is the imaginary part of the frequency dependent dielectric constant. In a crystal, light-matter interaction depends on the crystal symmetry and light propagation direction with respect to the crystallographic plane orientation, resulting $\tilde{\varepsilon}, \chi(\omega)$ and $\tilde{n}$ being tensors. In this section, for simplicity, we will assume that our solids are isotropic, lifting the tensor notation for all the optical constants discussed below.

Drude and Lorentz Model: semi-classical approach

The electron degrees of freedom within partially filled electron bands and interband transitions play an important role in the optical properties of both metals and semiconductors. In this subsection, we address the intraband Drude and interband Lorentz contributions to the dielectric function $\tilde{\varepsilon}$.

In the Section 1.2.2 we defined the electrical conductivity σ of a metal and introduced the average phenomenological electron and hole relaxation time τ_e. Now, we want to explore the action of EM field $\boldsymbol{E}(t) = E_0(\exp[-i\omega t])$ on nearly-free conduction-band electrons. The classical damped equation of motion, describing the change in electron position $\boldsymbol{r}$ in time is written as:

$$m_e\left(\frac{d^2\boldsymbol{r}}{dt^2} + \frac{1}{\tau_e}\frac{d\boldsymbol{r}}{dt}\right) = -e\boldsymbol{E}(t). \tag{1.62}$$

We can express the single-electron dipolar moment as $\boldsymbol{p} = e\boldsymbol{r}$. Then, the macroscopic polarization $\boldsymbol{P}$ created by the displacement of the electron cloud reads [23]:

$$\boldsymbol{P} = n\boldsymbol{r} = \varepsilon_0\chi(\omega)\boldsymbol{E}(t). \tag{1.63}$$

Combining the two previous equations, we can deduce the free-electron contribution to the electric susceptibility of the crystal. The so-called Drude susceptibility is:

$$\chi^D(\omega) = -\frac{ne^2}{\varepsilon_0 m_e}\frac{1}{\omega^2 + i\omega/\tau_e} = -\frac{\omega_p^2}{\omega^2 + i\omega/\tau_e}, \tag{1.64}$$

with

$$\omega_p = \sqrt{\frac{ne^2}{\varepsilon_0 m_e}} \tag{1.65}$$

being the plasma frequency, where τ_e is the electron scattering time . The electron scattering rate involves multiple mechanisms, and highly depends on the electron temperature. Different scattering mechanisms involve carriers energy loss via coupling with the phonons, defects, impurities, surfaces

and with other carriers [24]. From Eq.1.61, we can write the Drude dielectric constant as:

$$\tilde{\varepsilon}^D(\omega) = 1 - \frac{\omega_p^2}{\omega^2 + i\omega/\tau_e}. \tag{1.66}$$

This equation tells that the optical properties within the Drude model solely depend on the plasma frequency and τ_e. Hence, we can establish 3 fundamentally different regimes of light-matter interaction in metals, depicted in Fig.1.11a:

1. $\omega\tau_e \ll 1$: Hagen-Rubens regime, where optical properties mainly defined by the DC conductivity (see Eq.1.24), rendering ε_1^D frequency-independent;
2. $1/\tau_e < \omega < \omega_p$: Relaxation regime, defining the range of frequency-independent light reflectivity
3. $\omega_p < \omega$: Transparent regime, where the metal becomes transparent, with a monotonous decrease of ε_1^D and ε_2^D.

For the semiconductor, the complex dielectric function can be derived from a Lorentz model of the bounded electrons:

$$m_e\left(\frac{d^2\boldsymbol{r}}{dt^2} + \frac{1}{\tau}\frac{d\boldsymbol{r}}{dt} + \omega_{0,n}^2\boldsymbol{r}\right) = -e\boldsymbol{E}(t), \tag{1.67}$$

that differs from the Drude model only by an additional restoring force term, which corresponds to the interband transition. This model does not lead to well-defined energy gaps, but it is widely used to describe non-conducting materials [25]. The derived Lorentz complex dielectric function, for multiple electron transitions reads:

$$\tilde{\varepsilon}^L(\omega) = 1 + \sum_n \frac{\omega_{p,n}^2}{\left(\omega_{0,n}^2 - \omega^2\right) + i\omega/\tau_n}, \tag{1.68}$$

where $\omega_{p,n}$ denotes the characteristic frequency associated to the electronic population of the level n, τ_n is the phenomenological damping time, defining the width of the Lorentz oscillator and $\omega_{0,n}$ is the resonant frequency of the n-th type electron interband transition. Interestingly, the classical Lorentz model is really close to its quantum counterpart [24]:

$$\tilde{\varepsilon}^L(\omega) = 1 + \sum_n \frac{f_n\omega_{p,n}^2}{(\omega_j^2 - \omega^2) + i\omega/\tau_n}, \tag{1.69}$$

with oscillator strength defined as:

$$f_j = \frac{2m_e^*}{\hbar^2}\hbar\omega_n|r_n|^2, \tag{1.70}$$

where r_n is the displacement of the n-th electron. The simple Lorentz model, with only one oscillator (see Eq.1.68) has 4 distinct spectral regimes:

1. $\omega < (\omega_0 - 1/\tau)$: Low frequency range, where ε_2^L is infinitely small, resulting little to no absorption ($\hbar\omega < E_g$);
2. $\omega \approx \omega_0$: Absorption range, where electrons can be excited across the bandgap;

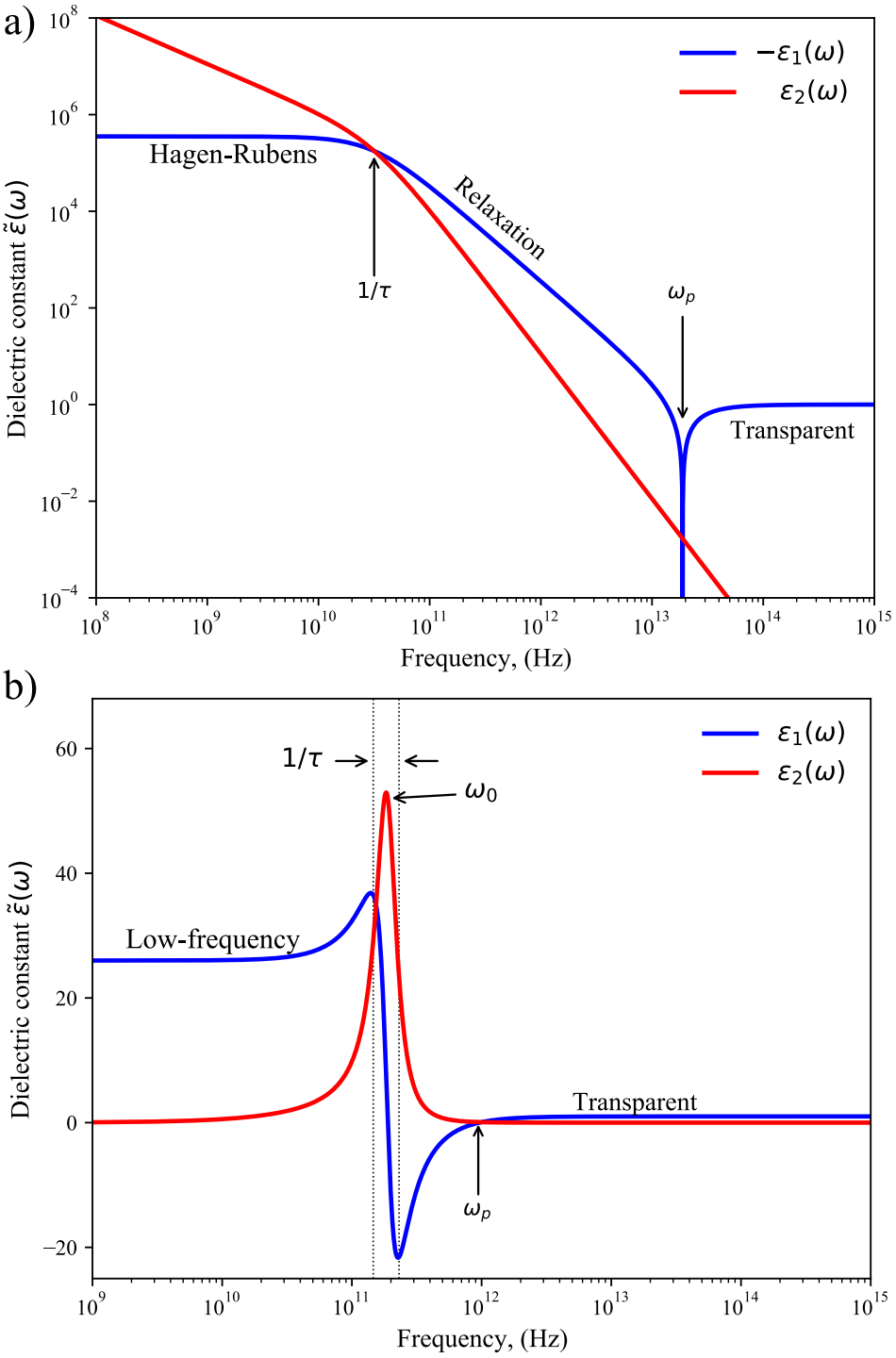

a) Complex Drude dielectric function of the metal, showing three different regimes of the light-matter interaction. Low-frequency Hagen-Rubens regime, with frequency-independent ε_1. Relaxation regime with $R = const$, and Transparent regime, where the metal becomes transparent. b) Complex dielectric function of a narrow-band semiconductor, calculated from the Lorentz model. The Low-frequency regime is an analogy to the Hagen-Rubens regime in metals. Around resonance frequency ω_0, photon absorption can excite the electrons over the bandgap, resulting in strong light absorption.

Figure 1.11 – *Free-electron Drude and restoring-force Lorentz models.*

3. $(\omega + 0 - 1/\tau) < \omega < \omega_n$: Reflection range, analogy of Drude relaxation regime;

4. $\omega > \omega_n$: Transparent regime, where reflectivity drops to zero, rendering material transparent.

Metals. Interband contribution

The Drude model shows good agreement with the experimental data in the low-frequency range, rapidly diverging from the experiment at higher frequencies. The reason is that the Drude model does not take into account the band structure of the metal. For the real 3D metal, the absorption of a photon with sufficiently high energy can provoke an interband transition of the electron from the valence band to the conduction band above the E_F. For example, we can separate the bound and free-electron contributions and account for possible interband transitions by introducing a Lorentz term into the Drude model. The combined Drude-Lorentz model gives:

$$\tilde{\varepsilon}^{DL}(\omega) = 1 - \frac{\omega_p^2}{\omega^2 + i\omega/\tau_e} + \sum_{n=1}^{n=k} \frac{\omega_{p,n}^2}{(\omega_{0,n}^2 - \omega^2) + i\omega/\tau_n}, \tag{1.71}$$

for k is the number for all allowed interband transitions. As seen from Fig.1.12a, the composite Drude-Lorentz model (with $n = 1$) slightly extends the prediction range of $\tilde{\varepsilon}(\omega)$. Even when accounting only for one Lorentz term, we still can estimate the energy of an interband transition threshold of Au ($\hbar\omega^{IB} \approx 2.7\,\text{eV}$), which is not so far from the real value of 2.4 eV. In a more general form, the dielectric constant of the metal is written as a function of both interband and intraband contributions as:

$$\tilde{\varepsilon}(\omega) = 1 + \chi^D(\omega) + \chi^{IB}(\omega), \tag{1.72}$$

where $\chi^{IB}(\omega)$ is interband electric susceptibility that accounts for all possible interband transitions. Interband transitions in metals can not be neglected in the high-frequency range and play an important role in the optical properties of metals. The optical frequencies above the interband transition threshold $\hbar\omega^{IB}$ will be highly absorbed. For example in Au, light with wavelengths below 520 nm will be strongly absorbed, translating to its "yellowish" color.

The excitation of an electron above the Fermi level will leave a vacancy at the electrons' initial position, known as a hole. Electron-hole pair excitation (due to intraband or interband absorption) must satisfy the law of momentum conservation:

$$\boldsymbol{k} = \boldsymbol{k}' + \boldsymbol{K}, \tag{1.73}$$

where $\boldsymbol{k}$ and $\boldsymbol{k}'$ are the electron and hole wave vectors, and $\boldsymbol{K}$ is reciprocal lattice vector. The momentum conservation can be fulfilled with two- or three-particle interactions.

The electron can absorb the photon if the photon energy corresponds to the energy difference between the hole and electron state:

$$\hbar\omega = \epsilon(\boldsymbol{k}) - \epsilon(\boldsymbol{k}'), \tag{1.74}$$

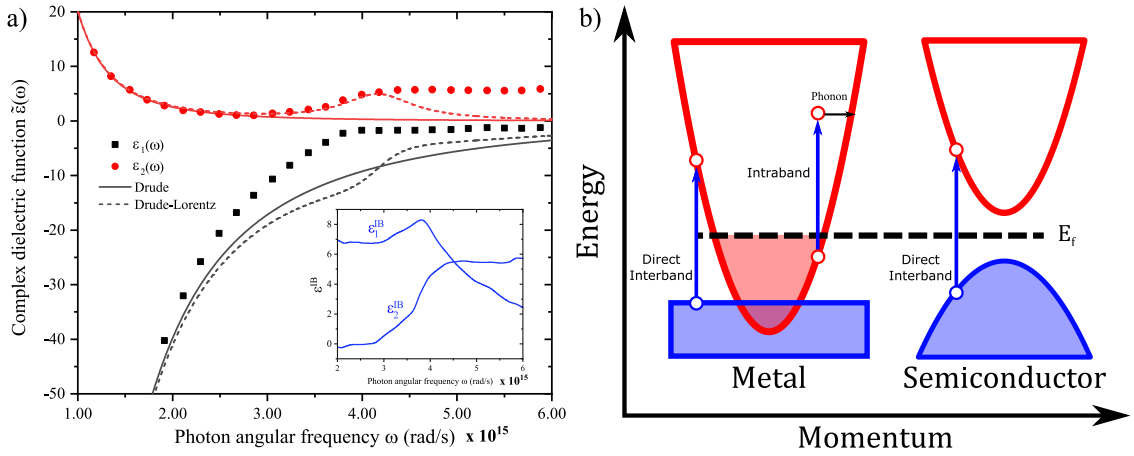

a) Comparison between the intraband Drude and composite Drude-Lorentz contributions to the real $\varepsilon_1(\omega)$ and imaginary $\varepsilon_2(\omega)$ parts of the experimental dielectric function of gold. Inset: Interband contribution, defined as the difference between experimental data and intraband Drude model to the real and imaginary parts of the Au's dielectric function. Experimental data are taken from [26]. b) Representation of the three possible electron transitions in metals and insulators. Direct interband absorption, mediated by the electron-photon interaction. Indirect intraband or interband transitions, followed by the phonon emission, are required due to the momentum conservation law.

Figure 1.12 – *Intraband and interband contributions to complex dielectric function of gold and schema of allowed transitions in metals and semiconductors.*

which defines the direct optical (or vertical) electron transition. In addition, the momentum conservation can be fulfilled by the emission/absorption of a third particle, for example, a phonon. In this case, the momentum conservation law reads:

$$\hbar\omega = \epsilon(\boldsymbol{k}) - \epsilon(\boldsymbol{k}') \pm \hbar\omega_{ph}, \tag{1.75}$$

where ω_{ph} is the frequency of emitted phonon. Normally, the direct optical transition requires the lowest amount of energy, and most of the time, it will be dominant during photon absorption.

Calculation of an interband contribution

The interband contribution to the dielectric constant can be calculated using the so-called Rosei model [27–29]. This model takes into account the effective masses of the electrons in the parabolic band structure of noble metals in different directions relative to the Γ point. If we consider the photon with energy $\hbar\omega$ that stimulates the transition from initial i to final f band, we can write:

$$\epsilon_f(\boldsymbol{k}) = \hbar\omega + \epsilon_i(\boldsymbol{k}), \tag{1.76}$$

with energies ϵ_f, ϵ_i in final and initial electron bands, respectively. With respect to [28, 30], we can write the joint density of states $J_{i\to j}$ as:

$$J_{i\to j}(\hbar\omega) = \int D_{i\to j}(\epsilon, \hbar\omega)[1 - f(\epsilon + \hbar\omega, \mu, T)]d\epsilon, \tag{1.77}$$

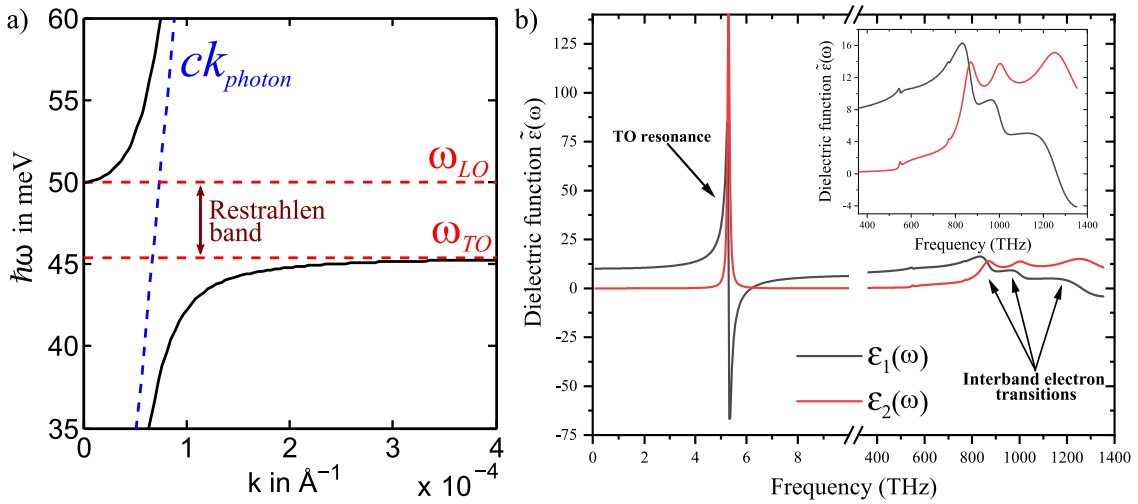

a) Coupling between photons and transverse optical phonon, called phonon-polariton. Redrawn from [32] and Wikipedia. b) High-frequency interband and low-frequency polariton contributions to ZnTe dielectric function. Both real and imaginary parts of the dielectric constant are flat in $8 - 400$ THz range. High-frequency properties are redrawn from [33].

Figure 1.13 – *Polariton dispersion curve and low-and-high frequency contributions to ZnTe dielectric constant* $\tilde{\varepsilon}(\omega)$.

where $D_{i\to j}(\epsilon, \hbar\omega)$ is the energy-dependent density of states, which depends on the type of the optical transition ($d \to s$ or $p \to s$, for example). Then, the imaginary part of the dielectric function can be calculated using the Lindhard theory [31]:

$$\epsilon_2^{IB}(\omega) \propto \frac{1}{\omega^2}\left|M^{i\to f}\right|^2 J_{i\to j}(\hbar\omega), \tag{1.78}$$

where $M^{i\to f}$ is the averaged electron momentum matrix element between the initial and final bands. The $1/\omega^2$ term comes from the electric dipole approximation. Interestingly, the Eq.1.78 can be used to calculate the dielectric constant for the semiconductor [24], which does not include the spin-orbit interaction. The real part of the dielectric function can be obtained by applying the Kramers–Kronig relationship to Eq.1.78.

Semiconductors. Ion contribution

As discussed in the Section 1.2.1, crystals with two (or more) atoms per unit cell can support optical vibrational modes. Furthermore, some polar optical phonons (also known as infrared active) can be directly coupled to the incident EM wave [32]. This happens due to the momentum conservation between the photons and phonons, resulting in the excitation of a quantized particle called phonon-polariton (see Fig.1.13a).

The coupling between photons and phonons can be modeled with slightly-modified Lorentz model [34]:

$$\tilde{\varepsilon}(\omega) = \varepsilon_\infty + \sum_j \frac{S_j\omega_j^2}{\omega_j^2 - \omega^2 - i\omega/\tau_j}, \tag{1.79}$$

where ε_∞ is the dielectric constant of the ion background (i.e that of the conduction electrons, see the Eq.1.71). Here, we account for the contribution of all lattice oscillations that can interact with EM fields, with eigenfrequency ω_j, damping time τ_j, and dimensionless oscillator strength S_j. For most semiconductors, this equation can be simplified by restricting the sum to the first low-frequency TO mode:

$$\tilde{\varepsilon}(\omega) = \varepsilon_\infty + \frac{S_{TO}\omega_{TO}^2}{\omega_{TO}^2 - \omega^2 - i\omega/\tau_{TO}}. \tag{1.80}$$

The oscillator strength S_{TO} can be deduced from the DC dielectric constant [34] as:

$$\tilde{\varepsilon}(0) = \varepsilon_{ion} + S_{TO}. \tag{1.81}$$

From the Lyddane-Sachs-Teller relation [35], Kurosawa [36] showed the direct connection between S_{TO} and the frequency difference between non-excited ω_{LO} and resonant ω_{TO} modes:

$$S_{TO}\omega_{TO}^2 = \omega_{LO}^2 - \omega_{TO}^2. \tag{1.82}$$

Due to the phonon-polariton coupling in ionic materials, this equation suggests that the lattice will strongly absorb photons with energies from $\hbar\omega_{TO}$ to $\hbar\omega_{LO}$. This frequency range is called the Reststrahlen band and ω_{TO} sometimes referred to as Restrahl frequency.

To give a real example of phonon-polariton, the complex dielectric function of ZnTe from DC to 1400 THz is displayed in Fig.1.13b. The high-frequency contribution was redrawn from [33], showing well-pronounced interband contribution [2] to the dielectric constant around $\approx$ 800 THz (375 nm wavelength). Low-frequency phonon-polariton contribution calculated with parameters from [37], showing strong photon absorption around 5.3 THz. The presence of the Reststrahlen band is the main limiting factor for the semiconductor optics in the THz frequency range.

1.3.1.1 Nonlinear Regime

Light-matter interaction can modify the macroscopic polarization of the crystal (see Eq.1.63) proportional to its electric susceptibility. The total electronic displacement under the applied electric field is defined as:

$$\boldsymbol{D} = \varepsilon_0\tilde{\varepsilon}(\omega)\boldsymbol{E}(t) = \varepsilon_0[1 + \chi(\omega)]\boldsymbol{E}(t) = \varepsilon_0\boldsymbol{E}(t) + \boldsymbol{P}(\omega, t). \tag{1.83}$$

For the electric fields with amplitudes comparable to the strength of the atomic field, i.e.:

$$E_{at} = \frac{e}{4\pi\varepsilon_0 a_0^2} = 5.14 \times 10^{11}, \quad \left[\frac{\mathrm{V}}{\mathrm{m}}\right] \tag{1.84}$$

where a_0 is the Bohr radius of the Hydrogen atom, can induce the nonresonant precession of the macroscopic polarization $\boldsymbol{P}$ [23]. This nonlinearity is accounted for by expressing the polarization

2. related to the excitation of excitons, which is not discussed here

Material	$\chi^{(2)}$ (pm/V)	r (pm/V)
ZnTe	137	4.04
GaP	49.6	1.94
BBO	3.6	2.1
$LiNbO_3$	336	30.9
GaAs	131.1	1.43

From [38]

Table 1.1 – *Values of second order susceptibilities for ZnTe, GaP, BBO, $LiNbO_3$ and GaAs.*

$\boldsymbol{P}$ as a power series in the field strength $\boldsymbol{E}$:

$$\boldsymbol{P}(t) = \varepsilon_0[\chi^{(1)}\boldsymbol{E}(t) + \chi^{(2)}\boldsymbol{E}^2(t) + \chi^{(3)}\boldsymbol{E}^3(t) + ...] \equiv \boldsymbol{P}^{(1)}(t) + \boldsymbol{P}^{(2)}(t) + \boldsymbol{P}^{(3)}(t) + ..., \quad (1.85)$$

with $\chi^{(1)}$ known as linear susceptibility, $\chi^{(2)}$ and $\chi^{(3)}$ are 2^{nd}- and 3^{rd}-order nonlinear optical susceptibilities, and so on. By isolating the linear contribution $\boldsymbol{P}^L$, Eq.1.85 becomes:

$$\boldsymbol{P} = \boldsymbol{P}^L + \boldsymbol{P}^{NL}, \quad (1.86)$$

with nonlinear contribution $\boldsymbol{P}^{NL}$ containing all power terms of $\boldsymbol{E}$. In this subsection, the discussion will be limited to the 2^{nd} order nonlinear processes, when relevant to this work higher-order nonlinearities will be mentioned in the experimental section.

Second Order Nonlinear Processes

Let us first estimate the value of second-order nonlinear susceptibility in condensed matter. In the nonlinear regime, at some peak value of E_{peak} one can expect electrons to "explore" the non harmonic part of ionic potential, resulting in equal contributions of linear $\boldsymbol{P}^{(1)}(t)$ and nonlinear terms $\boldsymbol{P}^{(2)}(t)$ to the total polarization $\boldsymbol{P}(t)$. In most solids, $\chi^{(1)}$ normally is in the order of unity. By setting $E_{peak} = E_{at}$, the Eq.1.85 gives:

$$\chi^{(2)} = \frac{1}{E_{at}} = 1.94 \times 10^{-12}. \quad \left[\frac{\mathrm{m}}{\mathrm{V}}\right] \quad (1.87)$$

This estimation is quite accurate compared to experimentally measured values displayed in Table 1.1. The value of $\chi^{(2)}$ can be interpreted as the efficiency of nonlinear interaction in a given solid.

In the case of centrosymmetric medium, the shape of electron potential obeys $V(\boldsymbol{r}) = V(-\boldsymbol{r})$ [23]. Simple estimation of the second-order nonlinear polarization induced by the EM wave with frequency ω:

$$-\boldsymbol{P}^{(2)} = \chi^{(2)}(\omega)[-\boldsymbol{E}(\omega)][-\boldsymbol{E}(\omega)] = \chi^{(2)}(\omega)\boldsymbol{E}^2(\omega) = \boldsymbol{P}^{(2)}. \quad (1.88)$$

Obtained equality $-\boldsymbol{P}^{(2)} = \boldsymbol{P}^{(2)}$ holds only when $\chi^{(2)} = 0$. The group theory predicts that each element of $\chi^{(2)}$ vanishes in the centrosymmetric crystals [23], allowing only nonlinear interactions

proportional to the odd powers of the electric field. However, nonlinear interactions of both odd and even power of $\boldsymbol{E}$ are allowed in noncentrosymmetric crystals, such as ZnTe, GaP, Beta Barium Borate (BBO), and more.

In the case of a noncentrosymmetric, isotropic medium with no dispersion, by taking into account linear and nonlinear polarization, the driven Maxwell wave-equation becomes [23]:

$$\nabla^2 \boldsymbol{E} - \frac{\tilde{\varepsilon}^{(1)}}{c^2}\frac{\partial^2 \boldsymbol{E}}{\partial t^2} = \frac{1}{\varepsilon_0 c^2}\frac{\partial^2 \boldsymbol{P}^{NL}}{\partial t^2}, \tag{1.89}$$

with $\tilde{\varepsilon}^{(1)} = 1 + \chi^{(1)}$, where the second order time derivative of nonlinear polarization acts as the source term. We now examine the set of possible frequencies of electron polarization precession in the nonlinear media. Let us apply two-color EM field:

$$\boldsymbol{E} = E_1 e^{-i\omega_1 t} + E_2 e^{-i\omega_2 t} + c.c., \tag{1.90}$$

where $E_1 = A_1 e^{ik_1 z}$ and $E_2 = A_1 e^{ik_2 z}$. With Euler's formula $\cos(x) = (e^{ix} + e^{-ix})/2$, the complete second-order nonlinear polarization induced by the two-color EM field:

$$\begin{aligned} &P^{(2)}(t) = \varepsilon_0 \chi^{(2)} \boldsymbol{E}(t)^2 = \\ &= \frac{1}{2}\varepsilon_0 \chi^{(2)} \left[\begin{array}{l} E_1^2[\cos(2\omega_1 t) + \cos((\omega_1 - \omega_1)t)] + \\ +E_2^2[\cos(2\omega_2 t) + \cos((\omega_2 - \omega_2)t)] + \\ +2E_1E_2\cos[(\omega_1 + \omega_2)t] + 2E_1E_2\cos[(\omega_1 - \omega_2)t] \end{array} \right]. \end{aligned} \tag{1.91}$$

With four different permutations between two frequencies $\omega_{1,2}$ the grouped contributions to the second order nonlinear polarization are:

$$\begin{aligned} &P^{(2)}(2\omega_{1,2}) = \frac{1}{2}\varepsilon_0 \chi^{(2)} E_{1,2}^2 \cos(2\omega_{1,2} t) \quad \text{Second harmonic generation (SHG);} \\ &P^{(2)}(0\omega) = \frac{1}{2}\varepsilon_0 \chi^{(2)} E_{1,2}^2 \quad \text{Optical rectification (OR);} \\ &P^{(2)}(\omega_1 + \omega_2) = \varepsilon_0 \chi^{(2)} E_1 E_2 \cos[(\omega_1 + \omega_2)t] \quad \text{Sum frequency generation (SFG);} \\ &P^{(2)}(\omega_1 - \omega_2) = \varepsilon_0 \chi^{(2)} E_1 E_2 \cos[(\omega_1 - \omega_2)t] \quad \text{Difference frequency generation (DFG),} \end{aligned} \tag{1.92}$$

with SHG and OR being the special cases of SFG and DFG. The nonresonant movement of dipole moments $\boldsymbol{P}^{NL}$ will create the nonlinear current density $\boldsymbol{J}^{NL}$, equal to:

$$\frac{d\boldsymbol{P}^{NL}}{dt} = \boldsymbol{J}^{NL}. \tag{1.93}$$

Such transient precession of the $\boldsymbol{J}^{NL}$ can lead to the emission of light at different frequencies, as shown in Fig.1.14:

$$\boldsymbol{E}^{NL}(t) \propto \frac{\partial \boldsymbol{J}^{NL}}{\partial t} \propto \frac{\partial^2 \boldsymbol{P}^{NL}}{\partial t^2}. \tag{1.94}$$

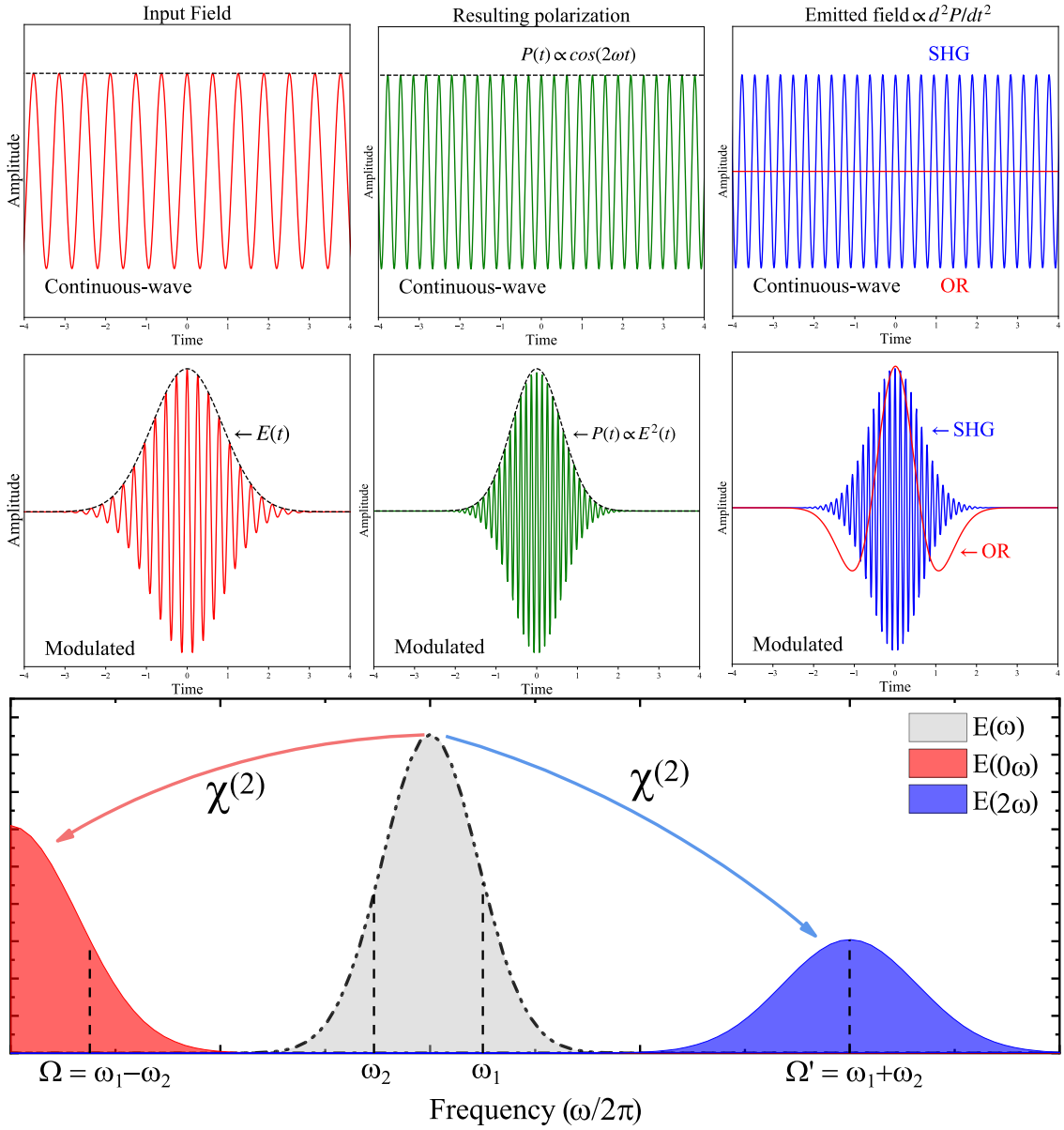

Second order nonlinear polarization for two different laser temporal profiles. OR for continuous-wave source creates DC inside the crystal. The modulated pulse envelope varies in function of time, resulting in the emission of low-frequency pulse via OR. Image adapted from the lecture of Dmitry Turchinovich. Bottom: SHG and OR mediated by the $\chi^{(2)}$ interaction in the frequency domain.

Figure 1.14 – *SHG and OR for Continuous-Wave and Modulated laser pulses.*

However, it adds an important constraint: the driven wave equation (see Eq.1.89) must hold for all frequencies, including the newly created ones.

Let us consider only the SFG created by the two-color field. Under slowly varying field amplitude approximation [23], Eq.1.89 can be reduced to the spatial variation of $\omega_3 = \omega_1 + \omega_2$:

$$\frac{dA_3}{dz} = \frac{i\chi^{(2)}(\omega_1 + \omega_2, \omega_1, \omega_2)\omega_3}{n_3 c} A_1 A_2 e^{i[k_1 + k_2 - k_3]z}, \tag{1.95}$$

where n_3 is crystal refractive index at ω_3. This relation shows that the amplitude of the EM wave A_3 at ω_3 depends on the coupling between A_1 and A_2. We can introduce the so-called wavevector-, momentum- or phase mismatch as Δk:

$$\Delta k = k_1 + k_2 - k_3. \tag{1.96}$$

By integration of Eq.1.95 over the distance d, the intensity of SFG radiation will be $\propto \mathrm{sinc}^2(\Delta k z/2)$. This means that the most efficient coupling between ω_1 and ω_2 is when $k_3 = k_1 + k_2$. Usually, the increase in light frequency ω is not compensated by the decrease in $\tilde{n}$, meaning that the perfect phase matching is rarely achieved. Multiple techniques were developed to minimize the Δk, with birefringent phase-matching being the most used one. In addition, wavevector mismatch is sensitive to the crystal imperfections, laser beam quality, laser polarization state, and more. The discussion about the phase-matching importance for the second-order nonlinear processes will continue in the experimental section.

The remaining second-order nonlinear process of interest is the linear electro-optic effect, known as the Pockels' effect. Pockels' effect explains the modification of refractive indices of the crystal with an applied electric field. The contracted notation of the electrooptic effect is given by [23]:

$$\Delta\left(\frac{1}{n^2}\right)_i = \sum_j r_{ij} E_j, \tag{1.97}$$

where r_{ij} is the electrooptic tensor. Electrooptic effect can be pictured as follows: external DC electric field will tilt the crystals' optical axes by an amount $\propto \pm\frac{1}{2} n_0^3 r_{ij} E_z$, introducing the phase retardation between two orthogonal light polarization components [23]:

$$\Gamma = (n_i - n_j)\frac{\omega L}{c} = \frac{n_0^3 r_{ij} E_j \omega L}{c}, \tag{1.98}$$

with the speed of light in vacuum c, crystal thickness L and refractive index n_0 in the absence of electric field. Electrooptic effect is used for the high-frequency light modulation and detection of the THz radiation, for example. Interestingly, the response time of a Pockels' effect is in the order of femtoseconds [39], allowing ultrafast switching of the light polarization with picosecond electromagnetic pulses [40].

1.3.2 Polarization, reflection, and transmission of an electromagnetic wave

Polarization

Light can be described as the periodic oscillation of the EM field in the xy plane travelling along the z axis in Cartesian space. Mathematically, we can write equation of the complex EM field as:

$$\boldsymbol{E} = \boldsymbol{E_0} \exp\left[i(\boldsymbol{k}z - \omega t + \phi)\right], \tag{1.99}$$

where $\boldsymbol{E}$ is the electric field with the field-wave vector $\boldsymbol{k}$ frequency ω and phase ϕ. At the given time t, the direction of electric field can be expressed through the unit vectors $\mathbf{x}$ and $\mathbf{y}$:

$$\boldsymbol{E} = E_{0x} \exp\left[i(kz - \omega t + \phi_x)\right]\mathbf{x} + E_{0y} \exp\left[i(kz - \omega t + \phi_y)\right]\mathbf{y}. \tag{1.100}$$

The direction of the electric field vector $\boldsymbol{E}$ along $\mathbf{x}$ and $\mathbf{y}$ axes is known as polarization of EM wave, and it is completely determined by the amplitudes and phase difference of the two orthogonal electric field components. It can be written in the form of the two-element matrix, called Jones vector:

$$\boldsymbol{E_0} = \begin{bmatrix} E_{0x} e^{i\phi_x} \\ E_{0y} e^{i\phi_y} \end{bmatrix}. \tag{1.101}$$

With the Jones matrix notation, it is easy to represent the linearly, elliptically, and circularly polarized light, including the polarization handedness direction. Randomly polarized or nonpolarized light does not require the use of the matrix notation. Linear polarization of the light in the xy plane, according to the Jones vector notation defined as:

$$\boldsymbol{E_0} = \begin{bmatrix} E_{0x} \\ E_{0y} \end{bmatrix}, \tag{1.102}$$

with both E_{0x} and E_{0y} being real, non-zero field amplitudes. The periodically varying amplitude of the electric field is inclined relative to the origin by the angle $\alpha = \tan^{-1}(E_{0y}/E_{0x})$ [41]. $E_{0x} = 1, E_{0y} = 0$ correspond to the linear light polarization along the x axis.

The general expression for the elliptically polarized light given as:

$$\boldsymbol{E_0} = \begin{bmatrix} E_{0x} \\ E_{0y} e^{\pm i\phi_y} \end{bmatrix}, \tag{1.103}$$

where the sign of the ϕ_y defines the direction of the polarization rotation. If ϕ_y is positive, electric field direction will rotate in counterclockwise direction, when negative ϕ_y corresponds to the clockwise handedness. The inclination angle of a polarization ellipse equals to the absolute value of ϕ_y. If $E_{0x} = E_{0y}$ and $\phi_y = \pi/2$, such EM wave has left-handed circular polarization.

Reflection and Transmission. Transfer matrix formalism

The transmission and reflection of an EM radiation at the singular plane surface depends on the following set of variables: the angle of incidence θ_1 and refraction θ_2, the refractive indices of incident n_1 and refractive media n_2, and the light polarization direction. The ratio between the total, reflected and transmitted EM amplitudes can be derived from the Maxwell equations at the boundary condition as shown elsewhere [41]. Obtained equations, namely, the polarization

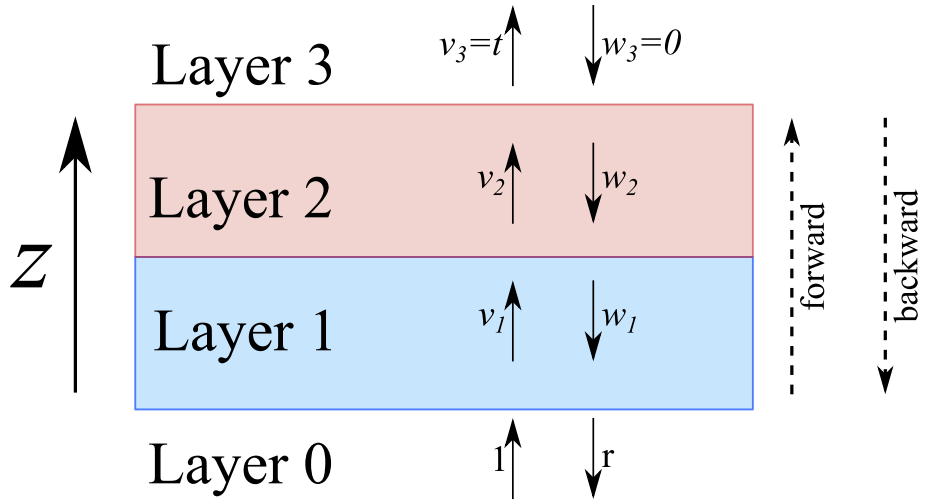

Optical stack (two layers between the two half-spaces) with N=4. v_i, w_i are the amplitudes of the forward and backward propagating waves. Boundary conditions defined as $v_{N-1} = t, w_{N-1} = 0$ and $v_0 = 1, w_0 = r$. The image adapted from [42]

Figure 1.15 – *Beam transmission and reflection from a multi layer film stack.*

dependent Fresnel reflection r and transmission t coefficients read:

$$\begin{aligned} r_s &= \frac{n_1 \cos\theta_1 - n_2 \cos\theta_2}{n_1 \cos\theta_1 + n_2 \cos\theta_2}, \qquad & r_p &= \frac{n_2 \cos\theta_1 - n_1 \cos\theta_2}{n_2 \cos\theta_1 + n_1 \cos\theta_2} \\ t_s &= \frac{2n_1 \cos\theta_1}{n_1 \cos\theta_1 + n_2 \cos\theta_2}, \qquad & t_p &= \frac{2n_1 \cos\theta_1}{n_2 \cos\theta_1 + n_1 \cos\theta_2} \end{aligned} \tag{1.104}$$

where subscripts p and s correspond to the parallel and perpendicular alignment of the electric field polarization relative to the lights' plane of incidence.

The transmission and reflection of light in a complex multilayer system can be approached from the view of the superposition of EM waves within the given layer. For example, the arbitrary N layer configuration has $n = 0, 1, ..., N-1$ optically different interfaces, that contribute to the total transmission and reflection. An example of the N=4 stack system is shown in the Fig.1.15, defining the amplitudes of the forward and backward propagating waves. The amplitudes of transmitted and reflected light arriving at the interface $n = 1, 2, \ldots, N-2$ can be expressed in the matrix notation as:

$$\begin{pmatrix} v_n \\ w_n \end{pmatrix} = \mathbf{M}_n \begin{pmatrix} v_{n+1} \\ w_{n+1} \end{pmatrix}, \tag{1.105}$$

where the n^{th} layer transfer matrix M_n is equal:

$$\mathbf{M}_n \equiv \begin{bmatrix} e^{-i\delta_n} & 0 \\ 0 & e^{i\delta_n} \end{bmatrix} \begin{bmatrix} 1 & r_{n,n+1} \\ r_{n,n+1} & 1 \end{bmatrix} \frac{1}{t_{n,n+1}}, \tag{1.106}$$

with the n^{th} layer phasor $\delta_n = d_n \boldsymbol{k}_n$, where d_n is the thickness of the layer. Here, the M_n is the product of so called phase/absorption matrix:

$$\mathbf{P}_n = \begin{bmatrix} e^{-i\delta_n} & 0 \\ 0 & e^{i\delta_n} \end{bmatrix}, \tag{1.107}$$

and refraction/transmission matrix

$$\mathbf{D}_n \mathbf{D}_{n-1}^{-1} = \begin{bmatrix} 1 & r_{n,n+1} \\ r_{n,n+1} & 1 \end{bmatrix} \frac{1}{t_{n,n+1}}, \tag{1.108}$$

with Fresnel reflection $r_{n,n+1}$ and transmission $t_{n,n+1}$ coefficients for the light directed from the interface n towards the interface $n+1$. The repeated application of phase/absorption and refraction/transmission matrices over N-2 layers and N-1 interfaces will result in the following expression [43]:

$$\begin{aligned} \begin{pmatrix} 1 \\ r \end{pmatrix} &= \mathbf{D}_0^{-1} \left[\prod_{n=1}^{N-2} \mathbf{D}_n \mathbf{P}_n \mathbf{D}_n^{-1} \right] \mathbf{D}_{N-1} \begin{pmatrix} t \\ 0 \end{pmatrix} \\ &= \begin{bmatrix} T_{11} & T_{12} \\ T_{21} & T_{22} \end{bmatrix} \begin{pmatrix} t \\ 0 \end{pmatrix}. \end{aligned} \tag{1.109}$$

This 2×2 matrix accounts for the coherent interaction of the reflected and transmitted beams at each interface of the multilayer optical media. Usually, $\left[\begin{smallmatrix} T_{11} & T_{12} \\ T_{21} & T_{22} \end{smallmatrix}\right]$ is referred to as system transfer matrix $\mathbf{T} = \mathbf{T}_{0/(N-1)}$.

1.3.3 Temporal evolution of optical properties

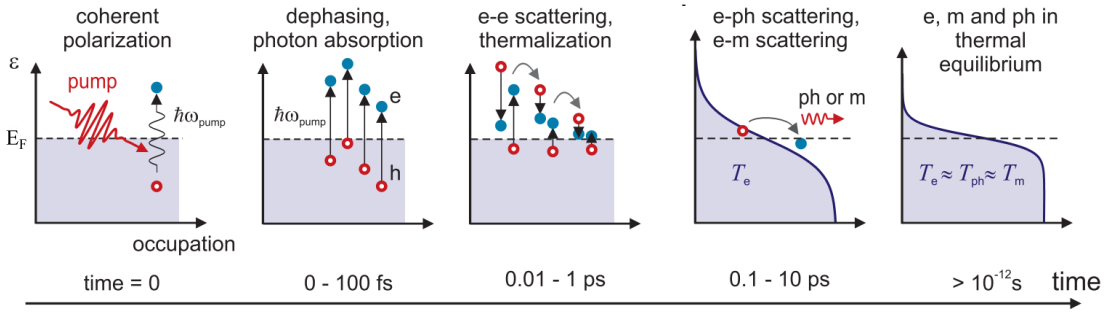

Ultrafast processes induced by the absorption of an ultrashort laser pulse in metals. Image is reprinted from the thesis of T.Seifert [44]

Figure 1.16 – *Evolution of the electronic distribution after an ultrashort laser action.*

The development of ultrashort laser pulses allowed to study the ultrafast dynamics of solids, molecules, and chemical compounds on the timescales comparable to the carrier relaxation times [45]. For example, let us consider interaction of the fs laser pulse with the matter. Ultrafast laser action and the carrier-photon absorption will initially create highly-nonlinear photoexcited electronic distribution, which will then try to reach new equilibrium state between electron, lattice, and spin subsystems.

In metals, immediately after laser irradiation, the light-induced dipole polarization will create the superposition of the electron states above and below E_F. Simultaneously, light absorption will lead to an athermal, nonlinear distribution of the electron-hole pairs. The following energy transfer from the photoexcited carriers involves the multiple-particle interactions (electron-electron, electron-phonon, and electron-magnon), in order to bring the excited system to the thermal equilibrium.

The fastest many-particle relaxation process in the electron-electron interaction, which is happening at the sup-picosecond time scale. Electron subsystem will thermalize via carrier multiplication, reaching the Boltzmann distribution at elevated temperature [45]. Subsequently, the thermalization process between electronic, ionic, and spin baths occurs at the timescales of 0.1-10 picoseconds. After electrons, magnons, and phonons have thermalized, heat dissipation to the environment will occur, lasting more than 10 picoseconds. The sketch of the electron thermalization process is displayed in the Fig.1.16.

Phenomenological Two and Three-Temperature Models

The phenomenological macroscopic model was established to explain the interaction between electron, phonon, and spin subsystems of a solid at the ultrashort timescale with the evolution of experimental techniques. The first description of electron-phonon interaction after the absorption of the laser pulse was proposed by the introduction of the energy balance equation [46]:

$$\begin{cases} c_e(T_e)\dfrac{dT_e}{dt} = -G_{e-ph}(T_e - T_l) + I(t); \\ c_L(T_l)\dfrac{dT_l}{dt} = -G_{e-ph}(T_l - T_e), \end{cases} \tag{1.110}$$

where G_{e-ph} is the electron-phonon coupling constant and $I(t)$ is the laser source term. The carriers and phonon (heat) diffusion terms are neglected to simplify the model. $I(t)$ applied only to the electron subsystem since the initial energy absorption is mediated only by the electrons. These equations were then denoted as the phenomenological two-temperature model (TTM) [47].

In the work of Beaurepaire et al. studying the ultrafast response of a ferromagnetic Ni, an extension of the TTM, which includes the electron-phonon-spin interaction was proposed [48]. Beaurepaire's system of equation, named as the three-temperature model (3TM), reads:

$$\begin{cases} c_e(T_e)\dfrac{dT_e}{dt} = -G_{e-ph}(T_e - T_l) - G_{e-m}(T_e - T_s) + I(t); \\ c_s(T_s)\dfrac{dT_s}{dt} = -G_{e-m}(T_s - T_e) - G_{m-ph}(T_s - T_l); \\ c_L(T_l)\dfrac{dT_l}{dt} = -G_{e-ph}(T_l - T_e) - G_{m-ph}(T_l - T_s), \end{cases} \tag{1.111}$$

with additional electron-magnon G_{e-m} and magnon-phonon G_{m-ph} coupling constants. Similar to the TTM, this model suggests that the heat exchange between electron, phonon, and spin subsystems is proportional to the temperature difference between the two given baths. The respective coupling constant then defines the efficiency of the heat transfer (see Fig.1.17a). The coupling constants in simple metals G_{e-m}, G_{m-ph} and G_{e-ph} can be derived from the complex considerations

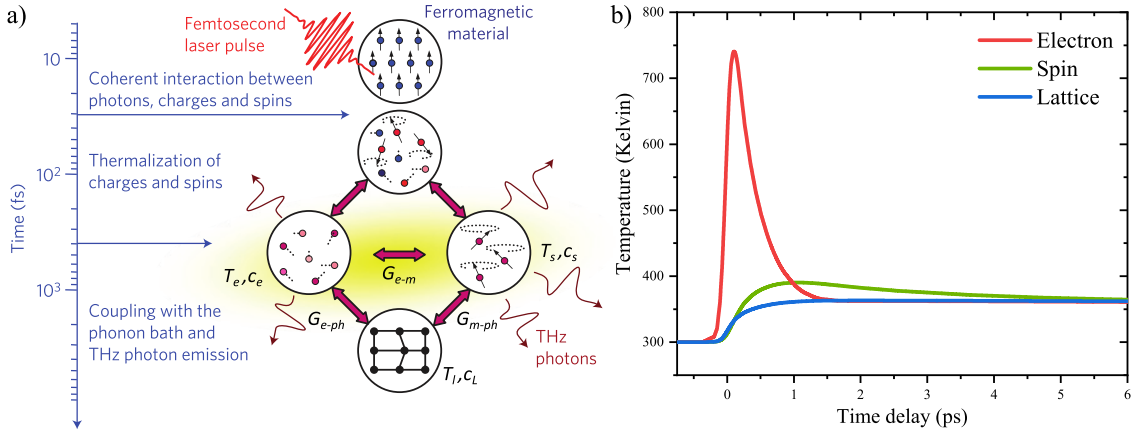

a) Sketch of the three-temperature model suggested by Beaurepaire et al. [48]. Solid arrows depict the energy flow between the respective subsystems in the solid-state. Figure taken from [49] b) Calculated temperatures of the electron, phonon, and spin subsystems in CoFeB 5 nm layer after the absorption of the ultrashort laser pulse. The coupling constants were taken from [50]

Figure 1.17 – *The three-temperature model sketch and temporal evolution of electron, phonon and spin temperatures of CoFeB film.*

of the magnon, phonon, and electron dispersion curves, Boltzmann statistics, and with knowledge about the respective particles' scattering times [7, 9, 24]. However, the magnitudes of coupling constants and characteristic population decay times can be extracted with specific time-resolved measurements. For example, some coupling constants can be derived in the frame of 3TM-based molecular dynamics simulations, where experimental data used as the reference [51].

With the knowledge of CoFeB coupling constants from the literature [52–57], we can use 3TM, neglecting weak magnon-phonon energy exchange, to display the temporal evolution of electron, spin, and magnon temperatures upon laser absorption (see Fig.1.17b). The slow spin thermalization in CoFeB is explained with G_{e-m} being ≈ 60 times smaller compared to G_{e-ph}.

Chapter 2

Experimental Methods

Contents

2.1 Introduction

This chapter will focus on the description of the experimental techniques. First, we address the principle of the stroboscopic measurements, allowing us to record the transient dynamics of the material at the femtosecond and picosecond timescales. Second, we discuss the THz generation via second-order nonlinear processes, and its particular configuration, the tilted-pulse front method. The next part is devoted to the field-resolved detection of the pulsed THz radiation. After describing the electrooptic sampling technique, we calculate the detector response function for the crystals used in this work. In addition, we introduce and characterize the method of the electrooptic detection improvement, which made possible the detection of the THz emission from the spintronic emitters discussed in the Chapter 4. The last subsection is about the basics of the THz Time domain spectroscopy (THz-TDS), where we present measured properties of silicon, silica, and x-cut Quartz in the THz range.

2.2 Pump-probe spectroscopy

Since its first implementation, the stroboscopic approach has dramatically improved and now it is widely used in science, art, and the entertainment industry. For example, the fastest high-speed camera can record up to 1 Million frames per second (Phantom v2512) and is used in the field of microfluidics and particle velocimetry [58]. In addition, the ultrafast photodiodes with the rise-time of about 15 ps are now commercially available. However, since the temporal resolution

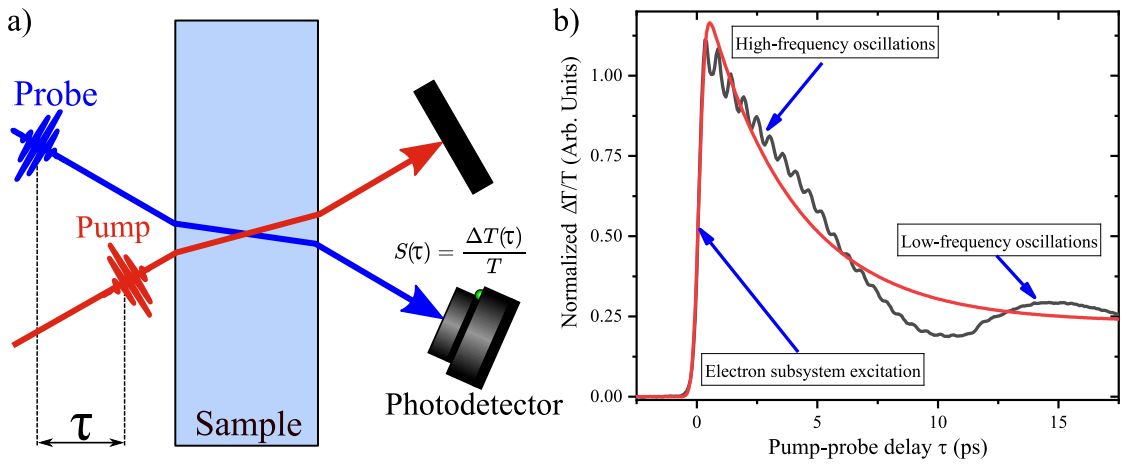

a) Sketch of the pump-probe experiment in transmission. The probe pulse is delayed in time with respect to the pump beam. We record the relative change in the probe's transmission for the different temporal overlaps between the pump and the probe. **b)** Example signal, obtained with the Bi_2Te_3 15 nm film, while excited with 800 nm pump and probed with 400 nm pulse. The sharp increase in the $\Delta T/T$ corresponds to the temporal overlap between the pump and the probe and consequent electron subsystem excitation. The subsequent exponential decay of the relative transmittance corresponds to electron-electron, electron-phonon coupling, and heat dissipation. In addition, one can reveal some coherent dynamics (high and low-frequency modulation of the $\Delta T/T$) with the pump-probe spectroscopy.

Figure 2.1 – *Two-color pump-probe: Setup geometry and a typical recorded* $\Delta T/T$ *variation of* 15 nm Bi_2Te_3.

is limited by the shutter speed or carrier velocities in electronic detectors, it is impossible to use these gating devices at the sub-picosecond timescales.

However, one can achieve sub-picosecond temporal resolution with pulsed laser radiation, where the width of the sampling pulse envelope can be as short as a couple of tens of attoseconds (10×10^{-18} s) [59–61]. In this thesis, ultrafast nonlinear spectroscopy was performed in pump-probe geometry. For this, the output laser beam is spatially split into two parts. The first part, called the pump, is used to excite the electronic subsystem of the sample, triggering the change of the dielectric, structural or magnetic properties. The second part of the laser beam, is used to monitor or probe the change in reflectance ($\Delta R(\tau)/R$) or transmittance ($\Delta T(\tau)/T$) of the probe beam as the function of temporal delay τ between the pump and the probe pulses. The τ is adjusted by changing the optical path length of one of two beams ($\tau = \Delta l/c$), as shown in Fig.2.1a.

Today, various pump-probe based experimental techniques can measure the dynamics of a solid at the sub-picosecond timescales, using different parts of the EM spectrum of light. For example, experiments can be done with different configurations, such as all-optical pump-probe, time-resolved magneto-optical Kerr effect [48], time-resolved X-ray diffraction [62], and many more. All those pump-probe "derivatives" are designed to probe and/or excite a specific degree of freedom of matter. For example, during the all-optical pump-probe experiment, one measures the relative change in the intensity of probing light with a central frequency of ω_{pr} over the time τ, linked to the temporal change in the dielectric function of the excited material. Let us write the total

electric field inside the studied media as [63]:

$$E(\tau) = \frac{1}{2}\big[E_{\mathrm{pr}}(\boldsymbol{k}_{\mathrm{pr}},\tau) + E_{\mathrm{pump}}(\boldsymbol{k}_{\mathrm{pump}},\tau) + E^{*}_{pr}(\boldsymbol{k}_{\mathrm{pr}},\tau) + E^{*}_{\mathrm{pump}}(\boldsymbol{k}_{\mathrm{pump}},\tau)\big]. \tag{2.1}$$

From the perturbation theory, the first order interaction describes the absorption of either the pump and the probe beams, governed by $\chi^{(1)}$ susceptibility. Next, the second order field-interaction includes the second harmonic generation (SHG), optical rectification (OR) of pump and probe beam, and the frequency mixing between the pump and the probe ($\omega_{\mathrm{pr}} \pm \omega_{\mathrm{pump}}$) pulses, as discussed in the Section 1.3. In our case, we are only interested in the ω_{pr} field components able to reach the detector (i.e. propagating along the $\boldsymbol{k}_{\mathrm{pr}}$). Here, the pump-probe interaction inside the media, that does not affect the change in $\boldsymbol{k}_{\mathrm{pr}}$ could be described in terms of third-order modification of the nonlinear polarization as [63]:

$$\begin{aligned} P^{(3)}_{\text{pump-pr}}(\tau) = & \frac{3\epsilon_0}{2}\int \frac{d\omega_{\mathrm{pr}}}{2\pi}\frac{d\omega_{\mathrm{pump}}}{2\pi}\frac{d\omega_{\mathrm{pump}}}{2\pi}\chi^{(3)}(\omega_{\mathrm{pr}},\omega_{\mathrm{pump}},-\omega_{\mathrm{pump}})\times \\ & E_{\mathrm{pr}}(\omega_{\mathrm{pr}})E_{\mathrm{pump}}(\omega_{\mathrm{pump}})E^{*}_{\mathrm{pump}}(\omega_{\mathrm{pump}})\exp[-i(\omega_{\mathrm{pr}}+\omega_{\mathrm{pump}}-\omega_{\mathrm{pump}})\tau], \end{aligned} \tag{2.2}$$

where $\chi^{(3)}(\omega_{\mathrm{pr}},\omega_{\mathrm{pump}},-\omega_{\mathrm{pump}})$ is the third order susceptibility, governing the particular interaction when the two pump pulses arrive simultaneously:

$$\boldsymbol{k} = \boldsymbol{k}_{\mathrm{pr}} + \boldsymbol{k}_{\mathrm{pump}} - \boldsymbol{k}_{\mathrm{pump}} = \boldsymbol{k}_{\mathrm{pr}}, \tag{2.3}$$

where $\boldsymbol{k}_{\mathrm{pr}}$ is conserved. In other words, for the short time-delays τ, the pump-probe experiment allows us to access the population relaxation of the irradiated matter. In the low-perturbation regime (for small $\Delta\varepsilon$), we can express the time-dependent modification of the probe beam transmittance or reflectivity as [24]:

$$\begin{cases} \dfrac{\Delta T}{T}(\omega_{\mathrm{pr}},\tau) = \dfrac{\partial \ln T}{\partial \varepsilon_1}(\omega_{\mathrm{pr}})\Delta\varepsilon_1(\omega_{\mathrm{pr}},\tau) + \dfrac{\partial \ln T}{\partial \varepsilon_2}(\omega_{\mathrm{pr}})\Delta\varepsilon_2(\omega_{\mathrm{pr}},\tau); \\ \dfrac{\Delta R}{R}(\omega_{\mathrm{pr}},\tau) = \dfrac{\partial \ln R}{\partial \varepsilon_1}(\omega_{\mathrm{pr}})\Delta\varepsilon_1(\omega_{\mathrm{pr}},\tau) + \dfrac{\partial \ln R}{\partial \varepsilon_2}(\omega_{\mathrm{pr}})\Delta\varepsilon_2(\omega_{\mathrm{pr}},\tau), \end{cases} \tag{2.4}$$

where $\Delta\varepsilon_1(\omega_{\mathrm{pr}},\tau)$ and $\Delta\varepsilon_2(\omega_{\mathrm{pr}},\tau)$ are time-dependent change of the real and imaginary part of complex dielectric function $\tilde{\varepsilon}(\omega_{\mathrm{pr}})$, caused by the pump-pump population change within the material of interest.

In this work, we use a Ti:Al_2O_3 laser system based on the chirped-pulse amplification technique [64]. Our laser delivers 3 mJ pulses, centered around 800 nm wavelength, at 1 kHz repetition rate (3 W of mean power). The pulse duration was measured by a second-order intensity autocorrelator and was found to be ≈ 165 fs (at FWHM).

The sketch of the experimental setup is shown in Fig.2.2. The beam is split with the ratio of 90/10, where 90 % of power is used for the pump or THz pulse generation, and remaining 10 % of intensity is used as the probe. The 0.5 mm Beta Barium Borate (BBO) crystal, introduced in the probe beam path, via SHG process converts the 800 nm into 400 nm light. The probe beam is

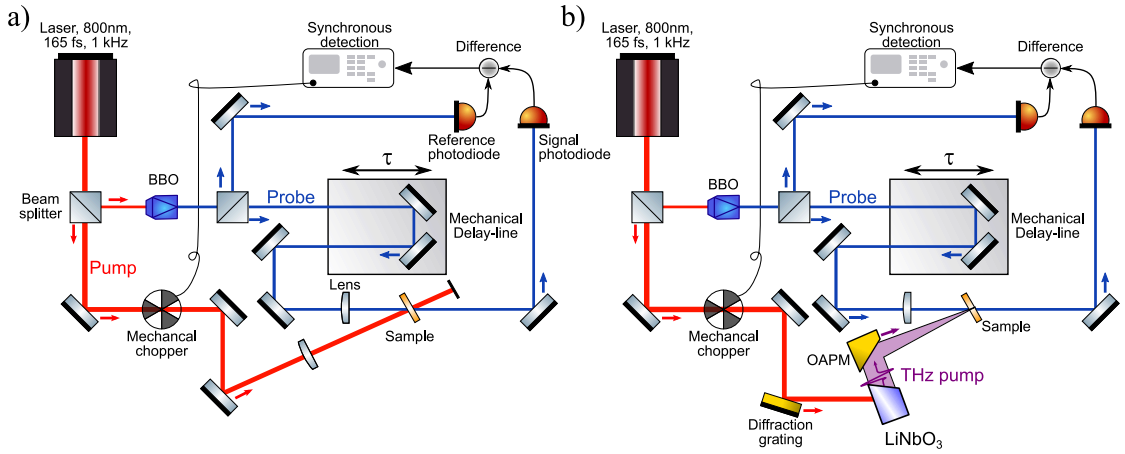

a) 800 nm pump and 400 nm probe setup. The Beta Barium Borate (BBO) crystal is used for the frequency doubling of the probe beam. **b)** 1 THz pump and 400 nm probe setup. The THz pulse is generated via the tilted-pulse front setup discussed in the manuscript. For both experimental configurations, the pump beam is incident close to the normal incidence regarding the sample surface. For the probe, the angle of incidence is about 10 to 15°.

Figure 2.2 – *Schema: The two pump-probe setups used in this work.*

incident at ≈ 10° to 15° angle to the sample surface. The measurement of change in the probe beam transmittance relies on the combination of balanced and lock-in synchronous detection techniques. For the balanced detection, 50 % of optical power is directed towards the reference photodiode. The signal part of the probe beam is focused onto the sample (with the spot size of ≈ 150 µm at FWHM) and is recorded by the signal photodiode of the NewFocus 2307 detector. The difference between the signal and reference inputs of NewFocus 2307 is fed to the SRS-830 Lock-in amplifier. The lock-in extracts the signal at the modulation frequency of the mechanical chopper (500 Hz) introduced in the pump beam path.

The conventional 800 nm pump/400 nm probe configuration is shown in the Fig.2.2a. Here, the pump is focused down to ≈ 200 µm spot diameter at normal incidence in respect to the sample surface. Visible probe and near-IR pump beam sizes were measured with a CCD camera.

The main experimental configuration in this work is the THz pump/400 nm probe, shown in the Figure 2.2b. Here, THz pulse with a central frequency of 0.64 THz is generated with the tilted-pulse front method, discussed later in the text. THz emitted from the lithium niobate crystal ($LiNbO_3$) is collected and focused with a one-inch off-axis parabolic mirror (OAPM), having a two-inch focal length. The THz beam size was measured with a knife-edge method and was estimated to be equal to roughly 615 µm in diameter. The maximum THz pulse energy used in the experiment is around 1.2 µJ. This gives us the maximum value of a peak electric field in the order of 275 kV cm^{-1}. Details about the tilted pulse front method are discussed in the Section 2.3.1, and THz beam size characterization is shown in the Appendix A.

2.3 Terahertz generation and detection

The part of the electromagnetic spectrum with corresponding photon energies in the range of 0.1 eV-120 meV is called the THz range. Nowadays, terahertz pulses can be routinely generated

Material	r_{eff}(pm/V)	$n_0^{800\,\text{nm}}$	$n_{\text{gr}}^{800\,\text{nm}}$	n^{THz}	$\alpha^{\text{THz}}\left(\text{cm}^{-1}\right)$
CdTe (SC)	4.5	2.92	3.73	3.23	4.8
GaAs (SC)	1.43	3.68	4.18	3.61	0.5
GaP (SC)	0.97	3.18	3.57	3.34	1.9
ZnTe (SC)	4.04	2.87	3.31	3.17	1.3
GaSe (SC)	1.7	2.85	3.13	3.72	0.07
$LiTaO_3$ (FE)	30.5	2.145	2.22	6.42	46
$LiNbO_3$ (FE)	30.9	2.159	2.23	5.16	16
DAST (OC)	77	2.38	3.31	2.4	150

Here, SC stands for semiconductor, FE is ferroelectric, and OC is an abbreviation of organic crystal.
From [38]

Table 2.1 – *Properties of the materials suitable for the optical rectification*

in laboratory conditions via optical rectification in semiconductors [37, 65], ferroelectrics [66], organic crystals [67], in air plasma [68], using synchrotron radiation [69], free-electron lasers [70], photoconductive switches [71] and spintronic emitters [1]. Furthermore, the THz radiation can be detected and measured with multiple techniques, such as pyroelectric detection, electrooptic sampling (EOS) [72], using photoconductive antennas [73, 74], bolometers, air biased coherent detection [75], and THz radiation enhanced emission of fluorescence [76]. This section will discuss the THz generation via optical rectification and EOS detection principles.

Light propagating inside a nonlinear optical medium can create second-order nonlinear polarization $P^{(2)}$. As discussed in the Section 1.3.1.1, the rapidly varying femtosecond pulse envelope may lead to transient precession of $P^{(2)}$ in the far- or mid-infrared frequency range due to the difference-frequency mixing of a spectrally-broad light pulse. The second-order nonlinear susceptibility ($\chi^{(2)}(\Omega, \omega_1, \omega_2)$) describes the efficiency of the optical rectification process. As an example, for $F\bar{4}3m$ space group (ZnTe, GaP, GaAs) the $\chi^{(2)}(\Omega, \omega)$ tensor has only one non-vanishing diagonal component and is linked to the nonlinear optic tensor $d_{ij}(\omega_i, \omega_j)$ and electrooptic coefficient r_{ij} as [23, 72]:

$$\chi_{ij}^{(2)}(\Omega, \omega_i, \omega_j) = 2d_{ij} = -\frac{n_i^2 n_j^2 r_{ij}}{4}. \tag{2.5}$$

For simplicity, we will drop the tensor notation, and will speak in terms of the effective nonlinear susceptibilities $\chi_{\text{eff}}^{(2)}(\Omega, \omega)$ and electrooptic coefficients $r_{\text{eff}}(\Omega)$. The list of some THz emitters suitable for optical rectification is shown in the Table 2.1.

2.3.1 Terahertz generation: optical rectification

Since OR is a second-order nonlinear effect, the efficiency of the THz generation depends on the so-called velocity matching along the volume of the nonlinear crystal. For the in-phase precession of $P^{(2)}$ inside the nonlinear crystal, the following condition needs to be satisfied [77]:

$$v_{\text{gr}}^{800\,\text{nm}} = v^{\text{THz}} \text{ or } n_{\text{gr}}^{800\,\text{nm}} = n^{\text{THz}}, \tag{2.6}$$

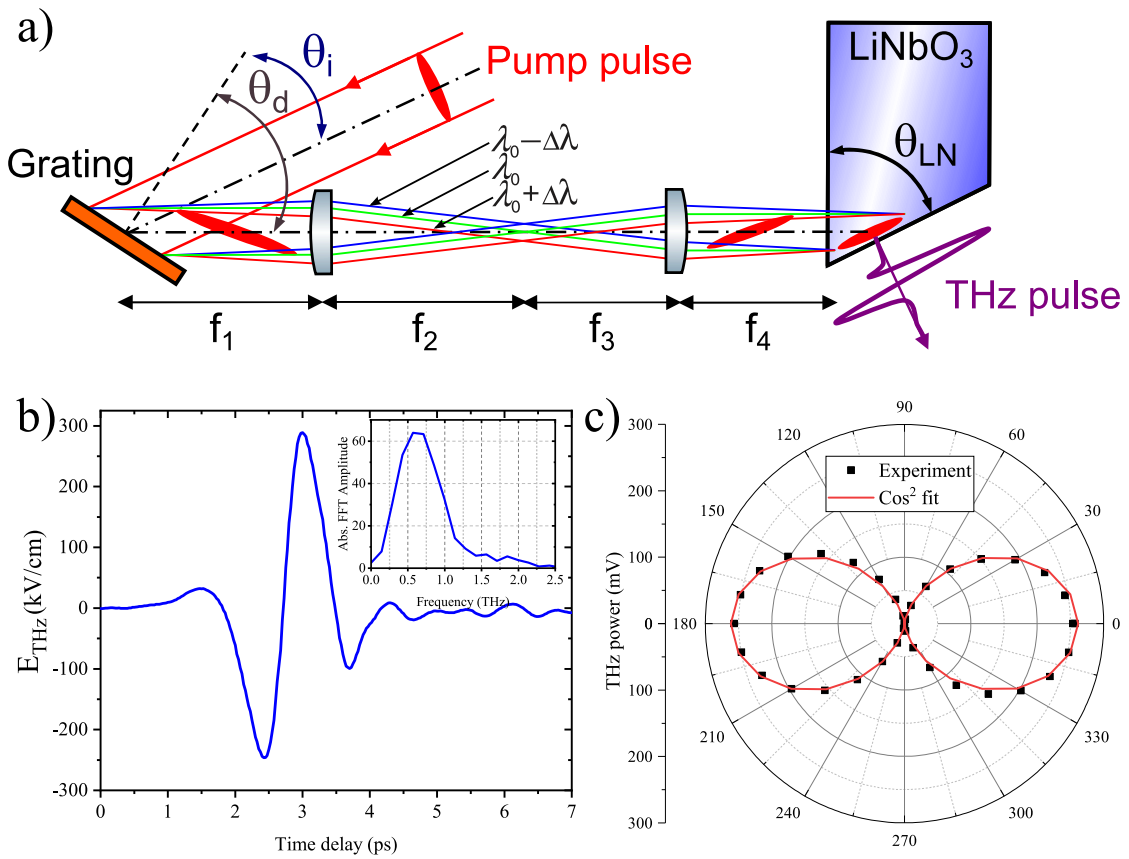

a) The 4f-lens tilted-pump-pulse-front generation scheme. The diffraction angle θ_d was set to 57.15°, with $\theta_{\mathrm{LN}} = 63°$. Two lenses with $f_1 = f_2 = 250\,\mathrm{mm}$ and $f_3 = f_4 = 150\,\mathrm{mm}$ were used, with a magnification factor $\beta = 0.6$. The pump pulse front is tilted by the angle γ_{tilt}, so that $v_{\mathrm{gr}}^{800\,\mathrm{nm}}\cos(\gamma_{\mathrm{tilt}}) \approx v^{\mathrm{THz}}$, leading to the efficient THz generation. Figure adapted from [66]. **b)** The temporal shape and spectrum (inset) of the THz radiation emitted from the MgO:$LiNbO_3$ source in the tilted pulse front experimental setup, measured with ⟨110⟩200 µm GaP. The E_{THz} at the entry surface of the crystal was extracted by accounting for the response function of the detection crystal, discussed in the Section2.3.2. The THz field value was cross-verified with the calibrated pyroelectric detector. **b)** The linear polarization of the MgO:$LiNbO_3$ THz source, measured with pyroelectric detector and Wire Grid polarizer.

Figure 2.3 – *Tilted pulse front generation layout and THz spectrum.*

i.e., the group velocity of the femtosecond pump should match the phase velocity of the emitted THz pulse. From the Table 2.1, we see that for some crystals (ZnTe and GaP), this condition is somewhat fulfilled, leading to the broadband THz emission (within 3-7 THz frequency range) [65,78]. However, the phonon-polariton coupling can severely reduce the optical rectification (OR) bandwidth for the photons with frequencies close to the lattice optical phonon modes (see Section 1.3.1).

The titled pulse front method:

From the table 2.1, we see that lithium niobate ($LiNbO_3$) ferroic crystal has high values of r_{eff}, almost one order of magnitude higher than the ones of ZnTe and GaP. But, due to the high-velocity mismatch between the optical pulse and THz wave, complemented with increased THz absorption, these crystals are not efficient THz emitters in the colinear geometry, with conversion efficiency less than 0.001 %. However, as proposed by Janos Hebling et al. [38,79], by tilting the pump-pulse

front, one can overcome the velocity matching restrictions inside the $LiNbO_3$ crystal. Using this technique, the group of K.Tanaka has achieved record generation efficiency of about 0.1 % with $LiNbO_3$ crystals, reaching the peak THz field values of $1.2\,\mathrm{MV\,cm^{-1}}$ [66].

Fig.2.3a shows the geometry of the tilted-pulse front THz generation method. The diffraction grating, in pair with the two lenses, is used to tilt the intensity front of the pump by an angle γ_{tilt}:

$$v_{\mathrm{gr}}^{800\,\mathrm{nm}}\cos(\gamma_{\mathrm{tilt}}) \approx v^{\mathrm{THz}}. \tag{2.7}$$

For the THz emission perpendicular to the crystal surface, the latter should be cut at the specific angle θ_{LN}, equal to the front-tilt angle γ_{tilt}. Then, the experimental parameters, such as diffraction angle θ_d, crystal angle θ_{LN}, and diffraction grating groove density p are chosen to satisfy the two following relations [66]:

$$\tan\gamma_{\mathrm{tilt}} = \frac{m\lambda_0 p}{n_{\mathrm{gr}}^{800\,\mathrm{nm}}\beta_1\cos\theta_d} \text{ and } \tan\theta_{\mathrm{LN}} = n^{800\,\mathrm{nm}}\beta_2\tan\theta_d, \tag{2.8}$$

with diffraction order m and pump pulse carrier wavelength λ_0, where β_1 and β_2 are the horizontal magnification factors of the 4-f system for the pump pulse front and the grating image, respectively.

In this work, we use MgO doped $LiNbO_3$ cut at $\theta_{\mathrm{LN}} = 63°$. The 4-$f$ imaging system is built with two spherical lenses with $f_1 = f_2 = 250\,\mathrm{mm}$ and $f_3 = f_4 = 150\,\mathrm{mm}$, leading to the magnification factors of $\beta_1 = \beta_2 = 0.6$. The deviation angle of $\theta = \theta_d - \theta_i \approx 17.3°$ was achieved with grating period $p = 1800\,\mathrm{mm^{-1}}$ and $m = -1$ diffraction order. The THz emitted from the $LiNbO_3$ crystal was collected with a one-inch off-axis parabolic mirror (OAPM) having a two-inch focal length. The THz temporal waveform, shown in Fig.2.3b, was recorded with a 200 µm ⟨110⟩ GaP crystal, in pair with two Wire Grid (WG) polarizers used as field attenuators. The estimation of peak THz power was done with the EOS response function (see Section 2.3.2) and with the help of calibrated pyroelectric detector, accounting for the focused THz beam profile (see Appendix A). In addition, the THz power measured as a function of the WG polarizer angle confirms the linear polarization of the $LiNbO_3$ source (see Fig. 2.3c), which is perpendicular to the polarization of the pump pulse.

2.3.2 Electrooptic terahertz detection

Back in the 1980s, Auston [72] introduced a method of time-resolved gating of the THz electric field with the stroboscopic approach, displayed in Fig.2.4a. Such EOS detection technique is based on the Pockels effect (or linear Kerr-effect) in noncentrosymmetric crystals describing the electric field induced birefringence. For the EOS detection, Pockels effect is used to measure the change in the sampling pulse ellipticity inside the electrooptic crystal in the presence of the THz field.

Let us use the Jones Matrix formalism to describe the final polarization state of the sampling pulse, initially polarized along the x-axis [41]:

$$\mathbf{p}_{pr} = \begin{bmatrix} 1 \\ 0 \end{bmatrix}. \tag{2.9}$$

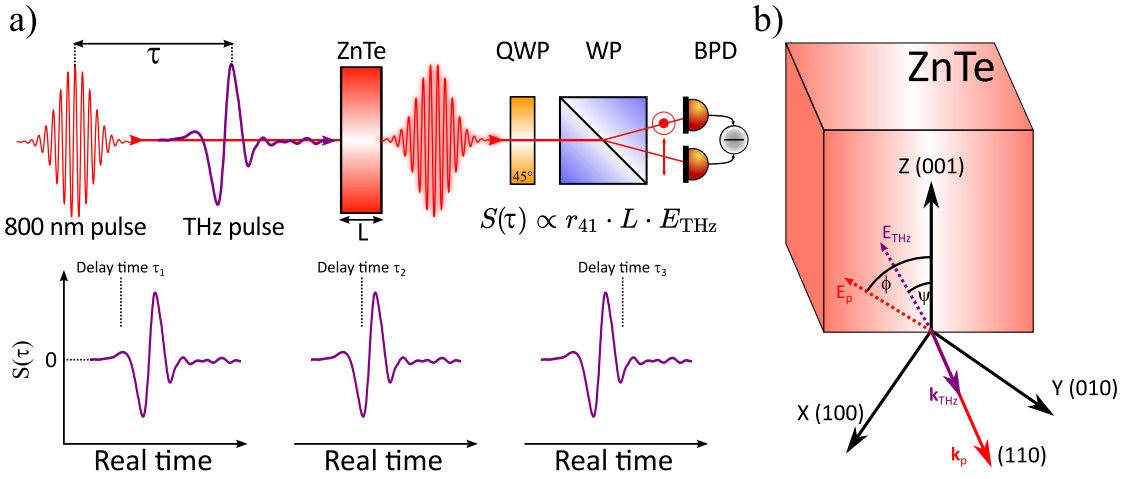

a) Both 800 nm probe and THz pulses are incident onto the electrooptic sampling crystal (⟨110⟩ ZnTe). With the controllable temporal overlap between the probe and THz pulses (via mechanical delay line, for example), one can point-by-point measure the ellipticity of the probe beam proportional to the E_{THz}. The ellipticity is then recorded by measuring the difference between the two orthogonal probe polarization components, equal to zero in the absence of the THz. **b)** THz detection geometry. In this thesis, we are always in $E_{\mathrm{THz}} \parallel E_{\mathrm{p}}$, $\phi = \psi$ experimental configuration, which is kept constant for all THz detection experiments. Image is redrawn from [80].

Figure 2.4 – *Principle of the field-resolved electrooptic detection.*

According to Eq.1.98, the electrooptic crystal will act as a THz field amplitude dependent phase retarder, where the phase shift Γ equal to:

$$\Gamma = \frac{2\pi n_0^3 r_{\mathrm{eff}} E_{\mathrm{THz}} L}{\lambda c}, \tag{2.10}$$

where L is the crystal thickness and λ is the wavelength of the probe beam. Then, the total phase shift experienced by the probe is equal to [41]:

$$\mathbf{C}_{\mathrm{ZnTe}} = \frac{1}{2}\begin{bmatrix} e^{i\Gamma} + e^{-i\Gamma} & e^{i\Gamma} - e^{-i\Gamma} \\ e^{i\Gamma} - e^{-i\Gamma} & e^{i\Gamma} + e^{-i\Gamma} \end{bmatrix}. \tag{2.11}$$

We then introduce Quarter wave plate (QWP) after the EOS crystal, with its fast axis oriented at +45° to probe beam polarization:

$$\mathbf{Q}_{+45} = \frac{1}{\sqrt{2}}\begin{pmatrix} 1 & i \\ i & 1 \end{pmatrix}. \tag{2.12}$$

Next, the resulting polarization state of the probe beam will write:

$$\mathbf{p} = \mathbf{Q}_{+45} \cdot \mathbf{C}_{ZnTe} \cdot \mathbf{p}_{pr} = \frac{1}{\sqrt{2}}\begin{pmatrix} \cos\Gamma - \sin\Gamma \\ i(\cos\Gamma + \sin\Gamma) \end{pmatrix}. \tag{2.13}$$

Finally, one can spatially separate two orthogonal probe polarization components (x and y) with a Wollaston prism (WP). Then, we can measure the difference between x and y intensities using the balanced detection (See Fig.2.4a). In the absence of THz electric field inside the crystal, since $|p_x|^2 = |p_y|^2$, measured signal will be zero. Then, in the presence of E_{THz} ($E_{\mathrm{THz}} \neq 0$), the normalized power seen by the balanced photodiodes is:

$$S = \frac{|p_y|^2 - |p_x|^2}{|p_x|^2 + |p_y|^2} = \sin(2\Gamma). \tag{2.14}$$

For $\Gamma \ll 1$, we can assume that $\sin(2\Gamma) \approx 2\Gamma$. Then, with Eq.2.10 and Eq.2.14 we can write:

$$\Gamma = \frac{2\pi n_0^3 r_{\mathrm{eff}} E_{\mathrm{THz}} L}{\lambda} \Rightarrow E_{THz} = \frac{S\lambda}{\pi n_0^3 r_{\mathrm{eff}} L} \tag{2.15}$$

By changing the temporal overlap between the short sampling pulse and the THz waveform, one can point-by-point record $S(\tau)$ (see Eq.2.14), and thus measure the shape of the THz electric field.

Moreover, the efficiency of the THz detection strongly depends on the orientation of the THz polarization (angle ψ) and the probe beam polarization with respect to the crystal z-axis (angle ϕ), depicted in the Fig.2.4b. Planken et al. [80] have deduced the dependence of the electrooptic signal strength on the angles ψ and ϕ:

$$S(\tau) \propto (\cos\psi \sin 2\phi + 2\sin\psi \cos 2\phi). \tag{2.16}$$

We remind that ψ and ϕ are the azimutal angles between the E_{THz} and E_{p} in respect to electrooptic detection crystal z-axis. In this thesis, we have set $\phi = \psi$ (meaning that $E_{\mathrm{p}} \parallel E_{\mathrm{THz}}$), and we rotated the crystal to obtain maximum possible signal.

THz detection sensitivity improvement: In Chapter 4, we sample low-amplitude $E_{\mathrm{THz}}(\tau)$ fields, which requires a lot of averaging in the conventional electrooptic detection scheme (with $\mathbf{Q}_{+45}$). To improve the sensitivity of the EOS, we use the simple experimental technique first described by J. A. Johnson et al. [81] and then further simplified by P. Krauspe et al. [82], with a theory established by J. Brunner et. al. [83].

Experimentally, this approach could be regarded as the decrease in the ratio between the optical bias and the effective electrooptic signal. In a general way, the measured EOS signal (see Eq.2.14) can be defined as the function of Γ and Quarter Wave Plate (QWP) angle α (see Fig.2.5a) as [82]:

$$\arcsin(S(\alpha, \Gamma)) = \frac{2\Gamma}{\sin(2\alpha)} + 2\cot(2\alpha)^2 \cdot \Gamma^2, \tag{2.17}$$

where the first term is the linear part of the signal, directly proportional to E_{THz}. The second term is the quadratic contribution, proportional to $|E_{\mathrm{THz}}|^2$. One can retrieve the conventional EOS equation (Eq.2.14) for $\alpha = \pm 45°$, since the quadratic term and the α-dependence can be

neglected. However, for small E_{THz}-induced phase ($\Gamma \ll 1$, $\sin(\Gamma) \approx \Gamma$), the subtraction of signals measured for $\pm\alpha$ yields:

$$S(\alpha, \Gamma) - S(-\alpha, \Gamma) = \frac{4\Gamma}{\sin(2\alpha)}, \tag{2.18}$$

returning only the linear contribution to the $S(\tau)$, but improved (or enhanced) by the factor of $1/\sin 2\alpha$. In analogy, the addition of the two signals recorded for $\pm\alpha$:

$$S(\alpha, \Gamma) + S(-\alpha, \Gamma) = 4\cot(2\alpha)^2 \cdot \Gamma^2 \tag{2.19}$$

will contain only information about the quadratic contribution to the measured EOS signal.

To check this method, we first use the 500 µm ZnTe emitter and detector, and measure THz waveform in the function of the QWP angle α. For $\alpha \neq 45°$, a variable attenuator (VA, shown in Fig.2.5a) needs to be used to re-balance the photodiodes. Fig.2.5b depicts the change in $S(\tau)$ with the decrease of QWP angle α. The data for $\alpha > 1.7°$ is not shown, since the waveform is indistinguishable from the one recorded for $\alpha \approx 45°$. For $\alpha < 1.7°$, the nonlinear contribution starts to dominate, resulting in the noticeable distortion of the measured THz field [81].

Since we can not control QWP angle α with high precision, manual rotation of the mechanical components can lead to questionable eperimental reproducibility of the undistorted THz waveform retrieval, especially for small values of α. Due to this mechanical limitation, the study of the THz emission from spintronic emitters was done for the fixed value of α. QWP angle α was selected so that the quadratic contribution to $S(\tau)$ is negligible (i.e. $2\Gamma/\sin(2\alpha) \ll 2\cot(2\alpha)^2 \cdot \Gamma^2$, see Eq.2.17). In this case, the measurement for $\pm\alpha$ can be avoided.

In order to select the appropriate value of α, we replaced the 500 µm ZnTe crystal with spintronic THz emitter CoFeB(20 nm)/MgO(6 nm) [1]. All other experimental parameters were kept the same as before. The recorded THz waveforms for $\alpha \approx 0.25°$ and $\alpha \approx 45°$ are shown in the Fig.2.5c. When two measurements normalized by the peak-to-peak amplitude of the respective signal, perfect overlap of the normalized THz waveforms indicates the absence of nonlinear distortion (see inset of Fig.2.5c). This is expected, since THz emitted from CoFeB(20)/MgO(6) is way weaker than the one generated with 500 µm ZnTe crystal, roughly by the factor of 800. In addition, the field-induced phase retardation Γ of CoFeB(20 nm)/MgO(6 nm) at $\alpha = 0.25°$ is still smaller than the signal obtained 0.5 mm ZnTe at $\alpha \approx 45°$.

From this, in the absence of the signal distortion, one can directly estimate the detectivity enhancement factor Λ_{EOS} as:

$$\Lambda_{\mathrm{EOS}} = \frac{S(\alpha, \Gamma)}{S(45°, \Gamma)}, \tag{2.20}$$

1. Discussed more in the Chapter 4

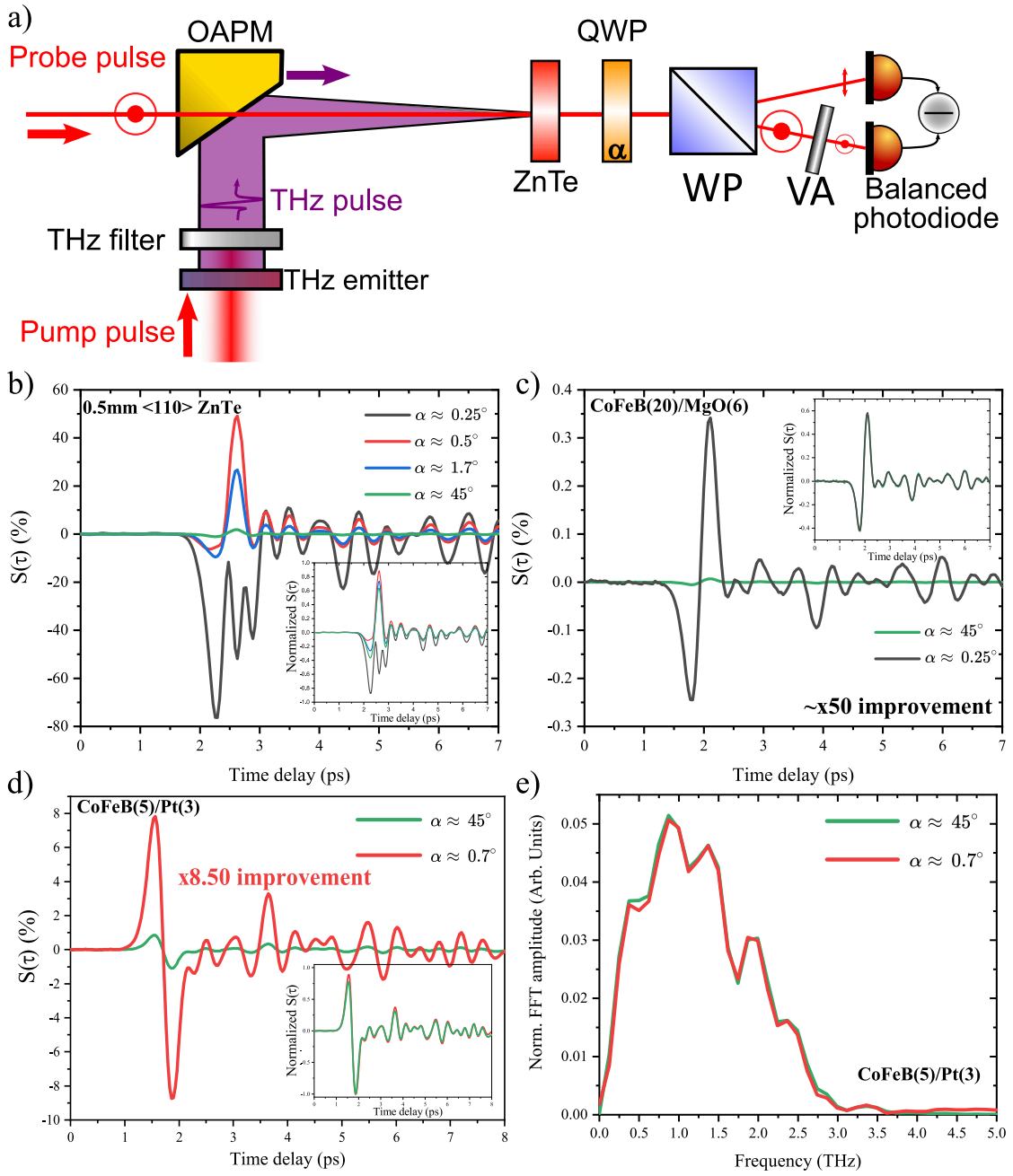

a) THz detectivity enhancement experimental setup. The Quarter Wave Plate (QWP) angle, different from $\alpha = 45°$ will break the balance between the orthogonal components of the probe pulse polarization. The Variable Attenuator (VA) is then used to match the intensities at the two channels of the balanced photodiodes.The different QWP angles α define the ratio between the effective EOS signal and the total laser intensity seen by the balanced photodiode. **b)** THz fields recorded for the $\langle 110 \rangle$ 0.5 mm ZnTe crystal. The distortion of the waveform for the low α is related to the dominance of the nonlinear contribution to the detected signal (see Eq.2.17). **c)** THz detectivity enhancement for the low-amplitude THz emitter CoFeB(20 nm)/MgO(6 nm). **Inset:** Normalized to the peak-to-peak field THz waveforms, showing the absence of distortion even at the low QWP angles α. **d)** THz emitted from the CoFeB(5 nm)/Pt(3 nm) before ($\alpha \approx 45°$) and after ($\alpha \approx 0.7°$) detectivity enhancement and its spectrum **e)**, showing the x8.5 increase of the signal with negligible nonlinear distortion.

Figure 2.5 – *Electrooptic sampling detectivity enhancement.*

which, for CoFeB(20 nm)/MgO(6 nm) is equal to:

$$\Lambda_{\mathrm{EOS}} = \frac{S(0.25°, \Gamma)}{S(45°, \Gamma)} \approx 50. \tag{2.21}$$

All the THz signals discussed in the Chapter 4, were measured with this technique. However, at first all signals were recorded without the EOS detectivity enhancement. Then, the experiment was repeated for the fixed value of $\alpha \approx 0.7°$, for which THz detected from all spintronic emitters showed no distortion. Figure 2.18d displays the "raw" ($\alpha = 45°$) and enhanced signal ($\alpha \approx 0.7°$) of the most efficient spintronic emitter in our disposal, CoFeB(5)/Pt(3). For the enhancement factor Λ_{EOS} of about 8.5, both the THz waveform and its spectrum remains unchanged, indicating the presence of only linear contribution to $S(\tau)$. In addition, the dependence of emitted E_{THz} amplitude on the NIR pump power was measured at conventional $\alpha \approx 45°$, in order to be free from the possible detection nonlinearities present for the higher-amplitude THz fields.

In theory, for the low electric field amplitudes, the improvement factor Λ_{EOS} can be increased even further, but mainly limited by the damage threshold of the EOS crystal and the reasonable amount of optical power required for the balanced detection. For example, one can increase the sampling beam size in order to reduce the optical fluence Φ inside the detection crystal. In addition, one can replace a conventional balanced detector by the pair of avalanche photodiodes for low $\alpha < 0.1°$. Ultimately, this technique can be applied for any polarization-sensitive detection. In principle, this THz detectivity enhancement technique based on the QWP-detuning can be used for both kHz and MHz oscillators, but it requires an excessive sampling pulse optical power density, and signal-to-noise ratio may be limited by the electronic noise in the case of MHz oscillators.

Electrooptic response function: Since EOS is governed by the crystals' effective electrooptic coefficient r_{eff}, the detection efficiency and bandwidth strongly depend on the ionic and the optical properties of the detector. For example, when THz phase - sampling pulse group velocity mismatch is negligible, and with THz pulse having frequency components out of the range of detection crystal lattice optical phonon resonances, measured signal will be the direct replica of the THz electric field, i.e., $S(\tau) \propto E_{\mathrm{THz}}$. In reality, however, detected signal $S(\tau)$ is a result of the convolution between the frequency-dependent detector response and THz electric field [37, 65, 78]:

$$S(\tau) = E_{\mathrm{THz}}(\tau) \circledast h_{\mathrm{EOS}}(\tau), \tag{2.22}$$

where $h_{\mathrm{EOS}}(\tau)$ is the EOS response function of the nonlinear medium, and $\circledast$ is the convolution operator. In the frequency domain, the latter equation can be rewritten as:

$$S(\Omega) = E_{\mathrm{THz}}(\Omega) \times h_{\mathrm{EOS}}(\omega, \Omega), \tag{2.23}$$

where ω and Ω are the angular frequencies of the Near-IR sampling pulse and THz waveform, respectively.

From the physics perspective, $h_{\mathrm{EOS}}(\omega,\Omega)$ contains the information about the phase-matching, sampling pulse-THz wave interaction, and EOS detection bandwidth. According to Kampfrath et.al. [84], $h_{\mathrm{EOS}}(\omega,\Omega)$ is expressed as:

$$h_{\mathrm{EOS}}(\omega,\Omega)=\frac{4it_{12}(\Omega)}{c^2}\int_{\omega>\Omega}d\omega E_{\mathrm{s}}^{*}(\omega)E_{\mathrm{s}}(\omega-\Omega)C(\omega,\Omega)T(\omega,\Omega)P(\omega,\Omega), \tag{2.24}$$

where t_{12} is the Fresnel transmission coefficient for the air-crystal interface, $E_{\mathrm{s}}(\omega)$ is the spectrum of a sampling pulse. The first coefficient $C(\omega,\Omega)$ describes the nonlinear terahertz - sampling pulse interaction:

$$C(\omega,\Omega)=\omega^2\times\chi_{eff}^{(2)}(\omega-\Omega,\Omega)/k(\omega), \tag{2.25}$$

with $k(\omega)=n(\omega)\omega/c$ being the sampling pulse wave-vector. Next, $T(\omega,\Omega)$ is the "composite" sampling pulse transmission coefficient:

$$T(\omega,\Omega)=t_{12}^{*}(\omega)\times t_{12}(\omega-\Omega)\times\exp[-2d_{tot}\mathrm{Im}\{k(\omega)\}]\times|t_{21}|^2, \tag{2.26}$$

with t_{21} being the crystal-air Fresnel coefficient, and d_{tot} is the total thickness of the EOS crystal (electrooptically active layer plus the substrate). The last term, $P(\omega,\Omega)$ is the phase-matching coefficient, describing the frequency-dependent velocity mismatch between the THz and sampling pulses:

$$P(\omega,\Omega)=\frac{\exp(i\Omega d[v_{ph}^{-1}(\Omega)-v_g^{-1}(\omega)])-1}{i\Omega[v_{ph}^{-1}(\Omega)-v_g^{-1}(\omega)]}, \tag{2.27}$$

with d being the thickness of the electrooptic crystal (only of the active layer).

Here, we use $\langle 110\rangle$ 500 µm thick ZnTe and $\langle 110\rangle$ 200 µm thick GaP for EOS detection. For ZnTe, refs [85] and [86] were used to calculate the NIR and THz refractive indices, respectively, with refs [87] and [88] containing information about GaP detector. The $\chi_{eff}^{(2)}(\omega-\Omega,\Omega)$ was calculated from [37] and [89] for ZnTe and GaP, respectively. For the NIR pulse parameters, we use the central wavelength of 800 nm and pulse duration of 165 fs.

The calculated response function $h_{\mathrm{EOS}}(\omega,\Omega)$ of the 500 µm thick ZnTe is shown in the Fig.2.6a. The rapid phase loss around 3 THz corresponds to the TO and LO phonon-polariton coupling with THz light, where $f_{TO}\approx 5.3$ THz [37]. For the $\langle 110\rangle$ 200 µm thick GaP the response function is mainly limited by the sampling pulse bandwidth [2], since the $f_{TO}\approx 11$ THz.

In order to check the correctness of the calculated $h_{\mathrm{EOS}}(\omega,\Omega)$, we measured THz emitted from the same $\langle 110\rangle$ 500 µm thick ZnTe emitter using two distinct GaP and ZnTe detectors. The "raw" signals recorded with 500 µm thick ZnTe and 200 µm thick GaP crystals are shown in the Fig.2.6c. We see roughly 10 times less signal for the GaP detector, which is expected due to the 4 times smaller r_{eff} (see Table 2.1), 2.5 times thickness difference and difference in the refractive indices

2. From Shannon-Nyquist sampling theorem, the detection bandwidth of the 165 fs pulse is in the range of ≈ 3 THz.

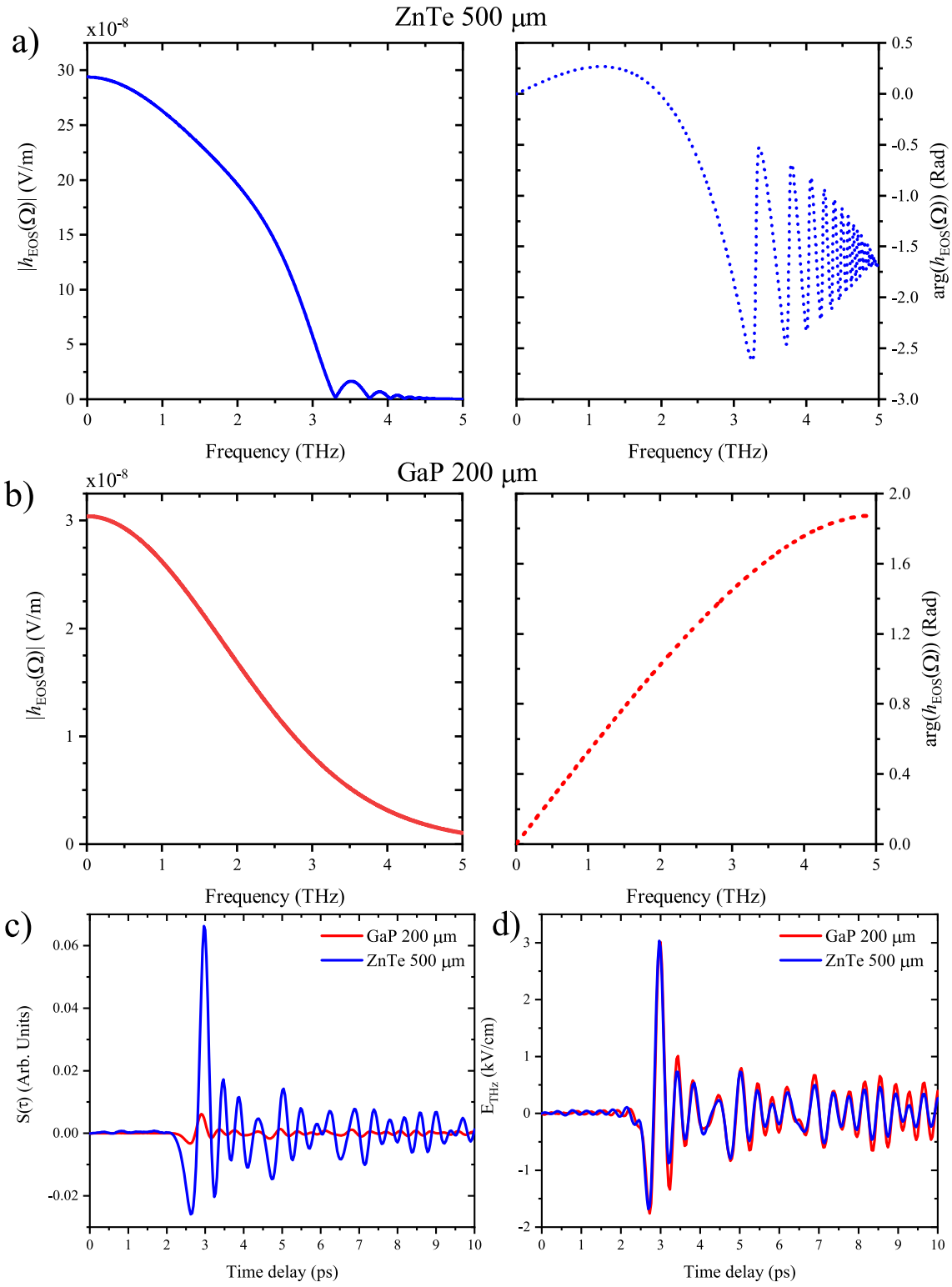

Electrooptic response functions $h_{\mathrm{EOS}}(\omega, \Omega)$ calculated for the $\langle 110 \rangle$ **a)** 500 µm thick ZnTe and **b)** 200 µm thick GaP crystals. **c)** The $S(\tau)$ measured for the ZnTe and GaP detectors. While using the GaP crystal, we observe the roughly 10 times less signal compared to the ZnTe detector. **d)** Retrieved waveforms, obtained with the Eq.2.23.

Figure 2.6 – *ZnTe and GaP response functions and retrieval of the E_{THz} shape.*

(see Table 2.1). However, after accounting for $h_{\mathrm{EOS}}(\omega, \Omega)$ of a given detector, we recover nearly identical shape of the E_{THz}, as shown in Fig.2.6d.

One should note that Fig.2.6d gives us the approximate shape of $E_{\mathrm{THz}}(\tau)$ in front of the detection crystal. In Chapter 3, we apply such $h_{\mathrm{EOS}}(\omega,\Omega)$-deconvolution to the THz emitted from $LiNbO_3$ crystal, since the information about the E_{THz} waveform just in front of the sample is essential for the measurements interpretation and first-principle calculations. However, due to the fact that the THz emission experiments presented in Chapter 4 were done for the same detection crystal, it allows us to directly compare all the measured signals. In addition, one can estimate the electric field waveform at the emitter position, taking into account the spatio-temporal transformation focusing distortions of the THz pulse [90, 91].

2.4 THz time-domain spectroscopy

The THz time-domain spectroscopy (THz-TDS) allows studying the static or transient material properties in the far-IR/THz range. The review of the different sources used for the THz-TDS, potential noise sources, the influence of the experimental settings were described by J. Neu and C. A. Schmuttenmaer [92].

Free-standing film or bare substrate: The dielectric function of the free-standing film can be measured as follows. First, the waveform of the reference pulse $S_{\mathrm{ref}}(\tau)$ with no sample in the path of THz, in pair with the noise $S_{\mathrm{noise}}(\tau)$ [3], propagating through the free space is recorded. Second, the sample with the thickness d is introduced in the THz beam path, and sample signal $S_{\mathrm{sam}}(\tau)$ is recorded. Next, one can write the ratio between the reference and sample signals in the frequency domain as:

$$H(\Omega) = \frac{S(\Omega)_{\mathrm{sam}}}{S(\Omega)_{\mathrm{ref}}} = \frac{E_{\mathrm{sam}}(\Omega)\times h_{\mathrm{EOS}}(\omega,\Omega)}{E_{\mathrm{ref}}(\Omega)\times h_{\mathrm{EOS}}(\omega,\Omega)} = \frac{E_{\mathrm{sam}}(\Omega)}{E_{\mathrm{ref}}(\Omega)}, \tag{2.28}$$

where the response function of the detector is mathematically irrelevant. In this type of experiment, the signal-to-noise ratio is really important, especially for frequencies close to the detector lattice resonance modes, for example.

Next, the amplitude $A(\Omega)$ and the phase $\phi(\Omega)$ of the THz-TDS ratio $H(\Omega)$ are calculated. By knowing the thickness of the sample d, the refractive index of the free-standing film $n(\Omega)$ is given as [93]:

$$n(\Omega) = 1 + \frac{c}{\Omega d}\phi(\Omega). \tag{2.29}$$

From the calculated refractive index, the absorption coefficient $\alpha(\Omega)$ can be estimated as:

$$\alpha(\Omega) = -\frac{2}{d}\ln\left\{A(\Omega)\frac{[n(\Omega)+1]^2}{4n(\Omega)}\right\} = \frac{2\omega\mathrm{Im}(k(\Omega))}{c}. \tag{2.30}$$

However, it is important to know the sensitivity of the experiment. The ratio between $S_{\mathrm{ref}}(\Omega)/S_{\mathrm{noise}}(\Omega)$

3. When the THz source is blocked.

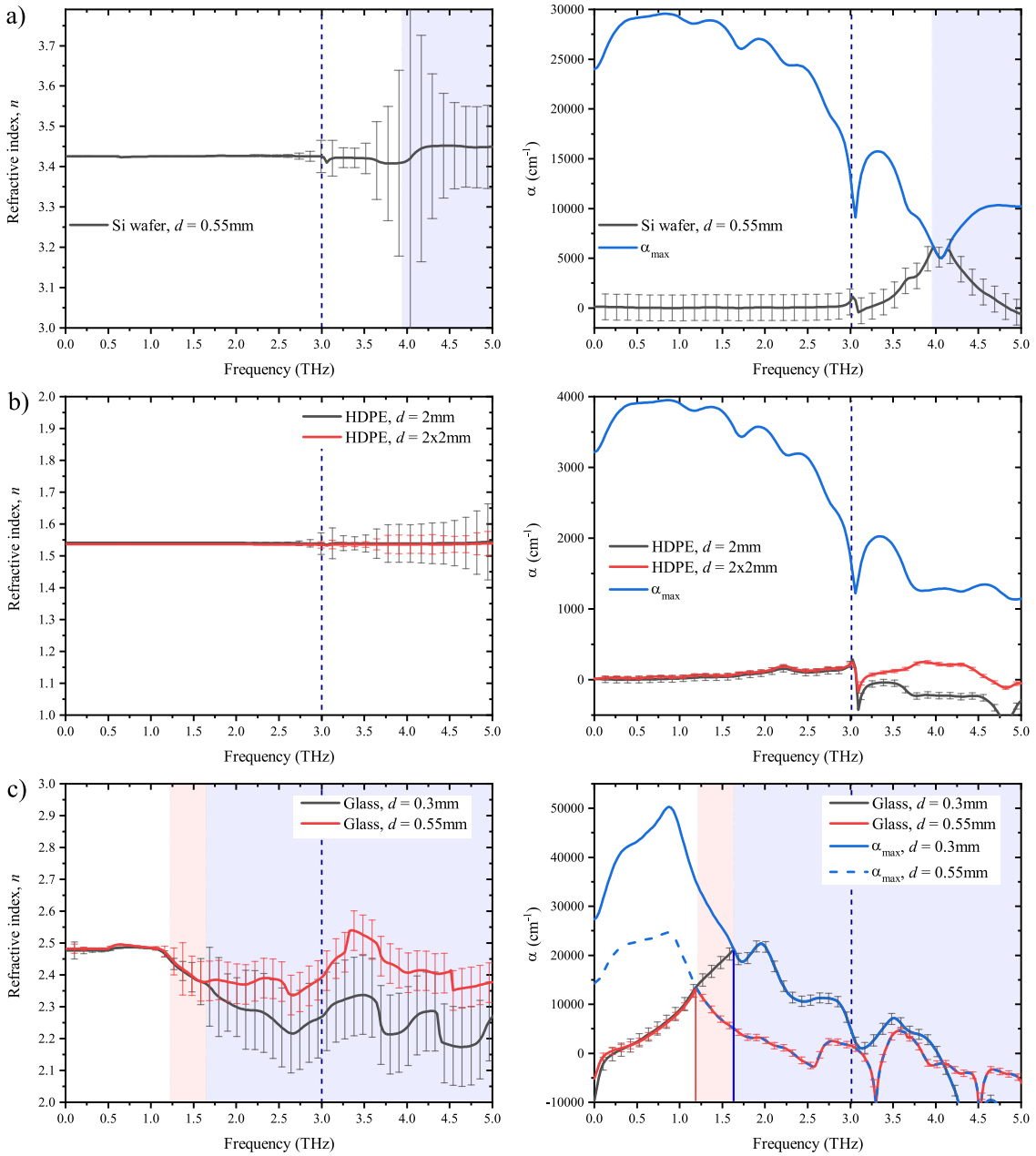

Refractive index n and absorbance α of **a)** High-resistivity float-zone Si wafer, **b)** High-Density Polyethylene (HDPE) and **c)** Float-Zone Glass substrate. Shaded regions represent the unreliable frequency range, i.e. where neither n nor α could be estimated with the THz-TDS experiment. The values were calculated with Eq.2.29 and Eq.2.30. Dashed blue line corresponds to the THz-TDS resolution limit, defined by the response function of ZnTe.

Figure 2.7 – *THz refractive indices and absorbance of the free standing Si, HDPE and Glass substrates.*

is used to estimate the experimental dynamical reserve (DR) [4] of the experiment [93]:

$$\alpha_{\max}(\Omega) = 2\ln\left\{DR(\Omega)\frac{4n(\Omega)}{([n(\Omega)+1]^2}\right\}. \tag{2.31}$$

4. Or signal-to-noise ratio.

It should be noted, that $\alpha(\Omega) < \alpha_{\max}(\Omega)$ is the criterion of the reliable measurement of both n and α. In addition, we manually limit the THz-TDS resolution up to 3 THz, close to the high-distortion of the h_{EOS} (see Fig.2.6a).

Next, we have measured refractive indices and absorption coefficients of the High-Resistivity Float-Zone Silicon (HRFZS) wafer, High-Density Polyethylene (HDPE), and Float-Zone Glass substrates (see Fig.2.7). We observe a flat refractive index and absence of absorption in HRFZS and HDPE, in good agreement with the literature [94, 95]. On the other hand, the glass shows strong $n(\Omega)$ and $\alpha(\Omega)$ frequency dependence, which leads to the strong distortion of the transmitted THz pulse [96].

The primary purpose of the HDPE sheet (with band-gap energy in the range of 4.6 eV or 270 nm [97]) is to diffuse and filter out the pump beam, used for the THz generation in the collinear configuration (ZnTe, GaP, spintronic emitters). In addition, we use HRFZS wafer to completely remove any remaining pump residue. The HRFZS THz transmission, placed after the single HDPE sheet, was estimated to $T_{\mathrm{HRFZS}} = 67\,\%$, in good agreement with multiple reports [66, 94, 98]. However, the removal of HDPE sheet before the HRFZS leads to the photoexcitation and pump-power dependent THz absorption of the latter, as discussed in the Appendix F.

Thin metallic films: For the thin film with the thickness d_{film} deposited onto the thick substrate, the THz amplitude transmission $H(\Omega)$ (see Eq.2.28) will be the product of the THz pulse multiple reflections at the film interfaces, paired with THz absorption in the metal film and the substrate [99]:

$$H(\Omega) = \frac{t_{12}t_{23}t_{31} \cdot \exp[ik_2(\Omega)d_{\mathrm{film}}] \cdot \exp[ik_3(\Omega)d_{\mathrm{sub}}]}{1 + r_{12}r_{23}\exp[2ik_2(\Omega)d_{\mathrm{film}}]}, \tag{2.32}$$

where k_1, k_2 and k_3 are the complex THz wave vectors in air, metallic film and substrate, respectively. However, one can simplify the latter equation,if the THz-TDS signal of the bare substrate $S_{\mathrm{sub}}(\Omega)$ was used as the reference [100]:

$$H(\Omega) = \frac{S_{\mathrm{sam}}(\Omega)}{S_{\mathrm{sub}}(\Omega)} \cdot \exp[i(n_3(\Omega) - 1)\Delta d_{\mathrm{sub}}\Omega/c], \tag{2.33}$$

where we account for the reference and sample substrate thickness mismatch with Δd_{sub}. If the metallic film is smaller than the THz wavelength and penetration depth, the Eq.2.32 becomes:

$$H(\Omega) = \frac{n_2(\Omega) + n_3(\Omega)}{n_2(\Omega) + n_3(\Omega) + Z_0 \int_0^{d_{\mathrm{film}}} dz\sigma(\Omega)}, \tag{2.34}$$

with the free space impedance $Z_0 = 377\,\Omega$. Here, the frequency dependent conductivity $\sigma(\Omega)$ can be calculated with the Drude model:

$$\sigma(\Omega) = \frac{\sigma_{\mathrm{DC}}}{1 - i\Omega/\tau_e}, \tag{2.35}$$

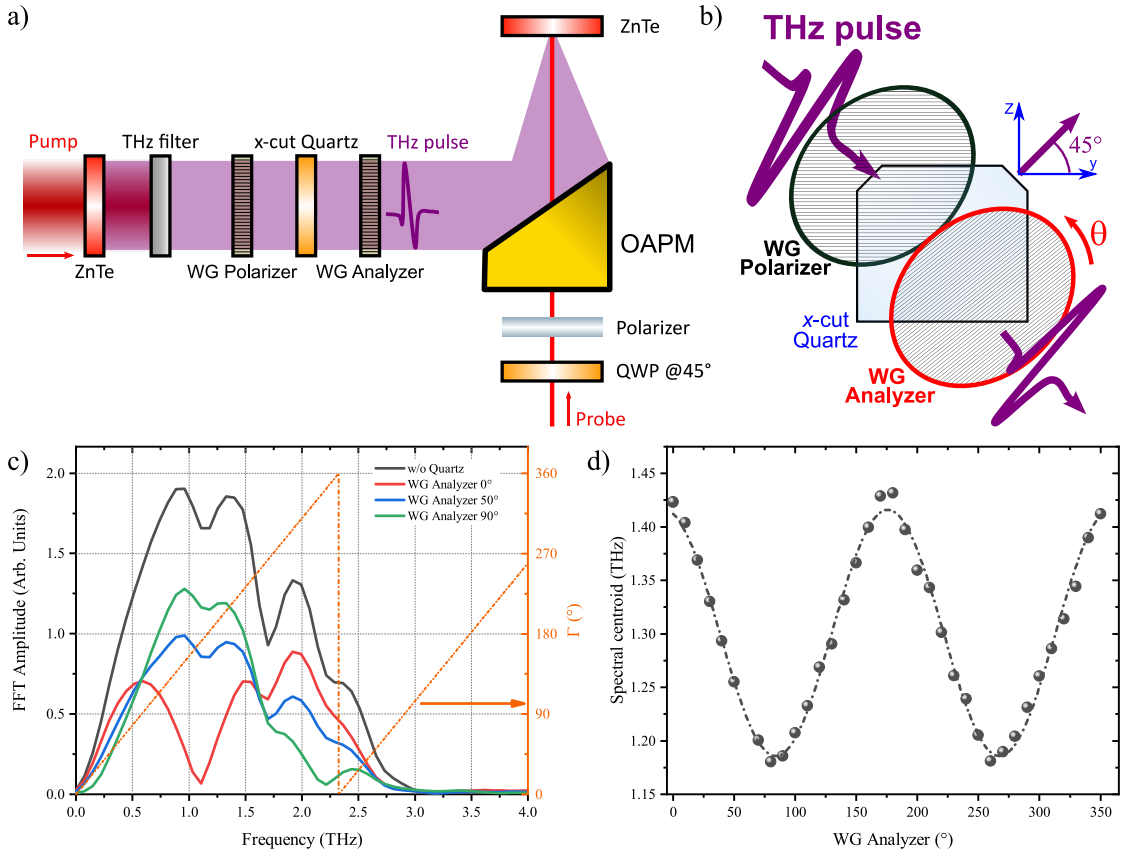

a) Schema of the THz beam-shaping experiment. The ZnTe crystal is used as the THz radiation and EOS THz detector source. THz filter is used remove the 800 nm pump residue. Both THz Wire Grid (WG) polarizer and WG analyzer are initially set for the maximum THz transmission. **b)** Sketch of the experimental geometry. x-cut Quartz, with its fast axis set at roughly 45° relative to E_{THz} polarization direction. x-cut Quartz is then placed between the fixed WG polarizer and the rotating WG Analyzer. **c)** Recorded FFT amplitude in the absence of 3 mm Quartz crystal (black line), and for the given angle of the WG analyzer. **d)** Plot of the THz spectral centroid (see Eq.2.37) as a function of the WG analyzer angle.

Figure 2.8 – *Influence of the x-cut Quartz on the THz spectrum.*

where τ_e is the electron scattering rate. It is relatively straightforward to measure the optical properties of a thin metallic film on the substrate, using THz transmitted though the bare substrate as the reference. In that case, the use of sophisticated THz-propagation models is not necessary [101].

THz-TDS is a powerful technique that allows directly measuring and extracting the material properties in the THz range, but it has its limitations. For example, too strong ($\alpha = \alpha_{max}$) or negligible absorption in the THz range define the sensitivity of the experiment. On the other hand, the physical properties of the detector and the environment the experiment is performed in (vacuum or air) ultimately define the detection bandwidth.

2.5 THz pulse shaping

Here, we present a method to modify the spectrum of the THz pulse after the propagation through the birefringent Quartz crystal. We then study the influence of 3 mm thick x-cut Quartz

crystal on the THz pulse polarization and spectrum. In this experiment, we use a 500 µm ZnTe crystal as both THz source and detector.

First, we have recorded the reference THz spectrum in the absence of the x-cut Quartz, displayed as a black curve in Fig.2.8c. Next, we placed the x-cut Quartz crystal between the Wire Grid WG polarizer analyzer, with its fast axis oriented at $\theta_{\text{Quartz}} \approx 45°$ relative to E_{THz} polarization, and measured the THz spectrum in the function of the WG analyzer angle (see Fig.2.8b).

The rotation of the WG analyzer will select a specific polarization component of the E_{THz}, which is then directed towards the EOS detector. To be in an optimal EOS detection condition, we have kept the angles between z-axis of the detection crystal, E_{THz} and E_{p} field vectors fixed through the experiment (as described in the Section 2.3.2).

THz spectra, measured for $\theta = 0°$, 50°, and 90° are shown in the Fig.2.8c. The observed modification of the THz spectrum amplitude, can be explained with the Eq.1.98. For this we can calculate the frequency-dependent phase shift within 0 to 4 THz range, experienced by the sampling pulse:

$$\Gamma(\Omega) = (n_e - n_o)\frac{\Omega L}{c}, \tag{2.36}$$

with x-cut Quartz thickness $L = 3$ mm. We took $n_o = 2.113$ and $n_e = 2.156$ values from the manufacturer, measured at 1 THz [5], and do not account for the possible frequency dependent $n_{e-o}(\Omega)$. The result of the calculation is shown in the Fig.2.8c as orange dash-dot line. For example, we see that the x-cut Quartz should be analogous to the half-waveplate at frequency of 1 THz, or act as quarter-plate at 0.5 THz. This is why we observe close to zero FFT amplitude at 1 THz for WG analyzer fixed at $\theta = 0°$ (behaves as $\lambda/2$ plate), and no change at 0.5 THz frequency (behaves as $\lambda/4$ plate).

We then can calculate the spectral centroid in the function of the WG analyzer angle, i.e. to see how spectrum center of mass evolves for selected E_{THz} projection:

$$\text{Spectral Centroid} = \frac{\sum_{n=0}^{N-1} nA[n]}{\sum_{n=0}^{N-1} A[n]}, \tag{2.37}$$

where $A[n]$ is the FFT amplitude corresponding to the n-th point of the spectrum. Figure 2.8d shows the Spectral Centroid as a function of the WG analyzer angle θ. As a result, due to the strong $\Gamma(\Omega)$ frequency dependence in Quartz, the THz spectral centroid of the ZnTe crystal can be tuned in 1.2-1.4 THz frequency range.

One should note that the most direct way to shape the spectrum of the THz pulse is to change the thickness of the electrooptic crystal (see Eq.2.27). As an alternative, the tilted pulse front setup (TPFS) can be realigned to satisfy the phase-matching condition within 0.5-3 THz range [38, 102]. However, due to the high realignment complexity of the TPFS setup, the 3 mm x-cut Quartz crystal could be a simple alternative for the post-emission THz pulse-shaping.

5. See THz materials section on the Tydex website.

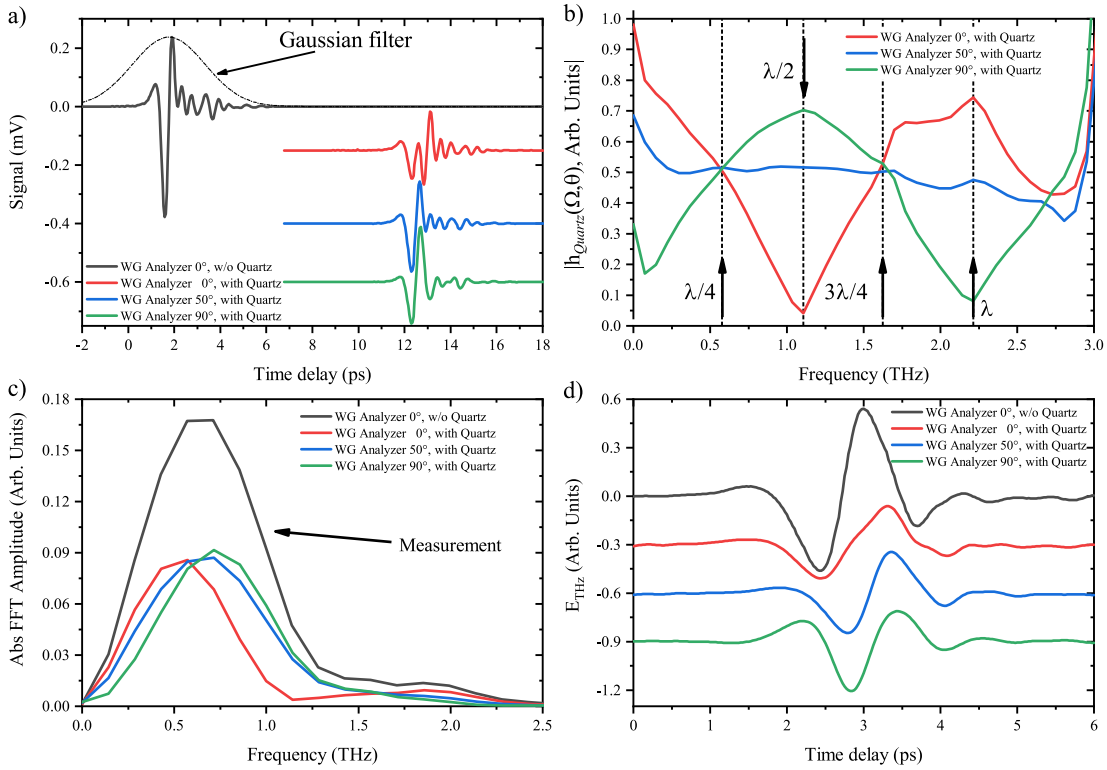

a) The black line is the pristine THz waveform of the ZnTe 0.5 mm emitter. Red, blue, and green lines are the signals measured with the x-cut Quartz introduced between fixed WG Polarizer and rotating WG Analyzer. **b)** The FFT amplitude ratios between the reference waveform and signal sampled for the specified WG Analyzer angle. **c)** Pristine, or reference spectrum of the $LiNbO_3$ THz source (black), and retrieved spectra of the $LiNbO_3$ source for the given WG analyzer angle. **d)** Retrieved THz transients obtained by performing the Inverse Fast Fourier Transform (IFFT) to spectra presented in **c)**. Signals shown in **a)** were multiplied by the Gaussian window of the constant width to eliminate ringing due to the water vapor absorption and THz reflection at the ZnTe-air interface.

Figure 2.9 – *Reconstruction of the $LiNbO_3$ THz waveform after the Quartz waveplate.*

Retrieval of the $LiNbO_3$ waveform: In the second part of the Chapter 3 we discuss the influence of the E_{THz} spectrum on the generation of the coherent phonon in Bi_2Te_3. However, due to the laser malfunction, we have not recorded the "real" THz waveform of the $LiNbO_3$ source as the function of the WG analyzer angle.

Despite this inconvenience, we still are able to estimate both the change in transient and spectrum of the $LiNbO_3$ source in the presence of the x-cut Quartz crystal. To do so, we mounted a separate THz-TDS setup, based on the RegA oscillator with 260 kHz repetition rate, 800 nm central wavelength, 4 µJ energy per pulse and 160 fs pulse duration. We have used the same experimental configuration as in the previous subsection (see Fig.2.8b), and approached this problem in terms of the THz-transfer function, discussed in the Section 2.3.2. In this case, we directly measure the response of the WG Polarizer-x-cut Quartz-WG Analyzer components, with 500 µm ZnTe crystal used as THz source and detector.

First, we have sampled the reference THz waveform without the x-cut Quartz in the path of the THz, shown as the black line in Figure 2.9a. Next, after the Quartz crystal was introduced in the path of the THz, we have recorded the shape of the E_{THz} waveform as the function of the WG

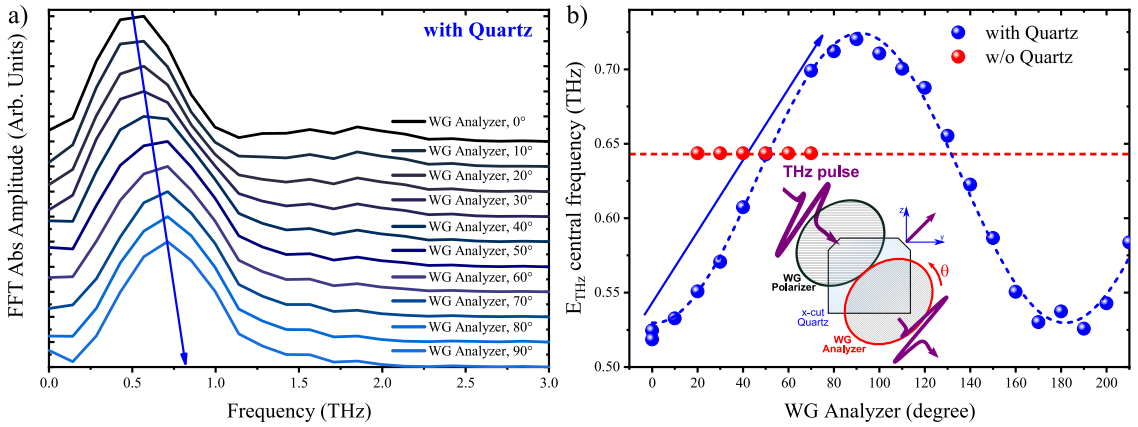

a) Reconstructed $LiNbO_3$ THz electric field spectrum as the function of the WG analyzer angle in the range of 0 to 90°. **b)** The $LiNbO_3$ THz electric field central frequency as the function of the Wire Grid (WG) analyzer angle, in the absence of the x-Cut Quartz (red dots) and with 3 mm x-cut Quartz plate introduced between WG polarizer and analyzer (blue dots). Dashed lines are guides for the eye.

Figure 2.10 – *Evolution of $LiNbO_3$ electric field spectrum in the presence of x-cut Quartz plate.*

analyzer angle θ, with both WG Polarizer x-cut Quartz fixed for maximum transmission and at 45° angle, respectively. Three signals, recorded for $\theta = 0$, 50 and 90° are shown in the Figure 2.9a.

In the frequency domain, we can calculate the change in the THz waveform, caused by the rotation of the WG analyzer, as:

$$h_{\text{Quartz}}(\Omega,\theta) = \frac{S(\Omega,\theta)_{\text{Quartz}}}{S(\Omega)_{\text{ref}}}, \tag{2.38}$$

where $S(\Omega)_{\text{ref}}$ is the signal recorded in the absence of the x-cut Quartz plate. Figure 2.9b shows the absolute value of the response function $|h_{Quartz}(\Omega,\theta)|$ for $\theta = 0°, 50°$ and 90°, where we can see that Quartz crystal behaves as the quarter-plate and half-plate at roughly 0.55 THz and 1.1 THz respectively, in the good agreement with values calculated from Eq.2.36.

Since we directly measure the waveform of the THz pulse, we have access to both the real and imaginary part of the $h_{\text{Quartz}}(\Omega,\theta)$. We then can use the measured $h_{\text{Quartz}}(\Omega,\theta)$ to estimate the shape of the $LiNbO_3$ THz waveform as a function of WG analyzer angle θ:

$$E_{\text{THz}}(\Omega,\theta) = E_{\text{THz}}(\Omega) \times h_{\text{Quartz}}(\Omega,\theta), \tag{2.39}$$

where $E_{\text{THz}}(\Omega)$ is the pristine $LiNbO_3$ THz electric field, shown as the black line in Fig.2.9c. The reconstructed $LiNbO_3$ spectra for $\theta = 0°, 50°$ and 90° are shown in the Figure 2.9c. By performing the inverse Fourier transform, we have access to the $LiNbO_3$ waveform, depicted in the Figure 2.9d. Since we measure the transfer function of the complete WG Polarizer-Quartz-WG analyzer, this approach indirectly accounts for the WG analyzer frequency dependent THz attenuation factor, discussed in the Appendix A.

Figure 2.10a shows the FFT of the reconstructed E_{THz} waveform for the 0-90° WG analyzer angles. The blue line shows the blue shift of the THz central frequency. Figure 2.10b links WG

analyzer angle θ the change in the THz central frequency (blue circles). The latter figure displays that we are able to tune the $LiNbO_3$ THz central frequency in the range from ≈ 0.52 and up to ≈ 0.73 THz. Red circles on Figure 2.10b show the measured $LiNbO_3$ source THz central frequency without the x-cut Quartz, which is equal to 0.64 THz. The correctness of this reconstruction procedure, based on the pump-probe signal sensitivity to E_{THz} around the time-delay zero, is discussed in the Appendix B.

As we demonstrated, such behavior of the x-cut Quartz crystal could be used to shape the spectrum of the hard-to-align THz sources. In this particular experiment, we change the THz spectrum as a function of the selected THz polarization component. However, the simultaneous rotation of both x-cut Quartz crystal with WG analyzer, such as $\theta_{WG} = \theta_{\mathrm{Quartz}}$ should allow for rotating the THz pulse polarization without significant distortion of its spectrum. Notably, one can achieve more robust control over the THz pulse spectrum by adjusting the Quartz crystal thickness.

Chapter 3

Ultrafast generation of acoustic and optical phonons with THz

Contents

3.1 Introduction

The works of H.J. Maris [103], J.M. Wiesenfeld [104], G. Eesley [105] and Y. Yan [106] have kick-started the field of picosecond laser acoustics, describing photogeneration and optical detection of picosecond acoustic pulses in metals and semiconductors. At nearly the same moment, ultrashort laser pulses allowed to explore the optical phonon dynamics [107, 108]. The detection of coherent acoustic and optical phonons is possible by analyzing the variation of the reflected or transmitted probe beam intensity or polarization, which is caused by change in material properties in the presence of the phonon strain field [109]. Most coherent phonons have been generated by near-infrared, visible [110, 111], or near-ultraviolet pulsed radiation [112, 113], i.e., a light pulse close to the resonant electronic excitation. In these cases, phonon generation is driven by different electron-phonon collisions processes (deformation potential or thermoelasticity, for example) that we will briefly describe in the first part of this chapter. Moreover, in some cases, stimulated Raman and Brillouin scattering can lead to coherent lattice motion [108].

Over the last decades, thanks to the recent developments in nonlinear optics, the tabletop amplified laser systems can be used to routinely generate high peak-amplitude THz pulses [114]. Such intense electric field transients (with peak electric field $> 100\,\mathrm{kV\,cm^{-1}}$) having characteristic energy in meV range, can be used to study the collective particle motion in a solid. In particular, resonant and nonresonant control over matter [1,115] is possible through electron acceleration in the presence of an intense THz field [116,117] up to impact ionization [118]. In addition, resonant antiferromagnon excitation with THz has also been reported [119]. THz radiation can also be directly coupled to phonons, and intense THz pulses are proclaimed as the ultimate tool of coherent lattice vibration control [2]. Once said, only a few reports of coherent acoustic phonon generation with THz exist at the moment, demonstrating that this area of research is almost unexplored. In the past few years, observation of acoustic phonon signatures in AlGaAs intrinsic semiconductor has been discussed but without establishing the nature of the microscopic mechanism at play [120]. Some reports of strain induced by microwave radiation (electromagnetic pulse in the GHz regime) also exist [121] without a clear conclusion at the moment. This situation deeply contrasts with the generation of coherent optical phonons by a THz pulse, for which there is much more experimental evidence. One can cite the optical phonon generation in Tellurium [122], diamond [123] and Bi_2Se_3 nanofilms [124, 125], for example. Despite numerous reports, there are still some debates about the microscopic origin of the THz-driven optical phonon dynamics, as a result of non-linear ionic Raman scattering [2, 126] or THz sum frequency excitation [127].

This Chapter will be split into two parts, where we are going to discuss the experimental evidence of acoustic and optical phonon generation with intense pulsed THz radiation. The first part starts by summarizing the theoretical background of the picosecond acoustic strain generation in metals and semiconductors through thermoelastic and deformation potential stresses. After this theoretical introduction, we will present our results of coherent acoustic phonon generation with THz. Then, to address the microscopic mechanism at play, we compare the experimental results of Near-IR (NIR) and THz excitation in metals such as nanometric films of Chromium (Cr) and Aluminum (Al) where no optical phonon exist. Finally, based on this comparison, we present the experimental evidence that thermoelastic stress in the studied metallic systems is the driving mechanism of coherent acoustic phonon generation with THz. In this work, we evidence an ultrafast Joule effect (carrier acceleration and electron-phonon scattering processes at the Fermi level in the presence of a THz pulse) that can lead to similar photoinduced strain amplitudes obtained by a lattice heating with interband NIR excitation. At the end of this part, to open new avenues, we show how it is possible to drive acoustic phonons in more complex material as the Bismuth Telluride (Bi_2Te_3) nanofilms. Such a system is a rich platform for studying phonon generation since we find that THz pulse can simultaneously generate both acoustic and optical phonons. Furthermore, this constitutes the second important part and achievement of this Chapter.

The second part of this Chapter will introduce phenomenological models describing coherent optical phonon excitation in transparent and opaque solids, including recently proposed THz ionic Raman scattering (THz-IRS) and THz-sum frequency excitation mechanisms (THz-SFE) [2, 126, 127]. Next, based on the discussion of our experimental results, we will suggest possible scenarios regarding the driving mechanisms of Raman active A_{1g}^1 coherent optical phonon excitation in a 16 nm thick Bi_2Te_3 film with high-peak field THz electric pulses.

3.2 Acoustic phonons generation by pulsed THz radiation

3.2.1 Theoretical Background

Following the Chapter 1 discussion, carriers generated by the absorption of the laser pulse undergo scattering and energy exchange through couplings between electron, phonon, and spin baths. Even though NIR-VIS-NUV light was mainly used as the pump pulse, the following model is relevant for any kind of initial electron excitation. The resulting conversion of optical into internal mechanical energy may lead to stress generation both at the macroscopic scale and at the unit-cell level. From the thermodynamic point of view, the energy increase of an adiabatic system will lead to the change in the internal pressure of a solid, known as the photoinduced stress σ_{PI} [128]. For the isotropic, 1D medium, we can write the classical equation of elastic motion, with σ_{PI} acting as the source term [129]:

$$\frac{\partial^2 u(t,z)}{\partial t^2} - V_{\mathrm{ph}}^2 \frac{\partial^2 u(t,z)}{\partial z^2} = \frac{1}{\rho} \sum_i \frac{\partial \sigma_{\mathrm{PI},i}(t,z)}{\partial z}, \tag{3.1}$$

where $u(t,z)$ is the particle displacement, V_{ph} is the strain pulse velocity, ρ is the density of the medium, and $\sigma_{\mathrm{PI},i}(t,z)$ is the spatio-temporal profile of the specific contribution to the photoinduced stress. In complex systems (for example, in multiferroics) σ_{PI} may have various simultaneous contributions of different physical origins [129]:

$$\sigma_{\mathrm{PI}} = \sigma_{\mathrm{TE}} + \sigma_{\mathrm{DP}} + \sigma_{\mathrm{PE}} + \sigma_{\mathrm{ES}} + \sigma_{\mathrm{MS}}, \tag{3.2}$$

where σ_{TE}, σ_{DP}, σ_{PE}, σ_{MS}, and σ_{ES} are the thermoelastic (TE), deformation potential (DP), inverse piezoeletric (PE), magnetostriction (MS) and electrostriction (ES) stresses. In this thesis, however, we will discuss only the most relevant contributions for a simple metal and a semiconductor, namely the σ_{TE} and σ_{DP}.

Thermoelastic stress: The most familiar mechanism of coherent GHz-THz acoustic phonon generation in metals is the thermoelastic stress $\sigma_{\mathrm{TE}}(z,t)$. The initial distribution of optical energy deposited per unit of volume can be estimated by [131]:

$$W_{opt}(z) = (1-R)\frac{Q}{A \cdot \xi} e^{-z/\xi} \quad \text{for d} \gg \xi, \tag{3.3}$$

where A is the irradiated area, Q is the pulse energy, ξ is the optical penetration depth, R is the laser intensity reflection coefficient and d is the film thickness. As one can notice, $W_{opt}(z)$ is initially defined over a finite distance, equal to ξ (see Fig.3.1a).

Following the very fast electron-electron scattering (see Fig3.1b, electron-electron thermalization), the hot carriers will interact with the phonons to decay to the lowest energy state (electron-phonon thermalization). This intraband process will lead to thermal (or incoherent) phonon emission. Such increase in incoherent phonon population of the phonon band m ($\rho_m^p(\boldsymbol{k})$) will contribute

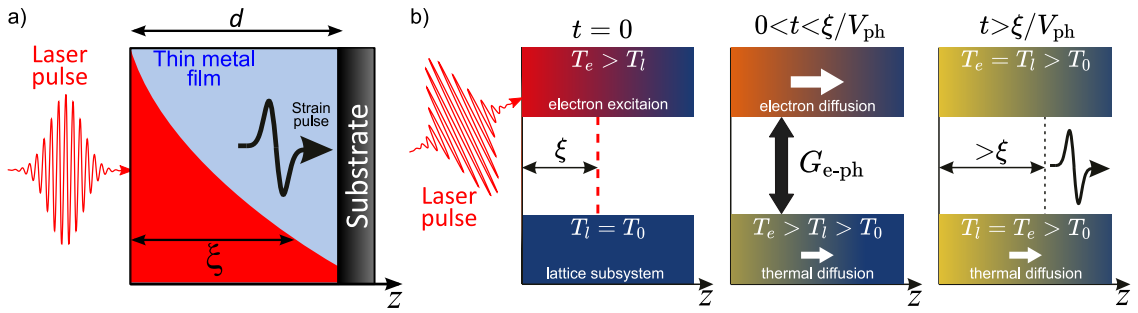

a) Simplified schematic of picosecond acoustic pulse generation in metals. The metal film absorbs the laser pulse within a finite volume, given by the optical penetration depth ξ, leading to the non-homogeneous deposited energy profile. The rapid lattice thermal expansion or contraction leads to the emission of the strain pulse. **b)** From left to right: The laser pulse is locally absorbed by the electron subsystem, reaching the temperature T_e. After the electron-electron thermalization, electrons transfer their excess energy to the lattice via electron-phonon coupling ($G_{\text{e-ph}}$). The lattice temperature increase will result in the contraction/dilatation of the lattice, leading to the emission of a strain pulse from the excited surface area. After [130].

Figure 3.1 – *Strain generation via the thermoelastic process.*

to the thermoelastic stress as [9, 129]:

$$\sigma_{\text{TE}}(z,t) = -\sum_{m,k} \delta\rho^p_m(\boldsymbol{k})\hbar\omega_{m,\boldsymbol{k}}\gamma^p_{m,\boldsymbol{k}} = -\gamma_L c_L \delta T_L(z,t), \tag{3.4}$$

where γ_L is the averaged Grüneisen coefficient for all $\boldsymbol{k}$-dependent Grüneisen factors over m phonon bands, c_L is the lattice heat capacity per unit of volume and δT_L is the increase in the lattice temperature. From the macroscopic point of view, the latter equation is equivalent to the one observed with the thermodynamic relation:

$$\beta = \frac{1}{3B}\frac{\partial P}{\partial T}\bigg|_V, \tag{3.5}$$

where β is the linear expansion coefficient, P is the pressure, and B is the bulk modulus. The lattice expansion is related to the increase in the internal pressure of a solid ($\sigma = -\Delta P$ by convention). With this, we arrive to the macroscopic formulation of the thermoelastic stress:

$$\sigma_{\text{TE}}(z,t) = -3B\beta\delta T_L(z,t). \tag{3.6}$$

One should note that temperature-driven lattice expansion is possible only for an anharmonic interatomic potential [9, 129]. For metals, if we assume the complete transfer of the energy from electron to phonon system, we can write [129]:

$$\delta T_L(z,t) = \frac{N(z,t)h\nu}{c_L}, \tag{3.7}$$

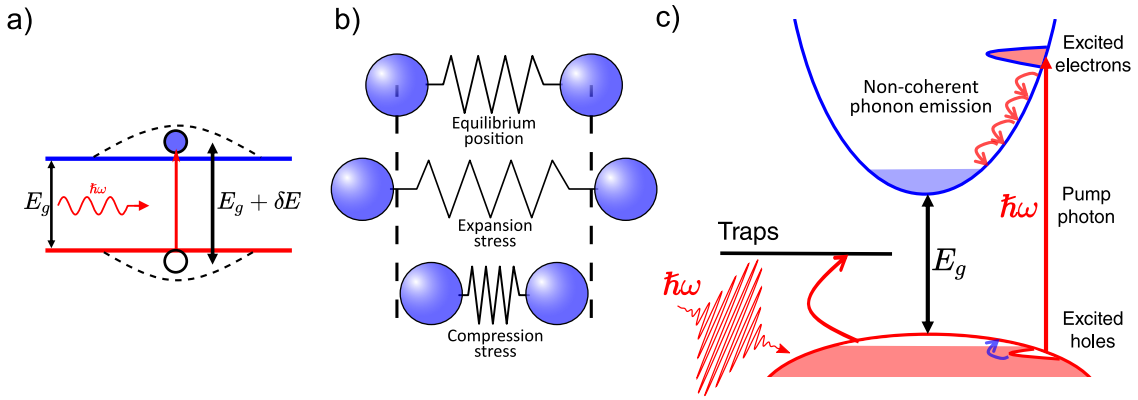

a) The absorption of the laser pulse leads to the electron-hole pair creation, and the change in the electronic distribution δE. **b)** In turn, this shift in the electronic distribution δE modifies the interatomic interaction which leads to the strain generation ($\delta V/V$). **c)** Over bandgap excitation ($\hbar\omega > E_g$) leads to both deformation potential stress (δE) and thermal phonon emission. Adapted from [129, 132].

Figure 3.2 – *Band-structure picture of the deformation potential stress.*

where N is the photoexcited carrier concentration and $h\nu$ is the pump photon energy. In addition to the stress generation through the lattice heating, one needs to account for the photoinduced change in the electronic distribution, i.e., deformation potential stress, resulting from the light-induced modification of the electron-cation interaction.

Deformation potential stress: The deformation potential stress (σ_{DP}) can be described as interatomic potential modification due to the change in the electronic distribution. For example, the change in electronic energy in the band n by an amount $\delta E_{n,\boldsymbol{k}}$ (see Fig.3.2a), may lead to the volume change of a solid [24, 129]:

$$\left.\frac{\delta V}{V}\right|_{n,k} = \frac{\delta E_{n,\boldsymbol{k}}}{d^{\mathrm{eh}}_{n,\boldsymbol{k}}}, \tag{3.8}$$

where $d^{\mathrm{eh}}_{n,\boldsymbol{k}}$ is the deformation potential coefficient of the energy level $E_{n,\boldsymbol{k}}$. The change in electron-hole distribution described by $\delta E_{n,\boldsymbol{k}}$ will affect the interatomic potential. This will result in the ion displacement and creation or annihilation of a phonon, as shown in the Fig.3.2b. The deformation potential stress is usually expressed in terms of the light-induced modification of carrier population $\delta\rho^e_n(\boldsymbol{k})$ at different energy levels $E_{n,\boldsymbol{k}}$ as [129]:

$$\sigma_{\mathrm{DP}} = -\sum_{n,k} \delta\rho^e_n(\boldsymbol{k}) E_{n,\boldsymbol{k}} \gamma^e_{n\boldsymbol{k}} = \sum_{n,k} \delta\rho^e_n(\boldsymbol{k}) \frac{\partial E_{n,\boldsymbol{k}}}{\partial \eta_{n,\boldsymbol{k}}}, \tag{3.9}$$

where $\eta_{n,k}$ is the strain generated by the change in electronic distribution, and $\gamma^e_{\boldsymbol{k}}$ is the electron Grüneisen coefficient.

General case: In reality, both σ_{DP} and σ_{TE} can simultaneously contribute to the total photoinduced stress in both metals and semiconductors. In metals, the non-negligible σ_{DP} can exist for high electron temperatures. Therefore, the total photoinduced stress, as a sum of thermoelastic

and electronic equivalent of the phononic pressure is defined as [129, 133]:

$$\sigma = \sigma_{\mathrm{TE}} + \sigma_{\mathrm{DP}} = -3B\beta\delta T_L - \gamma_e c_e \delta T_e \text{ (Metal) .} \tag{3.10}$$

with γ_e and c_e the electronic Grüneisen coefficient and the electronic heat capacity.

In the semiconductor, upon the electron and hole intraband thermalization (i.e. when the electrons and holes are localized at the bottom or top of the conduction or valence bands, respectively), the deformation potential can be written as:

$$\sigma_{DP} = N\frac{\partial E_g}{\partial \xi} = -NB\frac{\partial E_g}{\partial P} = -Nd^{\mathrm{eh}}, \tag{3.11}$$

where d^{eh} is the electron-hole deformation potential parameter for this particular electron-hole energy distribution. Finally, when the incident photon energy is larger than the bandgap ($\hbar\omega > E_g$, see Figure 3.2c), one should account for both the deformation potential and thermal phonon contributions [129, 131]:

$$\sigma = \sigma_{\mathrm{DP}} + \sigma_{\mathrm{TE}} = -Nd^{\mathrm{eh}} - 3B\beta N\frac{(\hbar\omega - E_g)}{c_L} \text{ (Semiconductor) ,} \tag{3.12}$$

where $\delta T_L = N\frac{(\hbar\omega - E_g)}{c_L}$ is the contribution to the heating of the lattice due to the intraband relaxation process. Usually, linear expansion coefficient β is positive for most solids, so incoherent phonons produce negative stress. On the other hand, the sign of d^{eh} may be positive or negative (case of photoexcited silicon [134]), so the total photoinduced strain may be the sum or difference of DP and TE contributions.

According to Eq.3.1, the non-uniform change in the internal pressure will lead to the generation of the strain pulse in the material. For the semi-infinite solids, Thomsen et al. have established the expression of the bipolar strain pulse emission from a free surface [103, 131]. As a first approximation, if there is no fast carrier or heat diffusion process, the spatial distribution of the strain pulse is limited by the optical penetration depth of the pump [128]. In that case, the characteristic frequency of the emitted acoustic pulse is $f = V_{ac}/2\xi$.

In addition, for a thin film with a thickness comparable with an optical penetration depth, as in the samples presented later, the photoinduced stress is defined over the entire film thickness H. The thin-film geometry restricts the spatial distribution of the photoinduced stress, which results in filtering the phonon spectrum (Fabry-Perot cavity effect) to specific values given by the equation:

$$f = \frac{lV_{ac}}{2H}, \tag{3.13}$$

with l, V_{ac}, and H the mode number, the longitudinal speed of sound, and the film thickness, respectively. Apart from these breathing modes of the thin film, the other frequencies interfere destructively.

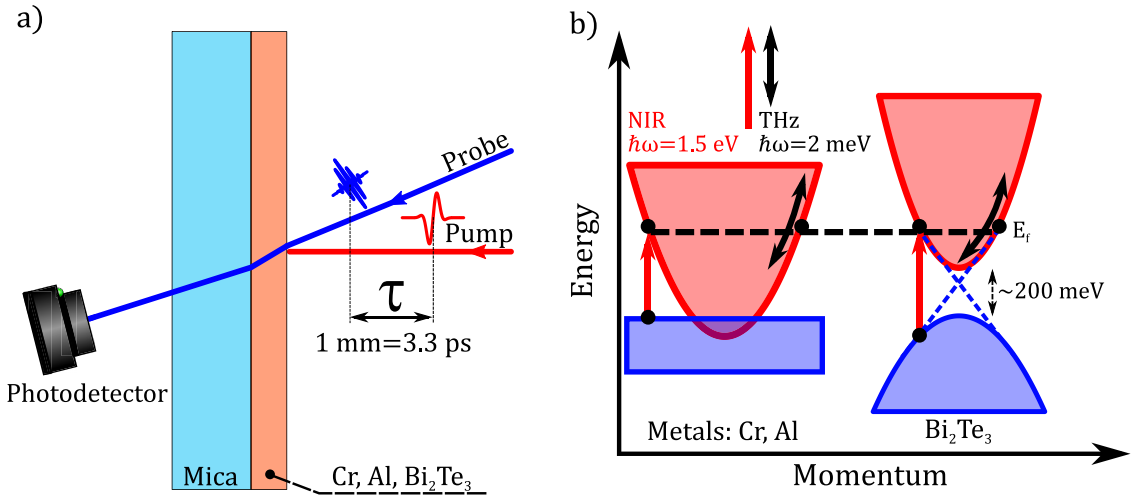

a) Sketch of the femtosecond time-resolved experiment in transmission geometry. **b)** Sketch of the electronic band structures of the metal and the degenerated n-doped Bi_2Te_3. Simple vertical arrows show the interband optical transition induced by the NIR pulse, and double black arrows represent carrier intraband acceleration by the THz electric field. The blue dashed lines represent the spin-polarized Dirac surface states.

Figure 3.3 – *Band structure sketch of the metal and topological insulator and experimental setup.*

3.2.2 Results and discussion

So far, the generation of coherent acoustic phonons has been studied only with laser pulses in the visible, near infrared and near ultraviolet range [112, 129]. In the meantime, it has been shown that the THz pulse can be coupled to optical phonons [122, 123], while there is no definitive report on the coherent generation of acoustic phonons with THz. Through the comparison of NIR and THz photoexcitation (1.54 eV versus 4 meV), we will attempt to identify the main mechanisms of acoustic phonon generation in metal and narrow-band semiconductor thin films. This Section is based on the already published paper "Coherent acoustic phonons generated by ultrashort terahertz pulses in nanofilms of metals and topological insulators," prepared by A. Levchuk, B. Wilk, G. Vaudel, F. Labbé, B. Arnaud, K. Balin, J. Szade, P. Ruello, and V. Juvé [135].

Experimental details

The experiments were done at room temperature, in the ultrafast pump-probe configuration in the transmission geometry, as shown in Fig.3.3a. As the THz source, we used the $LiNbO_3$ crystal in the tilted pulse front configuration discussed in the Chapter 2. In addition, two free-standing Wire Grid (WG) polarizers were introduced in the THz beam path for pump-power-dependent measurements. THz beam and THz optics characterization are presented in the Chapter 2 and Appendix A. The peak THz electric field amplitude used in the experiment was estimated to be around 275 kV/cm [1], which corresponds to a pulse energy of roughly 1.2 µJ (according to a calibrated pyroelectric detector).

In this section, we have compared THz to NIR (1.54 eV, 800 nm) pump/probe measurements. In both experiments (THz and NIR excitation), the probe wavelength has been kept to the same energy, 3.1 eV (400 nm), to avoid spurious effects due to the detection process.

1. $1/e^2$ radius of ≈ 615 µm measured by a knife-edge method, see Appendix A.

Samples

Chromium and Aluminum films : Thin polycrystalline films were prepared by pulsed-vapor deposition on a transparent mica substrate with the thicknesses of $H = 14 \pm 0.5\,\text{nm}$ (Cr) and $H = 20 \pm 0.5\,\text{nm}$ (Al) measured by x-ray reflectivity. Both deposition and x-ray reflectivity experiments were done at the IMMM laboratory by Dr. Mathieu Edely.

Bi_2Te_3 thin film: Bismuth Telluride, (Bi_2Te_3), is a narrow-gap semiconductor (with $E_g \approx 0.2\,\text{eV}$ [136]), known for its thermoelectric properties, with high electrical conductivity and low lattice thermal conductivity [137–139], making it appealing for industrial applications. In addition, Bi_2Te_3 can support unique surface conduction bands, first measured by Angle-Resolved Photoemission Spectroscopy (ARPES) by Noh et al. [140], making this material a topological insulator [141]. As depicted in the Fig.3.3b, topological insulators have a bulk bandgap like an ordinary insulator and so-called surface conducting Dirac states. The topological insulator nature of Bi_2Te_3 arises from both spin-orbit interaction (Z=83 for Bi and Z=52 for Te) and time-reversal symmetry breaking at the interface [136]. However, in this thesis, we do not probe the topological order of Bi_2Te_3. Firstly, due to the strong n-doping of the sample (see ARPES measurement of [142]) the Fermi level is shifted closer to the conduction band, therefore making the manipulation of Dirac states more difficult. Secondly, the visible probe has an optical penetration depth of around 9 nm [143] and is not sensitive to the surface states. The samples were grown by molecular beam epitaxy in the Physics Institute of Katowice, the University of Silesia, by Dr. K. Balin and Prof. J. Szade. As described in previous references [110, 142, 144, 145], the sample is of high quality with single-crystalline growth and trigonal axis oriented perpendicular to the surface. The Bi_2Te_3 layer was deposited onto the mica substrate.

Experimental results

In this part, we start first with experimental results on coherent acoustic phonon generation with THz and NIR ultrashort pulses in prototypical metals (Chromium and Aluminum). The second part will be an extension of this study to more complex materials such as topological insulator Bi_2Te_3.

Cr and Al nanofilms: The change in the 400 nm probe beam transmission ($\delta T(\tau)/T$) as the function of the pump-probe delay for the Cr and Al thin films are displayed in Figure 3.4a and b, with both samples showing similar transient behavior. The black line in Fig.3.4a shows the chromium thin film $\delta T(\tau)/T$ signal measured upon the THz excitation with pulse energy of roughly 1.2 µJ, which corresponds to peak $E_{\text{THz}} \approx 275\,\text{kV cm}^{-1}$. The signal consists of a sharp increase in the probe transmission followed by a slower exponential decay. This exponential decay is attributed to the lattice temperature elevation (δT_L, incoherent phonons) and subsequent heat diffusion [146–149]. On top of this thermal background, a clear oscillatory feature can be observed. To isolate only the oscillatory component, we fit the thermal background with the following function:

$$f(\tau) = a_0\left\{\cdot\left(1 + \text{erf}\left[\frac{\tau - \tau_0}{s}\right]\right) \cdot a_1 \exp\left[\frac{\tau - \tau_0}{\tau_1}\right]\right\}, \tag{3.14}$$

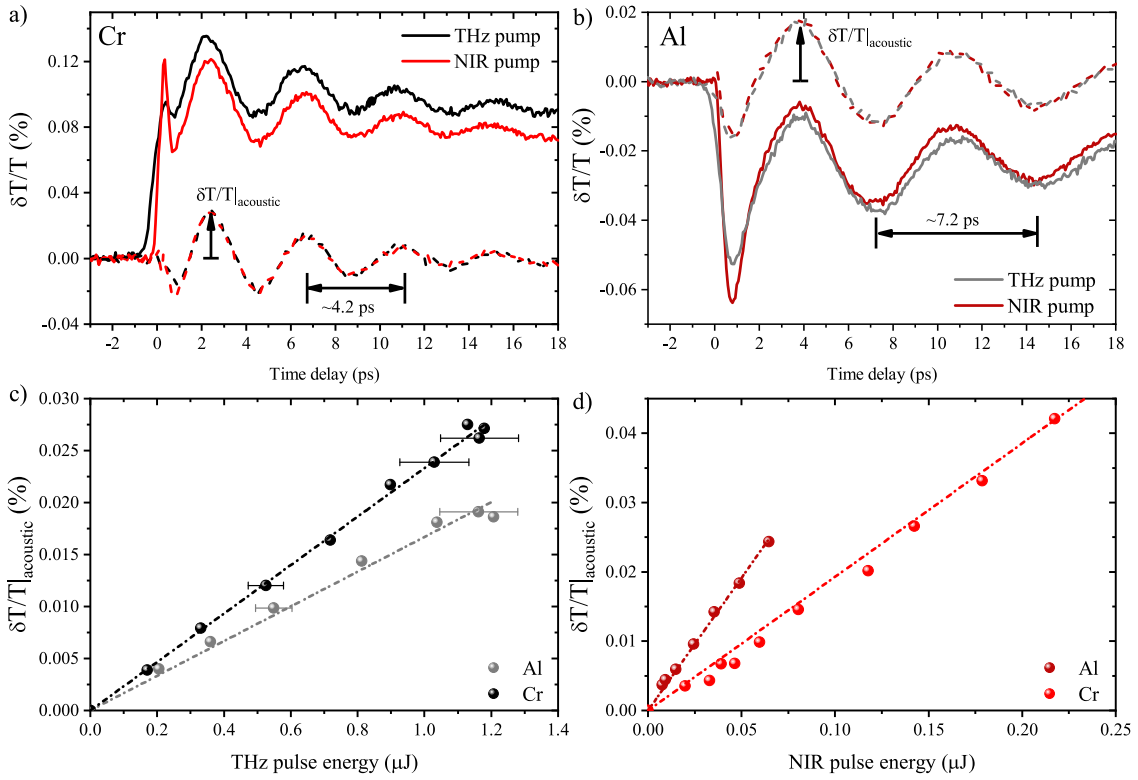

a) Transient optical transmission obtained with a THz or NIR pump excitation for a thin Cr film. Dashed lines correspond to the extracted oscillatory part of the signals. The pulse energy of the NIR is $\backsimeq 0.07\,\mu J$ and of the THz is $\backsimeq 1.2\,\mu J$. **b)** Same as a) but for a thin 20 nm Al film. The pulse energy of the NIR pulse is $\backsimeq 0.04\,\mu J$ and the THz is $\backsimeq 1.05\,\mu J$. **c)** THz pulse energy dependence of the acoustic phonon signal for the Cr (black) and Al (grey) thin films. **d)** NIR pulse energy dependence of the acoustic phonon signal for the Cr (red) and Al (dark red) thin films. Dash-dot lines are the respective linear fits.

Figure 3.4 – *Transient response and acoustic phonon amplitude of a thin Cr and Al film excited with* 800 nm *and THz pulses.*

where a_0 is the total fit amplitude, s is the slope of the error function (related to the temporal resolution of the experiment), with a_1 and τ_1 being the amplitude and decay time of the thermal background. The extracted oscillatory component ($\delta T(\tau)/T - f(\tau)$) of a signal has a temporal period of about 4.2 ps ($f_{\mathrm{Cr}} \approx 238\,\mathrm{GHz}$), and it is shown as the black dashed line in Figure 3.4a.

The signal measured for the 0.07 μJ NIR pump is shown as the red line in Fig.3.4a. Compared to the THz excitation, NIR signal has a similar general shape of a transient, except for the faster "rise and fall" of the probe beam transmission at short timescales ($\tau < 1\,\mathrm{ps}$). The presence of such well defined "peak" is attributed to the shorter temporal duration of the NIR pump compared to the THz pulse and to the fast electron-phonon scattering in Chromium [148]. Remarkably, the amplitude and the phase of the extracted oscillatory component (dashed line in Figure 3.3a) are found equivalent for $\backsimeq 0.07\,\mu J$ NIR and $\backsimeq 1.2\,\mu J$ THz pulse energies. Similar results are obtained for the thin Aluminum film (see Fig.3.4b). The observed period of the oscillatory component of the Aluminum signal has a period of roughly 7.2 ps ($f_{\mathrm{Al}} = 139\,\mathrm{GHz}$).

In addition, we measured the amplitude of the global maximum of the oscillatory part of the signal $\delta T/T|_{\mathrm{acoustic}}$ (marked as a black arrow in Figs.3.4a and b) as a function of THz and NIR power. Figure 3.4c shows that $\delta T/T|_{\mathrm{acoustic}}$ of Chromium and Aluminum thin films increases

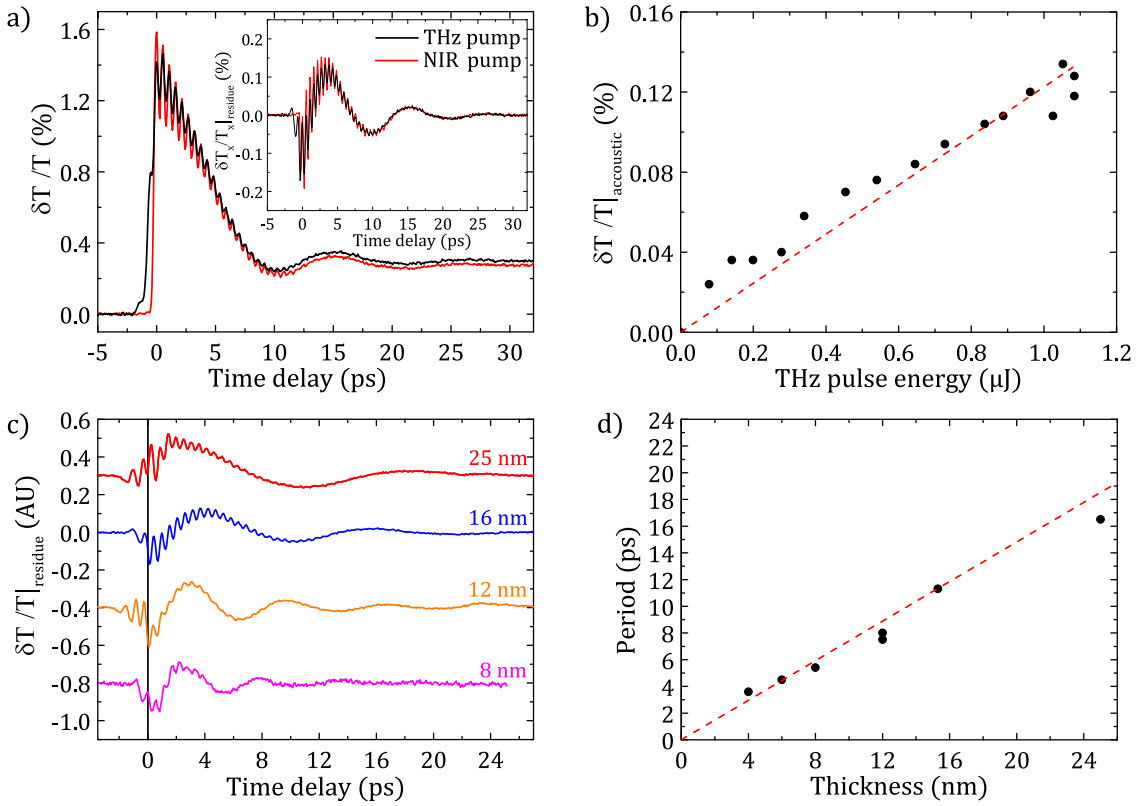

a) Transient optical transmission obtained with a THz or NIR pump excitation for a 16-nm Bi2Te 3 thin film with 51 nJ and 1.2 µJ for NIR and THz excitation, respectively. Inset: Oscillatory part of the signal. **b)** THz pulse energy dependence of the acoustic phonon amplitude for the 16 nm thin film. **c)** Thickness dependence of the coherent acoustic phonon signal generated by THz excitation. **d)** Coherent acoustic phonon oscillation period vs. the film thickness.

Figure 3.5 – *THz pump: Bi_2Te_3 thickness dependence on the coherent phonon signal.*

linearly with the THz pulse energy (quadratically with the E_{THz} amplitude). The same linear dependence is found for the NIR pump, as depicted in Fig.3.4d.

Bi_2Te_3 nanofilms: As the following step, we extended our study to thin Te rich and consequently n-doped Bi_2Te_3 films with various thicknesses ranging from 4 to 25 nm. Figure 3.5a shows the signal of Bi_2Te_3 16 nm film excited with THz and NIR pump pulse energy fixed at 1.2 µJ and 51 nJ, respectively. For both pump wavelengths, the transient optical transmission $\delta T/T$ shows a sharp increase after the initial excitation and a fast recovery followed by a slower decaying signal attributed to the thermal background. We extracted the oscillatory part of the signal with a similar fit (see Eq.3.14) having two exponential decays. Fast exponential decay was found to be equal to 1.8 ps, and it is related to the hot carrier relaxation [150–152].

When the thermal background is subtracted (see inset in Fig.3.5a), we observe the $\delta T/T_{\mathrm{residue}}$ modulation at two distinct frequencies: a fast oscillatory component at around 1.8 THz, which is attributed to the Raman active A^1_{1g} optical phonon [153] (will be discussed in the Section 3.3.2) and a slower, with a period of about 11.6 ps ($f_{BT} = 86$ GHz frequency). We report that the amplitude of the slow oscillatory component scales linearly with the THz pulse energy (see Fig. 3.5b). We then measured the $\delta T/T|_{\mathrm{residue}}$ change for Bi_2Te_3 films with different thicknesses, and the corresponding signals are shown in Figure 3.5c. We see that only the frequency of a slow oscillatory component

is drastically affected by the change of Bi_2Te_3 thickness. Figure 3.5d depicts clear linear sample thickness dependence of the low frequency mode. We found the highest frequency of this mode to be $\approx 250\,\mathrm{GHz}$, measured for the 4 nm thick sample.

Discussion

Nature of the acoustic mode: In the previous sections, we have shown that THz and NIR excitation of thin metallic and Bi_2Te_3 films grown on the mica substrate leads to similar transient behavior of $\delta T/T$ for the specific combination of THz and NIR pulse energies. Furthermore, the amplitude of the oscillatory part of the signal scales linearly with THz and NIR pulse energy (see Fig.3.4c and d). In addition, we show that the period of the low-frequency oscillatory component present in the Bi_2Te_3 transient response is directly proportional to the film thickness H (see Fig.3.5d) suggesting these oscillations are the mechanical resonances of the layers.

To confirm the nature of this low-frequency $\delta T/T$ modulation, we start by analysing the mechanical boundary conditions, in order to establish which acoustic modes can be excited. We first note that since pump light penetration depth ξ is bigger than the film thickness H, it means that the photoinduced stress will be confined within the acoustic layer. Next, we estimate the acoustic reflection coefficient at the metal/mica interface, defined as [128]:

$$R_{ac} = \frac{Z_{mica} - Z_{layer}}{Z_{mica} + Z_{layer}}, \tag{3.15}$$

where Z is the acoustic impedance :

$$Z = \rho V_{ac}, \tag{3.16}$$

with the material density ρ and the acoustic velocity V_{ac}. With the values from the literature, the acoustic impedance of all the materials chosen as the layer here (Cr, Al, Bi_2Te_3) is larger than the acoustic impedance of the substrate [2]. This leads to $R_{ac} < 0$ for all interfaces. The $R_{ac} < 0$ value means that the acoustic wave reflected at the interface will be phase-shifted by π [128] after a single trip, repeating each time it bounces back and forth within the acoustic layer. This leads to the resonator-like vibration of the nanometric film at the frequency $f = lV_{ac}/2H$ (see Eq.3.13). Then, the straightforward estimation of the eigenmode frequencies for all layers gives:

$$\begin{aligned} f_{Cr} &= \frac{1 \cdot 6600\,\mathrm{m\,s^{-1}}}{2 \cdot 14\,\mathrm{nm}} = 235.7\,\mathrm{GHz}\ \text{(Experiment: 238 GHz)};\\ f_{Al} &= \frac{1 \cdot 6320\,\mathrm{m\,s^{-1}}}{2 \cdot 20\,\mathrm{nm}} = 158\,\mathrm{GHz}\ \text{(Experiment: 139 GHz)};\\ f_{BT} &= \frac{1 \cdot 2460\,\mathrm{m\,s^{-1}}}{2 \cdot 16\,\mathrm{nm}} = 77\,\mathrm{GHz}\ \text{(Experiment: 86 GHz)}, \end{aligned} \tag{3.17}$$

and they are in a rather good agreement with experimentally measured values. The about 12 % difference for the Al thin film could be related to a decrease in V_{Al} due to polycrystalline nature of the film, as observed before for Mg-Zn alloy for instance [154]. For the Bi_2Te_3, the speed of sound

2. $\rho_{mica} = 2880\,\mathrm{kg\,m^{-3}}$, $V_{mica} = 4300\,\mathrm{m\,s^{-1}}$, $Z_{mica} = 1.2 \times 10^7\,\mathrm{kg\,m^{-2}\,s^{-1}}$.

was taken from [110, 144]. In our study, the fit of acoustic period measured with THz excitation as a function of the film thickness (red dashed line in Figure 3.5d), gives the $V_{BT} = 2700\,\mathrm{m\,s^{-1}}$, which deviates by less than 10 % from previous reports [155].

Acoustic phonon generation mechanism in metals: We continue the discussion with the pump power dependence of coherent acoustic phonon amplitude, presented in Fig.3.4c and d. Importantly, for both THz and NIR excitation, $\delta T/T|_{\mathrm{acoustic}}$ scales linearly with the pump pulse energy. This means that for all samples in the study, linearity of $\delta T/T|_{\mathrm{acoustic}}$ for the THz excitation excludes highly nonlinear processes of energy deposition such as impact ionization [118] or Zener tunneling [116]. With this in mind, we can now estimate the absorbed energy density in the case of THz and NIR excitation within the usual dielectric response approach.

With the THz time-domain spectroscopy, we have first measured the complex dielectric function of the 14 nm thick Cr film in the 0.2-2.5 THz frequency range [99], shown in Figure 3.6a. By fitting the measured data with a simple Drude model, we extract Chromium plasma frequency $\omega_p \approx 350\,\mathrm{THz}$ and the electronic scattering rate $\tau_e \approx 14\,\mathrm{THz}$. These parameters lead to a nearly-frequency-independent [3] conductivity $\sigma_{Cr} \approx 4.5 \times 10^5\,\Omega\,\mathrm{m}^{-1}$. In addition, as the characteristic scattering frequency in metals is typically well above the frequency of our driving THz field [156], we limit our model to the stationary drift electron transport regime and neglect any ballistic transport effects. These two assumptions allow us to ignore the E_{THz} retardation effects, and we can write the time-dependent current density associated to the electron acceleration in the presence of the local THz pulse as:

$$\boldsymbol{j}(t') = \sigma \int_{-\infty}^{t'} \boldsymbol{E}_{\mathrm{THz}}^{\mathrm{loc}}(t'')dt''. \tag{3.18}$$

Here, $\boldsymbol{E}_{\mathrm{THz}}^{\mathrm{loc}}(t)$ is the local THz electric field acting on the electrons, and σ is the frequency-independent metal conductivity. Then, we can estimate the temporal profile of the absorbed energy with the ultrafast analogy of the well-known Joule effect:

$$W_{\mathrm{THz}}^{\mathrm{Abs.}}(t) = \int_{-\infty}^{t} \boldsymbol{E}_{\mathrm{THz}}^{\mathrm{loc}}(t') \cdot \vec{j}(t')dt' = \sigma \int_{-\infty}^{t} \left[\boldsymbol{E}_{\mathrm{THz}}^{\mathrm{loc}}(t')\right]^2 dt'. \tag{3.19}$$

In the case of THz excitation, since our samples are much thinner than the driving field's wavelength, the local electric field can be approximated by the electric field inside the sample $E_{\mathrm{THz}}^{\mathrm{loc}}$. Prof. Brice Arnaud (Theory group at IMMM) has implemented the finite difference time domain (FDTD) method to simulate the electric field value in the sample and the substrate:

$$E_{\mathrm{THz}}^{\mathrm{loc}}(t) = s \cdot E_{\mathrm{THz}}(t), \tag{3.20}$$

with $E_{\mathrm{THz}}(t)$ being the vacuum THz electric field and $s \approx 0.45$ is the electric field attenuation coefficient, estimated from FDTD.

3. Within the experimental THz frequency range.

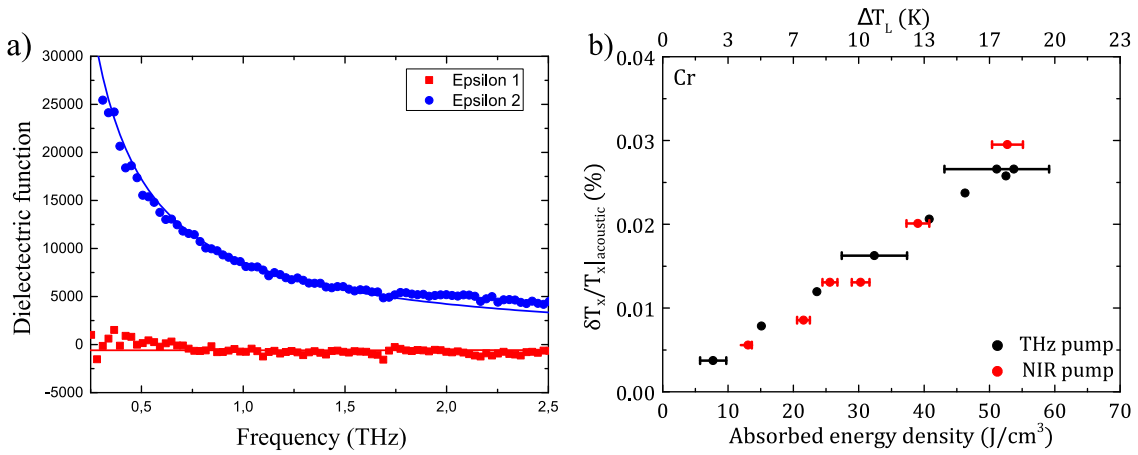

a) Dielectric function of Chromium in the THz frequency range. Experimental dielectric function of the Cr thin film measured by THz-TDS (dots and squares). The lines are fitted with the Drude model. **b)** Acoustic phonon amplitude as a function of the absorbed density energy for the Cr sample, calculated with Eq.3.19.

Figure 3.6 – *The dielectric function of Cr and acoustic phonon amplitude in the absorbed density of energy for THz and NIR excitation.*

Using Eq.3.19 and the experimental parameters, for the highest experimental THz field value (roughly 275 kV cm^{-1}, pulse energy of about 1.2 µJ) we can now estimate the total absorbed energy density, which becomes $W_{\mathrm{THz}}^{\mathrm{Abs.}} \approx 52\,\mathrm{J\,cm^{-3}}$. Using the value of Chromium heat capacity from the literature ($c_{\mathrm{L}} \approx 3 \times 10^6\,\mathrm{J\,m^{-3}}$), we can finally calculate the lattice temperature increase via the ultrafast THz Joule effect:

$$\delta T_{\mathrm{L}}(\mathrm{THz}) = \frac{W_{\mathrm{THz}}^{\mathrm{Abs}}}{c_{\mathrm{L}}} \approx 17\,\mathrm{K}. \tag{3.21}$$

In contrast to the THz excitation, the absorbed energy induced by NIR excitation is mediated by the direct optical transitions, which gives:

$$W_{\mathrm{NIR}}^{\mathrm{Abs}} = \frac{AN\hbar\omega_{\mathrm{NIR}}}{V}, \tag{3.22}$$

with A being the optical absorption coefficient, N is the number of incident photons of energy $h\nu_{\mathrm{NIR}}$, and the excited volume V. The NIR absorption coefficient A was modeled by the transfer matrix method using tabulated optical constants [156]. Remarkably, for the NIR pulse energy of 0.07 µJ (see Fig.3.4a) we obtain an absorbed energy of $W_{\mathrm{NIR}}^{\mathrm{Abs}} \approx 53\,\mathrm{J\,cm^{-3}}$, equivalent to the one obtained with Eq.3.21, for the THz pulse energy of 1.2 µJ. Consequently, for both scenarios (NIR and THz excitation), the maximum lattice temperature increase is estimated around $\delta T_L \approx 17\,\mathrm{K}$. Figure 3.6b shows that this equivalence is valid over the entire absorbed energy range under investigation: the acoustic phonon amplitude is driven solely by the total absorbed energy and is not dependent on the photon energy of the excitation pulse. This indicates that the amplitude of the acoustic phonon is not drastically dependent on the pathway of energy relaxation from the electron to the phonon subsystem (which is supposed to be different for a NIR and THz excitation) but only on the total absorbed energy by the lattice.

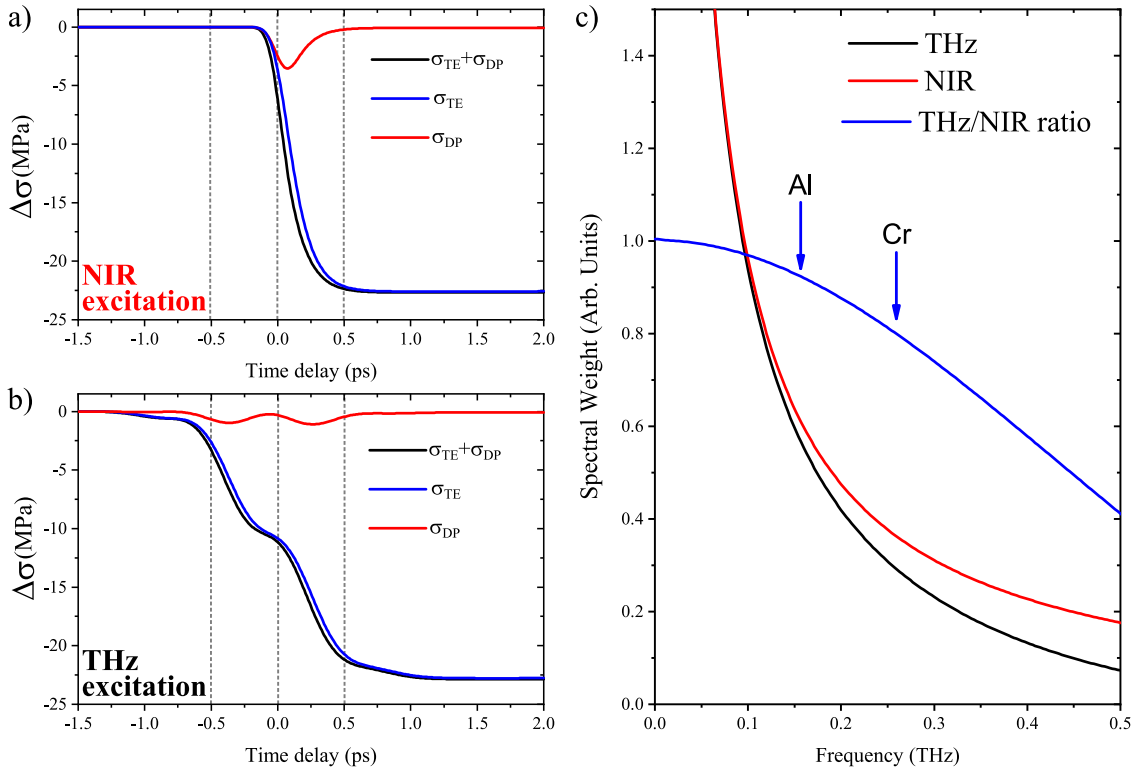

Dynamics of the photoinduced stresses originating from the electrons (σ_{DP}) and from the non-coherent phonons (σ_{TE}) calculated for the prototypical 20 nm thick Aluminum film. The total absorbed energy density equal to $\approx 10\,\mathrm{J\,cm^{-3}}$ in the case of **a)** the NIR light pulse with duration of 165 fs, and **b)** Experimentally measured THz pulse. **c)** Calculated phonon spectrum (FFT of σ_{TE}) for the NIR excitation (red) and THz excitation (black) in the relevant acoustic phonon frequency range. The ratio between THz and NIR is displayed as blue line, where the two eigenmode frequencies for the Aluminum and Chromium nanometric films are marked with the arrows.

Figure 3.7 – *Thin metallic films: Calculated dynamics of the photoinduced stress and associated phonon spectrum for NIR and THz excitation.*

In order to better understand this result, it is useful to study the spectral components of the photoinduced stress. For this purpose, Prof. Brice Arnaud has computed, using the ab initio DFT calculation, the lattice and electron heat capacities for the 20 nm thick Al film. Then, the phenomenological two-temperature model, with the computed heat capacities allows us to estimate the dynamics of the electron and lattice pressure. In the case of the NIR excitation, Figure 3.7a shows that the lattice stress contribution (σ_{TE}, blue line) dominates the electron stress contribution (σ_{DP}, red line), meaning that acoustic waves are indeed mainly driven by thermoelastic stress (σ_{TE}). Assuming that the thermoelastic stress is one of the possible mechanisms at play for the THz excitation, we can estimate the approximate shape of the σ_{TE} using the phenomenological TTM model. To do so, we calculate the transient shape of the Joule effect with Eq.3.21, which gives us the associated change in the thermoelastic stress, depicted as the blue curve in Fig.3.7b.

Here, for the same amount of absorbed energy, i.e. $W^{\mathrm{Abs}}_{\mathrm{NIR}} = W^{\mathrm{Abs}}_{\mathrm{THz}}$, we arrive to the same maximum value of σ_{TE} as shown in Fig.3.7a and b. We immediately see that the time evolution of the lattice stress around the time-delay zero is very distinct for the THz and NIR excitation. This is somewhat expected, since the interaction time, defined by the NIR and THz pump pulse duration, differs by close to one order of magnitude. We thus perform a Fast Fourier transform of σ_{TE},

and restrict ourselves to the relevant coherent acoustic phonon frequency range (up to 500 GHz), displayed in Fig.3.7c. Interestingly, we observe that the relevant ratio of the NIR and THz phonon spectral components (see blue line in Fig.3.7b) is close to 1 in the region of interest. This perfectly confirms what we discussed before: for this rather low acoustic frequency, the more rapid lattice heating with a NIR compared to THz pulse is not important as soon as the characteristic rise of the σ_{TE} (either for NIR or THZ excitation) is much shorter that the acoustic phonon period of interest.

As a short summary, the analysis of the pump fluence dependence, the existence of the linear response, the presentation thermoelastic stress based on the TTM model, including the discussion of the spectrum of the photoinduced stress, strongly suggest that the lattice heating, as a result of ultrafast Joule effect, is the driving mechanism of the coherent acoustic phonon generation in thin metallic films with THz.

Acoustic phonon generation mechanism in Bi_2Te_3: Concerning Bi_2Te_3, the linear increase in both thermal background (not shown here) and $\delta T/T|_{acoustic}$ in the function of the THz pulse energy strongly suggests that we can rule out highly-nonlinear light-excitation processes such as Zener tunneling [116] and impact ionization [118] similarly to the observations we made in the previous subsection. Since the Bi_2Te_3 bandgap is in the order of 200 meV [157], we can exclude the multiphoton absorption and excitation process as well ($E_g \approx 50\hbar\Omega_{\mathrm{THz}}$). However, it is worth to note that the recent ARPES measurements of 15 nm Bi_2Te_3 film revealed a non-zero signal at the Fermi level [142] (see Fig.3.8b), and despite our sample was studied in air (passivated surface [142]), our Bi_2Te_3 could be very close to the metallic state. Moreover, we measure the nearly identical long-term residual signal (see Fig.3.5a and the inset) extracted with the same fit parameters for the THz and NIR excitation. This may indicate a similar coherent acoustic phonon generation mechanism for two different pump photon energies, either originating from thermoelastic, deformation potential stress, or a combination of two. Notably, the evolution of the phase of the coherent acoustic phonons excited in Bi_2Te_3 as a function of the sample thicknesses (see Fig.3.5c) might be related to differences in the driving excitation process [158] due to the change in the electronic band structure for the thin samples with, in particular, some confinement effects observed below around 6 nm [118, 144]. Due to the complexity of electron-phonon coupling in this correlated material, these assumptions about coherent acoustic phonon generation in Bi_2Te_3 need to be supported with first-principle calculations.

Outlook: As a final element of discussion, it worth to tell that we can expect some potential differences between NIR and THz excitation in metallic nanostructures through the thermoelastic process at least. As an illustration, Figure 3.8b reveals a dominating thermoelastic contribution driven by Thz excitation within 1-2 THz range. That larger contribution from THz excitation at around 1.5 THz is directly related to the spectrum of the THz pulse. Therefore, one can imagine that THz excitation of high-frequency acoustic modes may reveal the very different nature of heating based either on intraband relaxation (with NIR excitation) or by multiple electron scattering at the Fermi level (with THz excitation). This makes it interesting to study the THz excitation of metallic nanoparticles of various sizes, as one can tune their natural vibrations to THz frequencies [159].

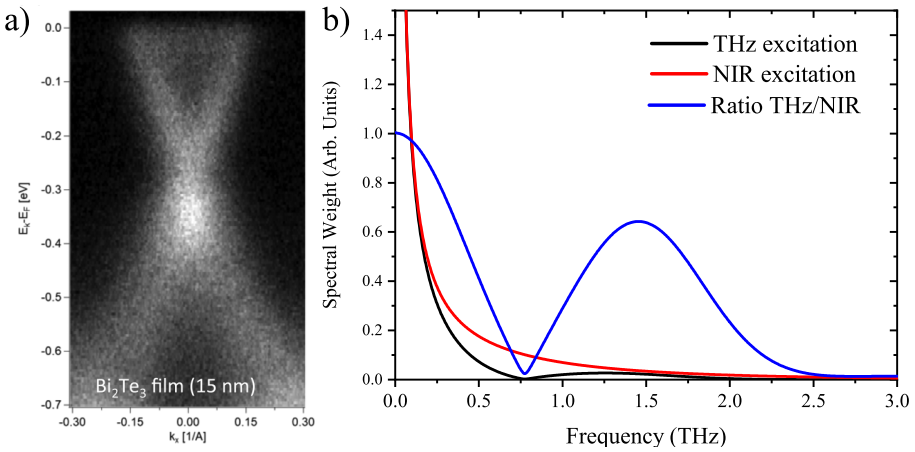

a) ARPES band structure for a thin film ARPES signal of a Bi_2Te_3 film (15 nm) measured at 85 K. The horizontal axis is the momentum along the ΓK direction of the Brillouin zone. From [142]. **b)** Calculated phonon spectrum after NIR excitation (red) and THz excitation (black) in the frequency range up to 3 THz. The ratio between NIR and THz is displayed in blue.

Figure 3.8 – *The ARPES measurement of Bi_2Te_3 film and the extended frequency range of the thermoelastic stress.*

3.2.3 Conclusions

To conclude, we have evidenced the generation of coherent acoustic phonons in metallic and topological insulator thin films with pulsed THz radiation. The coupling efficiency is quadratic in the THz electric field strength (linear with the pulse energy) within the THz-power range of investigation. Remarkably, for both NIR and THz excitations of thin films of metals, the similar amount of light absorbed energy results in the nearly-identical contributions of the coherent acoustic phonons and the incoherent phonons to the experimental signal, as seen from Figure 3.6b. This direct comparison between the NIR and THz pulsed excitation, despite the well-distinguished microscopic lattice "heating" mechanisms, allows us to demonstrate that the thermoelastic process is the main driving mechanism of coherent acoustic phonon generation in metals of Aluminum and Chromium. While for NIR excitation, the ultrafast lattice heating is achieved by intraband hot electron-phonon thermalization, but when the THz pulse drives the system, multiple electron-phonon scattering processes in the vicinity of the Fermi level are responsible for the lattice temperature increase (ultrafast Joule effect). Although the relaxation channels are different, we demonstrate that they do not impact the coherent acoustic phonon generation for the low-frequency interest range (<500 GHz).

Regarding the nanofilms of n-doped Bi_2Te_3 topological insulator, at this moment, we cannot conclude about the physical origin of the light-induced coherent acoustic phonon generation. The linear pump fluence dependence might indicate at least a possible contribution of the thermoelastic (coming from free carriers in this n-doped sample) and/or deformation potential mechanisms. In contrary to metals, the existence of long-lived carriers due to the bandgap (even in the range of ≈ 200 meV) and the rather large deformation potential constant [110, 144] could lead indeed to an important contribution of non-thermal deformation potential stress $\Delta\sigma_{\mathrm{DP}}$ to the total $\Delta\sigma_{\mathrm{PI}}$. In the future, in parallel with the first principle calculations needed to clarify the physics in this complex material, we plan to perform more experiments. For example, studying Bi_2Te_3 film with various doping and different Fermi level positions should help us disentangle possible acoustic phonon

generation mechanisms at play. In addition, ultrafast THz experiments at low-temperature could also be beneficial, as they will reduce the amount of thermally activated carriers in the conduction band of Bi_2Te_3.

In the future, the generation of coherent acoustic phonons by an ultrashort THz pulse could open other fundamental opportunities for controlling the macroscopic pressure and even be used to probe the elasticity or viscoelasticity in the soft matter. Moreover, as the new research direction in our group, the understanding of the coupling between the THz and the large internal polarization in multiferroic materials may be crucial for the efficient control of the ferroic order.

3.3 Coherent optical phonon generation in Bi_2Te_3 with pulsed THz radiation

This section will focus on the discussion about the possible mechanisms of coherent A_{1g}^1 optical phonon generation in 16 nm thick Bi_2Te_3 film with intense THz pulses. First, we will briefly introduce different theoretical models of coherent optical phonon excitation with pulsed light radiation. Then, after the description of optical phonon properties of Bi_2Te_3 measured by Raman scattering in general, we will present the experimental results where we will show the A_{1g}^1 mode generation efficiency dependence on E_{THz} field amplitude and THz pump pulse central frequency, to finally discuss the possible scenarios which may lead to coherent A_{1g}^1 phonon excitation.

3.3.1 Theoretical background

Phenomenologically, the motion of coherent optical phonon can be modeled as the lattice response on the specific driving force, usually shorter than the inverse of the coherent phonon period of interest [160]. For example, one can use the classical equation of motion of the force-driven damped harmonic oscillator to model the displacement of coherent phonons in the lattice [160–162]:

$$\frac{\partial^2 Q_\alpha(t)}{\partial t^2} + 2\gamma_\alpha \frac{\partial Q_\alpha(t)}{\partial t} + \frac{\partial V(Q)}{\partial Q_\alpha} = F_\alpha^Q(t), \tag{3.23}$$

where $V(Q)$ is the total potential energy of the lattice, Q_α is the normal mode coordinate [4], γ_α and Ω_α are the phenomenological damping constant and frequency of the phonon mode α. The driving force $F_\alpha^Q(t)$ can originate either from phonon-EM wave interaction (IR absorption or Raman scattering) or have the displacive nature due to immediate modification of the electronic distribution [108, 163]. For example, NIR-VIS-NUV excitation of opaque materials can lead to a Displacive Excitation of Coherent Phonons (DECP), mediated by the deformation potential stress [164].

The internal force ("harmonic and anharmonic restoring forces") is defined as the gradient of the lattice (phonon) potential energy $V(Q)$. The $V(Q)$ can be expressed as the polynomial expansion

4. With already included correction for the effective mass.

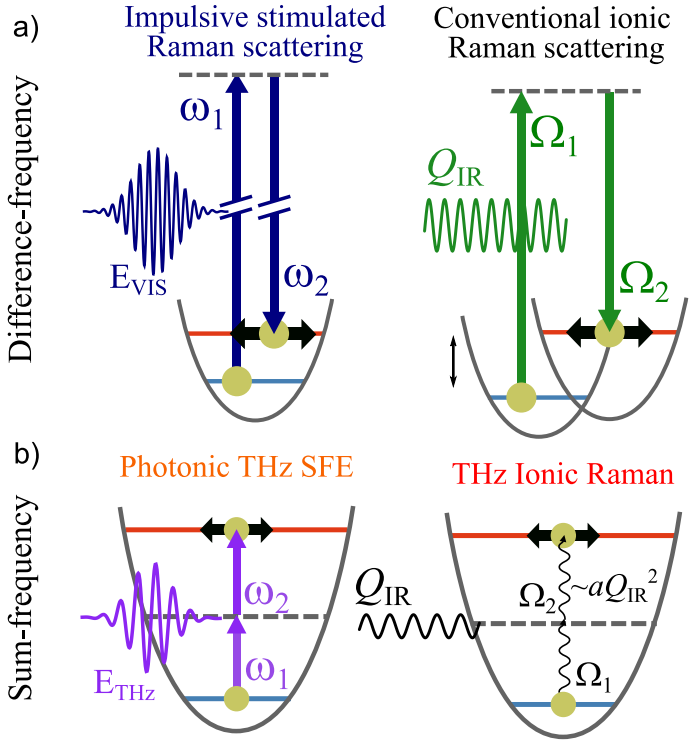

a) The difference-frequency excitation mechanisms of a coherent Raman phonon: Impulsive stimulated Raman scattering, where $\omega_1 - \omega_2$ is resonant with Raman active phonon Ω_R, and conventional ionic Raman scattering, leading to the shift of the Raman phonon potential. **b)** The sum-frequency coherent phonon excitation mechanisms: sum-frequency excitation (THz-SFE) and sum-frequency counterpart of ionic Raman scattering (THz-IRS). Adapted from [127].

Figure 3.9 – *Photonic and ionic mechanisms of Raman phonon excitation.*

of the all phonon modes that exist in a material, as [162, 165]:

$$V(Q) = \sum_{\alpha} \frac{\Omega_\alpha^2}{2} Q_\alpha^2 + \sum_{\alpha,\beta,\gamma} a_{\alpha\beta\gamma} Q_\alpha Q_\beta Q_\gamma + \sum_{\alpha,\beta,\gamma,\delta} b_{\alpha\beta\gamma\delta} Q_\alpha Q_\beta Q_\gamma Q_\delta + \ldots, \tag{3.24}$$

where the first term is the harmonic phonon potential, and other terms describe the higher-order phonon anharmonicities (i.e., the nonlinear phonon-phonon interaction), and $a_{\alpha\beta\gamma}$ and $b_{\alpha\beta\gamma\delta}$ are the corresponding anharmonic coefficients. The subscripts α, β, γ, etc., denote the different lattice eigenmodes. For example, when $\alpha = \beta = \gamma$, $c_{\alpha\alpha\alpha} Q_\alpha^3$ is the anharmonic potential of the phonon mode α. For $\alpha = \beta \neq \gamma$, $c_{\alpha\alpha\gamma} Q_\alpha^2 Q_\gamma$ is the anharmonic coupling between phonon modes α and γ. However, some specific anharmonic interaction terms between IR and Raman phonon modes can be forbidden due to the crystal symmetry [2, 166].

"Conventional" phononics: stimulated IR and Raman active modes The lowest-order allowed electric field-phonon interaction is the absorption of the EM radiation by the IR active

phonon mode. In this case, the IR mode equation of motion in the linear regime will read [166]:

$$\frac{\partial^2 Q_I R(t)}{\partial t^2} + 2\gamma_{IR}\frac{\partial Q_{IR}(t)}{\partial t} + \Omega_{IR}^2 Q_{IR}(t) = Z_{IR}^* E(t), \tag{3.25}$$

where Z_{IR}^* is the effective charge of IR active mode, and $E(t)$ is the incident electric field. A classical example of such coupling is the phonon-polariton interaction, described in the Section 1.3.1.

The lowest-order excitation of the Raman-active phonon, due to its zero effective charge ($Z_R^* = 0$), can be mediated via the two-photon Raman process [161]. In this case, the Raman active phonon driving force is given as the second-order interaction of the electromagnetic field E and the Raman tensor R_{jk} [160]:

$$F_R^Q(t) = R_{jk} E_j E_k, \tag{3.26}$$

where E_j, E_k are the field components of the incident electromagnetic pulse. The latter equation is sometimes expressed in terms of Raman polarizability tensor [161]. The Raman tensor of a given phonon mode is defined as [165, 167]:

$$R_{jk} = V_c \frac{\partial \chi_{jk}}{\partial Q_R}, \tag{3.27}$$

where χ_{jk} is the linear electric susceptibility. In this case, coherent phonon excitation is driven by the impulsive stimulated Raman Scattering (ISRS), which is possible due to the energy and wavevector conservation rules discussed before in Chapter 1. The driven, damped equation of motion for the Raman active phonon will be equivalent to Eq.3.25, but with the following driving force [123]:

$$F(Q_R) \propto \frac{\partial \chi}{\partial Q_R} E^2(t). \tag{3.28}$$

One should note that this force-term, proportional to $E^2(t)$, consists of both sum- and difference-frequency components of the incident electric field $E(t)$. For example, the difference frequency components of sub-picosecond VIS-NIR pulses are linked to the ISRS excitation of coherent phonons in transparent materials (see Fig.3.9a) [106, 163, 168]. In the case of an electric field in the THz frequency range, if the sum-frequency component is resonant with a Raman-active phonon, excitation can occur via photonic THz sum-frequency excitation process [123], depicted in the Figure 3.9b.

Nonlinear phononics: coupled IR and Raman active modes Notably, a population decay of optical phonons is believed to be dominated by lattice anharmonicity and can lead to the generation of lower-energy acoustic and sometimes optical phonon modes [160]. About forty years ago, it was proposed that excitation of an infrared-active phonon could serve as the intermediate state for Raman scattering through a process that relies on lattice anharmonicities rather than second-order electron-phonon interactions [115,126,162]. As an example, let us expand the Eq.3.24 including only one Raman Q_R and one IR Q_{IR} mode, taking into account only the lowest-order

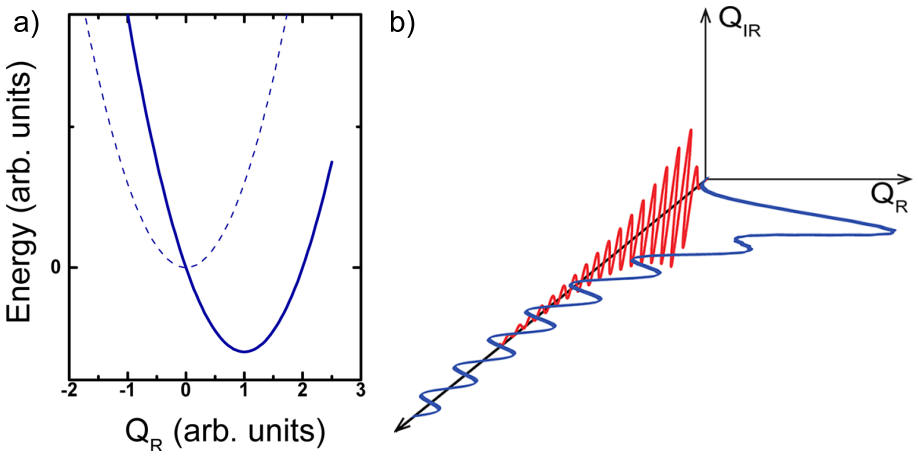

a) Parabolic energy potential of a Q_R phonon mode (dashed curve), displaced under the cubic coupling with Q_{IR} phonon mode (solid curve). From [2]. **b)** Dynamic response of the coupled IR Q_{IR} and Raman Q_R modes. The ion oscillation along Q_{IR} mode (red) leads to a directional displacement of Q_R mode (blue). This displacement is proportional to Q_{IR}^2.

Figure 3.10 – *Anharmonic coupling between IR and Raman modes.*

anharmonic terms [2]:

$$V(Q_R, Q_{IR})_{NL} = \frac{1}{2}\Omega_R^2 Q_R^2 + \frac{1}{2}\Omega_{IR}^2 Q_{IR}^2 + a_{12} Q_{IR} Q_R^2 + a_{21} Q_{IR}^2 Q_R, \tag{3.29}$$

where a_{12} and a_{21} are anharmonic coupling constants. It should be noted, that $a_{12} Q_{IR} Q_R^2$ term is zero in centrosymmetric crystals, like in the sample of study, Bi_2Te_3. With this nonlinear phonon potential, the coupled equations of motion for the centrosymmetric medium [2, 115, 127]:

$$\begin{aligned} \frac{\partial^2 Q_{IR}}{\partial t^2} + 2\gamma_{IR}\frac{\partial Q_{IR}}{\partial t} + \Omega_{IR}^2 Q_{IR} &= 2a_{21} Q_{IR} Q_R + Z_{IR}^* E_{\mathrm{THz}}, \\ \frac{\partial^2 Q_R}{\partial t^2} + 2\gamma_R \frac{\partial Q_R}{\partial t} + \Omega_R^2 Q_R &= a_{21} Q_{IR}^2, \end{aligned} \tag{3.30}$$

where the time dependence of Q_R, Q_{IR} and E_{THz} was omitted for the clarity of the notation.

As a result, strong nonlinear coupling between IR and Raman modes may "shift" or displace the energy potential of a Raman mode Q_R, as shown in Figure 3.10a. This will result in simultaneous lattice oscillations along the infrared coordinate Q_{IR} (red curve in Fig.3.10b), extorting a displacive force on the Raman active phonon coordinate Q_R (blue curve in Fig.3.10b). As a result, the force-term driving the Q_R coherent phonon is proportional to [127, 166]:

$$F(Q_R) \propto a_{21} Q_{IR}^2 \propto E^2. \tag{3.31}$$

Importantly, for both Raman excitation [123] and anharmonic IR-Raman coupling [124, 127] (see Figure 3.9b), the effective driving force should be proportional to the square of the incident EM field (E^2). Note also that according to Eq. 3.29, due to large coupling with a Raman active mode R, the IR mode frequency is re-normalized to $\Omega_{IR}^2 - 2a_{21} Q_R$.

Interestingly, since the majority of coherent optical modes exist within the 1-40 THz frequency range, pulsed, broadband THz radiation can resonantly or non-resonantly couple to the optical vibrational modes. For example, there have been several observations of THz-driven anharmonic coupling between optical phonons in manganite $PrMnO_3$ (PMO) [169] [5], $LaSrMnO_3$ [166] and Bismuth Selenide (Bi_2Se_3) [124,125]. In addition, there are experimental [123] and theoretical [127] reports of the impulsive Raman THz sum-frequency excitation of coherent phonons in the diamond. Before proceeding to the experimental section discussing the optical phonon generation with pulsed THz radiation, let us recall the phonon properties of the Bi_2Te_3.

Bi_2Te_3 coherent optical phonon properties

Bi_2Te_3 is a trigonal rhombohedral crystal with five atoms in a primitive unit cell, and it belongs to the $D^5_{3d}(R\bar{3}m)$ space group. The Bi_2Te_3 crystallographic structure is usually described within the hexagonal unit cell along the [111] direction, consisting of 3 quintuple layers (QL) of Te^1-Bi-Te^2-Bi-Te^1 atoms [6]. The Bi_2Te_3 quintuple layers are linked with Van der Waals bonds. According to the group theory, Bi_2Te_3 can support 15 normal phonon modes at the zone center Γ [153, 170]:

$$\Gamma = 2A_{1g} \oplus 2E_g \oplus 3A_u \oplus 3E_u, \tag{3.32}$$

where two E_u and one A_u are acoustic transverse and longitudinal modes, respectively. This leaves a total of 12 optical modes, shown in Fig.3.11a. Since Bi_2Te_3 is a centrosymmetric crystal, two A_{1g} and two doubly-degenerate E_g optical modes are Raman active [171], when two A_{1u} and two doubly-degenerate E_u are the IR active modes [172]. The Raman tensors of A_{1g} and E_g modes are defined as [153]:

$$\begin{aligned} A_{1g} &= \begin{bmatrix} a & & \\ & a & \\ & & b \end{bmatrix}, \\ E_g &= \begin{bmatrix} & -c & -d \\ -c & & \\ -d & & \end{bmatrix}, \text{ and } \begin{bmatrix} c & & \\ & -c & d \\ & d & \end{bmatrix}. \end{aligned} \tag{3.33}$$

The Table 3.1 gives the frequency of the optical Bi_2Te_3 modes in THz, measured with Raman, IR, and femtosecond spectroscopy, in pair with molecular dynamics (MD) simulations. As one can notice, all the optical modes are within 1 to 4 THz frequency range.

The coherent optical phonon detection, in analogy to the expression established in the Chapter 2, can be explained as the transmittance δT (or reflectance δR) modulation by the first-order Raman tensor $(\partial\chi)/(\partial Q)$ [161]:

$$\delta T = \frac{\partial T}{\partial n}\Delta n \approx \frac{\partial T}{\partial \chi}\frac{\partial \chi}{\partial Q}Q. \tag{3.34}$$

5. With the theory provided by A.Subedi et.al. [162].
6. Superscripts denote different positions of the Te atoms.

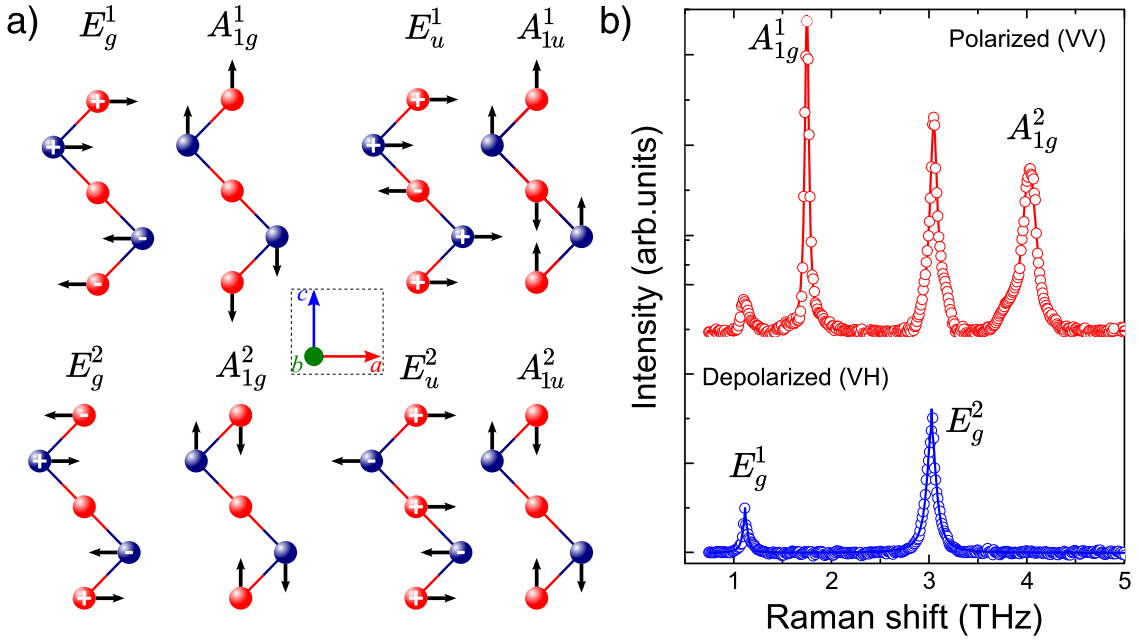

a) Optical phonon modes in Bi_2Te_3. The red and blue circles denote Te and Bi atoms, respectively. After [172]. **b)** Raman spectra of Bi_2Te_3 in backscattering geometry in parallel (VV) and crossed (VH) polarization of incident and scattered electric field, respectively. After [153].

Figure 3.11 – *Sketch and Raman spectra of the optical phonon modes in the Bi_2Te_3.*

	Raman spectroscopy		Femtosecond spectroscopy	MD simulation
Mode	Raman	IR		
A_{1g}^1	1.88		1.82	1.84
A_{1g}^2	4.02		3.91	3.74
A_{1u}^1		2.82		2.88
A_{1u}^2		3.60		3.58
E_g^1	1.1			1.47
E_g^2	3.09			3.42
E_u^1		1.50		1.43
E_u^2		2.85		2.90

Subscripts u and g correspond to the Raman (in-plane) and IR (out-of-plane) lattice vibration modes, respectively. After [170–172].

Table 3.1 – *Bi_2Te_3 optical phonon frequencies in THz.*

Figure 3.11b displays the Raman spectra of Bi_2Te_3 crystal, showing that one can probe specific modes selectively via polarization analysis of the probe pulse [160]. For example, modes containing only diagonal terms (A_{1g}) will only cause intensity modulation of the transmitted or scattered light and therefore they are absent in depolarized spectrum in Figure 3.11b. However, modes containing off-diagonal tensor terms (E_g) will only affect the polarization state of the scattered or transmitted light, which, ideally, can be probed only by the polarization sensitive anisotropic detection.

3.3.2 Results and discussion

Experimental results

Before discussing the experimental results on coherent optical phonon generation with THz pulses in 16 nm thick Bi_2Te_3 film, let us first define the time delay zero of the experiment. For

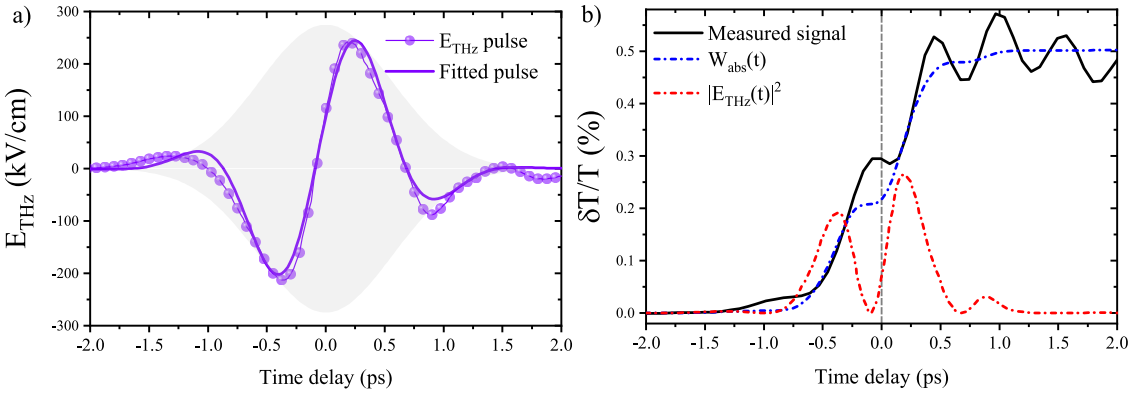

a) Electrooptic trace of the THz pulse, and its fit by Eq.3.35. **b)** Experimental signal in THz pump-400 nm probe of the Bi_2Te_3 16 nm thin film at $\tau < 2$ ps time scale (black curve). The signal is overlapped with squared THz electric field (dash dot red) and the THz absorbed energy (dash dot blue).

Figure 3.12 – *Bi_2Te_3 THz pump/400 nm probe: Time-delay zero definition.*

this, we first fit the electrooptic trace of E_{THz} of the $LiNbO_3$ source [7] with the following equation:

$$E_{\mathrm{THz}}(\tau) = E_0 \exp\left[-\frac{4\ln 2\tau^2}{\sigma^2_{\mathrm{FWHM}}}\right] \sin[\Omega_0\tau + \phi_0], \tag{3.35}$$

where E_0 is the value of the peak electric field, σ_{FWHM} is the pulse width at FWHM, Ω_0 is the angular THz central frequency, and ϕ_0 is the carrier-envelope phase (CEP). Figure 3.12a shows the THz pulse waveform $E_{\mathrm{THz}}(\tau)$ (line-dot) and its fit (solid line) with the following parameters: $\sigma_{\mathrm{FWHM}} = 1.317$ ps, $E_0 \approx 275\,\mathrm{kV\,cm^{-1}}$, $\Omega_0/2\pi = 0.64$ THz and $\phi_0 = 0.12\pi$. Next, with the Eq.3.19 we can calculate the approximate shape of $W_{\mathrm{abs}}(\tau)$:

$$W_{\mathrm{abs}}(\tau) \propto \int_{-\infty}^{\tau} E^2_{\mathrm{THz}}(t')dt'. \tag{3.36}$$

Both $E^2_{\mathrm{THz}}(\tau)$ and calculated $W_{\mathrm{abs}}(\tau)$ are shown in the Fig.3.12b (blue and red dash-dot lines, respectively). In this case, Bi_2Te_3 conductivity in the THz range, electron-electron, and electron-phonon scattering rates, that all may affect the shape of $W_{\mathrm{abs}}(\tau)$ were not taken into account. In particular, such calculation of W_{abs} assumes an immediate dissipation of the electromagnetic energy. Finally, we manually superpose the measured signal $\delta T/T$ with calculated $W_{\mathrm{abs}}(\tau)$ profile as shown in the Fig.3.12b, which gives us the time-delay zero position of the experiment.

In the following, we will focus only on the optical phonon part of the signal, extracted by fitting the acoustic mode, electronic and thermal background with the following function:

$$\begin{aligned}\delta T/T|_{\mathrm{bg}} =& A \cdot \left(1 + \mathrm{erf}\left[\frac{\tau}{s}\right]\right) \cdot \left\{a_1 \exp\left[-\frac{\tau}{\tau_1}\right] + a_2 \exp\left[-\frac{\tau}{\tau_2}\right] + \right. \\ &\left. + a_{ac}\cos[\Omega_{ac}(\tau) + \phi_{ac}] \exp\left[-\frac{\tau}{\tau_{ac}}\right]\right\},\end{aligned} \tag{3.37}$$

7. Deconvoluted from the detection crystal response.

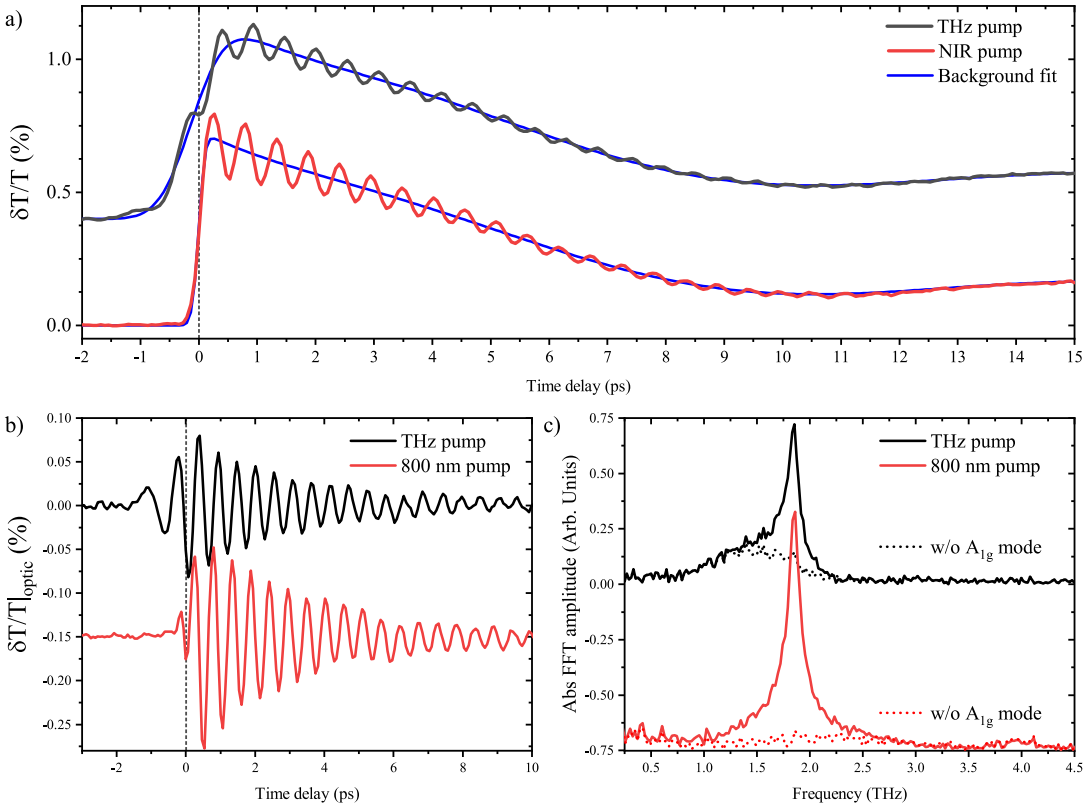

a) Measured change in transmittance of Bi_2Te_3 16 nm thick film for THz (black) and NIR (red) excitation. The blue lines are the background fit, defined by Eq.3.37. **b)** Extracted transient optical phonon part of the signal for the THz (black) and NIR (red) excitation. **c)** Fourier transform of the transients shown in b). Black dotted line corresponds to the spectrum with subtracted 1.85 THz oscillatory component. Compared to the NIR, THz excitation has a noticeable sideband, around 1.5 THz in the frequency domain. Plots are offset for clarity.

Figure 3.13 – *Bi_2Te_3, NIR versus THz excitation: extraction of the optical phonon part of the signal.*

where τ_1, τ_2 and τ_{ac} are the characteristic decay times, with their respective amplitudes a_1 ,a_2 and a_{ac}, and s is linked to the rising-time of the signal [8]. Ω_{ac} and ϕ_{ac} are the angular frequency and the phase of breathing acoustic phonon mode. The background fits for NIR and THz excitation are shown as the blue solid line in Figure 3.13a. In the following, we define $\delta T/T|_{\text{optic}}$ as the difference between "raw" measured signal and the background fit, as:

$$\delta T/T|_{\text{optic}} = \delta T/T - \delta T/T|_{\text{bg}}. \tag{3.38}$$

The Figure 3.13b displays $\delta T/T|_{\text{optic}}$ of the sample, excited with THz (black) and 800 nm (red) pulses. Interestingly, for both THz and NIR (800 nm) photoexcitation we see the signal modulation with approximately 540 fs period (1.85 THz frequency), attributed to the Raman active optical phonon mode A^1_{1g} (see Table 3.1). The observation of the A^1_{1g} mode with NIR pump is also consistent with previous measurements in the group [110].

8. Defined as convolution of the pump and the probe pulses.

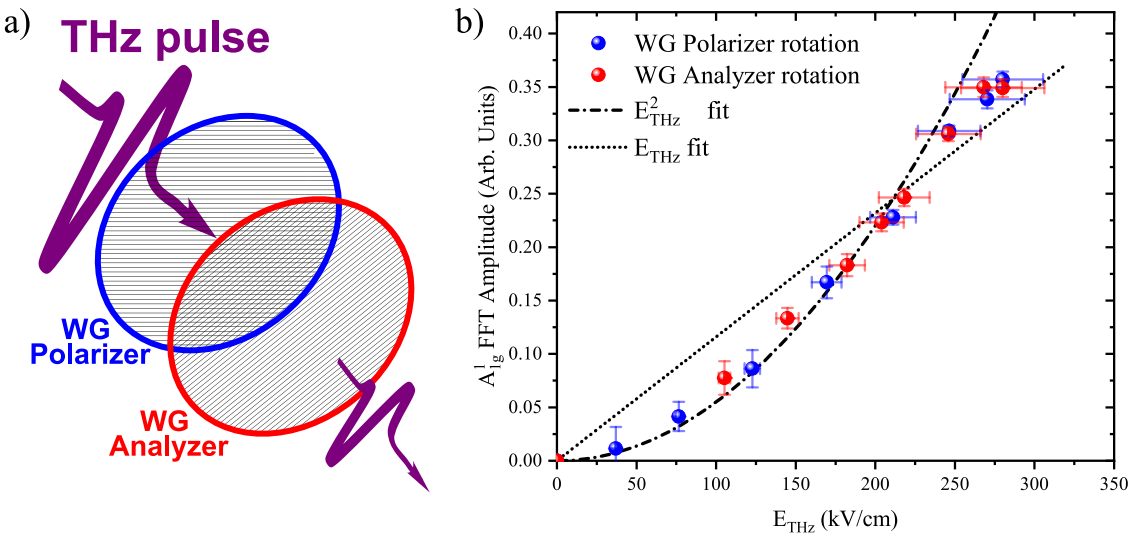

a) Experimental configuration: Two Wire Grid (WG) polarizers were introduced in the THz beam path. The rotation of the WG analyzer changed THz field amplitude or/and polarization. **b)** Amplitude of the optical phonon part of the signal plotted as a function of the E_{THz} field amplitude for static WG analyzer with rotating WG polarizer (blue dots) and fixed WG polarizer, with rotating WG analyzer (red dots). Black dot and dash-dot lines are the respective linear and square with E^2_{THz} fits.

Figure 3.14 – *Bi_2Te_3 A^1_{1g} generation efficiency - E_{THz} field amplitude dependence.*

Moreover, the FFT spectrum of the signal recorded with the NIR pump (red curve in Figure 3.13c) displays a shallow signature of the A^2_{1g} mode around 4.1 THz, which was already observed before [153, 172]. In our case, such low detected A^2_{1g} amplitude may be related to pump and probe pulse duration of about 160 fs at FWHM, insufficient to properly sample A^2_{1g} mode with a period of 240 fs [173]. In addition, since coherent phonon generation in Bi_2Te_3 with pulsed NIR radiation using both isotropic and anisotropic detection techniques was already presented elsewhere [153, 172], we will focus on the results of optical phonon generation with THz pulses only.

It is worth to underline that we can excite the 1.85 THz coherent motion with a THz pulse having a central frequency of 0.64 THz indicating the non-linear nature of the phonon generation process. In addition, another noticeable feature arising from THz photoexcitation is 1.4 THz "sideband" (see black line in Fig.3.13b). Such THz-pump characteristic "sideband" was also observed at the short time-delays by Melnikov et al. in Bi_2Se_3 [124], and by Huber et. al. in Te [122]. To investigate the physical mechanism of A^1_{1g} phonon generation and the origin of this "sideband", we studied the influence of the THz-field amplitude and THz-central frequency on the overall shape of $\delta T/T|_{\mathrm{optic}}$ and amplitude of A^1_{1g} phonon.

First, we have measured the E_{THz} field amplitude - A^1_{1g} phonon amplitude dependence. Figure 3.14a shows the experimental configuration, where the THz pulse emitted from $LiNbO_3$ crystal propagates through a set of Wire-Grid (WG) polarizers. Two WG polarizers allow us to selectively change only E_{THz} amplitude (fixed WG analyzer, rotating WG polarizer), or E_{THz} amplitude and polarization (fixed WG polarizer, rotating WG analyzer).

Figure 3.14b shows the Bi_2Te_3 A^1_{1g} optical phonon generation efficiency as the function of E_{THz} field strength when we change only E_{THz} field amplitude (blue circles) or E_{THz} field amplitude and

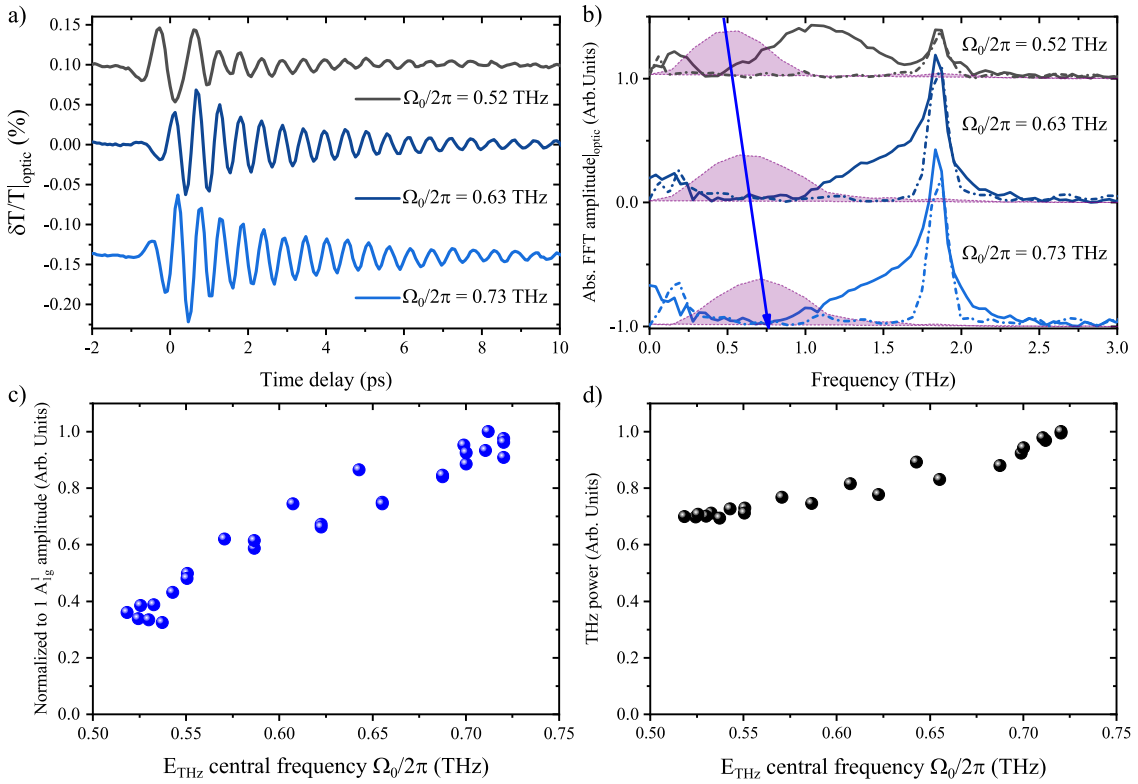

a) Optical phonon part of the signal recorded for the THz pump with indicated THz central frequency $\Omega_0/2\pi$, and **b)** it is Fourier transform. Dashed-dot line is the FFT for time-delays > 1 ps. The purple-filled area is the respective spectrum of the THz pump pulse. Data are offset for clarity. **c)** Normalized to 1 amplitude of the A^1_{1g} mode as the function of the THz central frequency $\Omega_0/2\pi$. **d)** Normalized to 1 THz power measured with the calibrated pyroelectric detector.

Figure 3.15 – *Bi_2Te_3: Influence of the THz pump spectrum on the optical phonon part of the signal.*

polarization (red circles). The error bars are set to $\pm 10\,\%$ of the estimated value of peak E_{THz} [9]. As seen from Figure 3.14b, two measurements overlap perfectly, meaning that A^1_{1g} amplitude does not depend on the THz pump polarization. This finding is in good agreement with previous reports [153]. In addition, A^1_{1g} amplitude scales with the square of the THz field ($\delta T/T|_{\mathrm{optic}} \propto E^2_{\mathrm{THz}}$), underlining the nonlinear mechanism of this Raman active excitation.

Next, we recorded the $\delta T/T|_{\mathrm{optic}}$ for slightly different E_{THz} pump spectrum. In order to tune the THz central frequency $\Omega_0/2\pi$ from ≈ 0.52 and up to ≈ 0.73 THz, we have used the x-cut Quartz plate, as discussed in the Section 2.5. Figure 3.15a shows measured signals for $\Omega_0/2\pi = 0.52, 0.63$ and 0.73 THz. We see that both amplitude of A^1_{1g} phonon and signal around $\tau = 0$ is strongly affected by the E_{THz} change in $\Omega_0/2\pi$.

The Fig. 3.15b displays the FFT $\delta T/T|_{\mathrm{optic}}$ signals discussed above. We observe that both A^1_{1g} amplitude and characteristic to THz excitation "sideband" are strongly correlated to the incident E_{THz} spectrum (violet dashed line in Figure 3.15b). This sideband seems to be related to the sum-frequency component of E_{THz} and completely disappears when the FFT is performed on the signal for > 1 ps time delays (see dash-dot lines in Fig. 3.15b) [122]. Indeed, as presented in Appendix B, we find the correlation between the "sideband" and E_{THz} SF component for all signals recorded

9. Related to the discrepancy in the values measured with calibrated pyrodetector and THz-TDS.

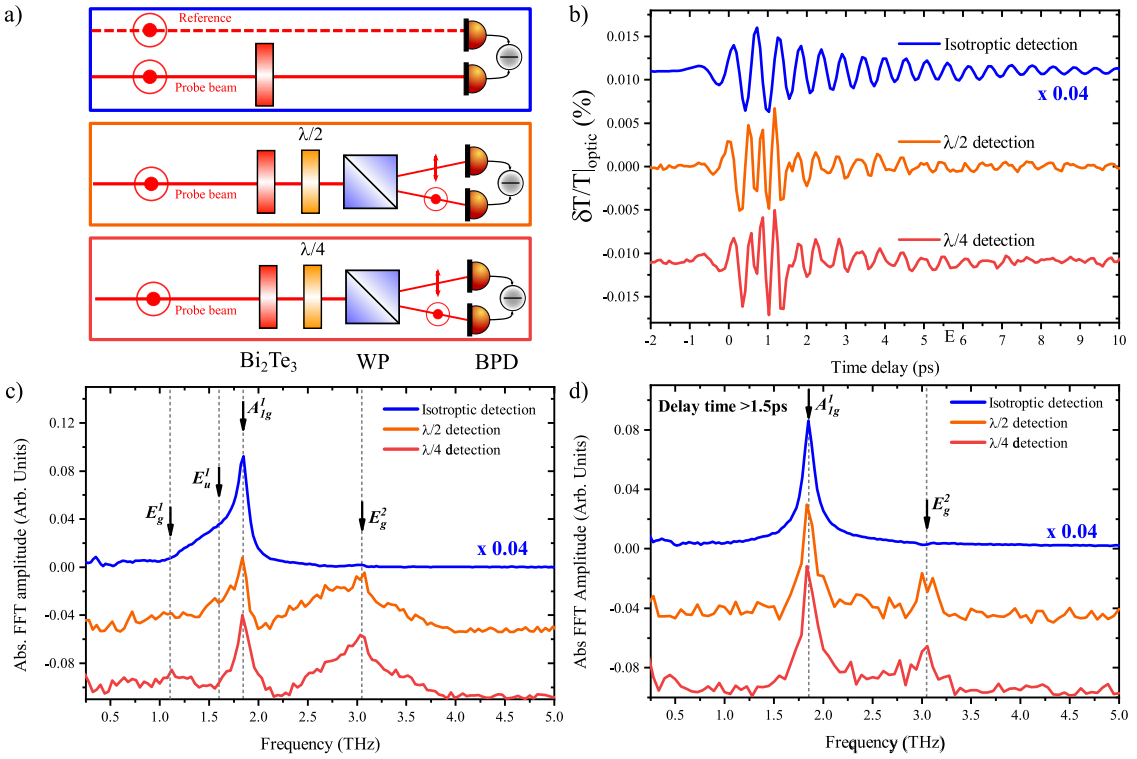

a) Three different detection schemes: isotropic (blue box), anisotropic rotation (orange) and elipticity (red) sensitive detection. **b)** Transient optical phonon response of the Bi_2Te_3 16 nm thick film pumped with $\Omega_0/2\pi \approx 0.64$ THz pulse, recorded in the isotropic (blue), anisotropic rotation (orange) and elipticity (red) detection configurations and **c)** their respective spectra. The arrows indicate the frequencies of the different coherent optical phonon modes, with values extracted from [174] and Table 3.1 **d)** The FFT transform of the phonon signal part for the >1.5 ps time delays.

Figure 3.16 – *Bi_2Te_3 response measured in polarization sensitive detection configurations.*

in the experimental THz central frequency range, and even for the Chromium thin film, having no optical phonons.

Figure 3.15c displays normalized to maximum A^1_{1g} amplitude as the function of THz central frequency $\Omega_0/2\pi$. We see approximately three times increase in the A^1_{1g} generation efficiency between central frequency of $\Omega_0/2\pi$=0.52 THz and $\Omega_0/2\pi$=0.73 THz. Remarkably, the measured change of the THz power, associated with the change of THz central frequency $\Omega_0/2\pi$ increases only the factor of roughly 1.4, as shown in Figure 3.15d.

In addition to the study of the $\delta T/T|_{\text{optic}}$ signal as a function of the THz field amplitude and its spectrum, we attempted to measure the signatures of other phonon modes. For this purpose, with the pristine THz pump pulse waveform ($\Omega_0/2\pi$ fixed to ≈ 0.64 THz), we have measured the Bi_2Te_3 sample response employing two anisotropic detection schemes (using $\lambda/2$ and $\lambda/4$ wave plates, as shown in Fig.3.16a). One should note that we kept the polarization of the probe beam and THz pulse crossed. Ideally, anisotropic detection should be sensitive to only non-fully symmetric optical modes (E_g, in the case of Bi_2Te_3) [153, 160].

Figure 3.16b depicts isotropic signal (blue line), in comparison to anisotropic change of $\delta T/T|_{\text{optic}}$ (orange and red lines). Interestingly, within the 0 to 1.5 ps time delay, we observe high-frequency

modulation of $\delta T/T|_{\text{optic}}$ for both anisotropic signals. Next, Figure 3.16c shows the FFT of the isotropic and anisotropic signals presented above. Anisotropic detection reveals the pressence of $\approx$3.1 THz E_g^2 phonon mode (see Table 3.1). Notably, close to the natural frequency of the E_g^2 mode, we see again this asymmetric "sideband", which corresponds to $\delta T/T|_{\text{optic}}$ modulation at $\approx 4\Omega_0/2\pi$, indicating the possible of higher-than-two order ion-electric field interaction (i.e., a fourth harmonic of the E_{THz} component, see Eq.3.28).

Figure 3.16d shows the FFT of the same signals, but for the time delays >1.5 ps. We see that neither E_g^1 nor E_u^1 phonons were detected. This absence of E_g^1 mode in the anisotropic spectrum could be attributed to a non-optimal angle between the THz pump/probe polarization with respect to Bi_2Te_3 azimuth angle, as was observed for the NIR excitation of Bi_2Te_3 [153] and a similar system, Bi_2Se_3 [124]. In principle, the signatures of the E_u modes can be revealed with THz-TDS. However, since the sensitivity of the THz-TDS depends on the sample absorption and the volume of interaction, THz transmission of the 16 nm thick Bi_2Te_3 film, compared to 490 nm thick one [175] gives no signature of IR absorption (not shown here). Finally, the study of the E_g and E_u modes are to be continued in the future. In the following, we concentrate on the discussion of the generation mechanisms of the largest detected optical phonon mode in Bi_2Te_3, i.e., A_{1g}^1.

Discussion

In the section above, employing isotropic detection scheme, we detected the A_{1g}^1 coherent Raman phonon in 16 nm thick Bi_2Te_3, excited by THz pulses with central frequency $\Omega_0/2\pi$ from $\approx$ 0.53 THz and up to $\approx$ 0.73 THz. For the fixed $\Omega_0/2\pi \approx 0.64$ THz we have shown that the amplitude of the A_{1g}^1 phonon seems to scale with E_{THz}^2, and is not affected by the polarization of the THz pulse (according to Fig.3.14b). Next, Figure 3.15c shows that the amplitude of A_{1g}^1 phonon is sensitive to the change of the THz pump central frequency and can be increased by a factor of 3, which is not fully explained by the increase in THz power (see Fig.3.15b). The latter observation underlines the crucial role of the THz spectrum on the non-linear process efficiency. Moreover, preliminary anisotropic detection experiments revealed the presence of E_g^2 phonon, detectable at >1.5 ps time delays. Both E_u^1 and E_g^1 phonons were not observed, most likely due to non-optimal experimental conditions. Note, since the strongest A_{1g}^1 mode is Raman active, the resonant excitation ($Q_{A_{1g}^1} \propto E_{\text{THz}}$) is forbidden by the means of symmetry.

We first briefly compare our work to previously published results on coherent phonon excitation with THz. First, T. Huber et al. reported the resonant THz excitation of non-symmetric TO phonons in Tellurium (Te) [122]. Then, A. Melnikov et al. proposed THz-ionic Raman scattering mechanism of E_g^2 phonon excitation in Bi_2Se_3 (THz-IRS, depicted in the Fig.3.17a) [124, 125]. In addition, the nonlinear phononics chapter in the L. Braun's Ph.D. thesis discusses E_g^2 coherent phonon generation in Bi_2Te_3 and Sb_2Te_3 [176], suggesting the displacive THz-IRS mechanism of E_g^2 phonon generation. Next, S. Maerhrlein et al. reported the generation of F_{2g} 40 THz Raman active phonon in Diamond via an impulsive THz-sum frequency excitation (THz-SFE) mechanism (see Fig.3.17a) [123]. They observe the maximum of F_{2g} phonon amplitude for THz pulse central frequency equal to the half of natural frequency of F_{2g} mode (i.e. for $\Omega_0/2\pi = 2 \times \Omega_{F_{2g}}$). As a result, in the absorbing, semi-metallic Bi_2Te_3, the A_{1g}^1 phonon generation may be governed by the THz-SFE and/or THz-IRS processes.

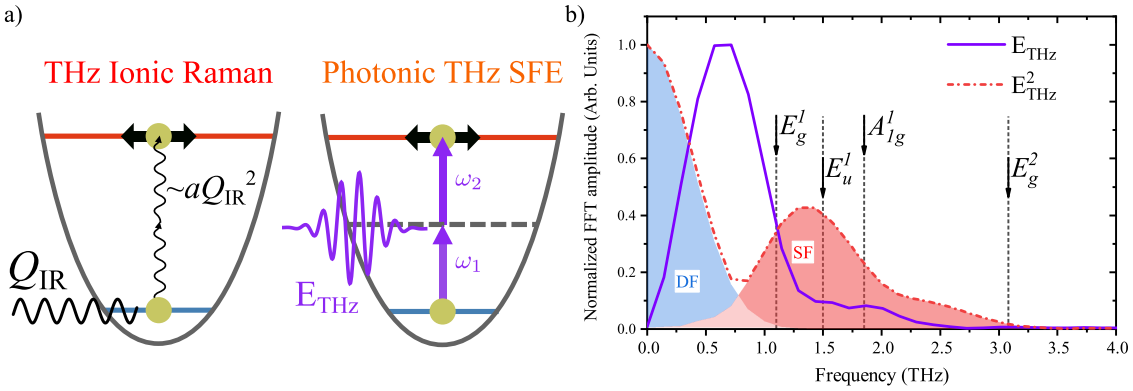

a) Two proposed scenarios of the A_{1g}^1 mode excitation: THz ionic Raman scattering (THz-IRS) and THz sum-frequency excitation (THz-SFE). Figure adapted from [127]. **b)** Spectrum of the E_{THz} (violet) and E_{THz}^2 (dash dot red), showing difference-frequency (DF) and sum-frequency(SF) components. Arrows indicate optical phonon modes in Bi_2Te_3.

Figure 3.17 – *Two proposed pathways of A_{1g}^1 phonon excitation in Bi_2Te_3.*

Let us now discuss in more detail the experimental THz spectrum. The violet line in Figure 3.17b shows the FFT of the pristine E_{THz} (for $\Omega_0/2\pi = 0.64\,\mathrm{THz}$). We can note that the high-frequency shoulder of the THz pulse overlaps with the IR-active E_u^1 mode, allowing for the resonant excitation of the latter. As established in the Theory section of this Chapter, the driving force of E_u^1 phonon was defined as $F(Q_{E_u^1}) = Z^*_{E_u^1} E_{\mathrm{THz}}$. Assuming high-amplitude $Q_{E_u^1}$ displacement in the presence of E_{THz}, it may result in A_{1g}^1 phonon excitation through anharmonic IR-Raman interaction, where the force-term is $F(Q_{A_{1g}^1}) \propto aQ_{E_u^1} \propto E_{\mathrm{THz}}^2$(see Eq.3.31 and Fig.3.17a).

Next, let us examine the frequency components of the square of the THz electric field. In the Fourier domain, $E_{\mathrm{THz}}^2(\Omega)$ will be given as:

$$\mathcal{F}\left[E_{\mathrm{THz}}^2(\tau)\right] = \underbrace{\int_0^\infty \int_0^\infty d\Omega_1 d\Omega_2 \widetilde{E}(\Omega_1)\widetilde{E}(-\Omega_2)}_{\mathcal{F}\left[E_{\mathrm{THz}}^2(\Omega)\right]_{\mathrm{DF}}} + \underbrace{\int_0^\infty \int_0^\infty d\Omega_1 d\Omega_2 \widetilde{E}(\Omega_1)\widetilde{E}(\Omega_2)}_{\mathcal{F}\left[E_{\mathrm{THz}}^2(\Omega)\right]_{\mathrm{SF}}}, \tag{3.39}$$

where the first and the second terms are the difference-(DF) and sum-frequency (SF) contributions, respectively, that are shown in blue and red in Figure 3.12b. In our case, only the SF components of E_{THz} have non-negligible spectral amplitude in the range of A_{1g}^1 mode. Therefore, one can imagine A_{1g}^1 phonon excitation through the photonic THz-SFE, in analogy to the similar effect observed in the diamond [123]. Importantly, in the case of both THz-SFE and THz-IRS, coherent phonon amplitude is expected to increase quadratically with applied E_{THz} field amplitude, making the distinction between these processes not straightforward. At this stage, we can only compare the phase of the experimentally measured A_{1g}^1 phonon to the one expected from THz-SFE and THz-IRS mechanisms, as explained below.

For example, the displacive THz-IRS and impulsive THz-SFE of A_{1g}^1 phonon generation should result in different phase of excited coherent phonon motion. To compare the expected A_1^{1g} phonon

phase as a result of THz-IRS and THz-SFE mechanisms, we phenomenologically solve the two sets of the differential equations describing the two distinct pathways of A^1_{1g} excitation. However, since we do not have any information about the values of frequency-dependent Raman tensor $R(\Omega)$, the life-time of IR E^1_u mode, its effective charge $Z^*_{E^1_u}$, and strength of the anharmonic interaction between E^1_u and A^1_{1g} mode, the further discussion is based on simple numerical modeling. These crucial parameters and the likelihood of THz-SFE and THz-IRS processes are yet to be confirmed by the first-principle calculations.

Despite the absence of the theoretical parameters, we still able to numerically solve the set of differential equations for $Q_{A^1_{1g}}$ displacement. For the THz-IRS, based on Eq.3.29 we write:

$$\begin{aligned} \ddot{Q}_{E^1_u} + 2\gamma_{E^1_u}\dot{Q}_{E^1_u} + \Omega^2_{E^1_u} Q_{E^1_u} &= 2aQ_{E^1_u}Q_{A^1_{1g}} + Z^*_{E^1_u} E_{\mathrm{THz}}, \\ \ddot{Q}_{A^1_{1g}} + 2\gamma_{A^1_{1g}}\dot{Q}_{A^1_{1g}} + \Omega^2_{A^1_{1g}} Q_{A^1_{1g}} &= aQ^2_{E^1_u}, \end{aligned} \tag{3.40}$$

where a is the anharmonic coupling coefficient, $\gamma_{E^1_u}$, and $\gamma_{A^1_{1g}}$ are the IR and Raman damping constants, and $Z^*_{E^1_u}$ is the effective charge of the E^1_u mode. For E_{THz}, we used the experimental THz pulse shown in Fig.3.12a. The $\gamma_{A^1_{1g}}$ was set to $0.285\,\mathrm{ps}^{-1}$, and it corresponds to A^1_{1g} phonon damping time of 3.5 ps, extracted from fitting the experimental data. We set $Z^*_{E^1_u} = -1$, $a = -1$, [10] and $\gamma_{E^1_u} = 1\,\mathrm{ps}^{-1}$. The frequency of the E^1_u mode ($\Omega_{E^1_u} = 1.5\,\mathrm{THz}$) was taken from Table 3.1. The solution for $Q_{A^1_{1g}}$, normalized to match the experimental data, and the driving force $\propto aQ^2_{E^1_u}$ are shown in the Figure 3.18a (as red line and pink filled area, respectively).

In the case of THz-SFE, one can write the following equation of motion [127, 177]:

$$\ddot{Q}_{A^1_{1g}} + 2\gamma_{A^1_{1g}}\dot{Q}_{A^1_{1g}} + \Omega^2_{A^1_{1g}} Q_{A^1_{1g}} = RE^2_{\mathrm{THz}}. \tag{3.41}$$

Here, we disregard the frequency dependence of the Raman tensor and set it to unity ($R = 1$). We use the same shape of E_{THz} as in the THz-IRS model. Solution for $Q_{A^1_{1g}}$ along with its driving force $\propto E^2_{\mathrm{THz}}$ are shown in the Figure 3.18a (as orange line and filled red area, respectively).

Now, let us compare the experimental data and $Q_{A^1_{1g}}$ displacement calculated with two models proposed above. Figure 3.18a compares the around time-delay zero experimental signal and solutions of the two models. Especially for the negative time delays, we see the big difference between the $\delta T/T|_{\mathrm{optic}}$ (black line) and calculated $Q_{A^1_{1g}}$ displacement for both THz-IRS (red line) and THz-SFE (orange line). We believe this is because we model only part of the signal $\propto \frac{\chi}{Q_{A^1_{1g}}} Q_{A^1_{1g}}$. In addition, "parasitic" E_{THz} and E^2_{THz} contributions may be present in the "raw" $\delta T/T$ experimental signal [123, 178], that are not included in our simple model.

From Figure 3.18c, we see that the THz-SFE model (orange line) describes better the phase of the experimental signal (black line). However, it should be noted that both $\gamma_{E^1_u}$ damping constant and an anharmonic coefficient a used in the THz-IRS model heavily alter the phase of $Q_{A^1_{1g}}$ displacement, making this comparison inconclusive. As a result, there is always an open question about the time delay zero definition (see Fig.3.12b), making the direct experiment-simulation phonon phase comparison quite a delicate task.

10. The minus was chosen to better match the phase of experimentally measured A^1_{1g} phonon.

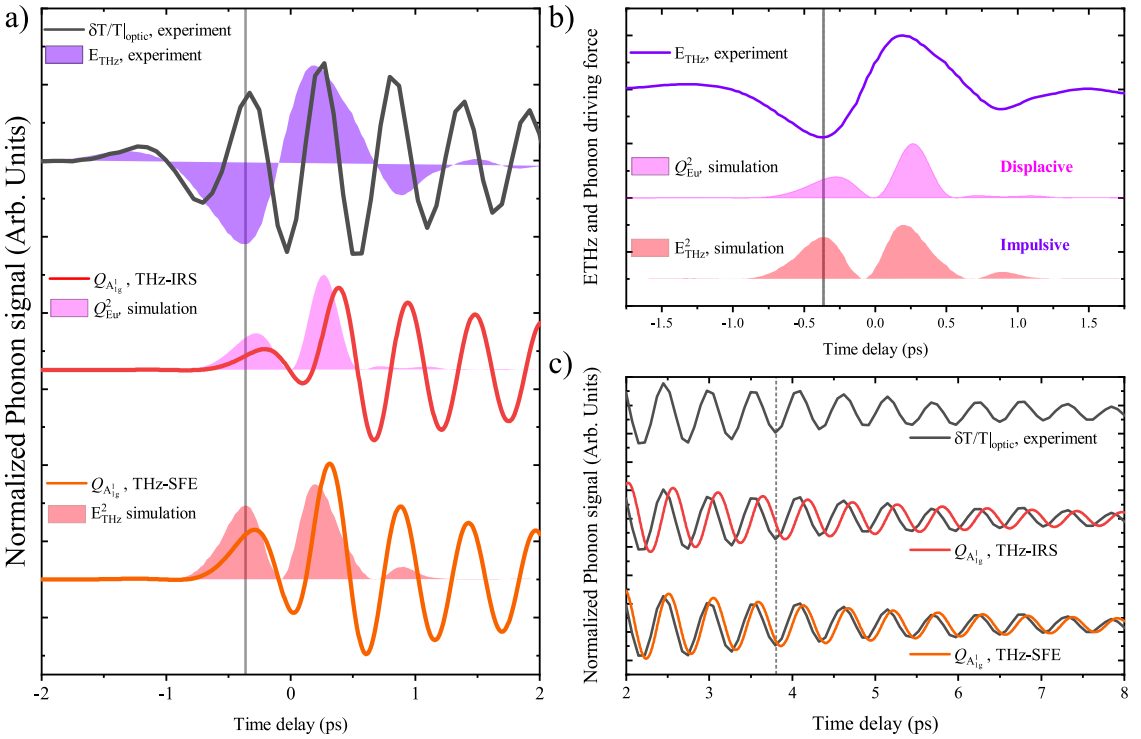

a) Comparison between the experimentally measured signal (black) curve, THz-IRS (red curve) and THz-SFE (orange) models, with their respective driving forces shown around the time-delay zero (shaded color lines). **b)** Temporal overlap between the experimental E_{THz}, and modeled $Q^2_{E^1_u}$ with E^2_{THz}. **c)** $\delta T/T|_{\mathrm{optic}}$ versus $Q_{A^1_{1g}}$ displacement calculated with THz-IRS and THz-SFE models at the $> 2\,$ps time delays.

Figure 3.18 – *Two proposed models of A^1_{1g} phonon excitation: experiment vs. phenomenological modeling.*

As a final step, using the same numerical modeling, we can calculate the effect of the E_{THz} pump central frequency on the A^1_{1g} phonon amplitude for both THz-IRS and THz-SFE mechanisms. Figure 3.19a displays the experimental data (blue circles, presented in Fig.3.15c) superimposed with the results of the THz-IRS and THz-SFE models. Surprisingly, we have a good agreement between the experiment and each proposed pathway of A^1_{1g} phonon generation. In addition, we see that the maximum of $Q_{A^1_{1g}}$ displacement is expected for the THz central frequency of $\Omega_0/2\pi = 0.925\,$THz (half of A^1_{1g} phonon mode natural frequency), which is out of reach in current experimental conditions. Finally, at this stage, without first-principle calculations, we can not assign the generation of A^1_{1g} phonon in 16 nm thick n-doped Bi_2Te_3 to either THz-SFE or THz-IRS.

3.3.3 Conclusion

In this section, we have demonstrated the excitation of A^1_{1g} coherent optical phonon in Bi_2Te_3 with THz pulsed radiation. We show that the generation efficiency of the A^1_{1g} phonon scales quadratically with THz field amplitude, and is affected by the change in the THz central frequency. We have compared the experimental results to the two recently-proposed models of A^1_{1g} phonon excitation, namely impulsive THz-SFE and displacive THz-IRS. Given our time-delay zero definition, defined as the temporal overlap between the "raw" $\delta T/T$ signal and calculated W^{abs}_{THz} profile, we find that the THz-SFE model does a better job in matching the experimental phase of

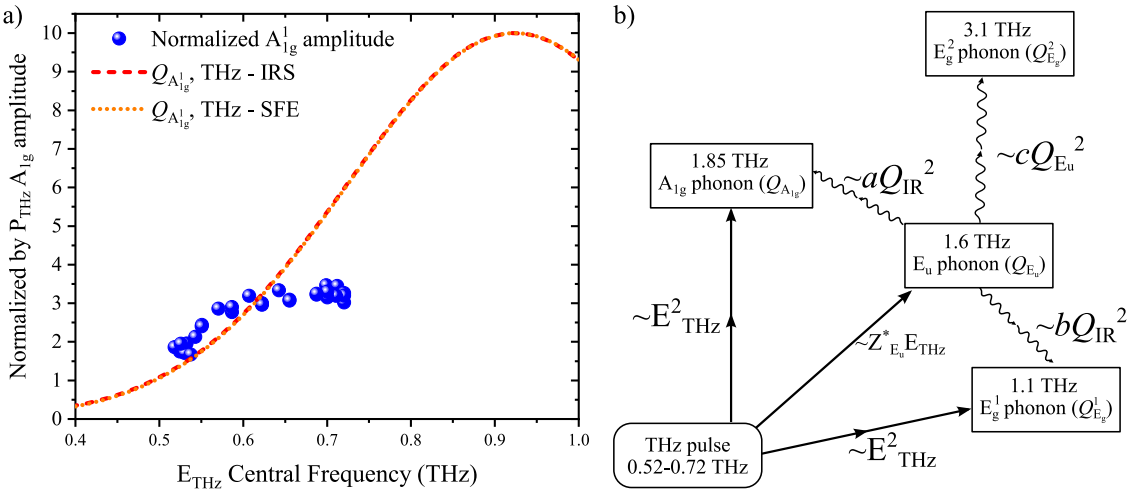

a) A_{1g}^1 phonon amplitude, normalized by the THz pump power as a function of the central frequency of the THz pulse (blue), overlapped with $Q_{A_{1g}^1}$ calculated from THz-IRS and THz-SFE models (dashed and dotted lines). **b)** Different possible pathways of Raman phonon excitation in Bi_2Te_3 with pulsed THz radiation.

Figure 3.19 – *THz pump central frequency - A_{1g}^1 phonon amplitude dependence and the sketch of possible scenarios of Raman active phonons generation in Bi_2Te_3.*

the A_{1g}^1. In addition, preliminary anisotropic detection results have not revealed the presence of either Raman E_g^1 or IR E_u^1 phonons. At the same time, we saw a clear, long-lived signature of the E_g^2 mode, with a frequency roughly four times higher than the $\Omega_0/2\pi$ of the driving THz electric field. At this moment, we can not conclude on the possible mechanism of E_g^2 mode excitation, and more experimental studies are needed.

Finally, Bi_2Te_3 is a perfect system to study the complex nonlinear and anharmonic interaction between various optical phonon modes. One can imagine a rather complex nonlinear pathways of A_{1g}^1, E_g^1 and E_g^2 generation, which may be governed solely by the THz-SFE, THz-IRS, or combination of both, as sketched in Fig.3.19b). To confirm or contradict this assumption, theoretical modeling and additional experimental developments are needed. From the theoretical point of view, our colleagues Brice Arnaud and Rémi Busselez are working on first-principle calculations (DFT) to evaluate the respective amplitudes of impulsive and displacive forces acting on the A_{1g}^1 phonon. Concerning the experimental developments, the Bi_2Te_3 sample orientation, E_{THz} and E_{probe} angular dependence of $\delta T/T$ are to be measured, both in isotropic and anisotropic detection configurations. In addition, an automated tilted-pulse front realignment feedback-loop could be built, which will allow us to tune the THz pulse central frequency in the range of 0.4-3 THz [102]. Such tunable THz source could help us to better understand the coherent phonon generation in the highly off-resonance THz-pumping conditions. In addition, a two-dimensional time-resolved pump-probe spectroscopy can be used to study and control the nonlinear interaction between selected phonon modes in Bi_2Te_3 [116, 179–181]. Understanding the nonlinear generation and coupling between optical phonon modes is crucial for the selective control over the coherent states of the lattice vibrations.

3.4 Conclusions and perspectives

This chapter demonstrates the generation of coherent acoustic phonons with THz pulses in nanometric films of metals (Chromium and Aluminum) and narrow-band semiconductor (Bismuth Telluride) with pulsed THz radiation. We show that the coherent acoustic phonon amplitude in Cr, Al, and Bi_2Te_3 nanofilms scale linearly with the THz pump pulse energy. In addition, the acoustic period is proportional to the thin film thickness, as demonstrated for the Bi_2Te_3 nanofilms. We conclude that the THz excitation leads to the ultrafast change in the thermoelastic stress due to the ultrafast Joule effect for the Cr and Al nanofilms. In comparison, while the THz-induced thermoelastic stress is the primary driving acoustic phonon generation mechanism in metals, the Bi_2Te_3's linear acoustic response as a function of the THz-pulse energy could be a preliminary indication of a thermoelastic and/or a deformation potential generation process. However, more controlled experiments and first-principle calculations are needed to determine the origin of coherent acoustic phonon generation with pulsed THz radiation in Bi_2Te_3.

In the second part of this chapter, we conduct the experimental study of coherent optical phonon generation in 16 nm thick Bi_2Te_3 film with pulsed THz radiation. For the first time, we demonstrate that the A_{1g}^1 Raman active optical phonon with 1.85 THz frequency can be excited with a THz pulse of a 0.64 THz central frequency. Furthermore, we show that the amplitude of the A_{1g}^1 mode scales quadratically with the amplitude of the applied THz electric field and does not depend on the THz pump polarization. In addition, we show that the change of the THz pump central frequency from 0.52 THz to 0.73 THz leads to the three times more efficient generation of the A_{1g}^1 phonon. We then compare the experimental data with the two phenomenological models: impulsive Raman THz-Sum Frequency excitation and displacive anharmonic THz-Ionic Raman scattering. We find that the phase of the THz-Sum Frequency excitation model fits better the phase of experimental A_{1g}^1 signal. However, first-principle calculations are necessary to estimate the relative amplitudes of displacive and impulsive forces that can contribute to the A_{1g}^1 phonon generation in 16 nm thick Bi_2Te_3 film.

In future work, the study of the acoustic phonon generation with THz could be extended to metallic nanoparticles that may be fabricated to support acoustic vibrations in the THz range. In addition, the experiments on the Bi_2Te_3 film with various doping and tunable Fermi levels could help identify the primary microscopic mechanism of acoustic phonon generation in narrow-band semiconductor films. Furthermore, the experimental developments in the frequency tunable THz source combined with the 2D time-resolved spectroscopy may allow us to explore the different excitation conditions of optical phonon modes in Bi_2Te_3. Finally, by comparing the experiment and first-principle calculations, we should be able to identify the dominant mechanism of A_{1g}^1 phonon generation in Bi_2Te_3.

Chapter 4

Ultrafast spin-to-charge conversion

Contents

4.1 Introduction

Over the last decade, electricity consumption by the information and communication technology sector (ICTS) has rapidly increased. It has been estimated that starting from 2020, ICTS will be responsible for more than 11% of Global use of electricity [182]. With an exponential increase in the generated and stored data, there is a necessity for energy-efficient, fast, non-volatile memory and energy-harvesting devices. Spintronics is regarded today as a promising field of physics capable of proposing some possible solutions of this problem [183].

The main goal of spintronics is to develop an efficient way to excite, "flip," transport, and convert spins under external stimuli. The study of the spin-transport and spin-to-charge conversion phenomena in the Magnetic/Non-Magnetic (NM) heterostructures in the DC regime displays the possibility of efficient control of the magnetic degrees of freedom with a relatively small amount of applied current (within $\approx$ nV $-$ µV range) [184–186]. However, the development of fast memory devices requires an understanding of the magnetic system response times upon rapidly-varying external stimuli, such as magnetic, electric and light pulses. Interestingly, the ultrafast response of a Ferromagnetic (FM)/NM heterostructure to an ultrashort laser pulse can be probed with THz emission spectroscopy, as discussed in the following Theoretical background section.

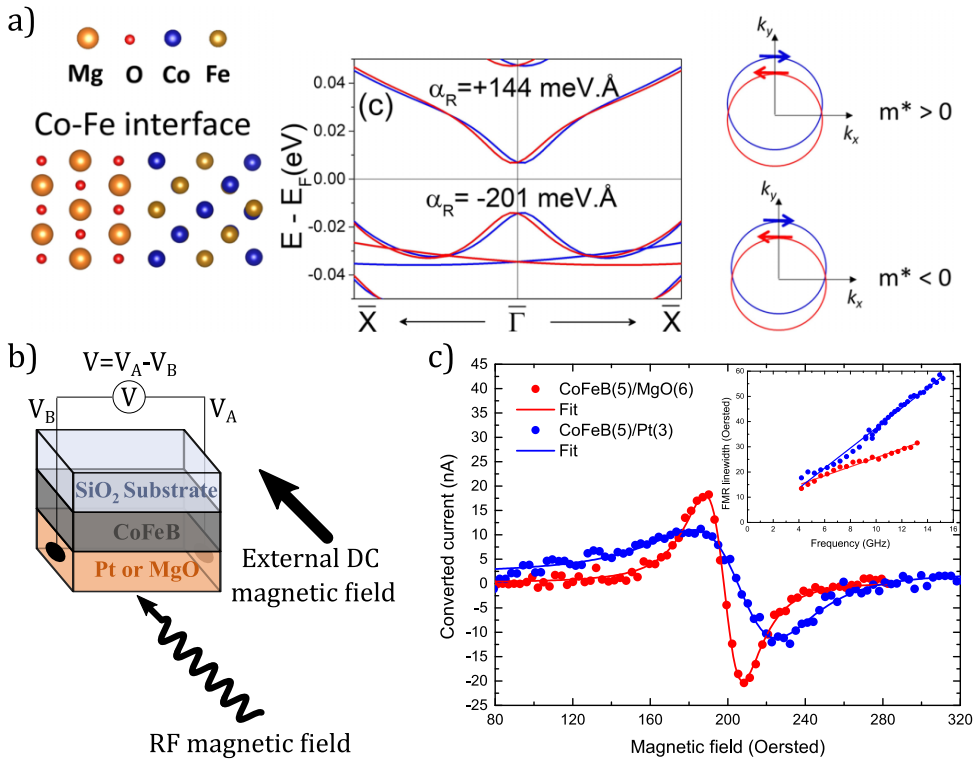

a) The deposition of the MgO on top of the CoFeB will lead to the creation of the Rashba states at the CoFeB/MgO interface. The left column represents Fermi surfaces of opposite magnetization orientations for CoFe/MgO interface and given sign of the electron effective mass m^*. **b)** The experimental configuration of the Ferro-magnetic resonance experiment. **c)** Detected spin-charge currents for CoFeB(5 nm)/Pt(3 nm) (blue closed dots) and CoFeB(5 nm)/MgO(6 nm) (red closed dots) with their respective fits. **Inset:** FMR line-widths as function of the RF exciting field frequency. Effective Gilbert damping of 5e-3 and 10e-3 can be extracted for CoFeB(5 nm)/Pt(3 nm) and CoFeB(5 nm)/MgO(6 nm) respectively. From [4].

Figure 4.1 – *The Rashba splitting (α_R) calculated from the band structure of Co-Fe terminated CoFe/MgO interface and FMR spin-pumping experiments.*

The physical mechanisms discussed in this Chapter are based on further development of the theory, introduced back in the Section 1.2.3. This will serve as literature review of the recent achievements in THz-spintronics based on the manipulation of spin precession and spin currents. The experimental part of this chapter is inspired by the existence of the Rashba states in CoFeB/MgO bilayers, recently observed with quasi-static ferromagnetic resonance spin-pumping measurements, where the samples are excited by a microwave magnetic field at a fixed frequency [4]. Interestingly, they show an identical spin-to-charge conversion efficiencies between the best-performing inverse spin Hall emitter (CoFeB/Pt) and Rashba converter (CoFeB/MgO) (see Fig.4.1)c). As a result, Rousseau et al. [4] claim that the deposition of a thin 6 nm MgO layer on top of the FM metal, such as Co, Fe, CoFe, or CoFeB, will lead to the creation of the Rashba states inside FM, in the vicinity to the MgO interface.

In the Experimental results section we show that ultrashort laser pulse illumination of some hybrid magnetic nanostructures leads to the emission of sub-ps THz pulses. In addition, we will demonstrate that the emitted THz is sensitive to different experimental parameters, allowing us to investigate different microscopic spin-to-charge conversion mechanisms. In particular, by

comparing the ultrafast light-induced THz-emission in CoFeB/Pt and CoFeB/MgO systems we will try to identify and estimate the relative amplitudes of ultrafast Inverse Spin Hall effect (ISHE), bulk conversion inside the ferromagnetic CoFeB, and the Inverse Edelstein effect (IREE). At last, we demonstrate the striking difference between the ISHE and IREE effects as a result of the pump photon energy sensitive IREE spin-to-charge conversion. To the best of our knowledge, this effect was never observed before, and opens prospects for light-controlled spin-orbit THz emitters.

4.2 Spin transport: Theoretical background

The spin-orbit interaction (SOI) can affect and alter the propagation direction of the spin and charge current in the material. For example, some FM/NM interfaces with broken time-reversal symmetry may act as the source of the so-called spin-galvanic effects [187]. In addition, particular spin and charge transport effects can arise from temperature gradient within the FM or at the FM/NM interface. These effects are often used for the spin-injection [188] and spin-to-charge conversion [189]. In the following subsections, we will discuss the main spin-dependent transport phenomena and how one can probe them at the sub-ps time scale.

4.2.1 Spin precession

In the Section 1.2.3, we discussed the undamped precession of the spins on the lattice as the result of the near-neighbor exchange interaction field $\hat{\boldsymbol{B}}_j^{ex}$ (see Eq.1.49). Here, let us look at the change of the expected value of the spin operator of a single electron subjected to the time-dependent external magnetic field $\hat{\boldsymbol{B}}_{ext}(t)$. Given the Zeeman term $\hat{H}_z = -\hat{\boldsymbol{\mu}}_e \cdot \hat{\boldsymbol{B}}_{ext}(t)$, the undamped spin-precession in the presence of an external magnetic field will read [190]:

$$\frac{d}{dt}\langle\hat{\boldsymbol{s}}\rangle = \frac{g_s\mu_B}{\hbar}\langle\hat{\boldsymbol{s}}\rangle \times \hat{\boldsymbol{B}}_{ext}(t), \tag{4.1}$$

where the time-dependent change in $\langle\hat{\boldsymbol{s}}\rangle$ will happen at the specific angular frequency $\omega_{Larmor} = \mu_B\hbar^{-1}B_{ext}$, known as Larmor precession frequency [11].

Moreover, the additional spin-dependent terms in the Hamiltonian for the many-electron system show that the spin-precession can be coupled to the magnetic anisotropy, lead to the demagnetization, modify the exchange interaction, and interact with various magneto-elastic contributions [13]. In reality, due to the dissipation of the angular momentum, the perturbed system will return to equilibrium, resulting in the damped precession of a spin around the field felt by the magnetic system. Therefore, the spin-damping is accounted for by an additional term, and the initial action of $\boldsymbol{B}_{eff}$ on the spin-operator named the spin-torque.

In the frame of macroscopic magnetization ($\boldsymbol{M}$, see Eq.1.43), the precessional damping of the magnetization can be described in terms of the Landau-Lifshitz-Gilbert (LLG) equation [191]:

$$\frac{\partial \boldsymbol{M}}{\partial t} = \gamma_G \boldsymbol{M} \times \boldsymbol{B}_{eff} - \frac{\alpha_G}{M}\boldsymbol{M} \times \frac{\partial \boldsymbol{M}}{\partial t}, \tag{4.2}$$

where M is the magnitude of $\boldsymbol{M}$, $\gamma_G = \gamma/(1+\alpha_G^2)$ with gyromagnetic ratio γ and the Gilbert damping parameter α_G. Importantly, while the direction of $\boldsymbol{M}$ is subject to change, the magneti-

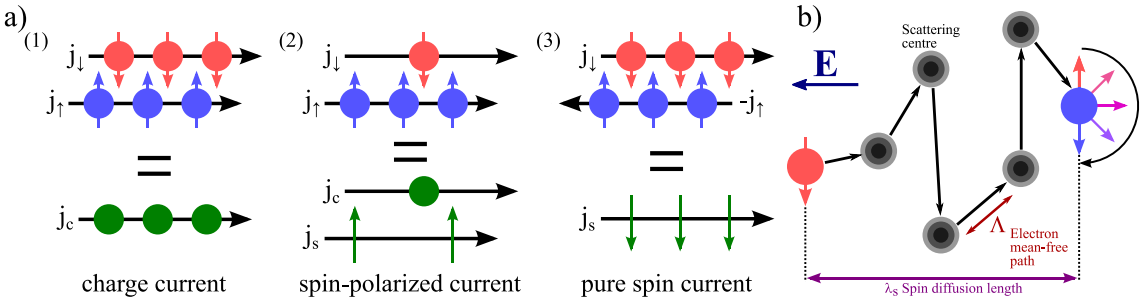

a) (1) The flow of electrons with equal density and velocity of up and down spins along the same direction results in the pure charge current, where no transfer of angular momentum can exist. (2) The electron flow where the mobility and concentration of up and down carriers are not equivalent, the charge transport will carry the information about the angular momentum, leading to the spin-polarized electron current. (3) When the current density with up and down spin polarization flows in the opposite direction, only flow of the angular momentum can exist. This corresponds to the pure spin current. Figure after [195]. **b)** Electron propagation in the presence of an external electric field is affected by the scattering and deflection of the impurities. The mean distance of the change in electron direction or energy is called mean free path Λ. The mean distance describing the flip of an electron's spin is denoted as spin diffusion length, λ_s. Figure adapted from [196].

Figure 4.2 – *Different types of the electron current and spin-diffusion length.*

zation magnitude M will not be affected [192]. The second term in Eq.4.2 describes the angular momentum loss via precessional damped-motion of magnetization through interaction with the conduction electrons, phonons, magnons, or lattice defects [191]. To summarize, this equation is valid for $T \ll T_C$ while the phenomenological damping term corresponds to the multitude of complex energy transfer processes within the magnetic material.

The generalized forms of the LLG equation are used to model the temporal dynamics of the magnetization precession $\boldsymbol{M}$ in magnetic materials [193] subjected to external stimuli [194]. For example, one can change the direction of $\boldsymbol{M}$: by exciting the FM with an EM wave of a specific polarization and frequency close to ω_{Larmor}, via spin accumulation in the adjacent NM layer or by thermal effects [192]. Notably, the opposite is true: dynamical magnetization will "pump" spins into the adjacent NM layer. We note that such pure spin current generation does not involve any contribution of electron transport.

4.2.2 Spin currents

Electron transport in magnetic materials can lead to the generation of the spin current. In addition to the charge current, usually defined as the flow of the electrons along the given direction (See Fig.4.2a), magnetic materials allow for the transport of the intrinsic angular momentum. Regarding the ongoing discussion about the definitive formulation of the spin-current [197, 198], we will address it in the frame of a phenomenological two spin-channel model described elsewhere [195, 199].

In the frame of the Stoner model introduced in the Section 1.2.3, one can express the the electron charge j_c and the angular momentum j_s in the terms of spin-dependent carrier density

$\rho^{\uparrow,\downarrow}$ and velocity $v^{\uparrow,\downarrow}$ as:

$$\begin{aligned} j_c &= j^{\uparrow} + j^{\downarrow} = -e(\rho^{\uparrow}v^{\uparrow} + \rho^{\downarrow}v^{\downarrow}); \\ j_s &= -\frac{\hbar}{2}(\rho^{\uparrow}v^{\uparrow} - \rho^{\downarrow}v^{\downarrow}) = -\frac{\hbar}{2e}(j^{\uparrow} - j^{\downarrow}). \end{aligned} \tag{4.3}$$

This equation summarizes three possible variations of the electron current depicted in Fig.4.2. Usually, in NM conductors, the equal density of the spin-up and spin-down electrons at the Fermi level renders $j_s = 0$, establishing the pure charge current flow. However, in the FM both $\rho^{\uparrow} \neq \rho^{\downarrow}$ and $v^{\uparrow} \neq v^{\downarrow}$ are true, allowing for simultaneous charge and spin-current flow called spin-polarized current (see Fig.4.2a2). However, when $j^{\uparrow} = -j^{\downarrow}$, as displayed in Fig.4.2a3, only the transport of the electron spin can exist, denoted as pure spin current. Moreover, the generation of the pure spin current is quite challenging task, sometimes requiring extreme experimental conditions and use of specific magnetic materials [200].

In analogy with the electron mean path Λ, the collision and scattering events may alter the particles' spin direction. The mean distance that thermalized electrons can travel without change in their angular momentum, or without so-called "spin-flip"(as shown in Fig.4.2b), is called spin diffusion length λ_s [201]:

$$\lambda_s = \frac{1}{\sqrt{3}} v_F \sqrt{\tau_s \tau_e}, \tag{4.4}$$

where τ_s is the spin-flip time or spin lifetime. λ_s is directly linked to the electron velocity at the Fermi level v_F and scattering time τ_e. This equation, however, does not take into account the different spin-flip diffusion lengths for the majority and minority of spin-polarized carriers due to the asymmetric scattering [201]. Most materials with strong SOI are known to have short λ_s in the order of tens of nanometers. The spin-flip is known to occur via two competing mechanisms: Elliot-Yafet, [202] which dominates for centrosymmetric conductors, and D'yakonov-Perel' [203], superior within the 2D systems and semiconductors (GaP, ZnTe, GaAs) lacking space-inversion symmetry. Interestingly, the Elliot-Yafet mechanism predicts the spin-rotation during the collisions, while the D'yakonov-Perel model describes spin-flip in-between scattering events.

4.2.3 Field-driven spin transport effects in DC (quasi-static)

Hall and Anomalous Hall effects

E.H. Hall in 1879 [204] discovered the transverse deflection of the charged particles in metals subjected to the presence of an external magnetic field B_{ext}. One can explain this observation in the means of the classical Lorentz force, which acts on moving charged particles with speed v:

$$\boldsymbol{F} = -e(\boldsymbol{E} + \boldsymbol{v} \times \boldsymbol{B}_{ext}). \tag{4.5}$$

About two years after, Hall discovered the same effect in ferromagnetic materials, which is of one order of magnitude stronger [205]. Newly discovered Anomalous Hall effect (AHE) was then combined with the Hall effect by Pugh and Lippert [206] to describe the total Hall resistivity (ρ_{xy}^{tot})

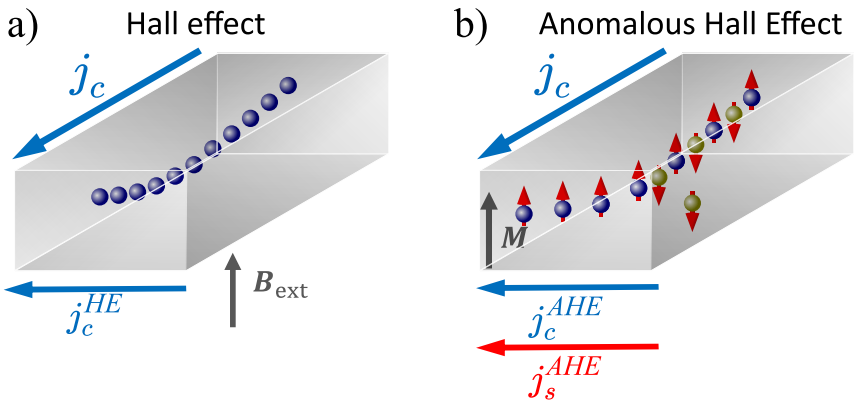

a) The ordinary Hall effect. Lorentz force is acting on the driving current j_c in the presence of the external field B_{ext}, resulting in the transverse Hall current j_c^{HE}. b) The extraordinary or Anomalous Hall effect. The j_c flow will generate the transverse spin-polarized current in the magnetic material with non-zero macroscopic magnetization $M \neq 0$ via the Anomalous Hall Effect. Figure adapted from [44].

Figure 4.3 – *The geometry of the Hall and Anomalous Hall effects.*

in terms of both Hall (ρ^{Hall}) and AHE (ρ^{AHE}) contributions:

$$\rho_{xy}^{tot} = \rho^{Hall} \boldsymbol{B}_{ext,z} + \rho^{AHE} \boldsymbol{M_z}. \tag{4.6}$$

It was observed that in the absence of $\boldsymbol{M}$, i.e., when working with NM conductor, ρ_{xy} is increasing linearly with $\boldsymbol{B}_{ext}$, as expected from Eqs.4.5,4.6. However, for the FM Ni, the ρ_{xy} linearly increases at low $\boldsymbol{B}_{ext}$ [207], and then rapidly saturates due to the parallel alignment of all spins along the direction of the applied magnetic field [208].

The AHE describes the charge to spin-polarized current conversion. In general, the total AHE conductivity tensor (σ_{xy}^{AH}) can be expressed as the sum of the following contributions [208]:

$$\frac{1}{\rho_{xy}^{AHE}} = \sigma_{xy}^{AHE} = \sigma_{xy}^{AHE-int} + \sigma_{xy}^{AHE-sj} + \sigma_{xy}^{AHE-skew}, \tag{4.7}$$

where $\sigma_{xy}^{AHE-int}$, σ_{xy}^{AHE-sj} and $\sigma_{xy}^{AHE-skew}$ are the intrinsic, side-jump and skew-scattering contributions shown in Fig.4.4.

Intrinsic deflection: The intrinsic contribution to the AHE ($\sigma_{xy}^{AHE-int}$) depends on the band structure of the perfect crystal [209]. The total velocity of a Bloch electron in the band n, with band momentum $\boldsymbol{k}$ in the real space, in the presence of the applied electric field $\boldsymbol{E}$ can be written as [208, 210]:

$$\frac{\partial \langle \boldsymbol{r} \rangle}{dt} = \underbrace{\frac{1}{\hbar}\frac{\partial \epsilon_n(\boldsymbol{k})}{\partial \boldsymbol{k}}}_{\text{normal velocity}} - \underbrace{\frac{\hbar \boldsymbol{k}}{\partial t} \times \boldsymbol{b}_n(\boldsymbol{k})}_{\text{anomalous velocity}}, \tag{4.8}$$

where the first term corresponds to the ordinary electron velocity in the band n at the energy level $\epsilon_n(\boldsymbol{k})$. The second term introduces the transverse (anomalous) electron velocity perpendicular to both applied $\boldsymbol{E}$ and Berry phase-curvature $\boldsymbol{b}_n(\boldsymbol{k})$. $\boldsymbol{b}_n(\boldsymbol{k})$ strongly depends on the electron band

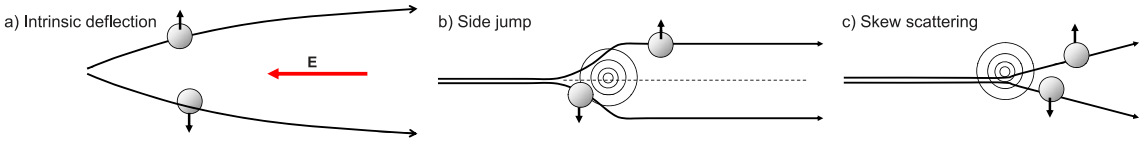

a) Intrinsic deflection. Electrons gain anomalous velocity perpendicular to the direction of the external electric field $\boldsymbol{E}$ that heavily depends on the electron band structure. **b)** Side-jump scattering. Electrons with opposite spins are deflected in the opposite directions due to the scattering of an impurity. **c)** Skew-scattering. Asymmetric, spin-dependent electron deflection as a result of the electron or impurity SOI. Adapted from [208]

Figure 4.4 – *Schema of Hall Effect contributions.*

structure, and it is the gauge-invariant representation of Bloch wave function geometric properties. The anomalous contribution is similar to the classical Lorentz force (see Eq.4.5). Still, it originates from the SOI where $\boldsymbol{b}_n(\boldsymbol{k})$ acts as a magnetic field in the momentum space [210]. The intrinsic contribution usually dominates the side-jump and skew-scattering in pure crystals with large SOI and does not require electron scattering [211].

Side-jump scattering: The side-jump contribution (σ_{xy}^{AHE-sj}) to AHE is the scattering process where electron momentum and energy are not affected. The scattering of the electron wave packet from the impurity will lead to spin-dependent transverse displacement. The electrons with opposite spins will experience an equal shift in the opposite directions, as shown in Fig.4.4b. Interestingly, the numerical prediction of the σ_{xy}^{AH-sj} is highly challenging since it depends on the intricate details of the material disorder.

Skew-scattering: Skew-scattering alters the electron momentum after interaction with the impurity. Its efficiency is proportional to the electron scattering time τ_e [208]. Skew-scattering can occur in the presence of a strong SOI, leading to the spin-dependent change in the electron momentum, as shown in Fig.4.4. Additionally, the skew-scattering can happen in the absence of SOI, when the electrons are subject to motion in the spin-orbit-coupled band structure. The latter can be thought of as the impurity-analogy of the heavy-atoms Mott-scattering [211].

Spin Hall and Inverse Spin-Hall effects

The description of the Spin Hall effect (SHE) and Inverse Spin Hall Effect (ISHE) are directly related to the physics of the AHE. SHE and ISHE effects describe the conversion of the conserved charge quantity to the decaying and dephasing amount of spin [211]. This defines the SHE and ISHE as charge-to-spin and spin-to-charge conversion mechanisms respectively, first predicted by Dyakonov and Perel in 1971 [212]. Similarly to the AHE, the SHE conductivity tensor σ_{xy}^{SH} can be expressed as the sum of three mechanisms:

$$\sigma_{xy}^{SH} = \sigma_{xy}^{SH-int} + \sigma_{xy}^{SH-sj} + \sigma_{xy}^{SH-skew}, \tag{4.9}$$

with σ_{xy}^{SH-int}, σ_{xy}^{SH-sj} and $\sigma_{xy}^{SH-skew}$ being the intrinsic, side-jump and skew-scattering contributions, already discussed in the previous subsection.

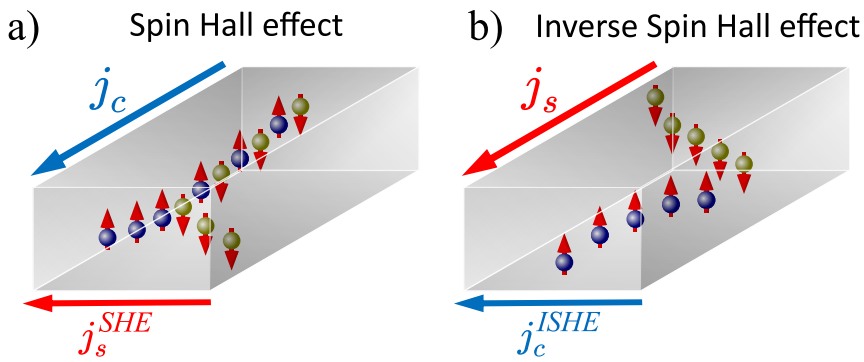

a) Spin Hall Effect. In the non-magnetic material (NM), the charge current flow will establish the transverse spin current, due to the effective spin-orbit field experienced by the charged particles, in analogy with Lorentz force. **b)** Inverse Spin Hall Effect. The pure spin current injected in the NM will result in the transverse charge current due to the SOI. The figure is redrawn from [44, 195]

Figure 4.5 – *The geometry of the Spin Hall and Inverse Spin Hall effects.*

The vital distinction between the AHE and the SHE is that AHE can happen only in magnetic materials, while the SHE and the ISHE are suitable for all materials with strong SOI. For example, injection of pure spin current in the NM will establish transverse charge current due to the asymmetric scattering arising from different concentration of the minority and majority spin populations at the Fermi level. Inversely, NM will convert pure spin current into pure charge current.

The amount of spin or charge generated via the SHE and ISHE can be described with the following equations [211]:

$$\begin{aligned} \boldsymbol{j}_s^{SHE} &= -\frac{\hbar}{2e}\theta_{SHE}[\boldsymbol{j}_c \times \boldsymbol{\sigma}_s], \\ \boldsymbol{j}_c^{ISHE} &= -\frac{2e}{\hbar}\theta_{SHE}[\boldsymbol{j}_s \times \boldsymbol{\sigma}_s], \end{aligned} \tag{4.10}$$

where θ_{SHE} is the so-called spin Hall angle that describes the conversion efficiency, and $\boldsymbol{\sigma}_s$ is the unit vector of the spin-/spin-current polarization.

The well-studied field-driven effects, such as AHE, SHE, and ISHE, are routinely used to measure and characterize spin currents. The magnitude of the θ_{SHE} can be measured by studying the efficiency of the spin-to-charge conversion with a variety of different techniques: FMR spin-pumping [213], thermal spin injection via the spin Seebeck effect [214], spin Hall magneto-resistance [215], and spin torque FMR [216].

Rashba-Edelstein and Inverse Rashba-Edelstein effects

As discussed in the Section 1.2.3, the Zeeman Hamiltonian can lift the spin degeneracy of the electronic band structure, leading to the Dresselhaus and Rashba splitting. However, special conditions have to be fulfilled regarding the time-reversal and space-inversion symmetries of the material.

Symmetry considerations: When the time-reversal symmetry is preserved, i.e., $T : t \to -t$, following the Kramer's degeneracy theorem, the energies of fermions with opposite momentum

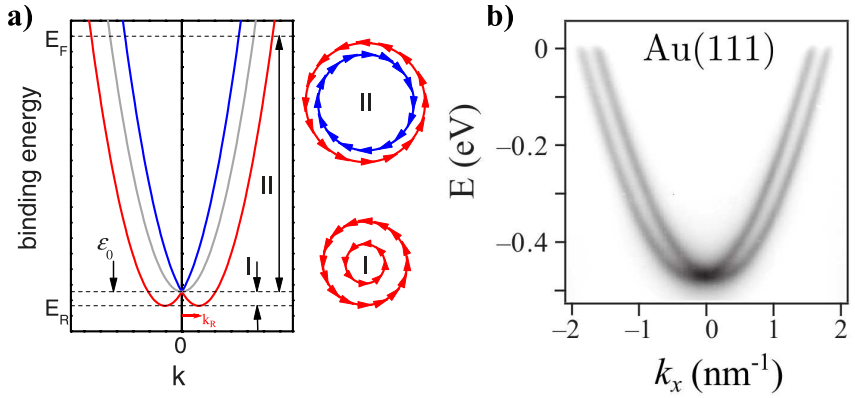

a) The band structure of electrons in 2D system in the absence of the SOI (grey). In the presence of SOI, blue and red curves denote spin-split electron dispersion curves. Region I is the energy interval between the bottom of the bands, defined as E_R and the binding energy ϵ_0, with similar spin-dependent dynamics of the inner and outer branches. At high energy, inner and outer branches show opposite spin-direction dynamics. **b)** Angle-resolved photoemission spectroscopy (ARPES) intensity from the Au(111) surface state, showcasing the existence of the inner and outer electron branches. Adapted from [217]

Figure 4.6 – *Schema of the parabolic spin-split band structure in pair with Rashba splitting observed in Au* $\langle 111 \rangle$.

$\boldsymbol{k} \rightarrow -\boldsymbol{k}$ and spin are the same:

$$E_{\boldsymbol{k},\uparrow(\downarrow)} = E_{-\boldsymbol{k},\downarrow(\uparrow)}. \tag{4.11}$$

This equation leads to the parabolic electron dispersion relation. However, the effective SOI field can affect the trajectory of charged particles depending on their spin. Therefore, the SOI may lift the time-reversal symmetry. In the case of centrosymmetric medium with SOI, both spin- and $\boldsymbol{k}$-dependent effects are allowed, establishing the well-known SHE and ISHE effects in Pt and Ta, for example.

Non-centrosymmetric medium, by definition, lacks the space-inversion symmetry, so that:

$$E_{\boldsymbol{k},\uparrow(\downarrow)} \neq E_{-\boldsymbol{k},\uparrow(\downarrow)}. \tag{4.12}$$

Space and time-reversal symmetries will be lifted if we introduce the SOI in non-centrosymmetric crystals. In addition, broken space-inversion symmetry can indirectly create the intrinsic, stray electric field, which can be coupled to the electron spin via SOI. Such electric field ($\boldsymbol{E}$) can also exist as a result of a junction effect when two layers are in contact (as in the case of the hybrid nanostructures studied in this Chapter). Thereby, the electrons with velocity $\boldsymbol{v}$ feel in their frame of refference a local magnetic field called the Rashba field ($\boldsymbol{B}^*$) given by $\boldsymbol{B}^* = c^{-2} \cdot \boldsymbol{v} \times \boldsymbol{E}$ [11], creating the Rashba-split band-structure (an example is shown in Fig.4.6).

The Rashba Hamiltonian can be expressed as the interaction between the spin-vector $\boldsymbol{s}$ and the electron momentum vector $\boldsymbol{k}$ as [184]:

$$\hat{H}_R \propto \boldsymbol{B}^* \times \boldsymbol{s} = \alpha_R(\boldsymbol{k} \times \boldsymbol{z}) \cdot \boldsymbol{s}, \tag{4.13}$$

with the coordinate normal to the interface $\boldsymbol{z}$, and the Rashba coefficient α_R that is proportional to the splitting-electric field. The Rashba Hamiltonian $\hat{H}_R$ will lead to the following electron dispersion relation [4]:

$$E_{\uparrow,\downarrow}(\boldsymbol{k}) = \varepsilon_0 + \frac{\hbar^2 \boldsymbol{k}^2}{2m_e^*} \pm |\alpha_R||\boldsymbol{k}|, \tag{4.14}$$

where ε_0 is the band-crossing energy at $k = 0$ (see Fig.4.6a). Importantly, α_R is not a constant, and can be expressed as:

$$\alpha_R = \frac{2E_R}{k_R}, \tag{4.15}$$

with E_R being the band-splitting energy at $k = k_R$ [4], displaying the relationship between the Rashba coefficient and the electron momentum.

The Rashba-split band structure allows for the charge-to-spin and spin-to-charge conversion. It was first theoretically predicted in 2D systems [218] and was later called Edelstein or spin-galvanic effect [187]. The spin-galvanic effect was then first measured at the Ag/Bi interface [219].

Rashba Edelstein Effect: Let us consider the direct Rashba Edelstein effect (REE). The action of an external electric field $\boldsymbol{E_x}$ leads to a shift of the Fermi sphere. As a consequence there is a total non-zero electron momentum in the x-direction with $\Delta k_x \propto -\boldsymbol{E_x} \propto -\boldsymbol{j}_c^x$, as shown in Fig.4.7a. The net spin current density generated under the action of $\boldsymbol{E_x}$ can be expressed as:

$$\delta s = \delta s_\uparrow - \delta s_\downarrow \propto k_F^{out}\delta k_x - k_F^{in}\delta k_x, \tag{4.16}$$

where k_F^{out} and k_F^{in} are the radii of the outer and inner Fermi contours. Considering similar electron scattering times for both contours, the finite spin accumulation will happen under the action of $\boldsymbol{E_x}$ or the injection of the charge current $\boldsymbol{j}_c^x$.

Inverse Rashba Edelstein Effect: Like the ISHE, the Inverse Rashba Edelstein effect (IREE) describes the charge current generation upon injection of the spin current at the Rashba interface. As shown in Fig.4.7b, the injection of the spin-current polarized along the y-direction will shift the outer and inner Fermi contours by an equal amount δk_x. However, the total displacement δk_x^{total} will be proportional to:

$$\delta k_x^{total} \propto \Delta k_x^{out} - \Delta k_x^{in} \propto k_F^{out}\delta k_x - k_F^{in}\delta k_x. \tag{4.17}$$

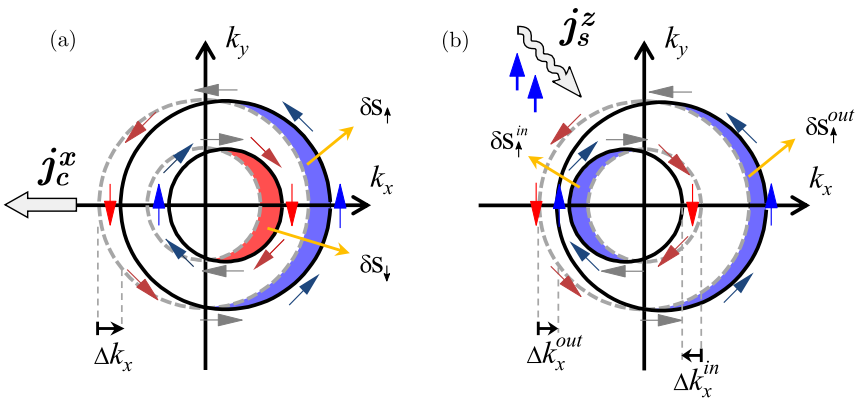

a) Direct Rashba-Edelstein effect (REE). Charge current j_c^x applied along the $-x$ direction will equally shift the Rashba-split Fermi contours by the amount Δk_x. This will create two unequal spin densities $\delta s_\downarrow$ and $\delta s_\uparrow$ (red and blue shaded regions, respectively) that will lead to the finite spin accumulation. **b)**. Inverse Rashba-Edelstein effect (IREE). The injection of the spin-current along z, polarized along the y-axis, will lead to the unequal displacement of the Rashba contours by the amount of Δk_x^{out} and Δk_x^{in}. Uneven carrier acceleration in the opposite directions will lead to the charge flow along the x-axis. Redrawn from [195]

Figure 4.7 – *Schema of the spin-to-charge conversion at the Rashba interface.*

The non-zero δk_x^{total} will result in the generation of the charge current perpendicular to the polarization of the injected spin-current (along k_z). One can notice that the REE and IREE efficiency depends on the splitting of inner and outer contours, which is related to the magnitude of the Rashba coefficient α_R. The charge current generated by the IREE, sensitive to the spin-current polarization direction $\boldsymbol{\sigma}_s$, can be written as [219]:

$$\boldsymbol{j}_c^{IREE} \propto \lambda_{IREE} \cdot \boldsymbol{j}_s \times \boldsymbol{\sigma}_s, \tag{4.18}$$

where "effective Rashba length" $\lambda_{IREE} = \alpha_R \tau_s / \hbar$, with τ_s being effective eletron spin relaxation time.

4.2.4 Thermally-driven spin transport effects in DC (quasi-static)

Experimental and theoretical developments of the Hall-driven effects led to the discovery of thermally-driven spin-transport phenomena, such as the spin-Seebeck [220] and the Nernst [221] effects.

Seebeck effects

Seebeck effect: Let us take two metals with different transport properties. The thermal gradient ∇T applied along a given direction will lead to charge redistribution in the bulk of each metal. If we bring those two metals into electrical contact, we will establish the current flow along the junction due to the well-known Seebeck effect, as shown in Fig.4.8a. The current flow will be

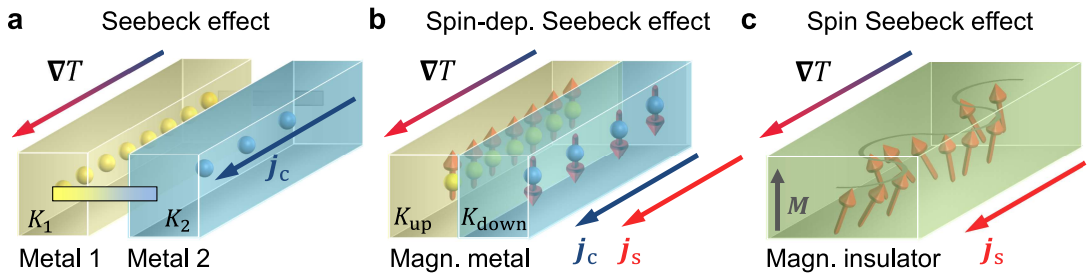

a) Seebeck effect. Temperature gradient ∇T applied to the two metals in contact, with different transport properties and Seebeck coefficients $K_{1,2}$, will lead to the charge flow along the junction $\propto \nabla T(K_1 - K_2)$. **b)** Spin-dependent Seebeck effect. The different mobility of the majority and the minority electrons in the magnetic metal will result in the different spin-dependent Seebeck coefficients S_{maj} and S_{min} respectively. The temperature gradient applied to the metal with the net magnetization will lead to the generation of the spin-polarized current $\propto \nabla T(S_{maj} - S_{min})$. **c)** Spin-Seebeck effect. The magnons excited by the temperature gradient ∇T will carry the pure spin current along the direction of the gradient. Dominant in the magnetic insulators. From [44].

Figure 4.8 – *Schemes of the multiple Seebeck effects.*

proportional to:

$$\boldsymbol{j}_c^{SE} \propto \nabla T(K_1 - K_2), \tag{4.19}$$

where K_1 and K_2 are the Seebeck coefficients. The Seebeck effect is the operational principle of the thermocouples with $K = \Delta V/\Delta T$ the Seebeck constant and V is the Seebeck voltage.

Spin-dependent Seebeck Effect: The spin-dependent Seebeck effect (SDSE) describes the generation of spin-polarized charge current ($\boldsymbol{j}_{s-c}^{SDSE}$) under heat gradient ∇T in the bulk of a FM metal, shown in Fig.4.8. It is explained by the different transport properties of the minority- and majority-spin electrons that are related to the spin-dependent Seebeck coefficients S_{maj} and S_{min} [222]:

$$\boldsymbol{j}_{s-c}^{SDSE} \propto \nabla T(S_{maj} - S_{min}). \tag{4.20}$$

However, the spin-diffusion length λ_s is the determining factor concerning the efficiency of the SDSE in the FM metals. The strong spin-flip scattering in the bulk of the FM layer can drastically reduce the number of spins injected in the neighboring NM layers [214, 223].

Spin Seebeck Effect: Contrary to the SDSE, the spin Seebeck effect (SSE) is related to the generation of pure spin current ($\boldsymbol{j}_s^{SSE}$) in magnetic insulators [220]. Here, the magnons carry the pure spin current, which is usually detected by the ISHE in a NM layer. As shown in Fig.4.8c, this spin-current in the NM material is generated through the temperature difference between the electron temperature T_e in the NM metal and magnon temperature T_M in the magnetic insulator [224]:

$$\boldsymbol{j}_s^{SSE} = \mathcal{K}_{SSE} \cdot (T_e - T_m), \tag{4.21}$$

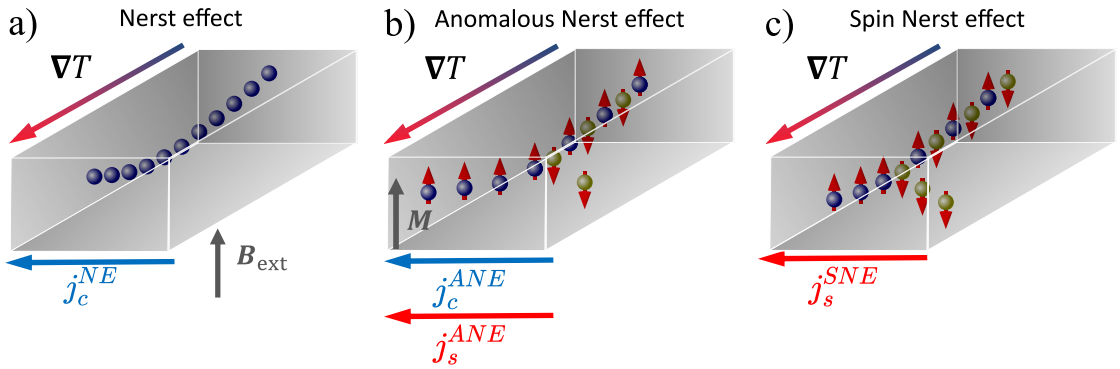

a) Nernst effect. When thermal gradient ∇T is applied normal to the direction of external field B_{ext}, the Nernst charge current j_c^{NE} is generated normal to both. **b)** Anomalous Nernst effect. In the materials with a spontaneous magnetization M, the Anomalous Nernst spin-polarized current $\boldsymbol{j}_{s-c}^{\mathrm{ANE}} \propto \nabla T \times \boldsymbol{M}$ will be generated. **c)** Spin Nernst Effect. Different scattering rates for the electrons below and above Fermi level flowing in the different direction will generate the pure spin current inside the material. Adapted from [226]

Figure 4.9 – *Geometry of an Anomalous Nernst and Spin Nernst Effect.*

where $\mathcal{K}_{SSE}$ is the spin Seebeck coefficient. In ferromagnetic metals, however, both Spin-Seebeck and Spin-dependent Seebeck effects can simultaneously exist [222, 225].

Nernst effects

Nernst Effect: The Nernst effect, discovered by v.Ettingshausen and Nernst in 1886, is the temperature analogy of the Hall effect [221]. In the presence of an external magnetic field $\boldsymbol{B}_{ext}$ applied perpendicularly to the thermal gradient ∇T, as the result of the SOI, the Nernst current will be generated perpendicular to both ∇T and $\boldsymbol{B}_{ext}$, as shown in Fig.4.9a.

Anomalous Nernst Effect: When the thermal gradient is applied to a FM metal, the macroscopic magnetization $\boldsymbol{M}$ can result in the strong Nernst effect even in the absence of the external magnetic field, as displayed in Fig.4.9b. Such thermal counterpart of AHE is called the Anomalous Nernst effect (ANE). One can express the transverse charge flow established by the ∇T in the FM metal as [227]:

$$\boldsymbol{j}_{s-c}^{\mathrm{ANE}} \propto \theta_{ANE} \nabla T \times \boldsymbol{\sigma}_s, \tag{4.22}$$

with θ_{ANE} being the anomalous Nernst coefficient, describing the longitudinal-to-transverse charge conversion efficiency. The study of the $\boldsymbol{j}_c^{\mathrm{ANE}}$ dependence on the FM layer thickness d_{FM} show the decrease of the θ_{ANE} due to the increase in resistance of FM. Importantly, for FM with thickness $d_{FM} > \lambda_s$, ANE can compete or even completely dominate the SDSE [188].

Spin Nernst Effect: The spin Nernst effect (SNE) describes the pure transverse spin current generation arising from the longitudinal heat gradient [177, 228]. The SNE originates from the different transverse scattering rates for the above Fermi level ("hot") and below Fermi level ("cold") electrons flowing respectively along and against the temperature gradient direction, as shown in

Fig.4.9c. Thus, spin current originating from the SNE can be expressed in terms of [229]:

$$\boldsymbol{j}_s^{SNE} \propto \boldsymbol{j}_s^{Hot} - \boldsymbol{j}_s^{Cold} \propto \theta_{SNE} \boldsymbol{j}_h \times \boldsymbol{\sigma}_s, \tag{4.23}$$

where θ_{SNE} is the Spin Nernst coefficient and $\boldsymbol{j}_h = -\kappa \nabla T$ is the heat current with κ being the thermal conductivity. The spin Nernst effect was directly observed in the heavy metal (HM) like Tungsten [230] or Platinum [177, 229].

4.2.5 Terahertz emission as the signature of the ultrafast spin-charge conversion

As of today, researchers are mainly focused on the characterization of the spin-to-charge conversion in the DC and GHz regimes via SHE and ISHE [211], AHE [208], SSE and SDSE [220,231], ANE [226], and IREE [184,232]. Hypothetically, all of these mechanisms can lead to the spin-charge conversion not only at the GHz and DC frequencies but in the THz range as well.

The charge current generated from the spin-to-charge and charge-to-charge conversion within the FM/NM heterostructures is usually detected in the DC/GHz regime by placing physical contacts on top of the NM layer, used to measure the transverse current. On the other hand, in the THz regime the spin-to-charge conversion can be probed in a non-contact manner [3, 233]. If we recall the Maxwell wave-equation (see Eq.1.93), the transient charge current ($\boldsymbol{j}_c$) generated in the heterostructure can act as the source term, responsible for the emission of an electromagnetic radiation:

$$\boldsymbol{E}_{\mathrm{THz}}(t) \propto \frac{\partial \boldsymbol{j}_c(t)}{\partial t}. \tag{4.24}$$

Let us consider what happens upon the excitation of the FM film by a femtosecond laser pulse propagating along the z-axis. By applying the external magnetic field $\boldsymbol{H}$ along the x-axis to fix the magnetization direction $\boldsymbol{M}$ of the FM layer (i.e. $\boldsymbol{H}^x \parallel \boldsymbol{M}^x \parallel \boldsymbol{\sigma}_s^x$), the total transverse spin-polarized current ($\boldsymbol{j}_{s,c}^y$) generated by the fs of laser pulse propagation inside the FM will be given as:

$$\boldsymbol{j}_{s,c}^y(t) \propto \sum_i \boldsymbol{\sigma}_s^x(t) \times \boldsymbol{j}_{c,s}^z(t), \tag{4.25}$$

and it could be the combination of all possible spin-to-charge conversion mechanisms (such as AHE, ISHE, and IREE, DMG), as displayed in the Fig.4.10. As of today, for THz spintronic emitters, the ISHE remains the most efficient conversion mechanism to date, completely overpowering ultrafast AHE and IREE conversion mechanisms [234, 235]. The following section will provide a brief literature overview of the most relevant and impactful studies about the THz spin-charge conversion in magnetic nanometric heterostructures and ultrafast spin-injection mechanisms at the picosecond timescale.

Supperdiffusive spin current injection

The ultrafast quenching of the magnetization in the ferromagnets at the 100 fs time scale was addressed with the superdiffusive spin transport theoretical model that relies on the spin-dependent

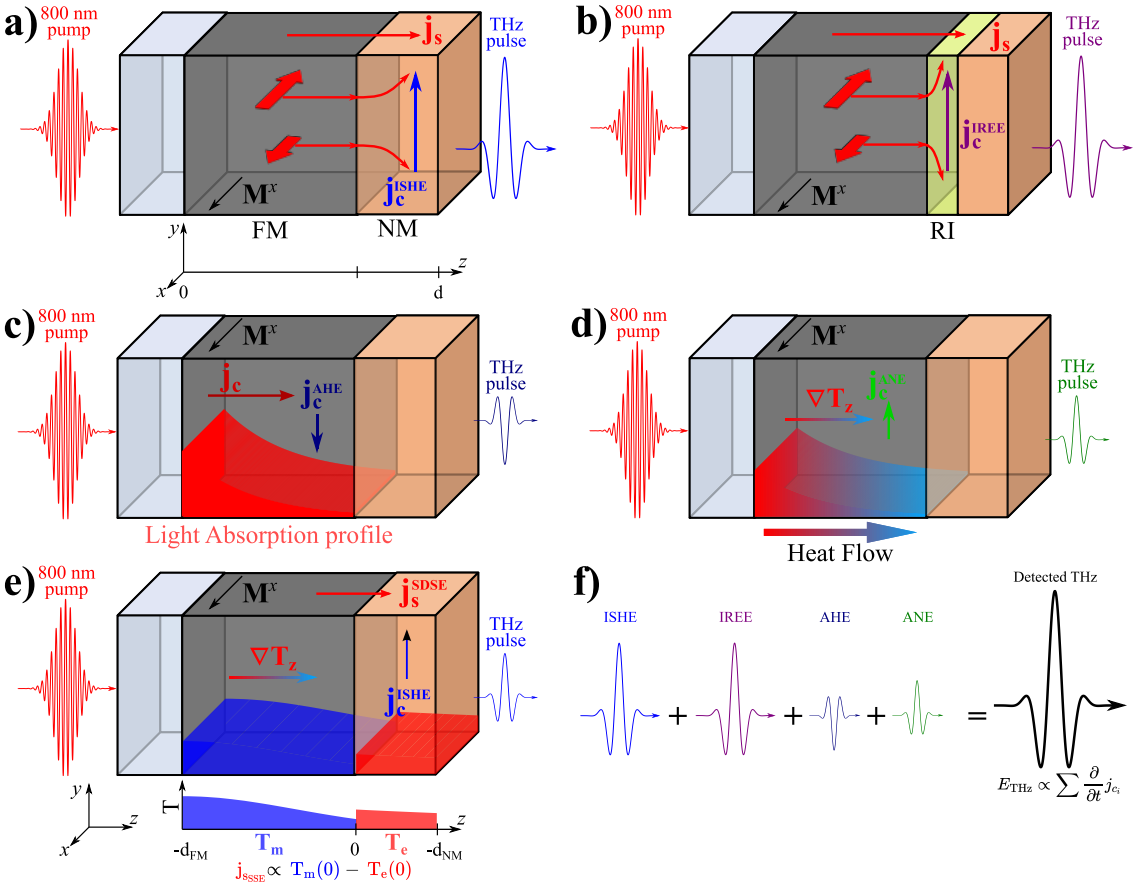

a) Inverse Spin Hall effect (ISHE) driven THz emission. The spin current generated upon photoexcitation of the Ferromagnetic (FM) layer gets injected into the Non-Magnetic (NM) layer with strong SOI, where it gets converted into the transverse charge current $\boldsymbol{j}_c^{ISHE} \propto \boldsymbol{j}_s \times \boldsymbol{M}$.
b) Inverse Rashba-Edelstein effect (IREE). Spin-polarized current that arrives at the Rashba-split interface (RI) will produce the transverse spin-polarized current due to the uneven displacement of the Rashba contours $\boldsymbol{j}_c^{IREE} \propto \boldsymbol{j}_s \times \boldsymbol{M}$.
c) Anomalous Hall Effect (AHE). The initial light absorption profile established in the FM layer upon laser irradiation can create the flow of the hot carriers in the bulk of the FM layer. The longitudinal charge current flow is then converted to the transverse charge current $\boldsymbol{j}_c^{AHE} \propto \boldsymbol{j}_c \times \boldsymbol{M}$.
d) Anomalous Nernst Effect (ANE). The temperature gradient ∇T established by the inhomogeneous light absorption and the different heat transport properties at the interfaces may establish non-equivalent charge distribution along ∇T direction. The resulting transverse current generated within FM is then given by $\boldsymbol{j}_c^{ANE} \propto \nabla T \times \boldsymbol{M}$.
e) Spin-dependent Seebeck effect (SDSE). The spins are pumped into the NM layer due to the difference in the magnon T_m and electron T_e temperatures. Then, the spin-current arriving into NM layer can be written as $\boldsymbol{j}_s^{SDSE} \propto \delta T_{me}$. As a result, THz can be emitted via ISHE conversion taking place within NM layer, for example.
f) In the case when all conversion mechanisms are permitted, the detected THz radiation will be the sum of all contributions. The signs of all THz waveform are arbitrary.

Figure 4.10 – *Possible contributions to the THz emission, originating from the different ultrafast spin-to-charge conversion mechanisms.*

transport of the hot electrons [236,237]. This model describes the competition between the diffusive and ballistic transport of the spin-polarized carriers at the fs timescale. Recent publications on

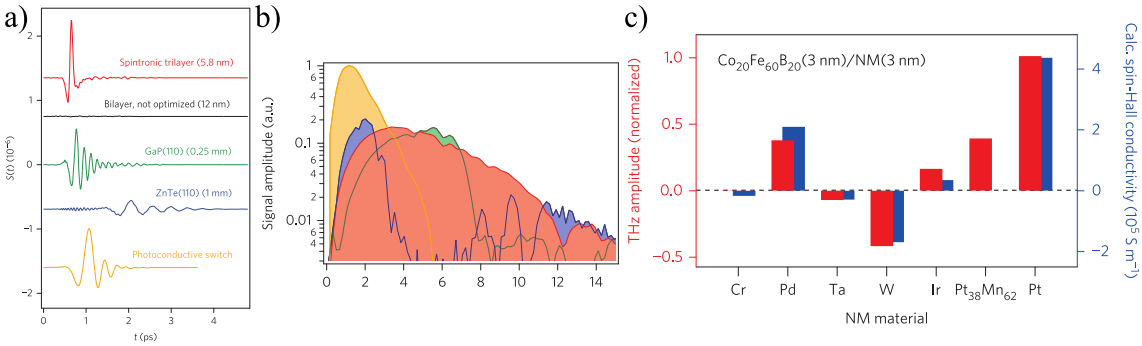

a) Terahertz signal waveforms and **b)** resulting amplitude spectra of the spintronic trilayer emitter in comparison to standard terahertz emitters. **c)** Terahertz signal amplitude (r.m.s.) as a function of the NM material used for the $Co_{20}Fe_{60}B_{20}$(3 nm)/NM(3 nm) stack (red bars) vs *ab initio* calculated values of the spin-Hall conductivity (blue bars). From [242]

Figure 4.11 – *ISHE based emitters: Efficiency and comparison to conventional THz sources.*

THz spintronic emitters use the superdiffusive spin model to compare the experimental data with Finite-difference time-domain simulations of the excited spin currents via femtosecond laser action [238,239]. As a result, the bipolar shape of the emitted THz pulse is explained by the superdiffusive transport and multiple carrier reflections within the magnetic heterostructure [240, 241].

ISHE-driven THz emission

In 2013, Kampfrath et al. reported the THz emission from FM metal/Metal heterostructures, such as Fe/Au and Fe/Ru [3]. They demonstrated that the polarity of the emitted $E_{\mathrm{THz}}(t)$ depends on the sign of the Spin-Hall angle θ_{SHE} and on the $\boldsymbol{H}$ direction. Furthermore, they show the influence of carrier mobility in Au and Ru on the amplitude and bandwidth of the detected THz radiation. Moreover, T.H. Dang et al. combined both FMR and THz-TDS to address the importance of the material-dependent electron transport properties and spin-dynamics on the spin-to-charge conversion [238].

Later, Seifert et al. studied the ISHE-driven emission from more than 70 FM/NM bilayer configurations [242]. They compared the bandwidth of the spintronic THz emitters (STE) to conventional OR- and photoconductive-based THz sources, as shown in Fig.4.11a and b. In the follow-up paper, they show the generation of the THz pulses with a peak amplitude of about $300\,\mathrm{kV\,cm^{-1}}$, achieved by the upsizing of the magnetic trilayer, made from the FM "sandwiched" between two HM layers with opposite θ_{SHE}. In addition, combining THz-emission and THz-TDS experiments, the THz conductivity and spin-diffusion length λ_s in Pt, W, Cu in pair with the magnitude and sign of the spin Hall angle θ_{SHE} were estimated [100, 243, 244].

Furthermore, various groups reported THz emission from stacked STEs [245], address the influence of the sample annealing on the detected THz waveform [246, 247], interface roughness [248], and temperature dependence on the ISHE conversion efficiency [249]. In addition, one can controll the THz emission from FM/HM bilayers depending on the sample geometrical orientation [250,251], and even by changing the type of the sample substrate [242, 243, 252].

Ultrafast SSE spin current injection

Seifert et al. reported the injection of ultrafast spin current from the FM insulator into HM via the SSE [253]. They note that the spin current injection is mediated by the thermal non-equilibrium between the electron and magnon baths in HM and FM insulators, respectively. The bandwidth of the THz-SSE was then attributed to the electron-phonon coupling speed, the few hundreds of femtoseconds after the laser excitation.

AHE-driven THz emission

Zhang et al. report that the THz emission can occur via AHE in the FM films with a thickness of less than 20 nm [235, 254]. In total, they measure the THz emission from four different FM/MgO(4 nm) bilayers on the Quartz substrate. They claim that the charge gradient established within the FM is governed by the back-flow charge current, created by non-equal hot-carrier reflectance at the interfaces:

$$j_c \propto \theta_{AHE}[r_1 - r_2], \tag{4.26}$$

where r_1 and r_2 are the different hot-electron reflection coefficients at the Substrate/FM and FM/NM interfaces, respectively. For the case when $r_1 \neq r_2$, in the thin FM layer with homogeneous light-absorption profile, the change in the geometrical orientation of the sample should lead to the THz polarity reversal. Their model explains the THz polarity flip when STE is excited from the side of the substrate or MgO layer but does not explain the absence of the sign-reversal in the thick samples. In addition, they performed an experiment where they vary the Pt concentration along with the FM layer, which resulted in the amplification of the THz emission or even to the reversal of the polarity of the emitted THz.

The two-current model proposed by Zhang et.al. does not include the effect of the substrate (Quartz) and the capping layer (MgO) on the Pt distribution in the FM layer, which may lead to the accumulation of Pt with a higher concentration close to the given interface or affect the distance between the scattering centers [255, 256]. Such interface-sensitive Pt buffer may amplify the charge current generation, and introduce the sample asymmetry, which could explain the THz polarity reversal in the thin samples observed by the authors [235]. In addition, they do not address the possible existence of the Rashba interface created at the FM/insulator interface [4, 257].

IREE-mediated THz emission

As of today, there are couple of papers speaking of an ultrafast spin-to-charge conversion via the IREE at the Ag/Bi interface [234, 258]. The authors demonstrate the importance of the Ag/Bi stacking order and discuss the possible contribution of ISHE in Bi. Both works stress that they measure the superposition of the THz emitted via IREE and ISHE. However, the reported efficiency of the THz emission with the IREE is about 50 times smaller than the one achieved with Pt-based ISHE emitters.

Importantly, for the Ag/Bi interface where the IREE leads to the THz emission, the phase of the emitted THz pulse depends on the Ag/Bi layer ordering, which should be equivalent to changing of the sample geometrical orientation [258]. As seen from Fig.4.12, the detected THz pulse is the sum or difference of the IREE contributions occurring at the Ag/Bi interface and

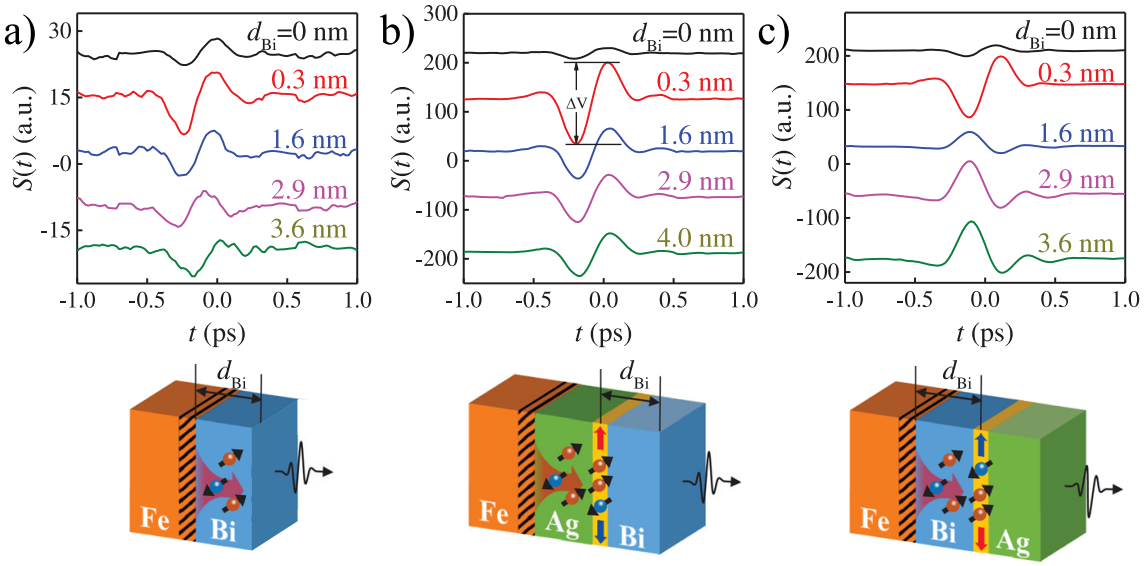

The time-domain THz signals at different Bi thickness for **a)** Fe(2)/Bi(wedge), **b)** Fe(2)/Ag(2)/Bi(wedge), and **b)** Fe(2)/Bi(wedge)/Ag(2) respectively. The number inside each pair of brackets indicates the corresponding film thickness. The difference in the phase of the emitted THz and non-zero signal from the bare Bi wedge sample shows the importance of the interface stacking ordering and the composite nature of the detected THz. Redrawn from [258].

Figure 4.12 – *THz emission from the Inverse Rashba Edelstein Effect (IREE) at the Bi/Ag interface.*

ISHE contribution from Bi. Later, experimental work of Vetter et al. suggests this orientation-dependent superposition model of the two possible spin-to-charge conversion mechanisms [257].

Additionally, the Schottky barrier may explain the enhancement of the THz emission at the FM/Semiconductor interface due to the difference in the FM and semiconductor work functions [257]. This may establish a "stray" electric field, leading to the Rashba splitting at the FM/semiconductor interface. As a result, they find that the THz generation efficiency heavily depends on semiconductor doping, opening the way to the IREE emitter optimization.

Demagnetization-driven THz emission (DMG)

Back in 2004, E. Beaurepaire et al. reported the emission of the THz radiation by the ultrafast demagnetization (DMG) of the Cr(3 nm)/Ni(4.2 nm)/Cr(7 nm) film [259]. They suggested that the emitted THz electric field, polarized along the y axis and propagating along the z direction, is proportional to the second time derivative of the ultrafast demagnetization:

$$E^y(t) \propto \frac{\mu_0}{4\pi^2 r} \frac{\partial^2 \boldsymbol{M}^x}{\partial t^2}(t - r/c), \tag{4.27}$$

where r is the distance to the magnetic dipole. However, they stress that this is only a phenomenological model, and it is far too simple and does not describe all the mechanisms related to the ultrafast spin dynamics.

A recent paper of W. Zhang et al. shows that one can access the ultrafast demagnetization dynamics from the THz emission experiments [260]. Furthermore, they stress the phenomenological nature of the DMG and conclude that the THz emission from the MgO/Fe(10 nm)/MgO comes

from ultrafast demagnetization in Fe. Importantly, they say that THz emission from single-layer ferromagnet could have a contribution of the coherent-phonon driven magneto-elastic effect.

From this brief literature overview, we see that there are many reports on different spin-to-charge (SCC) mechanisms at the ultrafast timescale. Therefore, the dominant mechanism of the SCC may vary depending on the sample orientation, the choice of FM metal/insulator and/or the capping layer. As a result, it might not be so straightforward to address and study the SCC conversion mechanism of interest. Therefore, in the next section, we will to propose a way how to experimentally identify the different contributions to the ultrafast SCC in CoFeB/MgO magnetic bilayers. At the end, we will compare the THz emission from the CoFeB/MgO samples and conventional CoFeB/Pt STEs.

4.3 Experimental results

Sample choice: In this section, we measure the THz emission from the MgO-based spintronic emitters and compare the results to the well-known CoFeB/Pt samples. Here, we are interested in the efficiencies of the injection-based IREE (CoFeB/MgO), ISHE (CoFeB/Pt), and bulk (CoFeB) SCC mechanisms at the sub-picosecond timescales. Furthermore, we will try to identify the different driving mechanisms of the SCC based on the sample experimental geometry, pump-fluence dependence, and the influence of the pump wavelength on the THz emission. Consequently, we discuss THz emission from four different STEs: CoFeB(5)/Pt(3), CoFeB(20)/Pt(3), CoFeB(5)/MgO(6) and CoFeB(20)/MgO(6) on the SiO_2 and Si substrates, where number in the parentheses is the thickness of the preceding layer in nm.

We chose the CoFeB layer with an equivalence ratio of $Co_{40}/Fe_{40}/B_{20}$ due to the highest reported efficiency of the THz emission [242] in pair with already measured THz conductivity [100].The capping layers, namely 3 nm of Pt and 6 nm of MgO were grown on top of the CoFeB in the same sputtering chamber. Pt layer was chosen as the "reference" since it is the most efficient spin-to-charge converting HM, and it is well characterized both in DC and at the picosecond timescale. As mentioned in the introduction, the deposition of MgO on top of the CoFeB layer creates the Rashba states inside the FM metal close to CoFeB/MgO interface [4]. All the samples were grown at the Condensed Matter Physics laboratory of IRAMIS (Saclay Institute for Radiation and Matter) by J.B. Moussy, A. Solignac, J.Y. Chauleau, and M Viret.

Experimental details: The experiments were performed with the 1 kHz 165 fs amplified laser, operating at the central wavelength of 800 nm. The output laser beam was split 90/10, where 90% of the laser power was used to pump the STE, while the remaining 10% used for electrooptic detection.

STE with the size of 0.5 mm × 0.5 mm was fixed in the sample holder with a hole of ≈ 0.45 mm in diameter. Unfocused pump beam with the ≈ 0.48 mm beam diameter at FWHM was incident normal to the surface of the STE. The THz pulse, emitted along with the pump direction, was separated with the combination of two two-millimeter thick HDPE sheets followed by the half-millimeter thick silicon wafer. The THz beam was then focused with one-inch gold, unprotected off-axis parabolic mirror (OAPM) with a six-inch focal length. The lateral position of the sample relative to the OAPM remained fixed through the experiment. The emitted THz was recorded with

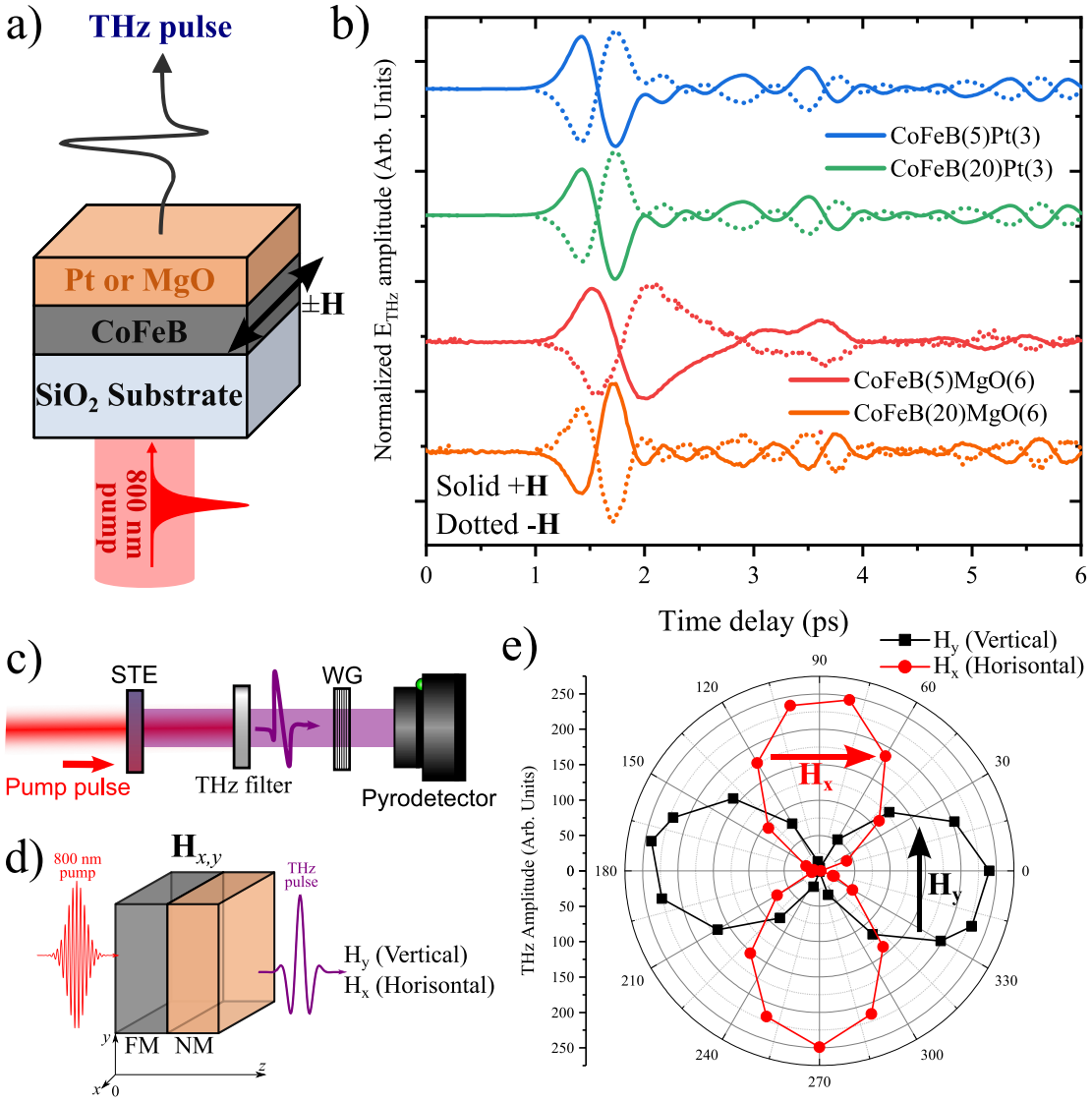

a) Experimental configuration, where the pump beam is incident from the side of the SiO_2 substrate. **b)** Detected THz signals, for the + (solid line) and − (dotted line) direction of the applied external magnetic field $\boldsymbol{H}$, where the number in parentheses corresponds to the thickness in nm of the preceding layer. **c)** THz polarization characterization setup. For a fixed direction of the external magnetic field **H** THz power is measured as a function of the Wire-Grid polarizer (WG) angle. **d)** Experimental geometry, displaying two orthogonal orientations of **H**. **e)** CoFeB(5)/Pt(3): THz power measured for the Vertical and Horizontal orientation of external applied **H**, with the setup shown in c). The polarization of the emitted THz is always perpendicular to the direction of the applied direction of **H**. The same behavior is observed for all samples.

Figure 4.13 – *Pt and MgO samples: Terahertz emission - External Magnetic field dependence.*

the EOS technique, discussed in the Section 2.4. The probe beam intensity was kept below the two-photon absorption limit of ZnTe, in pair with the constant optical power seen by the balanced photodiodes. In our experiment, the direction of the external magnetic field $\boldsymbol{H}$ was controlled by the pair of magnets introduced into the rotating sample holder, to insure the homogeneous magnetic field distribution across the sample. The applied magnetic field strength is in the order of 0.2 T, enough to saturate the CoFeB magnetization.

External magnetic field dependence and polarization of the emitted THz radiation

As the first experiment, we check the magnetic origin of the THz emission. For this, we install the samples (CoFeB covered either with Pt or MgO) in the sample holder with the two magnets, such as the pump beam first hits the substrate, as shown in Fig.4.13a. The emitted THz was then recorded for two opposite orientations of the external magnetic field $\pm\boldsymbol{H}$, shown in Fig.4.13b (solid and dotted lines). Figure 4.13b shows that all samples are sensitive to the direction of $\boldsymbol{H}$, and 180° rotation of $\boldsymbol{H}$ in the xy-plane leads to the complete polarity reversal of the emitted THz. We should note the slight difference in the emitted THz amplitude (up to 5 %) between waveforms recorded for $\pm\boldsymbol{H}$ that can be attributed to the manual rotation of the magnets.

In addition, we have measured the polarization of the THz emitted from the CoFeB(5)/Pt(3) sample, using the pyroelectric detector and a Wire Grid (WG) polarizer, as shown in Fig.4.13c. For two orientations of the external magnetic field $\boldsymbol{H}$ (displayed in Fig.4.13d), we find that the THz polarization is linear and perpendicular to the direction of the external magnetic field (see Fig.4.13e), in perfect agreement with previously published results [3]. Furthermore, the THz polarization of the CoFeB(20)/Pt(3) and CoFeB(5 or 20)/MgO(6) bilayer is linear and follows the same tendency.

Sample geometry-dependent THz emission

Next, we study the THz emission from the CoFeB(Pt or MgO) heterostructures within two different geometrical sample orientations: we define the Front Face sample orientation when the pump beam is incident from the side of the substrate, while the excitation from the nonmagnetic layer will be called the Back Face configuration, with the two displayed in Figure 4.14a. For the fixed laser pump fluence Φ, Figure 4.14b shows E_{THz} waveform, emitted in the Front Face (color) and Back Face (grey) experimental configurations. The Front Face signals were normalized to the peak-to-peak amplitude of the CoFeB(5)/Pt(3) emitter (blue line), with a scaling factor mentioned above respective signal in Fig.4.14b. First, we observe the additional temporal delay for the THz emitted in the Back Face related to the emitted THz pulse propagation through glass. In addition, the broadening of the THz waveform in the Back configuration occurs due to the frequency-dependent glass THz absorption (see Section 2.4). The same effect was already observed before [243, 261, 262]. Nevertheless, we report THz polarity reversal as a function of the sample orientation (color vs. grey line) for all the samples presented in Figure 4.14b, except for the CoFeB(20)/MgO(6).

To measure the undistorted THz waveform in the Back Face geometrical orientation, the samples were grown on the high-resistivity, float-zone silicone (Si) substrate. The pump fluence was then adjusted to equalize the absorbed density of energy in the CoFeB layer to the Front Face excitation [1]. All signals were normalized to the peak-to-peak amplitude of the CoFeB(5)/Pt(3) bilayer in the Front Face orientation. The Figure 4.14c shows a complete reversal of the CoFeB(5)/Pt(3) and CoFeB(20)/Pt(3) THz waveforms upon the sample flip around the y-axis. Such change in the THz polarity upon the flip of the ISHE emitter has been reported numerous times [242,245,262,263].

1. Calculated with the Transfer Matrix Method. The light absorption profiles are shown in the Appendix C.

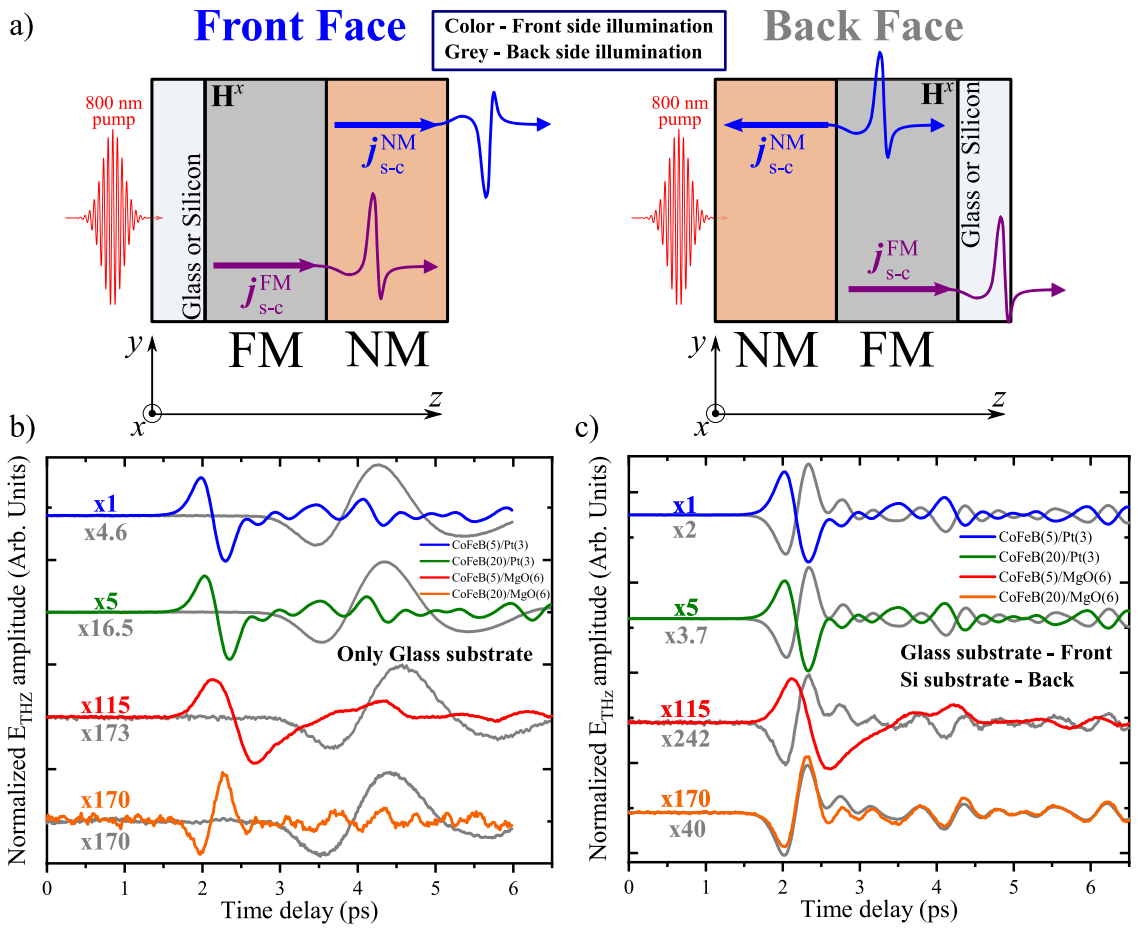

a). Schema of the geometry-dependent THz emission experiment. Front Face configuration denotes when the sample is excited from the side of the substrate and vice-versa for the Back Face. The sample rotation by 180° around the y-axis (or x) should only affect the direction of the injected spin-polarized current, $\boldsymbol{j}_{s-c}^{NM}$. **b)** THz signal measured in the Front (color) and Back (gray) face configurations for all samples deposited on the Glass substrate. **c)** The geometry-dependent THz emission in the Front (color, glass substrate) and Back (gray, Si substrate) configuration for all samples in the study. The number is the scaling factor used to normalize the signal to the CoFeB(5)/Pt(3) emitter peak-to-peak amplitude.

Figure 4.14 – *Spintronic emitters: Sample orientation-dependent THz emission.*

Remarkably, Figure 4.14c shows the CoFeB thickness dependent behaviour for the MgO-based bilayers (orange and red lines). Here, the Back and Front Face excitation of the CoFeB(5)/MgO(6) sample results in the THz polarity reversal (superimposed red and grey lines in Figure 4.14c). This change can not be attributed to the influence of the Si substrate, since THz waveforms detected from the reference CoFeB/Pt emitters behave as expected. Surprisingly, the polarity of the THz emitted from the CoFeB(20)/MgO(6) bilayer (superimposed orange and grey lines in Figure 4.14c) does not change upon the sample flip. Finally, despite the absence of the THz waveform reversal, the CoFeB(20)/MgO(6) emitter is more than four times more efficient in the Back Face configuration (see the orange and grey factors in Fig.4.14c). We stress that all scaling factors presented in the Figures 4.14b and c are given as is, without accounting for the THz glass or photoexcited Si substrate E_{THz} amplitude attenuation factor (see Appendix F). In addition, the substrate pressence in the path of the THz pulse has no influence on the THz polarity of transmitted THz waveform.

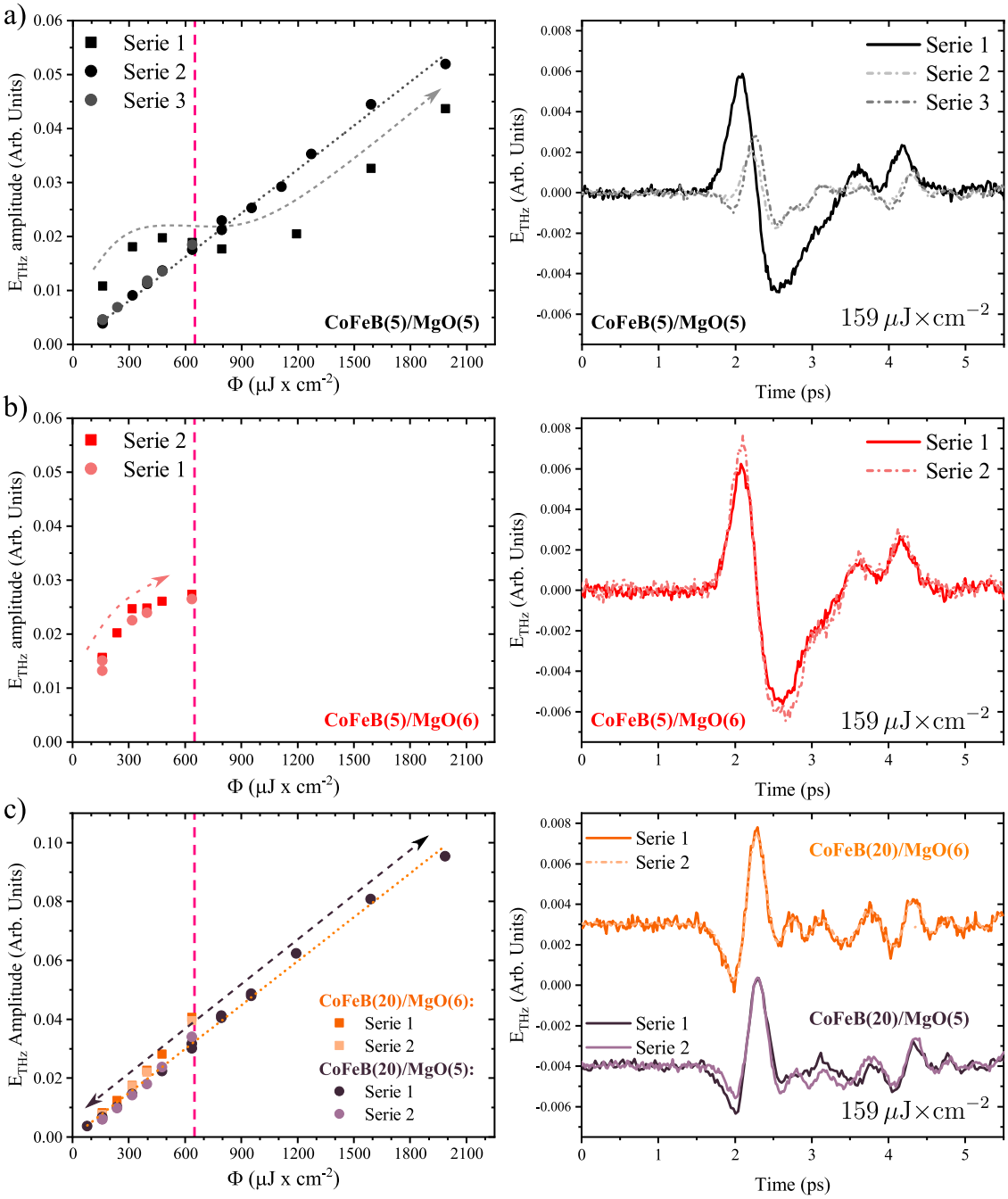

The emitted E_{THz} amplitude - 800 nm pump fluence dependence of the **a)** CoFeB(5)/MgO(5), **b)** CoFeB(5)/MgO(6) and **c)** CoFeB(20)/MgO(5 and 6) samples. Corresponding right figure shows the THz emitted at 159 μJ cm^{-2} for different sets of measurements. Dashed pink line at $\Phi = 650\,\mu\mathrm{J\,cm^{-2}}$ marks the threshold of the "high-Φ" regime. Arrows indicate the direction of the pump fluence increase.

Figure 4.15 – *CoFeB/MgO: Laser pump fluence dependence.*

CoFeB/MgO pump fluence dependence

In this subsection, we present the pump fluence dependence of the CoFeB/MgO samples, when the data for the CoFeB/Pt emitters is presented in the Appendix D. Here, we introduce the "control" samples CoFeB(5)/MgO(5) and CoFeB(20)/MgO(5), that were grown in the different batch and behave the same as their CoFeB/MgO(6) counterpart. The direction of the external magnetic field $\boldsymbol{H}$ and sample orientation (Front Face) was kept fixed through the experiment.

The first experiment was conducted for the "control" CoFeB(5)/MgO(5) bilayer grown on the glass substrate. All the experiments are performed as independent sets of measurements, denoted "Series". The Figure 4.15a shows that within Serie 1 measurement, the E_{THz} amplitude - laser pump fluence (Φ) dependence of CoFeB(5)/MgO(5) sample evolves in a highly nonlinear manner. In addition, from Figure 4.15a we see the presence of a turning point of E_{THz}-pump Φ dependence at the $\Phi_{crit} \approx 650\,\mu\mathrm{J\,cm^{-2}}$ (the dashed pink line). Surprisingly, the Serie 2 and Serie 3 measurements of CoFeB(5)/MgO(5) emitter show clear linear E_{THz} dependence as the function of Φ (see Fig.4.15a). In addition, the right panel of Fig.4.15a displays the complete change in the THz waveform and polarity between the Series 1 and Series 2, while the shape of the detected E_{THz} between Serie 2 and Serie 3 experiments remains unchanged. This indeed indicates that we have permanently modified the CoFeB(5)/MgO(5) emitter after it was exposed to Φ_{crit}. For the future refference, we will denote the "after Serie 1" state of this sample as CoFeB(5)/MgO(5)*.

As the next step, we measured laser pump fluence dependence for the CoFeB(5)/MgO(6) emitter, up to the pump laser fluence $\Phi_{crit} \approx 650\,\mu\mathrm{J\,cm^{-2}}$. From Fig.4.15b, we report the nonlinear increase in the E_{THz} amplitude as the function of Φ, already seen for the Serie 1 CoFeB(5)/MgO(5) sample measurement. The panels of Fig.4.15b shows that both E_{THz}-pump Φ dependence and THz waveform of CoFeB(5)/MgO(6) measured within Serie 1 and Serie 2 experiment remains mostly unchanged, which confirms the existence of the "threshold" effect above Φ_{crit}.

The last E_{THz} amplitude-Φ dependence was measured for the CoFeB(20)/MgO(5) and CoFeB(20)/MgO(6) samples. Here, only the CoFeB(20)/MgO(5) bilayer was measured above the threshold Φ_{crit}, while CoFeB(20)/MgO(6) was studied with $\Phi < 650\,\mu\mathrm{J\,cm^{-2}}$ range. As we see from the Figure 4.15c, both CoFeB(20)/MgO(5) and CoFeB(20)/MgO(6) samples show clear linear E_{THz} amplitude-pump Φ dependence. In addition, the right panel of Figure 4.15c (dark violet and light violet curves) shows no significant change in the polarity and the waveform of CoFeB(20)/MgO(5), even after Φ_{crit} exposure. The CoFeB(20)/MgO(6) emitter (solid and dash-dot lines in the left panel of Fig.4.15c) remains perfectly intact and unchanged between the Serie 1 and Serie 2 experiments. Therefore, we conclude that CoFeB(20)-based samples seem not to be affected by the high-laser fluence.

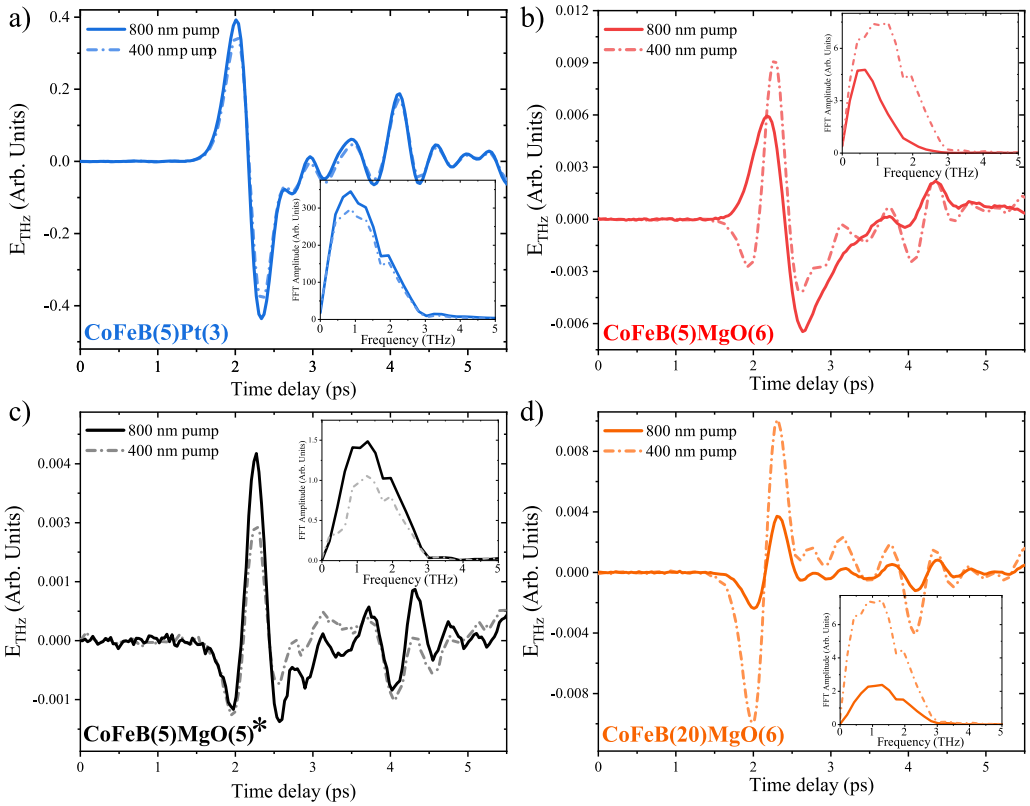

THz waveform emitted from the **a)** CoFeB(5)Pt(3), **b)** CoFeB(5)MgO(6), **c)** CoFeB(5)MgO(5)*, and **d)** CoFeB(20)MgO(6) samples. All samples were excited at the fixed pump fluence at 800 nm (solid line) and at 400 nm (dash-dot line). * star indicates that the sample was exposed to the high laser fluence $\Phi > \Phi_{crit}$.

Figure 4.16 – *Influence of the pumping wavelength on the THz emission.*

Influence of the pump wavelength on the THz emission

As the last experiment, we study the influence of the pump wavelength on the THz emission from the CoFeB/MgO samples and the reference CoFeB(5)/Pt(3) emitter. For this experiment, we have set pump fluence to the fixed value of 159 µJ cm^{-2} for two different pump wavelengths (800 nm and 400 nm). The absorbed optical density of energy was estimated to differ only within ±10 % margin for the two pump wavelengths. The direction of the external magnetic field $\boldsymbol{H}$ and sample orientation (Front Face) was kept fixed through the experiment.

As the first benchmark, we compare 800 nm (solid line) and 400 nm wavelength (dash-dot line) excitation of the CoFeB(5)/Pt(3) emitter, shown in the Figure 4.16a. For this ISHE-based STE, we do not observe a significant change in the shape, spectrum, and amplitude of the emitted E_{THz}. This observation is in good agreement with the literature [264, 265].

As the next test, the same experiment was conducted for the CoFeB(5)/MgO(6) sample, and is displayed in the Fig.4.16b. We note drastic change in the detected THz spectrum for this emitter (see inset of Fig.4.16b) which results in more broadband THz emission, in contrast with CoFeB(5)/Pt(3). In addition, CoFeB(5)/MgO(6) excited at 400 nm wavelength leads to the complete reversal of THz polarity. We should note, that this behaviour is completely reversible, and sample is not modified in the process. Furthermore, the same experiment was performed for

CoFeB(5)/MgO(5)* [2] and is shown in Figure 4.16c. Interestingly, CoFeB(5)/MgO(5)* does not seem to be affected by the change of the pump wavelength, similarly to CoFeB(5)/Pt(3).

Finally, the pump wavelength dependence measured for the CoFeB(20)/MgO(6) is shown in Fig4.16d. Again, this sample behaves differently from the CoFeB(5)/MgO(6) bilayer. Figure 4.16d demonstrates that CoFeB(20)/MgO(6) excited at 400 nm wavelength does not show the modification in the polarity and spectral components of emitted THz radiation, but results in the three-fold increase of the E_{THz} amplitude.

4.4 Discussion

First off all, we will speak about the "prototypical" ISHE-based emitters, i.e., the conventional CoFeB(5 and 20)/Pt(3) bilayers. We observe that the THz emission from CoFeB(5 and 20)/Pt(3) samples is affected by the external magnetic field orientation and is polarized perpendicular to the direction of external magnetic field $\boldsymbol{H}$ (see Figs.4.13b and e). Next, Figures 4.14b and c demonstrate the THz waveform polarity reversal when bilayer is excited from the side of the substrate (Front Face) or from the side of the Pt capping layer (Back Face). Finally, we find that THz emission from CoFeB(5)/Pt(3) is not affected by the change of the pump wavelength, as seen from Figure 4.16a. All these observations are in perfect agreement with previously published results [3, 242, 264, 265].

For the novel samples in this study, i.e., CoFeB/MgO bilayers, we find that the polarity of the emitted THz is sensitive and perpendicular to $\boldsymbol{H}$ (see Fig.4.13e), similarly to CoFeB/Pt emitters. However, for the geometry, pump fluence Φ, and pump wavelength measurements, the CoFeB/MgO emitters behave differently depending on the CoFeB thickness. For example, Figures 4.14b and c demonstrate that THz polarity reversal between the Back and Front Face bilayer orientation was observed only for CoFeB(5)/MgO(6), while we report no change for CoFeB(20)/MgO(6) sample. In addition, the excitation of the CoFeB(5)/MgO(6) emitter at 400 nm, compared to 800 nm pump wavelength leads to the THz polarity reversal and broadening of the THz spectrum (see 4.16b). The excitation of the CoFeB(20)/MgO(6) results in the three times more important E_{THz} amplitudes, as depicted in Fig.4.16d. No E_{THz} polarity/spectrum modification was observed for this sample.

At last, pump Φ dependence has revealed the highly nonlinear increase in the emitted THz field amplitudes for the CoFeB(5)/MgO(6) bilayer (see Fig.4.15b), but clear linear dependence for CoFeB(20)/MgO(6) (Fig.4.15c). Moreover, Figure 4.15a reveals that the power dependence and E_{THz} waveform of the "control" CoFeB(5)/MgO(5) sample [3] could be altered when exposed to pump fluence $\Phi > 650\,\mu\mathrm{J\,cm^{-2}}$. In addition, the E_{THz} emitted from "modified" CoFeB(5)/MgO(5) sample is no longer sensitive to the change of the pump wavelength, as shown in the Figure 4.16c.

Based on the Section 4.2.5 discussion and Figure 4.10, multiple SCC mechanisms can contribute to the total detected E_{THz}, and can be split into two "categories": the one that originates from the SCC within the bulk of the FM metal (AHE and/or DMG, for example), and another emerging from the addition of the capping layer like Pt or MgO (ISHE and IREE, respectively). With this in mind, for two separate systems (CoFeB/Pt and CoFeB/MgO) this concept of combined THz

2. Reminder: star means the sample state after high-Φ exposure.
3. Which in its pristine condition was equivalent to CoFeB(5)/MgO(6).

emission can be phenomenologically formulated as:

$$\begin{cases} E^{tot}_{\mathrm{THz}}(\mathrm{CoFeB/MgO}) = \xi_{\mathrm{CoFeB}} \cdot E^{bulk}_{\mathrm{THz}} + \beta_{\mathrm{MgO}} \cdot E^{IREE}_{\mathrm{THz}}, \\ E^{tot}_{\mathrm{THz}}(\mathrm{CoFeB/Pt}) = \xi_{\mathrm{CoFeB}} \cdot E^{bulk}_{\mathrm{THz}} + \gamma_{\mathrm{Pt}} \cdot E^{ISHE}_{\mathrm{THz}}; \end{cases} \tag{4.28}$$

where ξ_{CoFeB} , β_{MgO} and γ_{Pt} are the phenomenological coefficients describing the SCC efficiency inside the bulk of the CoFeB (ξ_{CoFeB}), at the Rashba interface (β_{MgO}), and due to the ISHE within the Pt layer (γ_{Pt}). ξ_{CoFeB} is present in both CoFeB/Pt and CoFeB/MgO systems and can originate from DMG [259,266–268] and/or Anomalous Hall Effect (AHE) [44,269]. One should note that we neglect the possible existence of the Rashba interface at the CoFeB/Pt interface [239]. With this phenomenological formulation, we will proceed with the discussion about the sample geometry, pump fluence Φ and wavelength dependence, in order to evaluate the relative bulk and IREE contributions of CoFeB/MgO-based samples.

External magnetic field dependence: We now address why the direction of the external magnetic field $\boldsymbol{H}$ affects the polarization of the emitted THz radiation. Following the discussion of Section 4.2 and Eq.4.25, the direction of the converted transverse charge current ($\boldsymbol{j}_c$) is defined as the vector product between spin-polarized current flow ($\boldsymbol{j}^z_{c,s}$) and direction of the FM macroscopic magnetization ($\boldsymbol{M}$), defining the polarization of the spin current $\boldsymbol{\sigma}_s$ as:

$$\boldsymbol{j}_c(t) \propto \sum_i \boldsymbol{M}(t) \times \boldsymbol{j}^z_{c,s}(t), \tag{4.29}$$

where the sum over i represents all possible spin-to-charge (SCC) contributions to the transverse transient charge current $\boldsymbol{j}_c(t)$. From the latter equation, we see that the direction of generated $\boldsymbol{j}_c$ should be sensitive and perpendicular to $\boldsymbol{M}$. As the sample is subjected to an external magnetic field $\boldsymbol{H}$, its macroscopic magnetization $\boldsymbol{M}$ will be aligned parallel to $\boldsymbol{H}$. Therefore, from the Eq.4.29 the polarization of the emitted E_{THz} via SCC must be sensitive to $\boldsymbol{H}$ direction. As shown in the Figure 4.13b, the rotation of the $\boldsymbol{H}$ by 180° leads to the 180° THz polarity reversal for both CoFeB/Pt and CoFeB/MgO samples. This confirms the magnetic origin of the THz emission from CoFeB/MgO bilayers.

The following discussion will be split into two parts: first, we address the difference in the THz emission behavior from CoFeB(5)/MgO(6) and CoFeB(20)/MgO(6) emitters in the low-fluence regime, and in the second part we focus on the consequences of the permanent CoFeB(5)/MgO(5) sample modification.

Low-fluence regime (pristine samples):

This subsection deals only with the unchanged samples, i.e., that were not exposed to laser fluence above $\Phi_{crit} \approx 650\,\mu\mathrm{J\,cm^{-2}}$.

Sample geometry dependence: As the first step, we address the possible origin of the THz polarity reversal due to the different sample geometry. Since the IREE, as ISHE, is an injection-based SCC mechanism, the polarity of the emitted THz should depend on the $\boldsymbol{j}^z_{c,s}$ direction in respect to the Rashba interface. Consequently, the sample rotation around the y-axis will change

the direction of $\boldsymbol{j}^{z}_{c,s}$ ($\boldsymbol{j}^{z}_{c,s} \rightarrow \boldsymbol{j}^{-z}_{c,s}$, see Fig.4.14a) and, according to Eq.4.29 it will lead to the polarity reversal of the emitted THz field. This effect is well known for the ISHE-based emitters [242, 270], and an identical experiment conducted by Vetter et al. [257] (Front and Back Face pumping) on the n-GaN/NiFe bilayers IREE-based emitters. As seen from the Figure 4.14b and c, for the CoFeB(5)/MgO(6) STE we observe the complete E_{THz} polarity reversal between the Front Face and Back Face sample orientations (see red and grey curves). Hence, as a first element of conclusion, we can attribute the observed THz polarity reversal in CoFeB(5)/MgO(6) to the presence of the injection-based IREE SCC mechanism.

Now we discuss the symmetry of the bulk SCC contribution to the emitted THz. From the literature, it is well known that the efficiency of the injection-based ISHE emitters scales inversely with the FM layer thickness [245, 246, 251]. Moreover, for the Co films, Huang et al. demonstrated that the bulk SCC contribution increases with the FM layer thickness (i.e., $\xi_{\mathrm{Co(30\,nm)}} > \xi_{\mathrm{Co(5\,nm)}}$) to the point that the THz amplitudes detected from 30 nm Co are not affected by the deposition of the HM Tantalum ($\xi_{\mathrm{Co(30\,nm)}} > \gamma_{\mathrm{Ta}}$) [268]. The combination of these reports indicates that with an increase of the FM layer thickness, one should simultaneously increase the bulk contribution (ξ_{CoFeB}), while decreasing the injection-based SCC contribution (γ_{Pt} and β_{MgO}) to the total emitted E^{tot}_{THz}. This peculiar effect is usually attributed to the short hot-electron spin diffusion length in the CoFeB (in the order of couple of nm) [242, 251]. Since the THz emission from the bulk contribution (AHE, DMG, or combination of both) should be governed by the spin-polarized current flow inside the FM layer, its direction should not be altered upon the sample flip. As a result, the absence of the E_{THz} polarity reversal between Back and Front Face configurations should be a strong indication of the bulk-dominant SCC. Indeed, as shown in the Figure 4.14 (orange vs grey curves), we observe the absence of the E_{THz} polarity reversal between Back and Front Face configurations for the thick CoFeB(20)/MgO(6) sample. This means that the THz emission from CoFeB(20)/MgO(6) emitter is mainly governed by the bulk SCC (i.e. $\xi_{\mathrm{CoFeB(20)}} > \beta_{\mathrm{MgO}}$). It is worth to note that this argument does not hold when comparing CoFeB(5)/Pt(3) and CoFeB(20)/Pt(3) since $\xi_{\mathrm{CoFeB}} \ll \gamma_{\mathrm{Pt}}$, even for 20 nm thick CoFeB [251].

Laser pump fluence dependence: Let us now address the pump fluence Φ-E_{THz} amplitude dependence. From the CoFeB(5)/MgO(6) measurement, shown in Figure 4.15b, we see the clear nonlinear increase in the emitted THz field amplitudes as a function of Φ. This could be explained by the competition of bulk ξ_{CoFeB} and IREE β_{MgO} SCC mechanisms (see Eq.4.28) having opposite signs, and possibly different SCC pump fluence efficiencies. At the same time, for the CoFeB(20)/MgO(6) emitter, we measure linear $E_{\mathrm{THz}}(\Phi)$ dependence. Such linear behaviour, previously reported for the bare Co films [268] again confirms our suggestion that the THz emission from CoFeB(20)/MgO(6) is dominated by the SCC in the bulk of the CoFeB layer (i.e., $\xi_{\mathrm{CoFeB(20)}} > \beta_{\mathrm{MgO}}$). We do not expect the nonlinear behaviour from the bulk contribution since the pump-fluence dependent magnitude of the ultrafast demagnetization in the thin ferromagnetic layers is known to be linear for the fluence below $4\,\mathrm{mJ\,cm^{-2}}$ [271–273]. Regardless, time-resolved magneto-optical measurements for the set of CoFeB bilayers are to be measured in the future.

Laser pump wavelength dependence: From the Figure 4.16a we see that the change of the pump wavelength from 800 nm to 400 nm has no effect on the ISHE-based CoFeB(5)/Pt(3) emitter, as expected from the literature [264, 265]. The pump wavelength-independent THz emission from CoFeB(5)/Pt(3) can be attributed to the fact that spin-dependent electron deflection and scatter-

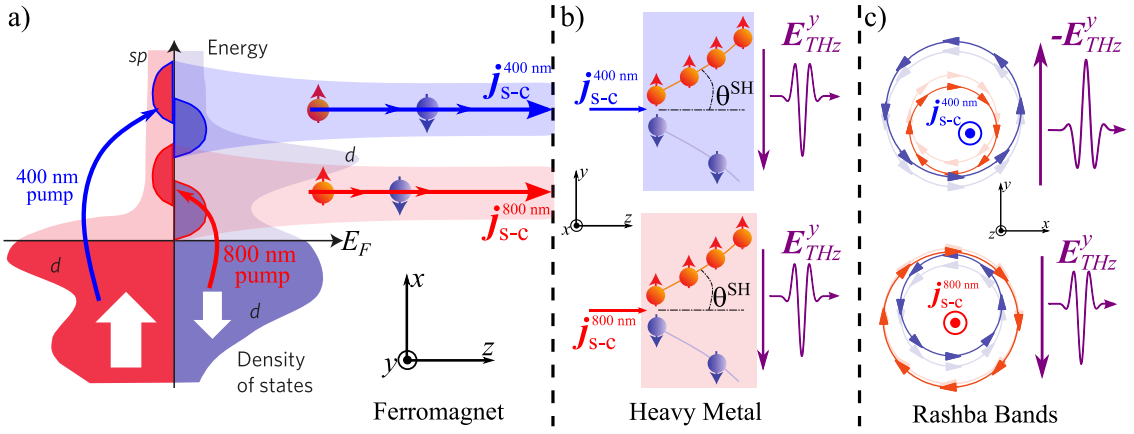

a) Sketch of the excitation with 800 nm and 400 nm pump wavelength. Supposedly, for the same amount of photoexcited carriers, the energy distribution of spin-polarized charge current will be higher for 400 nm pump. **b)** Since Inverse Spin-Hall efficiency in the heavy metal is mainly defined by the Spin-Hall angle (θ^{SH}), it should not be sensitive to the hot-carrier energy distribution, resulting in equivalent E_{THz} emission for 400 nm and 800 nm pump. **c)** For the Inverse Rashba Edelstein effect, the spin-polarized current with different energy hot-carrier energy distribution may couple to different Rashba bands, which may result in different spin-to-charge conversion efficiency or even change in the direction of the generated charge current j_c. Please note the change of axes between a), b) and c).

Figure 4.17 – *Sketch of the pump-wavelength dependent excitation: ISHE vs IREE.*

ing, governed by the spin-Hall angle (θ_{SHE}) depends solely on the hot electron velocities in heavy metal, which are only marginally modified by the change of the electron temperature above the Fermi level [274, 275]. This makes the ISHE-based emitters robust at all wavelength, as sketched in the Figure 4.17b. Furthermore, multiple reports mention that the demagnetization dynamics of ferromagnets at the sub-picosecond time scale should not depend on the pump wavelength, i.e. we assume that the ultrafast quenching of the magnetization ΔM should be constant for the same density of the absorbed energy [274–276].

On the other hand, theory predicts that the Rashba-splitting coefficient α_R, which defines the efficiency and sign of the IREE-based SCC, should depend on the electron energy distribution injected into the Rashba bands [4, 277, 278]. Hence, the IREE should be sensitive to the change of the pump laser wavelength creating different hot-carrier distribution (see Eq.4.15 and sketch in Fig.4.17c). With this in mind, we can establish the modified version of Eq.4.28, for both MgO and Pt-based samples as:

$$\begin{cases} E^{tot}_{\mathrm{THz}}(\mathrm{CoFeB/MgO}) = \xi_{\mathrm{CoFeB}} \cdot E^{bulk}_{\mathrm{THz}} + \beta_{\mathrm{MgO}}(\hbar\omega_p) \cdot E^{IREE}_{\mathrm{THz}}; \\ E^{tot}_{\mathrm{THz}}(\mathrm{CoFeB/Pt}) = \xi_{\mathrm{CoFeB}} \cdot E^{bulk}_{\mathrm{THz}} + \gamma_{\mathrm{Pt}} \cdot E^{ISHE}_{\mathrm{THz}}, \end{cases} \tag{4.30}$$

where we introduce the pump photon energy dependence $\hbar\omega_p$ of the IREE coefficient β_{MgO}. Indeed, for the 800 nm and 400 nm excitation of the CoFeB(5)/MgO(6) sample, Figure 4.16b shows the significant change in both the spectrum and polarity of the emitted THz pulse, which is a clear indication of IREE-based THz emission. One should note, that this interpretation is purely based on the measured change in the polarity and spectrum of the emitted E_{THz}, and we have no

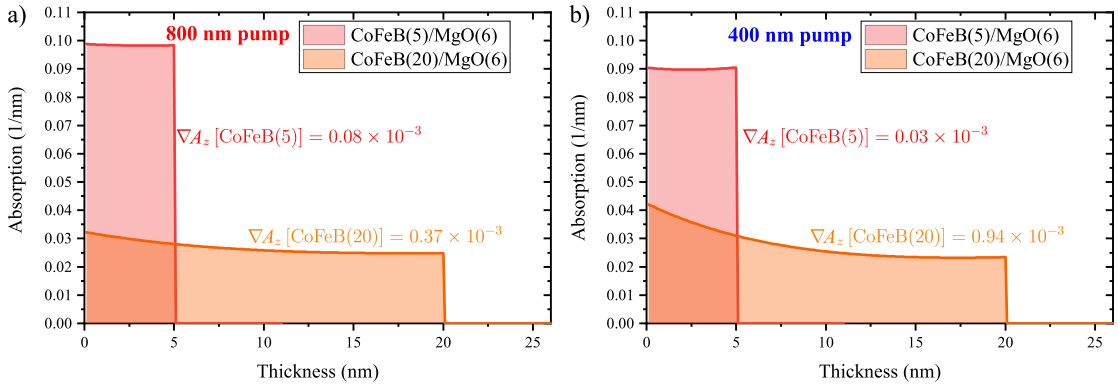

Figure 4.18 – *Light absorption profiles: in the CoFeB(5)/MgO(6) and CoFeB(20)/MgO(6) bilayers, in Front Face configuration on the Glass substrate, for 800 and 400 nm pump wavelengths.*

information about the electronic structure of the Rashba bands at the CoFeB/MgO interface. Moreover, multiple Rashba bands may simultaneously participate in the SCC, and laser light absorption may lead to electron-hole creation, furthermore modifying the ultrafast dynamics and efficiency of IREE-based THz emitter.

From the previous discussion, we concluded that the THz emission from CoFeB(20)/MgO(6) is mainly mediated by the bulk contribution ($\xi_{\mathrm{CoFeB(20)}} > \beta_{\mathrm{MgO}}$). However, for the same amount of the absorbed density of energy Figure 4.16d demonstrates no change in the THz polarity, but a three-fold increase in the E_{THz} amplitude when the sample is excited at 400 nm compared to 800 nm. We propose to explain this observation with the instantaneous hot-carrier flux/gradient inside the CoFeB, which should be important for the bulk spin-to-charge conversion, especially in thick single-layer FM films [259, 268]. Figure 4.18 shows the light absorption gradient calculated for both CoFeB(20)/MgO(6) (orange) and CoFeB(5)/MgO(6) (red) samples using the Transfer Matrix method [4]. The position 0 indicates the initial point of the laser impact. The average profile of the light absorption ∇A_z was then estimated using the following equation:

$$\nabla A_z = \frac{A_{\mathrm{abs}}(0) - A_{\mathrm{abs}}(d)}{d}, \tag{4.31}$$

where $A_{\mathrm{abs}}(0)$ and $A_{\mathrm{abs}}(d)$ are the fractions of the absorbed optical power at the beginning ($z = 0$) and the end of the FM layer ($z = d$). Importantly, for the CoFeB(20)/MgO(6) bilayer, the absorbed density of energy between 400 nm and 800 nm differs only by less than 10 %, while the ∇A_z has increased by the factor of 2.5. In this case, the three times increase in the E_{THz} observed for 400 nm excitation (see Fig.4.16d) may be directly linked to the 2.5 times more important light absorption gradient (see Fig.4.18) in the CoFeB layer. Even though such explanation does not contradict previous hypothesis of the bulk-dominant ultrafast SCC, it is yet to be confirmed with single-layer FM STEs with various thicknesses.

4. See Appendix C for more details.

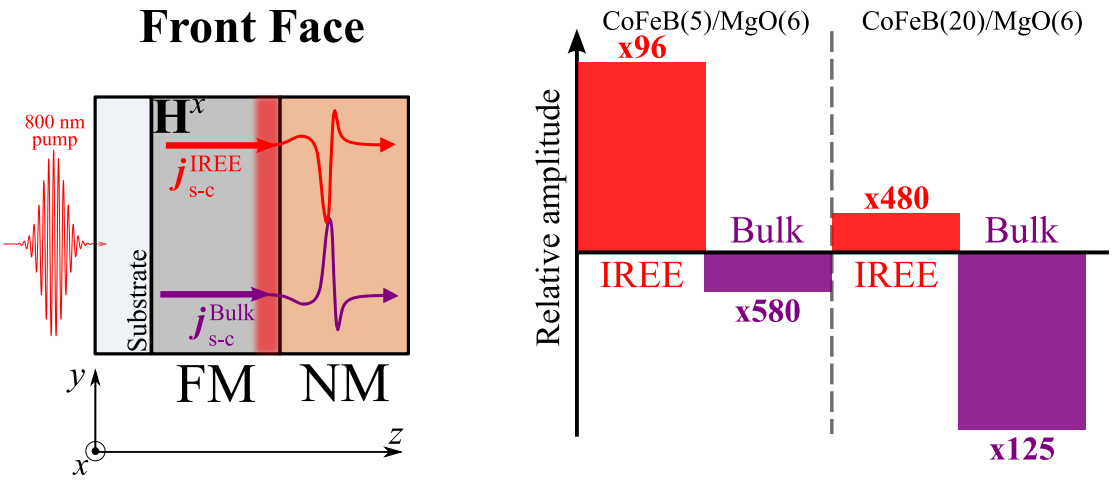

Left: Sketch of the injection-based IREE spin-to-charge conversion in the CoFeB/MgO emitters. Right: The relative amplitudes of the Inverse Rashba Edelstein (IREE) and bulk contributions to the THz emission from the CoFeB/MgO bilayers, estimated with Eq.4.32. Factors are the ratios between the peak-to-peak values of E_{THz} emitted from CoFeB(5)/Pt(3) and given contribution.

Figure 4.19 – *Sketch of the relative amplitudes of the IREE and bulk contributions to the emitted THz from CoFeB/MgO bilayers.*

Estimate of the bulk and IREE contributions: As the final step, we will make an attempt to evaluate the relative amplitudes of the IREE and bulk contributions to SCC from CoFeB/MgO emitters. To do so, we start with an estimate of the decrease in injection-based (ISHE, IREE) SCC related to the increase of the CoFeB thickness. From Fig.4.14b and c, we see that for the constant thickness of the Pt layer, the THz emission from the CoFeB(20)/Pt(3) bilayer is reduced by the factor of five when compared to CoFeB(5)/Pt(3) emitter (blue vs. green ratios). Such decrease in the total emitted THz can be attributed to the short spin-diffusion length in CoFeB [242, 251] and possible Fabry–Pérot cavity effect, that may enhance the THz emission due to the multiple pump and THz reflections at the CoFeB/Pt and substrate/CoFeB interfaces [242]. In this case, since $\gamma_{\mathrm{Pt}} \gg \xi_{\mathrm{CoFeB}}$, we can assign this five-fold decrease in THz emission to the reduced amount of the spin current injected in the HM Pt layer and diminished Fabry–Pérot for the thick CoFeB(20)/Pt(3) sample [251].

We then can use this factor to estimate the relative amplitudes of competing bulk and IREE contributions inside the CoFeB/MgO bilayers. Since the IREE-based conversion happens close to the CoFeB/MgO interface [4], we can assume the same five-fold decrease in IREE contribution for the CoFeB(20)/MgO(6) as was observed in CoFeB(20)/Pt(3). However, for the CoFeB/MgO emitters we cannot neglect bulk contribution so we have to account for the change in the light gradient absorption ∇A_z between CoFeB(20)/MgO(6) and CoFeB(5)/MgO(6) bilayers. From Figure 4.18a, for 800 nm pump wavelength we have calculated the factor of $0.37/0.08 = 4.625$, which reflects non-equal gradient of the light absorption in 5 and 20 nm of CoFeB. This 4.625 factor should correspond to the increase in the bulk contribution of CoFeB(20)/MgO(6) compared to CoFeB(5)/MgO(6), meaning $\xi_{\mathrm{CoFeB(20)}} \approx 4.625 \cdot \xi_{\mathrm{CoFeB(5)}}$. With this, the observed difference in the emitted THz amplitudes and polarities (see red and orange ratios from the Figure 4.14c) can be used to write the following linear system of equations (with arbitrary units, i.e., one can extract

	Sample geometry	Pump wavelength
CoFeB(5)/Pt(3)	Sensitive	Not sensitive
CoFeB(20)/Pt(3)	Sensitive	Not sensitive
CoFeB(5)/MgO(6)	Sensitive	Sensitive
CoFeB(20)/MgO(6)	Not sensitive	Sensitive
ISHE	Sensitive	Not sensitive
IREE	Sensitive	Sensitive
CoFeB bulk interconversion	Not sensitive	Not sensitive

Table 4.1 – *ISHE, Bulk, and IREE spin-to-charge conversion mechanisms sensitivity to the sample geometry and pump wavelength.*

only relative variations):

$$\begin{cases} \text{CoFeB(5)/MgO(6)} = -\xi_{\text{CoFeB(5)}} + \beta_{\text{MgO}}(\hbar\omega_p) = \dfrac{1}{115}; \\ \text{CoFeB(20)/MgO(6)} = -4.625 \cdot \xi_{\text{CoFeB(5)}} + 0.2 \cdot \beta_{\text{MgO}}(\hbar\omega_p) = -\dfrac{1}{170}. \end{cases} \tag{4.32}$$

Here, the minus sign corresponds to the opposite THz polarity of the bulk-dominant CoFeB(20)/MgO(6) sample compared to the CoFeB(5)/MgO(6) bilayer (see Fig.4.14c). Thus, solving this system of equations gives us the factors of roughly 96 and 580 for IREE and bulk SCC contributions, respectively. These factors, shown in Figure 4.19, correspond to the ratio between the peak-to-peak amplitude of the THz emitted from the refference CoFeB(5)/Pt(3) and the relative contribution to the THz measured from CoFeB/MgO bilayers. Please note that such rather "rough" subtraction can be performed only for the same experimental configuration, and it does not take into account any additional CoFeB thickness-related effects, apart from the change in ∇A_z.

Low-fluence regime summary: As a result of the previous subsection discussion, we find that the ultrafast IREE-driven THz emission from the CoFeB(5)/MgO(6) bilayers is roughly 96 times less efficient compared to the reference ISHE-based CoFeB(5)/Pt(3) emitter. These results are in stark contrast with the nearly-equivalent conversion efficiency of the quasi-DC FMR experiments [4], which again stresses the importance of the carriers energy distribution for the IREE mediated spin-to-charge conversion. In fact, the band structure-dependent IREE mechanism can be detrimental for the efficiency of the ultrafast spin-to-charge conversion, since most Rashba interfaces favor the conversion close to the Fermi level [4, 279, 280]. Therefore, one can expect a reduced efficiency from the hot electrons, mainly responsible for the ultrafast superdiffusive spin current transport. Within the 5 nm thick layer with a nearly homogeneous gradient of the light absorption, the energy distribution of the injected electrons carrying angular momentum is indeed highly nonlinear and band structure-dependent, and can be relatively broad and even structured [237, 281]. Hot-electron distribution was reported to spread up to about 1.5 eV from the Fermi level in the early stage of the optical excitation, with a typical center weight around 0.2 eV for thermalized carriers at relevant timescales [281]. In addition, several Rashba bands could simultaneously participate in the spin-to-charge conversion (as sketched in the Figure 4.17c), which may result in decreased efficiencies.

To conclude this part of the discussion, we present the Table 4.1, where we compare the sensitivity of the ISHE, bulk, and IREE conversion mechanisms on the sample geometrical orientation and pump wavelength. Therefore, we deduce that the THz emission from CoFeB(5)/MgO(6) bilayer is mainly mediated by the IREE mechanism. In contrast, the THz generation in CoFeB(20)/MgO(6) emitter mainly occurs via spin-charge conversion in the bulk of the CoFeB layer, and wavelength sensitivity is explained by more important FM light absorption gradient at 400 nm. The additional data on the CoFeB/Pt samples and power-dependence measurement for CoFeB/Pt and CoFeB/MgO on the Si substrate are presented in Appendix D and Appendix F, respectively.

High-fluence regime:

In this last subsection, we demonstrate that the delicate Rashba-split bands in CoFeB(5)/MgO(5) emitter could be modified or even destroyed at high laser fluence, leading to bulk-like THz emission. Here, we address the modification of the "test" CoFeB(5)/MgO(5) sample, when exposed to $\Phi > 650\,\mu J\,cm^{-2}$. As shown in Figure 4.15a, the pristine (Serie 1) CoFeB(5)/MgO(5) bilayer emits a similar waveform and has nonlinear pump-fluence dependence in $\Phi < 650\,\mu J\,cm^{-2}$ range, just as CoFeB(5)/MgO(6). However, when the CoFeB(5)/MgO(5) sample was exposed to $\Phi > 650\,\mu J\,cm^{-2}$, we observed the "threshold" effect, which resulted in a drastic change in both THz waveform and $E_{\mathrm{THz}}(\Phi)$ dependence (see Figs 4.15a, Serie 2 and Serie 3). Furthermore, the measured linear $E_{\mathrm{THz}}(\Phi)$ dependence for Serie 2 and Serie 3 measurements (see Fig.4.15a) suggests the irreversible sample modification.

We now compare the E_{THz} waveform emitted from CoFeB(5)/MgO(5) (black solid) and CoFeB(5)/MgO(5)* (black dash-dot), shown in the Figure 4.15a. For the convenience, the same data is displayed in the Figure 4.20b, and complemented with THz transients recorded for the Back and Front Face sample geometrical orientations. From the Figure 4.20b we see that the THz emission from CoFeB(5)/MgO(5)* bilayer is somewhat symmetric, as in the case of bulk-dominant CoFeB(20)/MgO(6) emitter. Moreover, as shown in the Figure 4.16c, CoFeB(5)/MgO(5)* sample 800 nm or 400 nm wavelength excitation shows no significant effect on the E_{Thz} amplitude and spectrum. This, compared to the reference ISHE-based emitter (CoFeB(5)/Pt(3), see Fig.4.16a) and bulk-dominant STE (CoFeB(20)/MgO(6), Fig.4.16d), strongly suggests the "disappearance" of the Rashba states, with preserved bulk contribution, such as $\xi_{\mathrm{CoFeB(5)}} \gg \beta_{\mathrm{MgO}}$. Since this irreversible modification happened to the same sample, we could re-write the Eq.4.28 as.

$$\begin{cases} E^{tot}_{\mathrm{THz}}(\mathrm{CoFeB(5)/MgO(5)}) = \xi_{\mathrm{CoFeB(5)}} \cdot E^{bulk}_{\mathrm{THz}} + \beta_{\mathrm{MgO}} \cdot E^{IREE}_{\mathrm{THz}}; \\ E^{tot}_{\mathrm{THz}}(\mathrm{CoFeB(5)/MgO(5)^*}) = \xi_{\mathrm{CoFeB(5)^*}} \cdot E^{bulk}_{\mathrm{THz}}. \end{cases} \tag{4.33}$$

Of course, the latter equation is valid under the assumption that Rashba bands do not affect the SCC within the CoFeB layer, i.e. $\xi_{\mathrm{CoFeB(5)^*}} = \xi_{\mathrm{CoFeB(5)}}$. In this case, the difference between the THz transients emitted by the CoFeB(5)/MgO(5) and CoFeB(5)/MgO(5)* should give us only the IREE contribution, shown as the red line in Figure 4.20c. For the CoFeB(5)/MgO(5) bilayer, we estimate the 1:2.75 ratio between the bulk and IREE contribution. This is a relatively good agreement with the estimation of IREE-to-bulk ratio of 1:6 made at the end of the low-fluence section. The factor of two difference between the low-fluence and high-fluence regime is most likely related to the fact that we used CoFeB/Pt to approximate the decrease in IREE contribution

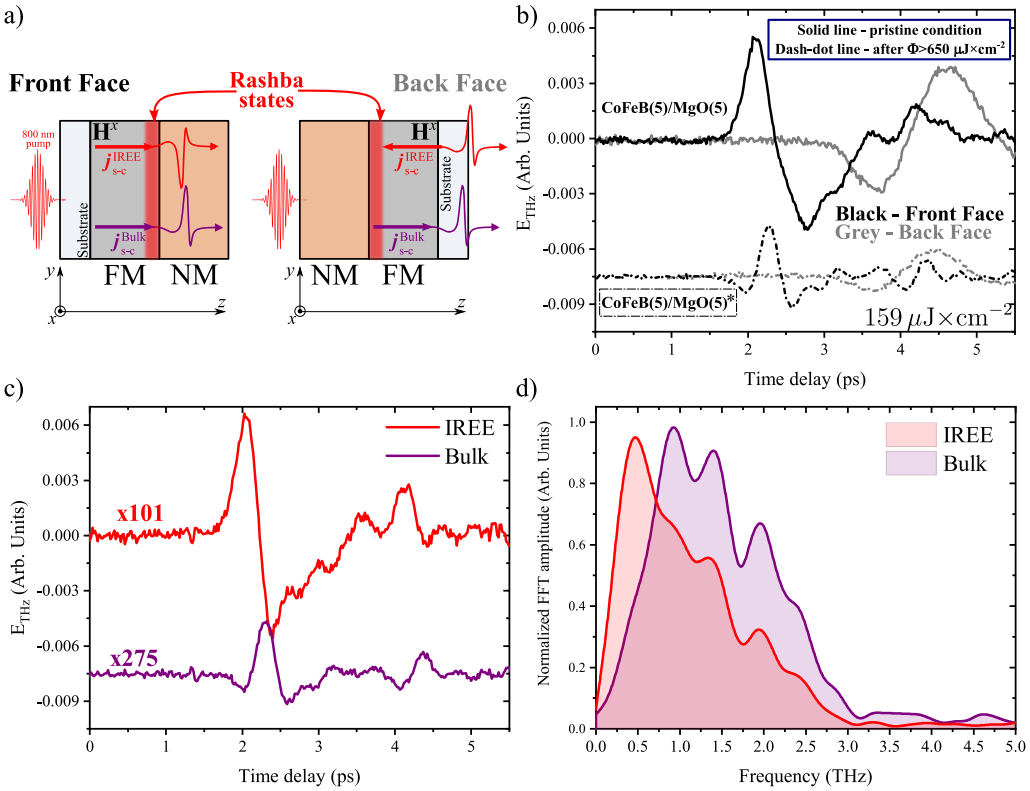

a). Schema of the geometry-dependent THz emission experiment. Front Face configuration denotes when the sample is excited from the side of the substrate and vice-versa for the Back Face. j_{s-c}^{IREE} is the spin-polarized current directed towards the Rashba interface. **b)** THz signal emitted from pristine CoFeB(5)/MgO(5) (solid) and CoFeB(5)/MgO(5)* (dash-dot) in the Front (color) and Back (gray) face configurations at 159 μJ cm^{-2} fluence and 800 nm pump wavelength. Temporal delay and waveform broadening for the Back Face orientation are due to the frequency-dependent THz absorption in the glass substrate. **c)** Extracted IREE contribution (red), obtained as the difference between the Front-Face signal, measured before and after sample modification. Bulk contribution is the CoFeB(5)/MgO(5)* waveform. The scaling factors indicate the ratio between the reference CoFeB(5)/Pt(3) emitter and the given signal. **d)** Normalized to 1 Fast Fourier transform of the **c)**.

Figure 4.20 – *CoFeB(5)/MgO(5): Sample orientation-dependent THz emission.*

for the CoFeB(20)/MgO(6) sample. Of course, at this moment, we can completely rely on the latter guesstimate of the relative amplitudes of IREE and bulk contributions using the permanent "modification" of the CoFeB(5)/MgO(5)* bilayer, since the absence of the Rashba states in the CoFeB(5)/MgO(5)* needs to be confirmed with ARPES or XPS measurements, if possible.

4.5 Conclusions and perspectives

In this chapter, we have discussed the THz emission as a result of the ultrafast spin-to-charge conversion from CoFeB/Pt and CoFeB/MgO magnetic bilayers. While CoFeB/Pt samples were chosen as the most characterized and best-performing bilayers to date, the choice of the CoFeB/MgO structures was stimulated by the recent discovery of the Rashba states created by the deposition of insulating MgO nanofilm on top of the ferromagnetic CoFeB layer. We show that by analyzing the effect of the sample geometrical orientation, laser pump fluence and wavelength dependence on the polarity and the shape of the emitted THz, one can identify the dominant spin-

to-charge conversion mechanism. On the first hand, we find that our measurements of CoFeB/Pt emitters are in the perfect agreement with the literature. On the other hand, we observed the strong thickness dependence of THz emission from the CoFeB/MgO bilayers, which we attribute to the combination of the spin-to-charge conversion in the bulk of the CoFeB ferromagnet and at the CoFeB/MgO Rashba interface. For the CoFeB(20 nm)/MgO(6 nm) sample, it appears that the bulk contribution is the dominant spin-to-charge conversion mechanism. In particular, we report that the sample reversal does not affect the polarity of the emitted THz, as expected from the spin-to-charge conversion inside the bulk of CoFeB layer. This claim is supported by the linear E_{THz} amplitude - pump fluence dependence, previously reported for the thick single-layer ferromagnetic films [268]. In contrast, in the CoFeB(5)/MgO(6) emitter we find that Inverse Rashba Edelstein effect contributes the most to the total detected E_{THz}, despite the presence of the bulk spin-to-charge conversion. This conclusion is supported by the sample-geometry dependent THz emission characteristic to the injection-based THz emitters, and highly-nonlinear emitted THz field amplitude - pump fluence dependence that indicates the competition of the bulk and Rashba contributions.

Consequently, we have estimated the 1:6 ratio between the amplitudes of the emitted THz fields driven by the bulk and Inverse Rashba Edelstein conversion in CoFeB(5)/MgO(6) emitter. This estimation makes the ultrafast Inverse Rashba Edelstein conversion in CoFeB(5)/MgO(6) nearly 100 less efficient than the Inverse Spin Hall effect in CoFeB(5)/Pt(3). At the same time, the Inverse Spin Hall and Inverse Rashba Edelstein effects are found to be equivalently efficient for the thermalized spin-polarized carriers [4]. Such difference in the Inverse Rashba Edelstein and Inverse spin Hall conversion rates at the ultrafast and quasi-DC timescales may indicate the reduced Rashba conversion efficiency when dealing with non-thermal distribution of injected spin-polarized carriers, since most Rashba bands favor spin-to-charge conversion close to the Fermi level [4, 279, 280]. Moreover, we evidenced pump wavelength sensitivity of the Inverse-Rashba Edelstein CoFeB/MgO emitters. While for CoFeB(20)/MgO(6) bilayer such change might be attributed to the more important light absorption gradient inside the CoFeB layer, the difference in THz emission (polarity of the emitted THz field, spectrum) observed for CoFeB(5)/MgO(6) sample is directly related to the spin-to-charge conversion at the Rashba interface. To the best of our knowledge, this finding was never mentioned in the literature before. Finally, we show that at the high laser pump fluence (higher than $650\,\mu\mathrm{J\,cm^{-2}}$) one may permanently modify or damage the delicate Rashba interface, which leads to the purely bulk spin-to-charge conversion.

As the future prospects, one can imagine tuning the Rashba bands to favor the conversion at high carrier-energies. This may result in a highly efficient, wavelength-sensitive spintronic device, allowing for an easy tunability of the generated THz waveform amplitude and spectrum. In addition, the estimation of the electrooptic response function, which includes the spatio-temporal transformation of the emitted THz pulse may allow us to access the shape of the transient charge current generated in the bulk of the CoFeB and at the Rashba interface. This information, complemented with a future in-lab time-resolved magneto-optical Kerr effect setup will certainly facilitate the first-principle calculations, anticipated in the near future.

General conclusion

In this thesis, we study how terahertz (THz) radiation could be used to excite or probe the ultrafast dynamics of electron, phonon, and spin in solids and nanostructures. In particular, we address the generation of coherent phonons in metals such as Chromium (Cr) and Aluminum (Al) and narrow-band topological insulator Bismuth Telluride (Bi_2Te_3) with picosecond THz pulses. In addition, we demonstrate how the specific aspects of the THz emission from optically-excited CoFeB/Pt and CoFeB/MgO magnetic nanostructures may provide insights into the relevant ultrafast spin-to-charge interconversion mechanisms.

The experiments in this manuscript were done using the ultrafast nonlinear spectroscopy in the pump-probe geometry with 1 kHz 800 nm 3 mJ amplified laser. For the ultrafast excitation of Cr, Al, and Bi_2Te_3 films, we have used the tilted-pulse front method for Lithium Niobate crystal ($LiNbO_3$) to generate the THz pulses with a peak electric field of about 275 kV cm^{-1} with a central frequency of 0.64 THz, that corresponds to a 1.2 µJ pulse energy. In the experimental section, we show how birefringent $x-$cut Quartz crystal could be used to shape the THz pulse, we calculate the electro-optic response function for the GaP and ZnTe electro-optic crystals and discuss the technique of THz time-domain spectroscopy sensitivity enhancement used for the detection of the weak THz fields in the Chapter 4.

As a first achievement of this thesis, we show that one can generate coherent phonons with pulsed THz radiation in the thin films of metals and narrow-band semiconductors. First, we discussed the THz excitation of 14 nm thick Cr and 20 nm thick Al films, and compared it to well-known 800 nm pump excitation. We find that the general shape of the time-dependent change in the 400 nm probe beam transmittance is similar for the THz and near-IR (NIR) excitation. We detect the thin metallic film first harmonic acoustic breathing mode for the NIR and THz pump excitation. Finally, comparing the electron (deformation potential) and lattice (thermoelastic) contributions to the total photoinduced stress for both types of excitation allowed us to identify thermoelastic stress as the main driving mechanism of acoustic phonon generation with THz. We conclude that the lattice heating is linked to the scattering of the accelerated electrons at the Fermi level, which leads to an ultrafast analogy of the well-known Joule effect.

The second achievement of this work is the investigation of the coherent optical phonon generation in Bi_2Te_3 16 nm thin film with THz. We demonstrate that 1.3 ps THz pulse with the central frequency of 0.64 THz is able to excite symmetric A_{1g}^1 1.85 THz Raman active phonon. We show that the A_{1g}^1 phonon amplitude increases quadratically with the THz field amplitude, indicating the second-order nonlinear process required to excite such coherent motion. We find as well that

A_{1g}^1 phonon amplitude does not depend on the THz pump polarization and is sensitive to the change of the central frequency of the THz pulse. We then compared the experimental findings with recently proposed THz ionic Raman scattering and THz sum-frequency excitation models of Raman phonon excitation. At this moment, we can only qualitatively compare the phase of experimentally measured A_{1g}^1 phonon with these two models and not the amplitude. Therefore, the first principle calculations under progress should shed new light on these observed mechanisms. Among other opened questions, preliminary anisotropic detection revealed the presence of an antisymmetric E_g^2 3.1 THz Raman active phonon, which will enrich the discussion about the highly-nonlinear coherent lattice mode control with THz in this correlated material.

In the last part of this thesis, we investigate the THz emission from the magnetic bilayers as the signature of the spin-to-charge conversion. We show that the THz emission from CoFeB/MgO heterostructures may result from the combination of the spin-charge interconversion in the bulk of the CoFeB ferromagnet and at the Rashba interface created by the deposition of the MgO on top of the ferromagnetic layer. Furthermore, we illustrate that by probing the sample sensitivity to the given experimental factor, such as pump wavelength and geometrical orientation, one can determine the dominant spin-to-charge conversion mechanism in the CoFeB/MgO bilayer. In addition, we show that the Rashba-dominant CoFeB(5 nm/MgO(6 nm) emitter is sensitive to the pump pulse wavelength, which leads to complete change in the phase and spectrum of the emitted THz. This finding could be beneficial for the tunability and improved efficiency of the Rashba-based devices.

In the future, we will try to address acoustic phonon generation with pulsed THz radiation in nanoparticles and multiferroic materials from these perspectives. In addition, we are planning to study the THz emission from the bare ferromagnetic Cobalt and Cobalt/MgO films, which may allow us to properly isolate the bulk and Rashba contributions to the ultrafast spin-to-charge conversion. Finally, the control over the pump pulse duration may allow probing the characteristic bandwidth of the spin-to-charge conversion, which is believed to be inversely proportional to the temporal bandwidth of the excitation pulse. To conclude, we show that THz radiation can be used to trigger and probe the rich interaction between multiple degrees of freedom in a condensed matter. However, further developments and research are needed to selectively excite and control electronic and magnetic properties of the solid-state, essential for the upcoming high-performance and low-energy consumption electronics that today industries and end-users are waiting for.

Appendix A

Pyroelectric characterization of the LNO THz source:

Pyroelectric detector sensitivity curve: For the alignment and THz-beam profiling, we have used the calibrated Microtech pyroelectric detector based on the $LiTa0_3$ electrooptic crystal. It has a 0.02 THz - 1.5 THz spectral range and is equipped with a black filter on the detector input to prevent parasitic illumination in visible and infrared regions. The Figure A.1 shows the detector responsivity plots provided by the manufacturer.

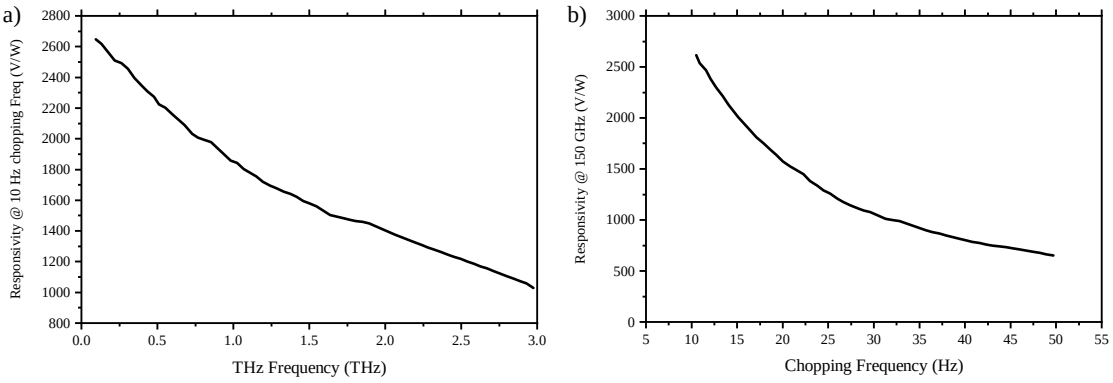

a) Responsivity vs. Signal Frequency measured at 10 Hz modulation frequency. **b)** Responsivity vs. Modulation Frequency measured at 150 GHz signal frequency. Data is extracted from Microtech datasheet (link)

Figure A.1 – *Microtech $LiTa0_3$ pyroelectric detector responsitivity curves.*

Polarization of the $LiNbO_3$ source: To measure the polarization state of the MgO: $LiNbO_3$ THz source, we have used a pair of free-standing Wire Grid (WG) polarizers (G30x10-S model number) from Microtech Instruments. They are made of Ta wires with 10 µm diameter and 30 µm spacing between the wires and have 88 mm clear aperture diameter, ≈3 bigger than the uncollimated THz beam. The THz-power - WG polarizer angular dependence displayed in Fig.A.2 shows the expected linear polarization of the MgO: $LiNbO_3$ THz source.

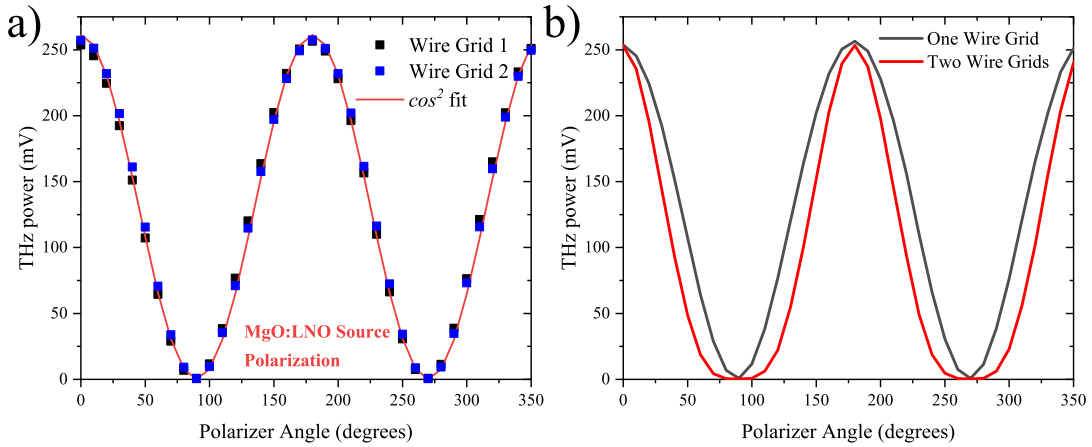

a) THz power transmission measured in the function of the single Wire Grid (WG) polarizer angle θ. **b)** THz power transmission measured for the single (black line) and two (red line) Wire Grid (WG) polarizers in the THz beam path in the function of the first WG polarizer angle θ.

Figure A.2 – *Wire Grid polarizer characterization with the $LiNbO_3$ THz source.*

$LiNbO_3$ beam size measurement: We measured the size of the THz beam with THz pyrocam I2S Vision (FigA.3a), and via the knife-edge method (FigA.3b), at the sample position. The i2S microbolometer [1] is optimized for the radiation in 1-3 THz range, has 320x240 matrix with 50 µm pixel size. Both measurements resulted in a similar estimation of the horizontal THz beam waist at $1/e^2$ of ≈ 0.72 mm (roughly 615 µm at FWHM).

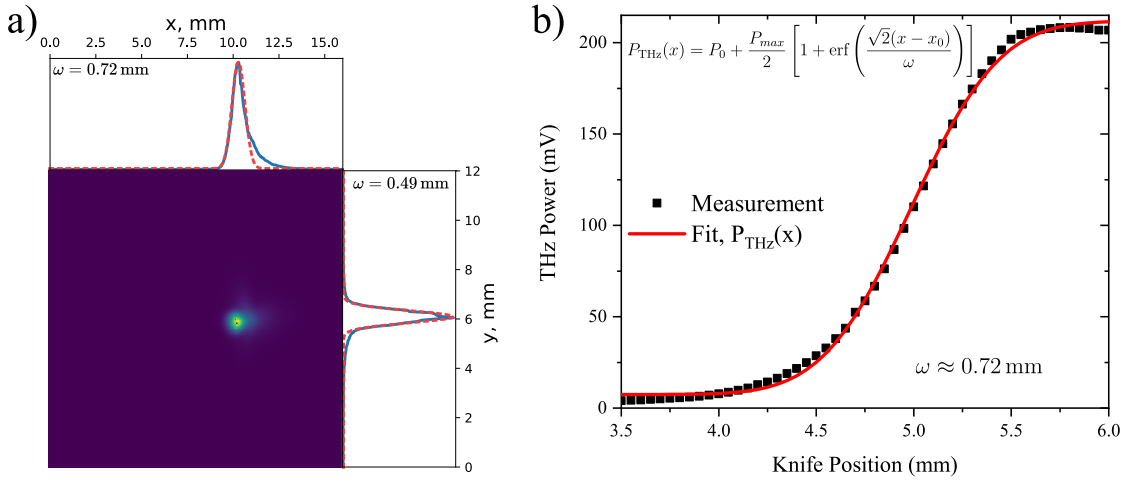

Measurement with **a)** THz pyrocam i2S Vision, and **b)** the pyroelectric detector using knife-edge method.

Figure A.3 – *$LiNbO_3$ THz beam size measurement.*

Peculiar effects of the WG polarizer: Finally, we address the THz-pulse distortions caused by the WG polarizer. From the manufacturer website [2], we should expect roughly 4 times less transmission at 0.5 THz compared to 1 THz frequency in $E_{\mathrm{THz}} \parallel$ wires configuration. This may result in an unintentional THz pulse distortion close to zero THz transmission configuration ($E_{\mathrm{THz}} \parallel$ wires).

1. i2S vision data-sheet can be downloaded here: link.
2. WG polarizer data-sheet can be downloaded here: link.

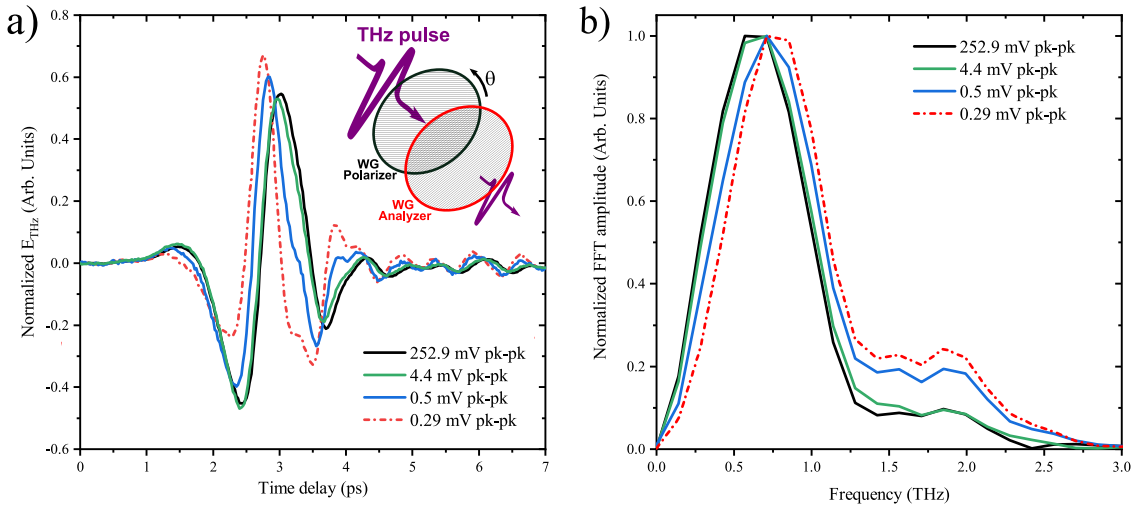

Normalized **a)** LNO THz waveform measured for the different THz power, and its **b)** spectra. Inset is the measurement layout.

Figure A.4 – *Peculiar effects of the WG polarizer.*

To investigate the WG frequency-dependent THz transmission, we have introduced the WG polarizer and analyzer in the THz beam path, as shown in the inset of Fig.A.4a. We then measured the THz waveform with 200 µm thick GaP crystal, as the function of the WG polarizer angle [3]. As seen from blue and red curves in Figure A.4a and b, THz gets highly distorted close to $E_{\mathrm{THz}} \parallel$ WG wires configuration. In the Chapter 3 the lowest THz power was higher than 25 mV pk-pk, for which the THz pulse distortions are negligible (see A.4b).

3. See Figure A.2 for WG Polarizer - THz power correspondence.

Appendix B

Cr and Bi_2Te_3 THz-spectrum dependent residuals

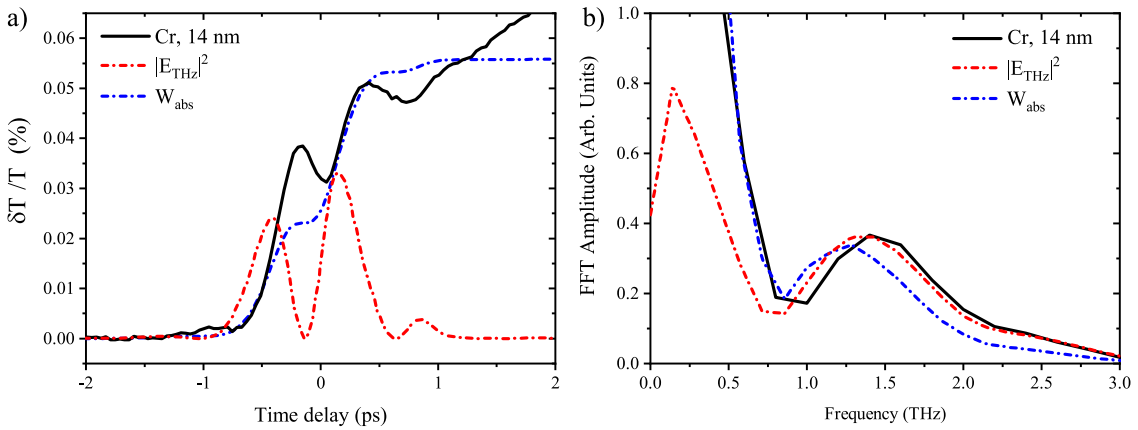

a) Transient optical transmission obtained with a THz excitation for a thin Cr film. Dash-dot lines correspond to the $|E_{\mathrm{THz}}|^2$ (red) and W_{abs} (blue). **b)** Same as a), but in the Fourier space. Data was normalized to overlap in the 1-2 THz range.

Figure B.1 – *Short time delays: Transient response of a thin Cr film and THz pulses vs absorbed THz power.*

From the main text, we concluded that the "sideband" observed close to the natural frequency of the A_{1g}^1 coherent phonon mode could be attributed to the "electronic" background of the signal, and is not related to excitation of a coherent phonon. To support this claim we present here the short time scale signal of 14 nm Chromium film discussed in the first part of a Chapter 3. We remind that Chromium does not have optical phonon, so we should not expect any additional high-frequency contributions to the time-delay zero signal. The $\delta T/T$ signal reveals the "double bump" around the time delay zero, shown as the black line in Figure B.1a. In addition, the approximate shape of the $W_{\mathrm{THz}}^{\mathrm{Abs.}}$ (calculated with Eq.3.19) overlaps nicely with the $\delta T/T$ signal around time delay zero (see blue line in Figure B.1a). Finally, Figure B.1b shows that difference and sum frequency components of the E_{THz} are present in the FFT of Chromium $\delta T/T$ (black), $W_{\mathrm{THz}}^{\mathrm{Abs.}}$ (blue dash-dot) and E_{THz}^2 (red dash-dot). This effect could be attributed to the THz-induced optical birefringence observed in liquids [178], transparent media [123] and metals [282].

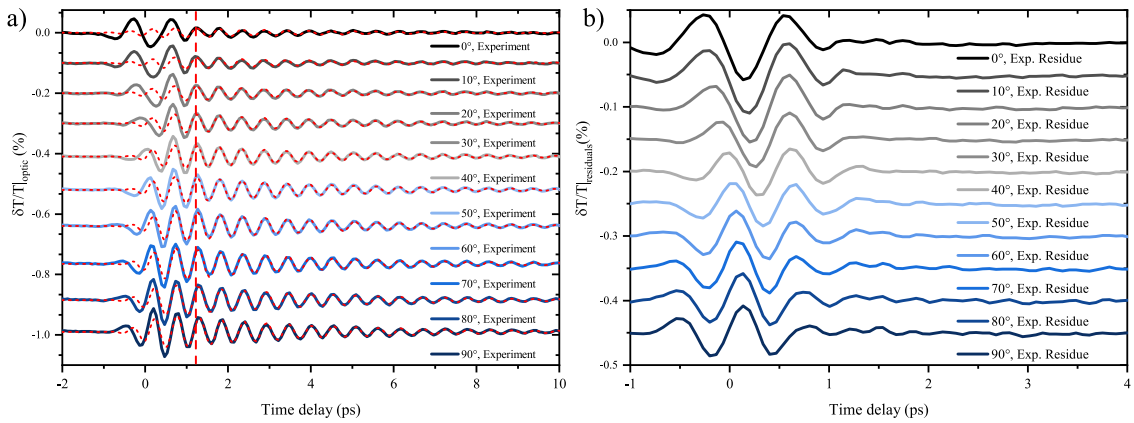

a) Subtracted phonon signal in the function of Wire Grid (WG) polarizer angle, and respective fit to the A_{1g}^1 phonon mode (red dotted line). **b)** The residual between the phonon signal and the A_{1g}^1 phonon mode fit.

Figure B.2 – *Bi_2Te_3: Extraction of the residual part of the signal.*

Now we move to the signals measured for the Bi_2Te_3 sample. We remind, that the optical phonon part of the signal was extracted only with a simple error-function fit, hence all nonlinear contributions apart difference frequency of the pump E_{THz} field should be still present in the signal. The idea is to compare the measured modulation of the $\delta T/T$ at the short time delays ($\leq 1.5\,\mathrm{ps}$) to the sum-frequency component of the reconstructed E_{THz} waveform, described in the Section 2.5.

In order to isolate the residual signal of interest, we remove the A_{1g}^1 phonon mode from the $\delta T/T|_{\mathrm{optic}}$, shown in Fig.B.2a, by fitting it with a simple damped cosine function:

$$f(\tau) = \left(1 + \mathrm{erf}\left[\frac{\tau}{s}\right]\right) \cdot a_{\mathrm{ph}} \cdot \cos[\Omega_{\mathrm{ph}}\tau + \varphi_{\mathrm{ph}}] \cdot \exp\left[-\frac{\tau}{\tau_{\mathrm{ph}}}\right], \tag{B.1}$$

where a_{ph} is the amplitude of the A_{1g}^1 optical phonons, Ω_{ph} is the frequency of the A_{1g}^1 mode, fixed to 1.85 THz, φ_{ph} is the phonon phase and τ_{ph} is the A_{1g}^1 mode damping time, set to 3.5 ps $\pm 3\,\%$. The s parameter was set to the same value we have fitted the "raw" signal $\delta T/T$. The best fits obtained for the set of the measured signals are displayed as the red dashed lines in the Fig.B.2a.

Then, with the following subtraction, we can isolate the residual signal as:

$$\delta T/T|_{\mathrm{residual}}(\tau) = \delta T/T|_{\mathrm{optic}}(\tau) - f(\tau). \tag{B.2}$$

The residual signals for all measured WG Analyzer angles are shown in the Fig.B.2b. We observe the increase in the modulation frequency of the residuals plot when we increase the WG Analyzer angle, which should normally correspond to the increase of the E_{THz} central frequency $\Omega_0/2\pi$.

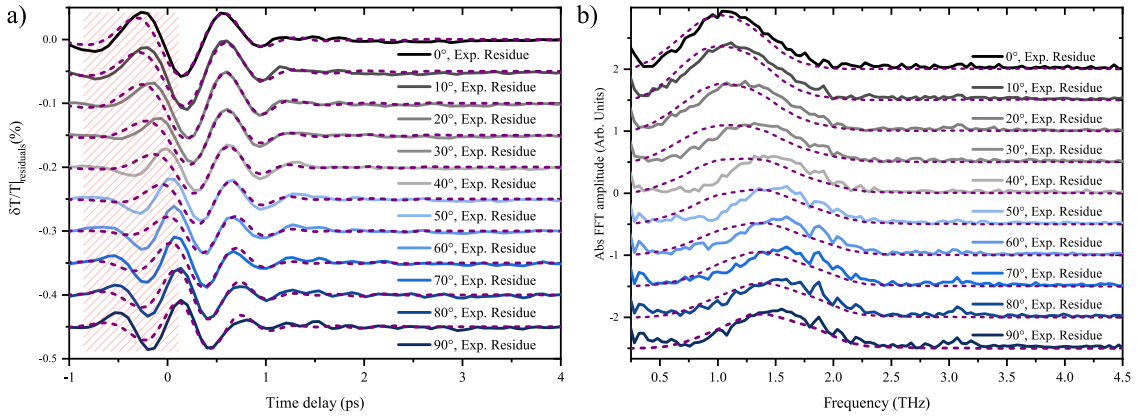

a) Residual signal in the function of Wire Grid (WG) polarizer angle, and respective calculated sum-frequency component of the pump THz pulse (purple dashed line). Red shaded region corresponds to the temporal window with the high fit-volatility/uncertainty. **b)** FFT of the signals presented in the panel a).

Figure B.3 – *Bi_2Te_3: Residual part of the signal vs SHG the THz pulse.*

As the next step, we will calculate the sum-frequency component of the E_{THz}, i.e., $E^2_{\mathrm{THz}}|_{\mathrm{SF}}$. In the Fourier space, the square of the pump field $E^2_{\mathrm{THz}}(\tau)$ will be equal to [176]:

$$\begin{aligned}\mathcal{F}\left(E^2\right)(\Omega) = &\underbrace{\int_0^\infty \int_0^\infty \mathrm{d}\Omega_1 \, \mathrm{d}\Omega_2 \widetilde{E}(\Omega_1)\widetilde{E}(-\Omega_2)}_{\mathcal{F}\left(E^2_{\mathrm{THz}}|_{\mathrm{DF}}\right)(\Omega)} \\ &+ \underbrace{\int_0^\infty \int_0^\infty \mathrm{d}\Omega_1 \, \mathrm{d}\Omega_2 \widetilde{E}(\Omega_1)\widetilde{E}(\Omega_2)}_{\mathcal{F}\left(E^2_{\mathrm{THz}}|_{\mathrm{SF}}\right)(\Omega)},\end{aligned} \tag{B.3}$$

where $E^2_{\mathrm{THz}}|_{\mathrm{SF}}$ and $E^2_{\mathrm{THz}}|_{\mathrm{DF}}$ are the sum-frequency (SF) and difference-frequency (DF) contributions. The difference frequency contribution was removed either by the FFT high-band pass filtering, or the Gaussian fit of the E^2_{THz} in the time domain. Both approaches gave the same result. The same procedure was repeated for the all waveforms, reconstructed for the different angles θ of the WG analyzer.

Finally, the solid lines in the Figure B.3a show the residual signal $\delta T/T|_{\mathrm{residual}}(\tau, \theta)$ (solid lines) as the function of the WG analyzer angle θ. It is overlapped with the purple dashed lines, that correspond to the respective calculated SF component of the THz pump as a function of the WG analyzer angle. As seen from both transient signals and their respective FFTs (see Fig.B.3b), we have relatively good overlap of the residual part of the signal and given $E^2_{\mathrm{THz}}|_{\mathrm{SF}}(\theta)$. The red shaded area corresponds to the region of the signal, that gets highly distorted by the slope of the error-function, used to fit the "raw" $\delta T/T$.

Appendix C

STEs Light absorption

In this appendix, we present the numerical simulations of the light absorption profiles in the set of the spintronic emitters CoFeB(5 and 20)/Pt(3) and CoFeB(5 and 20)/MgO(6), where number in brackets is the thickness of the layer in nm. Calculations are done using the Transfer Matrix Method approach, discussed in the Section 1.3.2. For the CoFeB nanolayers, the optical constant were extracted from the work of X.Liang et.al [283]. For Pt, we used the data from Rakic et.al. [156].

The plots presented in this appendix are shown in terms of the fraction of absorbed optical power per unit of the distance (nm). The amount of the absorbed optical power A_{abs} within the layer i of the thickness d was calculated as following:

$$A^i_{\text{abs}} = \frac{\sum_n A^n_{\text{abs}}(d_n)}{A^{tot}_{\text{inc}}}, \tag{C.1}$$

where n is the discrete value of the absorbed optical power per unit of distance within the range $d_{i-1} \leq d_n \leq d_{i+1}$, and $P^{\text{tot}}_{\text{inc}}$ is total incident optical power. The data for the Back and Front Face excitations are shown in the Table C.1

The light absorption gradient ∇A_z was estimated using this equation:

$$\nabla A_z = \frac{A_{\text{abs}}(0) - A_{\text{abs}}(d)}{d}, \tag{C.2}$$

	Front	Back	
	FM	FM	Si
CoFeB(5)Pt(3)	35%	10%	33%
CoFeB(20)Pt(3)	44%	19%	12.40%
CoFeB(5)MgO(6)	48.80%	13.60%	43.20%
CoFeB(20)MgO(6)	50.70%	24.10%	15.60%

Table C.1 – *Absorbed power in the CoFeB for the Front (SiO_2) and Back (Si) configurations*

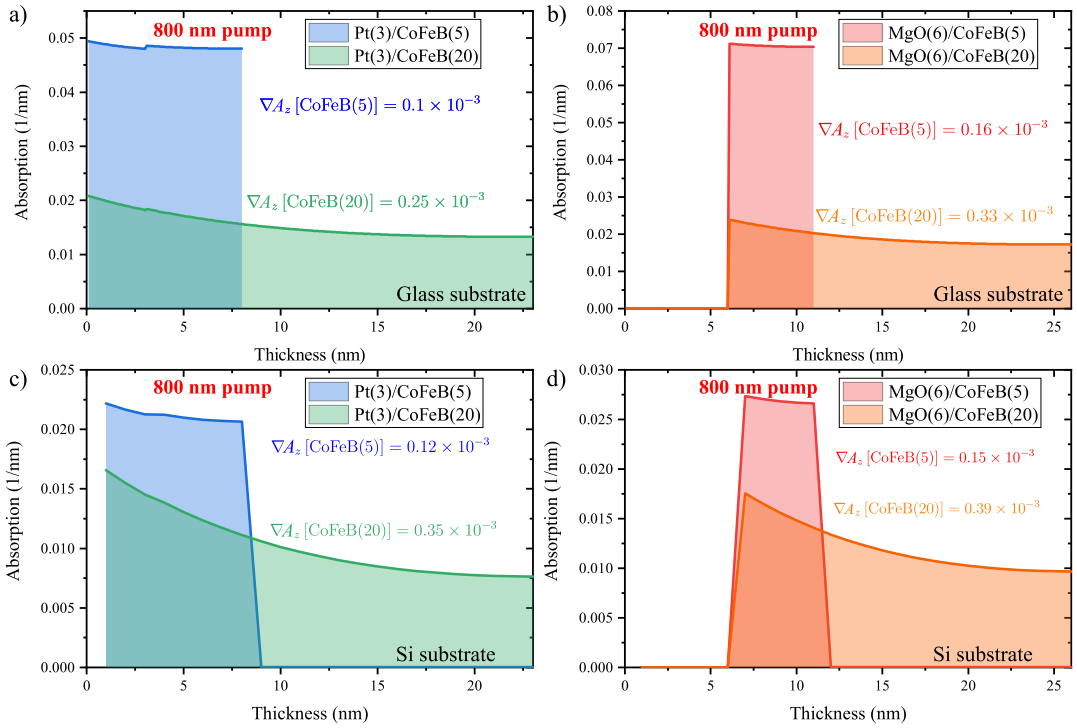

Figure C.1 – *Light absorption profiles: in the CoFeB capped with Pt and MgO, in Back Face configuration, on the Glass and Si substrates, 800 pump wavelength.*

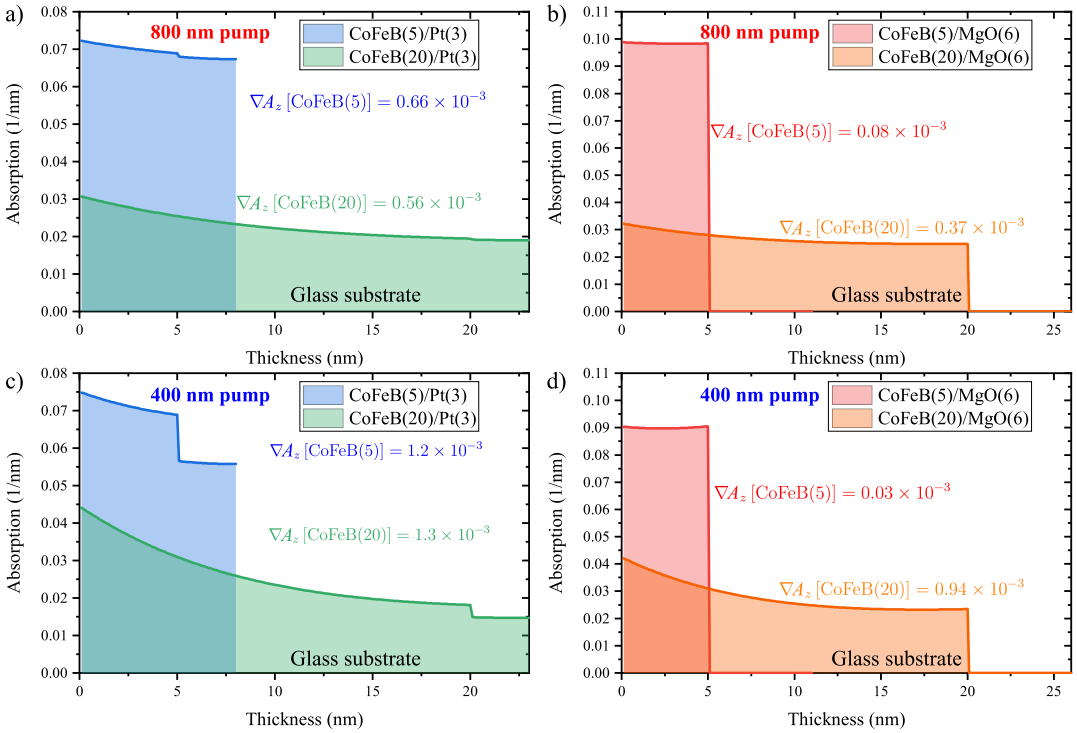

Figure C.2 – *Light absorption profiles: in the CoFeB(5)/MgO(6) and CoFeB(20)/MgO(6), in Front Face configuration on the Glass substrate, 800 and 400 nm pump wavelengths.*

where $A_{\text{abs}}(0)$ and $A_{\text{abs}}(d)$ are the fractions of the absorbed optical power at the beginning and the end of the FM layer. Calculations were performed by Vincent Juvé, and re-done by myself with TMM Python package.

Appendix D

THz emission from ISHE-based STEs

If we look at the amplitude ratio between CoFeB(5)/Pt(3) and CoFeB(20)/Pt(3) STEs, shown in the Figure D.1c (blue and green waveforms), the emission 20 nm thick CoFeB emits ≈ 5 times less THz compared to 5 nm thick one. Such attenuation factor can be addressed by an empirical model for ISHE THz emitters [239, 242, 245, 270], that links total emitted E_{THz} to the overall thickness of the FM+NM layers d_{tot} as:

$$E_{\mathrm{THz}}(d) \propto \frac{A_{abs}}{d_{tot}} \cdot \theta_{ISHE}^{\mathrm{NM}} \cdot \tanh\left(\frac{d_{\mathrm{NM}} - d_0}{2\lambda_{\mathrm{rel}}}\right) \cdot Z(\omega), \tag{D.1}$$

where A_{abs} is the absorbed fraction of the incident pump power, $\theta_{ISHE}^{\mathrm{NM}}$ is the Spin-Hall angle of the NM layer (Pt in our case), d_0 is the critical thickness of the FM layer [251, 284], λ_{rel} is the hot electron ballistic-transport relaxation length. Here, third term describes the generation of the spin-current in the FM, its ballistic transport and possible Fabry–Pérot cavity effect, that may enhance the THz emission due to the multiple pump and THz reflections at the FM/NM, NM/FM, NM/air interfaces. Last term, $Z(\omega)$ is the impedance of the STE given by:

$$\frac{1}{Z(\omega)} = \frac{n_1(\omega) + n_2(\omega)}{Z_0} + \int_0^d \mathrm{d}z\, \sigma(\omega), \tag{D.2}$$

with $\sigma(\omega)$ being the conductivity in the THz range , and $n_1(\omega)$ and $n_2(\omega)$ are NM and air refractive indices in the THz range respectively, with vacuum impedance $Z_0 = 377\,\Omega$.

If we use the Eq.D.1, calculated A_{abs} (see Appendix C.1), and CoFeB and Pt layer conductivities discussed in the Appendix E, we estimate the factor of ≈5.2 between CoFeB(5)/Pt(3) and CoFeB(20)/Pt(3), in the good agreement with experiment.

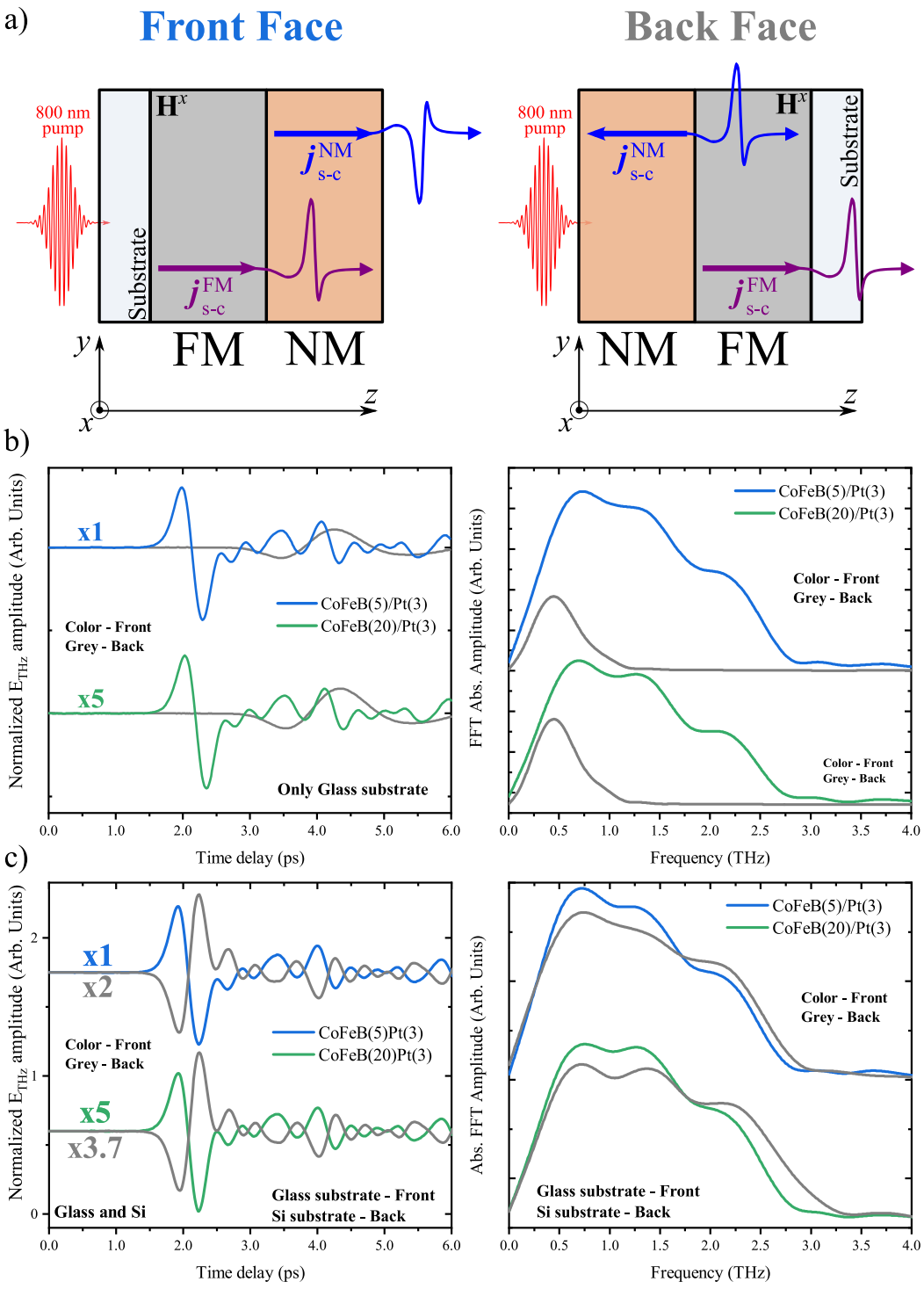

a). Schema of the geometry-dependent THz emission experiment. Front Face configuration denotes when the sample is excited from the side of the substrate, and vice-versa for the Back Face. **b)** THz signal and spectra measured in the Front (color) and Back (gray) face configurations for CoFeB(5 and 20)/Pt(3) samples deposited on the glass substrate. Temporal delay and waveform broadening for the Back Face orientation is due to the frequency dependent Glass absorption. **c)** Emitted THz and its spectra in the Front (color, glass substrate) and Back (gray, Si substrate) face orientation for CoFeB(5 and 20)/Pt(3) samples. THz polarity reversal of both emitters indicates the dominance of the injection-based ISHE conversion. Note: Si-substrate signals are temporally shifted to overlap with bilayers deposited on the glass-substrate STEs.

Figure D.1 – *CoFeB/Pt STEs: Sample orientation dependent THz emission.*

Appendix E

THz-TDS of the Pt- and MgO-based spintronic emitters

From the discussion of the THz emission in the Back Face configuration, in the absence of the substrate THz absorption, Torosyan et.al. [251] proposed to introduce an additional term into Eq.D.1, which accounts for the THz attenuation due to the propagation through the metal layer stack :

$$\kappa_{\mathrm{THz}} = \exp\left[-\frac{d_{FM} + d_{NM}}{\xi_{\mathrm{THz}}}\right], \tag{E.1}$$

where ξ_{THz} is the effective inverse attenuation coefficient of the THz radiation, proposed by the authors. We can experimentally check this model, since this term can be effectively measured by the means of THz-TDS.

In order to check the validity the latter equation, we performed simple THz-TDS spectroscopy on the set of the spintronic emitters. For this experiment, we recorded the THz pulse that propagates through the bare 500 µm silicone substrate $S_{ref}(t)$, and via FFT we extract the information about its spectral components, $S_{ref}(\omega)$. After, the 500 µm silicone substrate was replaced by the CoFeB(5 and 20)/Pt(3) grown on the 300 µm silicone substrate, and we recorded $S_{sam}(t)$ with $S_{sam}(\omega)$.

In the Fig.E.1a, we show the ratio between of the FFT magnitudes of $S_{sam}(\omega)$ and $S_{ref}(\omega)$, showing the E_{THz} amplitude transmission through given sample. The fringes observed in the Fig.E.1a and Fig.E.2a may correspond to the Fabry-Pérot effect induced by the thickness difference of the reference and sample silicone substrates. The data for CoFeB(Δ15) was obtained by taking the THz transmission from CoFeB(5)/Pt(3) as $S_{ref}(\omega)$, and CoFeB(20)/Pt(3) as $S_{sam}(\omega)$. THz transmission for all the samples show nearly frequency independent behaviour, well in the agreement with previous reports [100].

With Eq.E.1 with constant ξ_{THz} it is not possible to explain the measured THz attenuation factor, underlying the thickness and layer-dependent THz conductivity of the whole metal stack. We then change the the Eq.E.1 by accounting for the thickness change of the specific layer, which

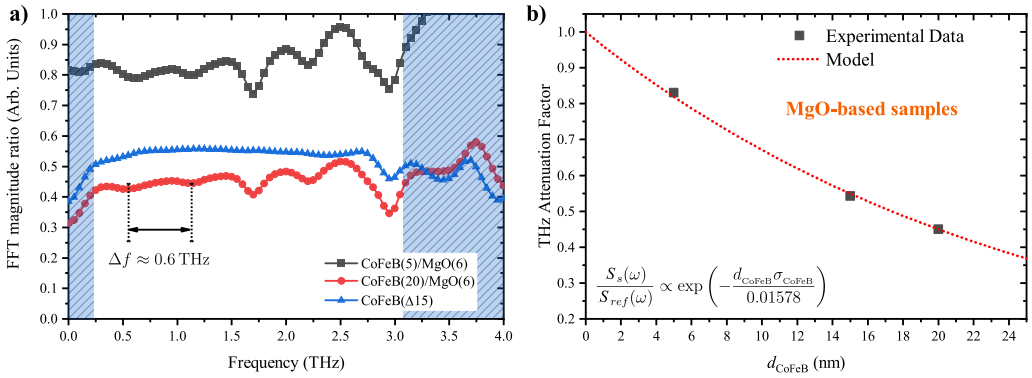

a) E_{THz} amplitude transmission for the CoFeB/Pt STEs. **b)** The average value of E_{THz} amplitude transmission plotted in the function of the CoFeB layer thickness.

Figure E.1 – *Pt based samples: THz metal stack amplitude absorption.*

gives:

$$\kappa^*_{\mathrm{THz}} = \exp\left[-\frac{d_{FM}\sigma_{FM} + d_{NM}\sigma_{NM}}{G^*_{\mathrm{THz}}}\right], \tag{E.2}$$

where G^*_{THz} is the effective sample conductance, in analogy to ξ_{THz} proposed before. With the Eq.E.2 for constant G^*_{THz} we can fit the experimental data for E_{THz} attenuation factor, shown in the Fig.E.1b. For $G^*_{\mathrm{THz}} = 0.0233\,\mathrm{S}$, we estimate the values of $\sigma_{Pt} = 3 \times 10^6\,\mathrm{S\,m^{-1}}$ and $\sigma_{CoFeB} = 0.63 \times 10^6\,\mathrm{S\,m^{-1}}$, in a good agreement with previously published results [100, 270].

Using the same values, but different effective sample conductance $G^*_{\mathrm{THz}} = 0.015\,78\,\mathrm{S}$, related to the Pt to MgO layer replacement, and $\sigma_{CoFeB} = 0.63 \times 10^6\,\mathrm{S\,m^{-1}}$ we fit the thickness dependent E_{THz} transmission for the CoFeB/MgO STEs shown in the FigE.2.

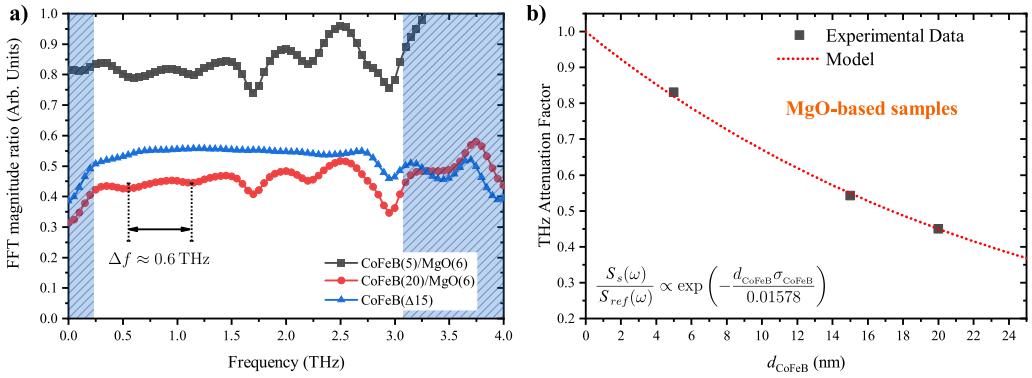

a) E_{THz} amplitude transmission for the CoFeB/MgO STEs. **b)** The average value of E_{THz} amplitude transmission plotted in the function of the CoFeB layer thickness.

Figure E.2 – *MgO based samples: THz CoFeB and MgO amplitude absorption.*

Appendix F

Appendix: STEs' emitted THz field amplitude - pump power dependence

Power/THz amplitude dependence. First and Second batches: In order to check the sample growth repeatability process, we have two batches of the same spintronic bilayers, grown on the float-zone glass substrate. We then measured the E_{THz} amplitude - pump fluence Φ dependence for all the samples discussed in this manuscript.

The E_{THz} pump power-dependence of the CoFeB/Pt samples is shown on the Figure F.1a. The observed nonlinear E_{THz} increase for CoFeB layers with 5 and 20 nm thickness can be attributed to both saturation of the magnetization quenching [275] and spin-trapping inside the HM layer [3]. At this stage, however, we cannot separate these two effects. Nevertheless, we show rather good consistency between the two batches, with E_{THz} peak-to-peak difference of about 20 %, that can be attributed to the CoFeB or Pt layer thickness incertitude, which highly affects spin-to-charge conversion efficiency [251].

Figure F.1b depicts the E_{THz} - Φ dependence of the CoFeB(20)/MgO(5 and 6) samples. These samples show better consistency, with the E_{THz} peak-to-peak difference of less than 10 %.

At last, Fig.F.1 shows the data for CoFeB(5)/MgO(5)/Ta(2) and CoFeB(5)/MgO(6) STEs. Similar E_{THz} - Φ dependence, and THz waveform of these two samples indicates that the Rashba states are not affected by the deposition of the metallic layer on top of MgO film. Lower THz peak-to-peak amplitudes for CoFeB(5)/MgO(5)/Ta(2) can be partially attributed to the additional THz absorption in the 2 nm Ta layer. The deposition of the thin metallic layer on top of the MgO could positively impact the damage threshold of the CoFeB/MgO Rashba states, which could be interesting to address in the future.

Pump-power dependent Si THz absorption: In order to better understand the power dependence of the STE in the Back and Front Face configurations, we have measured the dependence of the THz pulse transmission through photoexcited Si wafer. To simulate the Back-Face

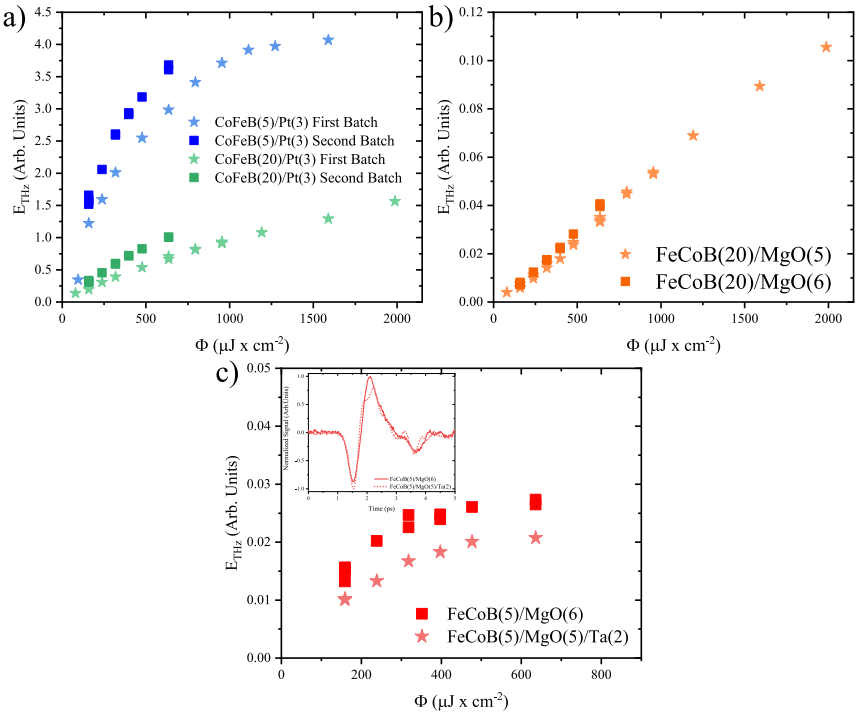

THz field peak-to-peak amplitudes in function of the pump fluence of **a)** CoFeB(5)/Pt(3) and CoFeB(20)/Pt(3) from different batches. THz amplitudes of the ISHE emitters show comparable amplitudes and power dependent behaviour, confirming the repeatability of the experiment. **b)** CoFeB(20)/MgO(5) and CoFeB(20)/MgO(6). **c)** CoFeB(5)/MgO(6) and CoFeB(5)/MgO(5)/Ta(2). The nonlinear behaviour of the CoFeB(5)/MgO(5)/Ta(2) and its similar waveform (see inset) points on the IREE conversion in the CoFeB(5)/MgO(5)/Ta(2).

Figure F.1 – *Different batches: THz peak-to-peak amplitude* - 800 nm *pump fluence dependence.*

excitation condition, we have overlapped, both spatially and in time, the 800 nm pump beam and the THz pulse emitted from ZnTe at the surface of Si wafer. Measured THz transmission loss due to the 800 nm pump absorption is shown in the Fig.F.2.

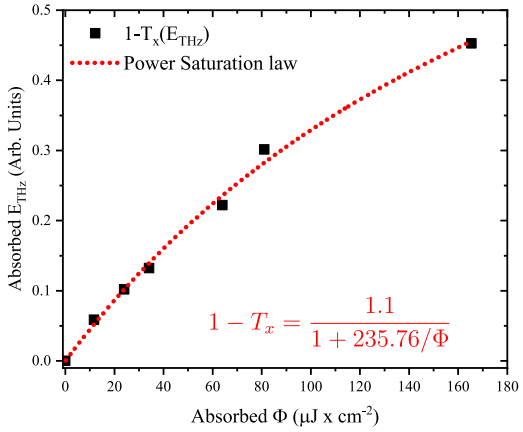

Figure F.2 – *Pump-power dependent Si THz absorption.*

Power/THz amplitude dependence: Front (Glass substrate) vs Back (Si substrate) experimental configurations: As the next step, we have recorded the THz emission from the set of samples in the Back and Front face experimental configurations, grown on the Glass and

Si substrates. Figure F.3 shows the peak-to-peak E_{THz} amplitude in function of the FM layer absorbed laser fluence Φ_{abs}. We see the highly nonlinear THz absorption as a function of the 800 nm pump fluence. This complicates the retrieval of the real STE THz amplitudes in the Back Face configuration for the samples grown on the Si substrate.

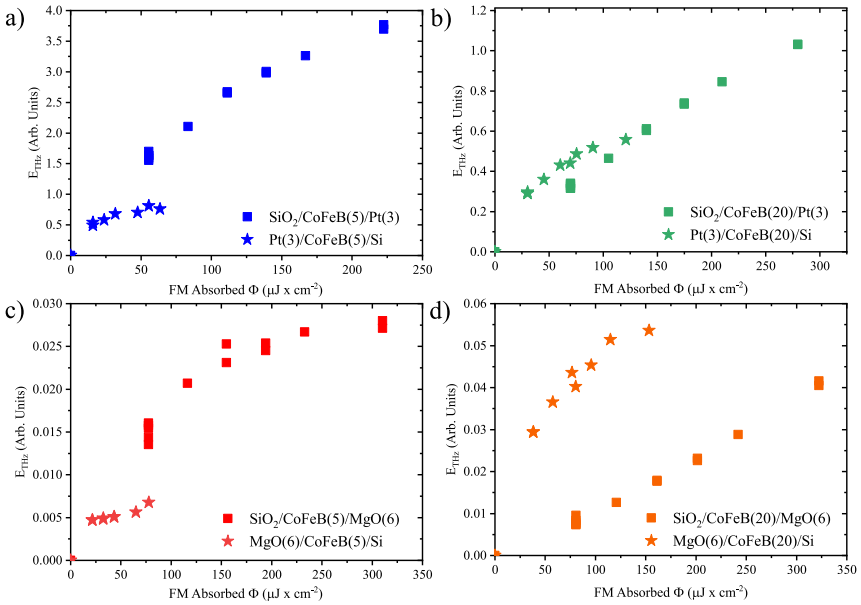

THz field peak-to-peak amplitudes in function of the pump fluence of **a)** CoFeB(5)/Pt(3) and CoFeB(20)/Pt(3) from different batches. THz amplitudes of the ISHE emitters show comparable amplitudes and power dependent behaviour, confirming the repeatability of the experiment. **b)** CoFeB(20)/MgO(5) and CoFeB(20)/MgO(6). **c)** CoFeB(5)/MgO(6) and CoFeB(5)/MgO(5)/Ta(2). The nonlinear behaviour of the CoFeB(5)/MgO(5)/Ta(2) and its similar waveform (see inset) points on the IREE conversion in the CoFeB(5)/MgO(5)/Ta(2).

Figure F.3 – *Glass and Si substrates: THz amplitude versus FM absorbed fluence.*

Let us take a look first at the CoFeB/Pt based samples. For the CoFeB(5)/Pt(3) (see Fig.F.3a), the Back Face configuration [1] is less efficient than the Front Face one [2], which is due to the power-dependent Si THz absorption, addressed in the previous paragraph.

On the other hand, for the same amount of the pump fluence absorbed by the CoFeB, THz emission from CoFeB(20)/Pt(3) in Back Face configuration is more efficient than the Front Face excitation, without even accounting for the Si photoexcitation loss. This could be related to the non-equivalent spin injection into the HM between the Back and Front face excitations, and it needs to be confirmed with first principle calculations. Importantly, the data for the Back Face excitation does not account for the THz absorption in the CoFeB and photoexcited Si.

Next, the same measurement done for the CoFeB(5)/MgO(6) sample (see FigF.3c). The Front Face E_{THz} pump fluence dependence of this sample was already discussed in the main text. Interestingly, the efficiency of the CoFeB(5)/MgO(6) THz emission looks like the inverse of the Front Face data, despite the fluence dependent Si absorption. Such evolution of the E_{THz} amplitude

1. Excitation from the side of the non-magnetic layer.
2. Excitation from the side of the substrate.

for the Back face configuration again suggests coexistence of the IREE and bulk [3] spin-to charge conversion contributions in CoFeB/MgO samples.

Finally, the pump fluence dependence of the CoFeB(20)/MgO(6) behaves as its ISHE counterpart, CoFeB(20)/Pt(3), indicating the existence of the IREE conversion in this sample. Interestingly, as shown in the Appendix C, light-absorption gradient within the CoFeB layer for the Back and Front Face excitations differs by <10 %, hence the more important THz field amplitude when pumped from the MgO side can not be explained solely by the more significant bulk conversion mechanism. Such non-expected behaviour of both 20 nm thick ISHE and IREE in the back face configuration can be promising for more efficient THz emission in the non-conventional STE geometry.

3. AHE and/or ultrafast demagnetization

Appendix G

Python data acquisition software

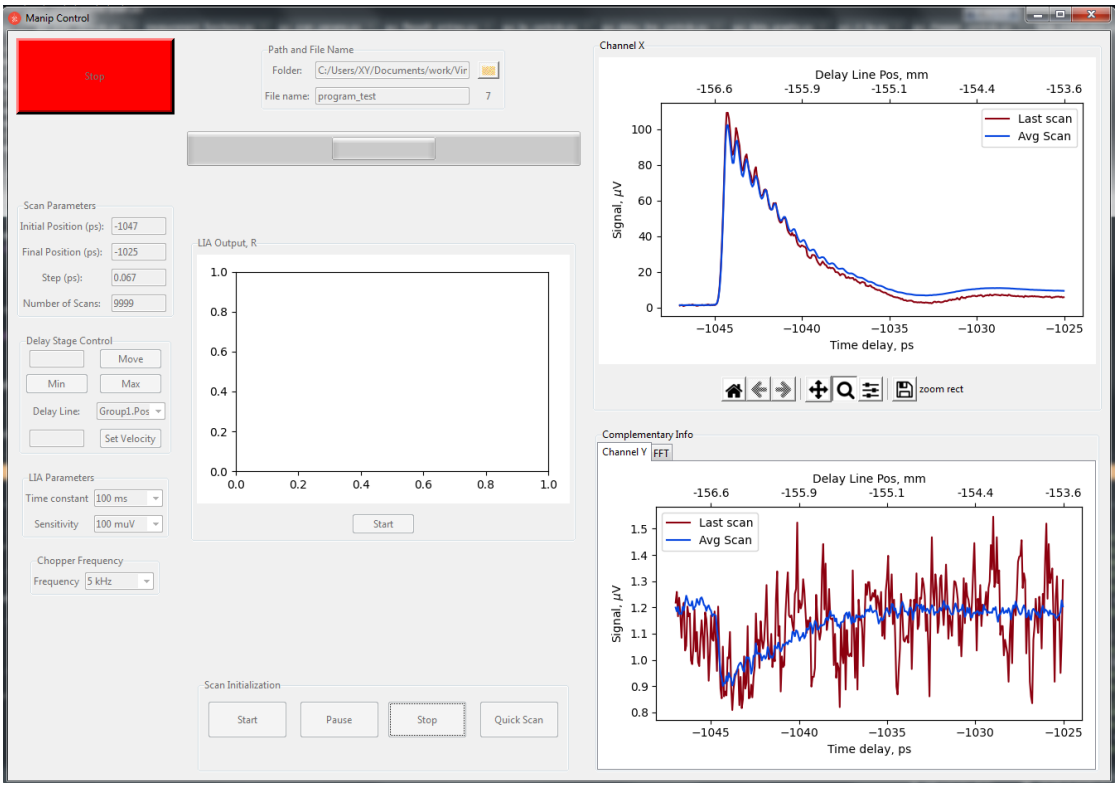

Figure G.1 – *Graphical user interface of the Python-based data acquisition software.*

I have developed the Pump-probe graphical user interface (GUI) to control the experiment and to simplify, automatize, and visualize the data acquisition process. The GUI shown in the Fig.G.1 is the "single-page" window with inputs for the time-resolved scan parameters, Lock-in Amplifier (LIA) controls, alignment tools, and plots with measured data sets. It was made with an intent of user-friendly software configuration, hardware initialization and adjustment of the GUI itself. No prior programming knowledge required [285].

More information is available on the GitHub, at https://github.com/artie-l/pump-probe-experiment-control.

Bibliography

[1] Tobias Kampfrath, Koichiro Tanaka, and Keith A. Nelson. Resonant and nonresonant control over matter and light by intense terahertz transients. *Nature Photonics*, 7(9):680–690, 9 2013.

[2] M. Först, R. Mankowsky, and A. Cavalleri. Mode-Selective Control of the Crystal Lattice. *Accounts of Chemical Research*, 48(2):380–387, 2 2015.

[3] T. Kampfrath, M. Battiato, P. Maldonado, G. Eilers, J. Nötzold, S. Mährlein, V. Zbarsky, F. Freimuth, Y. Mokrousov, S. Blügel, M. Wolf, I. Radu, P. M. Oppeneer, and M. Münzenberg. Terahertz spin current pulses controlled by magnetic heterostructures. *Nature Nanotechnology*, 8(4):256–260, 4 2013.

[4] Olivier Rousseau, Cosimo Gorini, Fatima Ibrahim, Jean-Yves Chauleau, Aurélie Solignac, Ali Hallal, Sebastian Tölle, Mairbek Chshiev, and Michel Viret. Spin-charge conversion in ferromagnetic Rashba states. *Physical Review B*, 104(13):134438, 10 2021.

[5] Michael Eckert. Disputed discovery: the beginnings of X-ray diffraction in crystals in 1912 and its repercussions. *Acta Crystallographica Section A Foundations of Crystallography*, 68(1):30–39, 1 2012.

[6] Richard J. D. Tilley. *Understanding Solids*. John Wiley & Sons, Ltd, Chichester, UK, 7 2004.

[7] Charles Kittel. *Introduction to Solid State Physics*. John Wiley and Sons, 7th edition, 6 1996.

[8] N. Vagelatos, D. Wehe, and J. S. King. Phonon dispersion and phonon densities of states for ZnS and ZnTe. *The Journal of Chemical Physics*, 60(9):3613–3618, 5 1974.

[9] Neil W. Ashcroft, N. David Mermin, and Sergio Rodriguez. *Solid State Physics*. CRC Press, 1 1978.

[10] James E. Bernard and Alex Zunger. Electronic structure of ZnS, ZnSe, ZnTe, and their pseudobinary alloys. *Physical Review B*, 36(6):3199–3228, 8 1987.

[11] J. M. D. Coey. *Magnetism and Magnetic Materials*. Cambridge University Press, 1 2001.

[12] Walther Gerlach and Otto Stern. Der experimentelle Nachweis der Richtungsquantelung im Magnetfeld. *Zeitschrift fur Physik*, 9(1):349–352, 12 1922.

[13] Robert M. White. *Quantum Theory of Magnetism : Magnetic Properties of Materials*. Springer Berlin Heidelberg, 2007.

[14] Paul Adrien Maurice Dirac. The quantum theory of the electron. *Proceedings of the Royal Society of London. Series A, Containing Papers of a Mathematical and Physical Character*, 117(778):610–624, 2 1928.

[15] Albert A. Michelson. XXX. On the application of interference methods to spectroscopic measurements. —II. *The London, Edinburgh, and Dublin Philosophical Magazine and Journal of Science*, 34(208):280–299, 9 1892.

[16] Wolfgang Nolting and Anupuru Ramakanth. *Quantum theory of magnetism*, volume 53. Springer Berlin Heidelberg, Berlin, Heidelberg, 2 2009.

[17] Joachim Stöhr and Hans Christoph Siegmann. *Magnetism: From fundamentals to nanoscale dynamics*, volume 152. Springer Berlin Heidelberg, Berlin, Heidelberg, 2006.

[18] Yehuda B. Band and Yshai Avishai. Electronic Properties of Solids. In *Quantum Mechanics with Applications to Nanotechnology and Information Science*, pages 381–544. Elsevier, 2013.

[19] N. F. Mott. A discussion of the transition metals on the basis of quantum mechanics. *Proceedings of the Physical Society*, 47(4):571–588, 1935.

[20] J. C. Slater. The Ferromagnetism of Nickel. *Physical Review*, 49(7):537–545, 4 1936.

[21] E C Stoner. Collective electron ferronmagnetism. *Proceedings of the Royal Society of London. Series A. Mathematical and Physical Sciences*, 165(922):372–414, 4 1938.

[22] A.Y. Morsy, S.S. Fouad, E. Hashem, and A.A. El-Shazly. Optical Properties of Thermally Deposited Bismuth Telluride in the Wavelength Range of 2.5-10 µm. *Acta Physica Polonica A*, 80(6):819–825, 1991.

[23] Robert W. Boyd. *Nonlinear Optics*. Elsevier, 4th edition, 2020.

[24] Peter Y. Yu and Manuel Cardona. *Fundamentals of Semiconductors*, volume 28 of *Graduate Texts in Physics*. Springer Berlin Heidelberg, Berlin, Heidelberg, 4 edition, 2010.

[25] Martin Dressel and George Grüner. *Electrodynamics of Solids*. Cambridge University Press, 1 2002.

[26] P. B. Johnson and R. W. Christy. Optical Constant of the Nobel Metals. *Physical Review B*, 6(12):4370–4379, 1972.

[27] W Lynch and R Rosei. Thermomodulation Spectra of Al, Au, and Cu. *Physical Review B*, 5(10):3883–3894, 1972.

[28] R. Rosei. Temperature modulation of the optical transitions involving the fermi surface in Ag: Theory. *Physical Review B*, 10(2):474–483, 1974.

[29] M. Guerrisi, R. Rosei, and P. Winsemius. Splitting of the interband absorption edge in Au. *Physical Review B*, 12(2):557–563, 1975.

[30] T O Otomalo. *Ultrafast optical response of complex plasmonic nanoparticles*. PhD thesis, Université Paris-Saclay, 2018.

[31] J Lindhard. On the properites of a gas of charged particles. *Dan. Mat. Phys. Medd.*, 28:8, 1954.

[32] James D Patterson and Bernard C Bailey. *Solid-State Physics*. Springer International Publishing, Cham, 2018.

[33] Kohzo Sato and Sadao Adachi. Optical properties of ZnTe. *Journal of Applied Physics*, 73(2):926–931, 1 1993.

[34] A. S. Barker. Transverse and Longitudinal Optic Mode Study in Mg F2. *Physical Review*, 136(5A):A1290–A1295, 11 1964.

[35] R. H. Lyddane, R. G. Sachs, and E. Teller. On the Polar Vibrations of Alkali Halides. *Physical Review*, 59(8):673–676, 4 1941.

[36] Tatsumi Kurosawa. Polarization Waves in Solids. *Journal of the Physical Society of Japan*, 16(7):1298–1308, 7 1961.

[37] A. Leitenstorfer, S. Hunsche, J. Shah, M. C. Nuss, and W. H. Knox. Detectors and sources for ultrabroadband electro-optic sampling: Experiment and theory. *Applied Physics Letters*, 74(11):1516–1518, 1999.

[38] J. Hebling, A. G. Stepanov, G. Almási, B. Bartal, and J. Kuhl. Tunable THz pulse generation by optical rectification of ultrashort laser pulses with tilted pulse fronts. *Applied Physics B: Lasers and Optics*, 78(5):593–599, 2004.

[39] Juejun Hu, Hongtao Lin, Okechukwu Ogbuu, Jifeng Liu, Lin Zhang, and Jurgen Michel. Breaking the energy-bandwidth limit of electro-optic modulators: theory and a device proposal. In *CLEO: 2013*, volume 31, Washington, D.C., 2013. OSA.

[40] Vincent Juvé, Gwenaëlle Vaudel, Zoltan Ollmann, Janos Hebling, Vasily Temnov, Vitalyi Gusev, and Thomas Pezeril. Ultrafast tunable modulation of light polarization at terahertz frequencies. *Optics Letters*, 43(24):5905, 12 2018.

[41] Frank L. Pedrotti, Leno M. Pedrotti, and Leno S. Pedrotti. *Introduction to Optics*. Cambridge University Press, 12 2017.

[42] Steven J. Byrnes. Multilayer optical calculations. *arXiv*, pages 1–20, 3 2016.

[43] Charalambos C. Katsidis and Dimitrios I. Siapkas. General transfer-matrix method for optical multilayer systems with coherent, partially coherent, and incoherent interference. *Applied Optics*, 41(19):3978, 7 2002.

[44] Tom Sebastian Seifert. *Spintronics with Terahertz Radiation : Probing and driving spins at highest frequencies*. PhD thesis, Universitat Berlin, 2018.

[45] E.G. Gamaly and A.V. Rode. Physics of ultra-short laser interaction with matter: From phonon excitation to ultimate transformations. *Progress in Quantum Electronics*, 37(5):215–323, 9 2013.

[46] SI Anisimov, BL Kapeliovich, and TL Perel'man. Electron emission from metal surfaces exposed to ultrashort laser pulses. *Sov. Phys. JETP*, 39(2):375–377, 1974.

[47] T. Q. Qiu and C. L. Tien. Heat Transfer Mechanisms During Short-Pulse Laser Heating of Metals. *Journal of Heat Transfer*, 115(4):835–841, 11 1993.

[48] E. Beaurepaire, J.-C. Merle, A. Daunois, and J.-Y. Bigot. Ultrafast Spin Dynamics in Ferromagnetic Nickel. *Physical Review Letters*, 76(22):4250–4253, 5 1996.

[49] Jean-Yves Bigot, Mircea Vomir, and Eric Beaurepaire. Coherent ultrafast magnetism induced by femtosecond laser pulses. *Nature Physics*, 5(7):515–520, 7 2009.

[50] Hyejin Jang, Luca Marnitz, Torsten Huebner, Johannes Kimling, Timo Kuschel, and David G. Cahill. Thermal Conductivity of Oxide Tunnel Barriers in Magnetic Tunnel Junctions Measured by Ultrafast Thermoreflectance and Magneto-Optic Kerr Effect Thermometry. *Physical Review Applied*, 13(2):024007, 2 2020.

[51] Pui-Wai Ma, S. L. Dudarev, and C. H. Woo. Spin-lattice-electron dynamics simulations of magnetic materials. *Physical Review B*, 85(18):184301, 5 2012.

[52] Aryan Navabi, Cai Chen, Anthony Barra, Mohsen Yazdani, Guoqiang Yu, Mohammad Montazeri, Mohammed Aldosary, Junxue Li, Kin Wong, Qi Hu, Jing Shi, Gregory P Carman,

Abdon E Sepulveda, Pedram Khalili Amiri, and Kang L Wang. Efficient Excitation of High-Frequency Exchange-Dominated Spin Waves in Periodic Ferromagnetic Structures. *Physical Review Applied*, 7(3), 2017.

[53] Xiaoyong Liu, Wenzhe Zhang, Matthew J Carter, and Gang Xiao. Ferromagnetic resonance and damping properties of CoFeB thin films as free layers in MgO-based magnetic tunnel junctions. *Journal of Applied Physics*, 110(3):33910, 2011.

[54] A Conca, B Heinz, M R Schweizer, S Keller, E Th Papaioannou, and B Hillebrands. Lack of correlation between the spin-mixing conductance and the inverse spin Hall effect generated voltages in CoFeB/Pt and CoFeB/Ta bilayers. *Physical Review B*, 95(17):174426, 2017.

[55] B Heinrich, C Burrowes, E Montoya, B Kardasz, E Girt, Young Yeal Song, Yiyan Sun, and Mingzhong Wu. Spin pumping at the magnetic insulator (YIG)/normal metal (Au) interfaces. *Physical Review Letters*, 107(6), 2011.

[56] Zhibin Lin, Leonid V. Zhigilei, and Vittorio Celli. Electron-phonon coupling and electron heat capacity of metals under conditions of strong electron-phonon nonequilibrium. *Physical Review B*, 77(7):075133, 2 2008.

[57] Niladri Chatterji, Ashwin A Tulapurkar, and Bhaskaran Muralidharan. Enhancement of spin-transfer torque switching via resonant tunneling. *Applied Physics Letters*, 105(23):232410, 2014.

[58] Yiwen Cui, Yu Wang, Jie Wu, Xiaokang He, Shouhu Xuan, and Xinglong Gong. Magneto-thermochromic coupling Janus sphere for dual response display. *RSC Advances*, 9(31):17959–17966, 2019.

[59] P. M. Paul, E. S. Toma, P. Breger, G. Mullot, F. Augé, Ph Balcou, H. G. Muller, and P. Agostini. Observation of a train of attosecond pulses from high harmonic generation. *Science*, 292(5522):1689–1692, 2001.

[60] A. L. Cavalieri, N. Müller, Th Uphues, V. S. Yakovlev, A. Baltuška, B. Horvath, B. Schmidt, L. Blümel, R. Holzwarth, S. Hendel, M. Drescher, U. Kleineberg, P. M. Echenique, R. Kienberger, F. Krausz, and U. Heinzmann. Attosecond spectroscopy in condensed matter. *Nature*, 449(7165):1029–1032, 2007.

[61] I. Orfanos, I. Makos, I. Liontos, E. Skantzakis, B. Förg, D. Charalambidis, and P. Tzallas. Attosecond pulse metrology. *APL Photonics*, 4(8), 2019.

[62] A. M. Lindenberg, I. Kang, S. L. Johnson, T. Missalla, P. A. Heimann, Z. Chang, J. Larsson, P. H. Bucksbaum, H. C. Kapteyn, H. A. Padmore, R. W. Lee, J. S. Wark, and R. W. Falcone. Time-resolved X-ray diffraction from coherent phonons during a laser-induced phase transition. *Physical Review Letters*, 84(1):111–114, 2000.

[63] Manuel Joffre. Optique non-linéaire en régimes continu et femtoseconde, 2014.

[64] Donna Strickland and Gerard Mourou. Compression of amplified chirped optical pulses. *Optics Communications*, 56(3):219–221, 12 1985.

[65] Q. Wu and X. C. Zhang. 7 terahertz broadband GaP electro-optic sensor. *Applied Physics Letters*, 70(14):1784–1786, 1997.

[66] H. Hirori, A. Doi, F. Blanchard, and K. Tanaka. Single-cycle terahertz pulses with amplitudes exceeding 1 MV/cm generated by optical rectification in LiNbO3. *Applied Physics Letters*, 98(9):091106, 2 2011.

[67] Arno Schneider, Max Neis, Marcel Stillhart, Blanca Ruiz, Rizwan U. A. Khan, and Peter Günter. Generation of terahertz pulses through optical rectification in organic DAST crystals: theory and experiment. *Journal of the Optical Society of America B*, 23(9):1822, 2006.

[68] H. Hamster, A. Sullivan, S. Gordon, W. White, and R. W. Falcone. Subpicosecond, electromagnetic pulses from intense laser-plasma interaction. *Physical Review Letters*, 71(17):2725–2728, 10 1993.

[69] C. Evain, C. Szwaj, E. Roussel, J. Rodriguez, M. Le Parquier, M. A. Tordeux, F. Ribeiro, M. Labat, N. Hubert, J. B. Brubach, P. Roy, and S. Bielawski. Stable coherent terahertz synchrotron radiation from controlled relativistic electron bunches. *Nature Physics*, 15(7):635–639, 2019.

[70] G. L. Carr, Michael C. Martin, Wayne R. McKinney, K. Jordan, George R. Neil, and G. P. Williams. High-power terahertz radiation from relativistic electrons. *Nature*, 420(6912):153–156, 11 2002.

[71] David R. Bacon, Julien Madéo, and Keshav M. Dani. Photoconductive emitters for pulsed terahertz generation. *Journal of Optics (United Kingdom)*, 23(6), 2021.

[72] David H. Auston and Martin C. Nuss. Electrooptic Generation and Detection of Femtosecond Electrical Transients. *IEEE Journal of Quantum Electronics*, 24(2):184–197, 1988.

[73] D. Grischkowsky, Søren Keiding, Martin van Exter, and Ch. Fattinger. Far-infrared time-domain spectroscopy with terahertz beams of dielectrics and semiconductors. *Journal of the Optical Society of America B*, 7(10):2006, 1990.

[74] P. Uhd Jepsen, R. H. Jacobsen, and S. R. Keiding. Generation and detection of terahertz pulses from biased semiconductor antennas. *Journal of the Optical Society of America B*, 13(11):2424, 1996.

[75] Jianming Dai, Xu Xie, and X. C. Zhang. Detection of broadband terahertz waves with a laser-induced plasma in gases. *Physical Review Letters*, 97(10):8–11, 2006.

[76] Jingle Liu and X. C. Zhang. Terahertz-radiation-enhanced emission of fluorescence from gas plasma. *Physical Review Letters*, 103(23):1–4, 2009.

[77] Ajay Nahata, Aniruddha S. Weling, and Tony F. Heinz. A wideband coherent terahertz spectroscopy system using optical rectification and electro-optic sampling. *Applied Physics Letters*, 69(16):2321–2323, 1996.

[78] G. Gallot, Jiangquan Zhang, R. W. McGowan, Tae In Jeon, and D. Grischkowsky. Measurements of the THz absorption and dispersion of ZnTe and their relevance to the electro-optic detection of THz radiation. *Applied Physics Letters*, 74(23):3450–3452, 1999.

[79] Janos Hebling, Gabor Almasi, Ida Kozma, and Jurgen Kuhl. Velocity matching by pulse front tilting for large area THz-pulse generation. *Optics Express*, 10(21):1161, 2002.

[80] Paul C. M. Planken, Han-Kwang Nienhuys, Huib J. Bakker, and Tom Wenckebach. Measurement and calculation of the orientation dependence of terahertz pulse detection in ZnTe. *Journal of the Optical Society of America B*, 18(3):313, 2001.

[81] Jeremy A. Johnson, Fabian D. J. Brunner, Sebastian Grübel, Andrés Ferrer, Steven L. Johnson, and Thomas Feurer. Distortion-free enhancement of terahertz signals measured by electro-optic sampling II Experiment. *Journal of the Optical Society of America B*, 31(5):1035, 5 2014.

[82] Philipp Krauspe, Natalie Banerji, and Julien Réhault. Effective detection of weak terahertz pulses in electro-optic sampling at kilohertz repetition rate. *Journal of the Optical Society of America B*, 37(1):127, 2020.

[83] Fabian D. J. Brunner, Jeremy A. Johnson, Sebastian Grübel, Andrés Ferrer, Steven L. Johnson, and Thomas Feurer. Distortion-free enhancement of terahertz signals measured by electro-optic sampling I Theory. *Journal of the Optical Society of America B*, 31(4):904, 4 2014.

[84] Tobias Kampfrath, Jan Nötzold, and Martin Wolf. Sampling of broadband terahertz pulses with thick electro-optic crystals. *Applied Physics Letters*, 90(23):1–4, 2007.

[85] D. T. F. Marple. Refractive Index of ZnSe, ZnTe, and CdTe. *Journal of Applied Physics*, 35(3):539–542, 3 1964.

[86] G Gallot and D Grischkowsky. 1999, G Gallot, Electro-optic detection of terahertz radiation.pdf. *Journal of the Optical Society of America B*, 16(8):1204–1212, 1999.

[87] Wengang Bi and Aizhen Li. The dispersion of the refractive index of III-V semiconductors. *Journal of Applied Physics*, 71(6):2826–2829, 1992.

[88] W. L. Faust, C. H. Henry, and R. H. Eick. Dispersion in the nonlinear susceptibility of GaP near the reststrahl band. *Physical Review*, 173(3):781–786, 1968.

[89] W. L. Faust and Charles H. Henry. Mixing of visible and near-resonance infrared light in GaP. *Physical Review Letters*, 17(25):1265–1268, 12 1966.

[90] Andreas Gürtler, Carsten Winnewisser, Hanspeter Helm, and Peter Uhd Jepsen. Terahertz pulse propagation in the near field and the far field. *Journal of the Optical Society of America A*, 17(1):74, 1 2000.

[91] Petr Kužel, Maxim A. Khazan, and Jan Kroupa. Spatiotemporal transformations of ultrashort terahertz pulses. *Journal of the Optical Society of America B*, 16(10):1795, 10 1999.

[92] Jens Neu and Charles A. Schmuttenmaer. Tutorial: An introduction to terahertz time domain spectroscopy (THz-TDS). *Journal of Applied Physics*, 124(23):231101, 12 2018.

[93] Peter Uhd Jepsen and Bernd M. Fischer. Dynamic range in terahertz time-domain transmission and reflection spectroscopy. *Optics Letters*, 30(1):29, 2005.

[94] Jianming Dai, Jiangquan Zhang, Weili Zhang, and D. Grischkowsky. Terahertz time-domain spectroscopy characterization of the far-infrared absorption and index of refraction of high-resistivity, float-zone silicon. *Journal of the Optical Society of America B*, 21(7):1379, 7 2004.

[95] Stefan Sommer, Thomas Raidt, Bernd M. Fischer, Frank Katzenberg, Jörg C. Tiller, and Martin Koch. THz-Spectroscopy on High Density Polyethylene with Different Crystallinity. *Journal of Infrared, Millimeter, and Terahertz Waves*, 37(2):189–197, 2 2016.

[96] M. Naftaly and R. E. Miles. Terahertz time-domain spectroscopy of silicate glasses and the relationship to material properties. *Journal of Applied Physics*, 102(4):1–6, 2007.

[97] Majeed Ali Habeeb and Ahmed Hamza Abbas. Effect of High Density Polyethylene (HDPE) on Structural and Optical Properties of (PP/PMMA) Blends. *International Letters of Chemistry, Physics and Astronomy*, 60(July):94–106, 9 2015.

[98] Cecilie Ro/nne, Lars Thrane, Per-Olof Åstrand, Anders Wallqvist, Kurt V. Mikkelsen, and So/ren R. Keiding. Investigation of the temperature dependence of dielectric relaxation in

liquid water by THz reflection spectroscopy and molecular dynamics simulation. *The Journal of Chemical Physics*, 107(14):5319–5331, 10 1997.

[99] N. Laman and D. Grischkowsky. Terahertz conductivity of thin metal films. *Applied Physics Letters*, 93(5):051105, 8 2008.

[100] T. S. Seifert, N. M. Tran, O. Gueckstock, S. M. Rouzegar, L. Nadvornik, S. Jaiswal, G. Jakob, V. V. Temnov, M. Münzenberg, M. Wolf, M. Kläui, and T. Kampfrath. Terahertz spectroscopy for all-optical spintronic characterization of the spin-Hall-effect metals Pt, W and Cu80Ir20. *Journal of Physics D: Applied Physics*, 51(36), 2018.

[101] Romain Peretti, Sergey Mitryukovskiy, Kevin Froberger, Mohamed Aniss Mebarki, Sophie Eliet, Mathias Vanwolleghem, and Jean Francois Lampin. THz-TDS Time-Trace Analysis for the Extraction of Material and Metamaterial Parameters. *IEEE Transactions on Terahertz Science and Technology*, 9(2):136–149, 2019.

[102] Ken Morita, Kento Shiozawa, Koji Suizu, and Yoshihiro Ishitani. Terahertz pulse generation by the tilted pulse front technique using an M-shaped optical system. *Japanese Journal of Applied Physics*, 57(5), 2018.

[103] C. Thomsen, J. Strait, Z. Vardeny, H. J. Maris, J. Tauc, and J. J. Hauser. Coherent Phonon Generation and Detection by Picosecond Light Pulses. *Physical Review Letters*, 53(10):989–992, 9 1984.

[104] Jay M. Wiesenfeld. Acoustic phonon generation in the picosecond dynamics of dense electron-hole plasmas in InGaAsP films. *Applied Physics Letters*, 47(2):143–145, 7 1985.

[105] G. L. Eesley. Generation of nonequilibrium electron and lattice temperatures in copper by picosecond laser pulses. *Physical Review B*, 33(4):2144–2151, 1986.

[106] Yong Xin Yan, Edward B. Gamble, and Keith A. Nelson. Impulsive stimulated scattering: General importance in femtosecond laser pulse interactions with matter, and spectroscopic applications. *The Journal of Chemical Physics*, 83(11):5391–5399, 1985.

[107] H. J. Zeiger, J. Vidal, T. K. Cheng, E. P. Ippen, G. Dresselhaus, and M. S. Dresselhaus. Theory for displacive excitation of coherent phonons. *Physical Review B*, 45(2):768–778, 1992.

[108] R Merlin. Generating coherent THz phonons with light pulses. *Solid State Communications*, 102(2-3):207–220, 4 1997.

[109] C. Thomsen, H. T. Grahn, H. J. Maris, and J. Tauc. Picosecond interferometric technique for study of phonons in the brillouin frequency range. *Optics Communications*, 60(1-2):55–58, 1986.

[110] M Weis, K Balin, R Rapacz, A Nowak, M Lejman, J Szade, and P Ruello. Ultrafast light-induced coherent optical and acoustic phonons in few quintuple layers of the topological insulator Bi2Te3. *Physical Review B - Condensed Matter and Materials Physics*, 92(1):014301, 7 2015.

[111] Mariusz Lejman, Gwenaelle Vaudel, Ingrid C Infante, Ievgeniia Chaban, Thomas Pezeril, Mathieu Edely, Guillaume F Nataf, Mael Guennou, Jens Kreisel, Vitalyi E Gusev, Brahim Dkhil, and Pascal Ruello. Ultrafast acousto-optic mode conversion in optically birefringent ferroelectrics. *Nature Communications*, 7:1–10, 2016.

[112] A. A. Maznev, F. Bencivenga, A. Cannizzo, F. Capotondi, R. Cucini, R. A. Duncan, T. Feurer, T. D. Frazer, L. Foglia, H. M. Frey, H. Kapteyn, J. Knobloch, G. Knopp, C. Masciovecchio, R. Mincigrucci, G. Monaco, M. Murnane, I. Nikolov, E. Pedersoli, A. Simoncig, A. Vega-Flick, and K. A. Nelson. Generation of coherent phonons by coherent extreme ultraviolet radiation in a transient grating experiment. *Applied Physics Letters*, 113(22), 2018.

[113] A. A. Maznev, R. Mincigrucci, F. Bencivenga, V. Unikandanunni, F. Capotondi, G. Chen, Z. Ding, R. A. Duncan, L. Foglia, M. G. Izzo, C. Masciovecchio, A. Martinelli, G. Monaco, E. Pedersoli, S. Bonetti, and K. A. Nelson. Generation and detection of 50 GHz surface acoustic waves by extreme ultraviolet pulses. *Applied Physics Letters*, 119(4):1ENG, 2021.

[114] József András Fülöp, Stelios Tzortzakis, and Tobias Kampfrath. Laser-Driven Strong-Field Terahertz Sources. *Advanced Optical Materials*, 8(3):1–25, 2020.

[115] Daniele Nicoletti and Andrea Cavalleri. Nonlinear light–matter interaction at terahertz frequencies. *Advances in Optics and Photonics*, 8(3):401, 2016.

[116] W. Kuehn, P. Gaal, K. Reimann, M. Woerner, T. Elsaesser, and R. Hey. Terahertz-induced interband tunneling of electrons in GaAs. *Physical Review B - Condensed Matter and Materials Physics*, 82(7):1–8, 2010.

[117] O Schubert, M Hohenleutner, F Langer, B Urbanek, C Lange, U Huttner, D Golde, T Meier, M Kira, S W Koch, and R Huber. Sub-cycle control of terahertz high-harmonic generation by dynamical Bloch oscillations. *Nature Photonics*, 8(2):119–123, 2 2014.

[118] H. Hirori, K. Shinokita, M. Shirai, S. Tani, Y. Kadoya, and K. Tanaka. Extraordinary carrier multiplication gated by a picosecond electric field pulse. *Nature Communications*, 2(1):8–13, 2011.

[119] Tobias Kampfrath, Alexander Sell, Gregor Klatt, Alexej Pashkin, Sebastian Mährlein, Thomas Dekorsy, Martin Wolf, Manfred Fiebig, Alfred Leitenstorfer, and Rupert Huber. Coherent terahertz control of antiferromagnetic spin waves. *Nature Photonics*, 5(1):31–34, 1 2011.

[120] J. M. Manceau, P. A. Loukakos, and S. Tzortzakis. Direct acoustic phonon excitation by intense and ultrashort terahertz pulses. *Applied Physics Letters*, 97(25), 2010.

[121] W. Grill and O. Weis. Excitation of Coherent and Incoherent Terahertz Phonon Pulses in Quartz Using Infrared Laser Radiation. *Physical Review Letters*, 35(9):588–591, 9 1975.

[122] T. Huber, M. Ranke, A. Ferrer, L. Huber, and S. L. Johnson. Coherent phonon spectroscopy of non-fully symmetric modes using resonant terahertz excitation. *Applied Physics Letters*, 107(9):091107, 8 2015.

[123] Sebastian Maehrlein, Alexander Paarmann, Martin Wolf, and Tobias Kampfrath. Terahertz Sum-Frequency Excitation of a Raman-Active Phonon. *Physical Review Letters*, 119(12):127402, 9 2017.

[124] A. A. Melnikov, K. N. Boldyrev, Yu G. Selivanov, V. P. Martovitskii, S. V. Chekalin, and E. A. Ryabov. Coherent phonons in a Bi2Se3 film generated by an intense single-cycle THz pulse. *Physical Review B*, 97(21):214304, 6 2018.

[125] A. A. Melnikov, Yu G. Selivanov, and S. V. Chekalin. Phonon-driven ultrafast symmetry lowering in a Bi2Se3 crystal. *Physical Review B*, 102(22):1–9, 2020.

[126] D. L. Mills. Ionic contributions to the Raman tensor of insulators. *Physical Review B*, 35(17):9278–9283, 1987.

[127] Dominik M. Juraschek and Sebastian F. Maehrlein. Sum-frequency ionic Raman scattering. *Physical Review B*, 97(17):174302, 5 2018.

[128] Vitalyi E Gusev and A.A. Karabutov. *Laser Optoacoustics*. American Inst. of Physics, 12 1993.

[129] Pascal Ruello and Vitalyi E. Gusev. Physical mechanisms of coherent acoustic phonons generation by ultrafast laser action. *Ultrasonics*, 56:21–35, 2015.

[130] Thomas Czerniuk. *Picosecond Ultrasonics for the Modulation and Nanoscopy of Semiconductor Lasers*. PhD thesis, TU Dortmund, 2017.

[131] C. Thomsen, H. T. Grahn, H. J. Maris, and J. Tauc. Surface generation and detection of phonons by picosecond light pulses. *Physical Review B*, 34(6):4129–4138, 1986.

[132] Pierre-Adrien Mante, Constantinos C. Stoumpos, Mercouri G. Kanatzidis, and Arkady Yartsev. Electron–acoustic phonon coupling in single crystal CH3NH3PbI3 perovskites revealed by coherent acoustic phonons. *Nature Communications*, 8(1):14398, 4 2017.

[133] M. Perner, S. Gresillon, J. März, G. von Plessen, J. Feldmann, J. Porstendorfer, K.-J. Berg, and G. Berg. Observation of Hot-Electron Pressure in the Vibration Dynamics of Metal Nanoparticles. *Physical Review Letters*, 85(4):792–795, 7 2000.

[134] O. B. Wright and V. E. Gusev. Acoustic generation in crystalline silicon with femtosecond optical pulses. *Applied Physics Letters*, 1190(1995):1190, 1995.

[135] A. Levchuk, B. Wilk, G. Vaudel, F. Labbé, B. Arnaud, K. Balin, J. Szade, P. Ruello, and V. Juvé. Coherent acoustic phonons generated by ultrashort terahertz pulses in nanofilms of metals and topological insulators. *Physical Review B*, 101(18):180102, 5 2020.

[136] Haijun Zhang, Chao Xing Liu, Xiao Liang Qi, Xi Dai, Zhong Fang, and Shou Cheng Zhang. Topological insulators in Bi 2 Se 3, Bi 2 Te 3 and Sb 2 Te 3 with a single Dirac cone on the surface. *Nature Physics*, 5(6):438–442, 2009.

[137] C. B. Satterthwaite and R. W. Ure. Electrical and thermal properties of Bi2 Te3. *Physical Review*, 108(5):1164–1170, 12 1957.

[138] Dambi Park, Sungjin Park, Kwangsik Jeong, Hong-Sik Jeong, Jea Yong Song, and Mann–Ho Cho. Thermal and Electrical Conduction of Single-crystal Bi2Te3 Nanostructures grown using a one step process. *Scientific Reports*, 6(1):19132, 5 2016.

[139] Ian T. Witting, Thomas C. Chasapis, Francesco Ricci, Matthew Peters, Nicholas A. Heinz, Geoffroy Hautier, and G. Jeffrey Snyder. The Thermoelectric Properties of Bismuth Telluride. *Advanced Electronic Materials*, 5(6):1–20, 2019.

[140] H.-J. Noh, H. Koh, S.-J. Oh, J.-H. Park, H.-D. Kim, J. D. Rameau, T. Valla, T. E. Kidd, P. D. Johnson, Y. Hu, and Q. Li. Spin-orbit interaction effect in the electronic structure of Bi 2 Te 3 observed by angle-resolved photoemission spectroscopy. *EPL (Europhysics Letters)*, 81(5):57006, 3 2008.

[141] M. Z. Hasan and C. L. Kane. Colloquium: Topological insulators. *Reviews of Modern Physics*, 82(4):3045–3067, 2010.

[142] M. Weis, K. Balin, B. Wilk, T. Sobol, A. Ciavardini, G. Vaudel, V. Juvé, B. Arnaud, B. Ressel, M. Stupar, K. C. Prince, G. De Ninno, P. Ruello, and J. Szade. Hot-carrier and

optical-phonon ultrafast dynamics in the topological insulator Bi 2 Te 3 upon iron deposition on its surface . *Physical Review B*, 104(24):1–12, 2021.

[143] D. L. Greenaway and G. Harbeke. Band structure of bismuth telluride, bismuth selenide and their respective alloys. *Journal of Physics and Chemistry of Solids*, 26(10):1585–1604, 1965.

[144] M Weis, B Wilk, G Vaudel, K Balin, R Rapacz, A Bulou, B Arnaud, J Szade, and P. Ruello. Quantum size effect on charges and phonons ultrafast dynamics in atomically controlled nanolayers of topological insulators Bi2Te3. *Scientific Reports*, 7(1):13782, 12 2017.

[145] Mateusz Weis. *Growth and spectroscopic studies (continuous and time-resolved) of ultrathin films of topological insulators*. PhD thesis, Le Mans, 2019.

[146] Carolyn A. Paddock and Gary L. Eesley. Transient thermoreflectance from thin metal films. *Journal of Applied Physics*, 60(1):285–290, 1986.

[147] David G. Cahill, Wayne K. Ford, Kenneth E. Goodson, Gerald D. Mahan, Arun Majumdar, Humphrey J. Maris, Roberto Merlin, and Simon R. Phillpot. Nanoscale thermal transport. *Journal of Applied Physics*, 93(2):793–818, 2003.

[148] T. Saito, O. Matsuda, and O. B. Wright. Picosecond acoustic phonon pulse generation in nickel and chromium. *Physical Review B*, 67(20):205421, 5 2003.

[149] Kazuo Watabe, Pavel Polynkin, and Masud Mansuripur. Optical pump-and-probe test system for thermal characterization of thin metal and phase-change films. *Applied Optics*, 44(16):3167–3173, 2005.

[150] Y. H. Wang, D. Hsieh, E. J. Sie, H. Steinberg, D. R. Gardner, Y. S. Lee, P. Jarillo-Herrero, and N. Gedik. Measurement of Intrinsic Dirac Fermion Cooling on the Surface of the Topological Insulator Bi2Se3 Using Time-Resolved and Angle-Resolved Photoemission Spe. *Physical Review Letters*, 109(12):127401, 9 2012.

[151] D. Hsieh, F. Mahmood, J. W. McIver, D. R. Gardner, Y. S. Lee, and N. Gedik. Selective probing of photoinduced charge and spin dynamics in the bulk and surface of a topological insulator. *Physical Review Letters*, 107(7):1–5, 2011.

[152] Yuri D. Glinka, Sercan Babakiray, Trent A. Johnson, Alan D. Bristow, Mikel B. Holcomb, and David Lederman. Ultrafast carrier dynamics in thin-films of the topological insulator Bi 2 Se 3. *Applied Physics Letters*, 103(15):151903, 10 2013.

[153] O. V. Misochko, J. Flock, and T. Dekorsy. Polarization dependence of coherent phonon generation and detection in the three-dimensional topological insulator B i2 T e3. *Physical Review B - Condensed Matter and Materials Physics*, 91(17):174303, 5 2015.

[154] D. J. Orzi, G. M. Bilmes, J. O. Tocho, N. Mingolo, and O. E. Martínez. Photoacoustic characterization of phase transitions in amorphous metal alloys. *Applied Physics B: Lasers and Optics*, 66(2):245–249, 1998.

[155] Yaguo Wang, Carl Liebig, Xianfan Xu, and Rama Venkatasubramanian. Acoustic phonon scattering in Bi2 Te3 / Sb 2 Te3 superlattices. *Applied Physics Letters*, 97(8):1–4, 2010.

[156] Aleksandar D. Rakić, Aleksandra B. Djurišić, Jovan M Elazar, and Marian L Majewski. Optical properties of metallic films for vertical-cavity optoelectronic devices. *Applied Optics*, 37(22):5271, 8 1998.

[157] Rafał Rapacz, Katarzyna Balin, Anna Nowak, and Jacek Szade. Spectroscopic characterization of high-purity polycrystalline Bi-Te films grown by thermal evaporation. *Journal of Crystal Growth*, 401:567–572, 2014.

[158] C. Voisin, N. Del Fatti, D. Christofilos, and F. Vallée. Time-resolved investigation of the vibrational dynamics of metal nanoparticles. *Applied Surface Science*, 164(1-4):131–139, 9 2000.

[159] Vincent Juvé, Aurélien Crut, Paolo Maioli, Michel Pellarin, Michel Broyer, Natalia Del Fatti, and Fabrice Vallée. Probing Elasticity at the Nanoscale: Terahertz Acoustic Vibration of Small Metal Nanoparticles. *Nano Letters*, 10(5):1853–1858, 5 2010.

[160] M. Först and T. Dekorsy. Coherent Phonons in Bulk and Low-Dimensional Semiconductors. In *Coherent Vibrational Dynamics.*, page 129–172. Taylor & Francis Group, 2008.

[161] Thomas Dekorsy, Gyu Cheon Cho, and Heinrich Kurz. Coherent phonons in condensed media. In *Light Scattering in Solids VIII*, volume 112, pages 169–209. Springer Berlin Heidelberg, 2008.

[162] Alaska Subedi, Andrea Cavalleri, and Antoine Georges. Theory of nonlinear phononics for coherent light control of solids. *Physical Review B - Condensed Matter and Materials Physics*, 89(22):1–5, 2014.

[163] T. K. Cheng, J. Vidal, H. J. Zeiger, G. Dresselhaus, M. S. Dresselhaus, and E. P. Ippen. Mechanism for displacive excitation of coherent phonons in Sb, Bi, Te, and Ti2O3. *Applied Physics Letters*, 59(16):1923–1925, 1991.

[164] A. V. Kuznetsov and C. J. Stanton. Theory of coherent phonon oscillations in semiconductors. *Physical Review Letters*, 73(24):3243–3246, 1994.

[165] Dominik M. Juraschek. *Coherent Optical Phononics*. PhD thesis, ETH Zurich, 2018.

[166] M. Först, C. Manzoni, S. Kaiser, Y. Tomioka, Y. Tokura, R. Merlin, and A. Cavalleri. Nonlinear phononics as an ultrafast route to lattice control. *Nature Physics*, 7(11):854–856, 2011.

[167] Dirk Porezag and Mark R. Pederson. Infrared intensities and Raman-scattering activities within density-functional theory. *Physical Review B - Condensed Matter and Materials Physics*, 54(11):7830–7836, 1996.

[168] T. K. Cheng, S. D. Brorson, A. S. Kazeroonian, J. S. Moodera, G. Dresselhaus, M. S. Dresselhaus, and E. P. Ippen. Impulsive excitation of coherent phonons observed in reflection in bismuth and antimony. *Applied Physics Letters*, 57(10):1004–1006, 1990.

[169] Matteo Rini, Ra'anan Tobey, Nicky Dean, Jiro Itatani, Yasuhide Tomioka, Yoshinori Tokura, Robert W. Schoenlein, and Andrea Cavalleri. Control of the electronic phase of a manganite by mode-selective vibrational excitation. *Nature*, 449(7158):72–74, 2007.

[170] W. Kullmann, J. Geurts, W. Richter, N. Lehner, H. Rauh, U. Steigenberger, G. Eichhorn, and R. Geick. Effect of Hydrostatic and Uniaxial Pressure on Structural Properties and Raman Active Lattice Vibrations in Bi2Te3. *physica status solidi (b)*, 125(1):131–138, 9 1984.

[171] W. Richter and C. R. Becker. A Raman and far-infrared investigation of phonons in the rhombohedral V2–VI3 compounds Bi2Te3, Bi2Se3, Sb2Te3 and Bi2(Te1-xSex)3, (Bi1-ySby). *Physica Status Solidi (b)*, 84(2):619–628, 12 1977.

[172] Yaguo Wang, Liang Guo, Xianfan Xu, Jonathan Pierce, and Rama Venkatasubramanian. Origin of coherent phonons in Bi2Te3 excited by ultrafast laser pulses. *Physical Review B*, 88(6):064307, 8 2013.

[173] Claude E. Shannon. Commnunication theory in the presence of noise. *Proceedings of the IRE*, 37(1):10–21, 1949.

[174] Jian Yuan, Meng Zhao, Wengzhi Yu, Yao Lu, Caiyun Chen, Meng Xu, Shaojuan Li, Kian Loh, and Bao Qiaoliang. Raman Spectroscopy of Two-Dimensional Bi2TexSe3x Platelets Produced by Solvothermal Method. *Materials*, 8(8):5007–5017, 8 2015.

[175] S. Kovalev, K. J. Tielrooij, J. C. Deinert, I. Ilyakov, N. Awari, M. Chen, A. Ponomaryov, M. Bawatna, T. V.A.G. de Oliveira, L. M. Eng, K. A. Kuznetsov, D. A. Safronenkov, G. Kh Kitaeva, P. I. Kuznetsov, H. A. Hafez, D. Turchinovich, and M. Gensch. Terahertz signatures of ultrafast Dirac fermion relaxation at the surface of topological insulators. *npj Quantum Materials*, 6(1):1–6, 2021.

[176] Lukas Braun. *Electron and Phonon Dynamics in Topological Insulators at THz Frequencies*. PhD thesis, Freien Universitat Berlin, 2016.

[177] S. Meyer, Y. T. Chen, S. Wimmer, M. Althammer, T. Wimmer, R. Schlitz, S. Geprags, H. Huebl, D. Kodderitzsch, H. Ebert, G. E.W. Bauer, R. Gross, and S. T.B. Goennenwein. Observation of the spin Nernst effect. *Nature Materials*, 16(10):97–981, 2017.

[178] Matthias C. Hoffmann, Nathaniel C. Brandt, Harold Y. Hwang, Ka Lo Yeh, and Keith A. Nelson. Terahertz Kerr effect. *Applied Physics Letters*, 95(23):2007–2010, 2009.

[179] W. Kuehn, K. Reimann, M. Woerner, T. Elsaesser, R. Hey, and U. Schade. Strong correlation of electronic and lattice excitations in GaAs/AlGaAs semiconductor quantum wells revealed by two-dimensional terahertz spectroscopy. *Physical Review Letters*, 107(6):2–6, 2011.

[180] Sarah Houver, L. Huber, M. Savoini, E. Abreu, and S. L. Johnson. 2D THz spectroscopic investigation of ballistic conduction-band electron dynamics in InSb. *International Conference on Infrared, Millimeter, and Terahertz Waves, IRMMW-THz*, 2019-Septe(8):10854–10865, 4 2019.

[181] Wonjune Choi, Ki Hoon Lee, and Yong Baek Kim. Theory of Two-Dimensional Nonlinear Spectroscopy for the Kitaev Spin Liquid. *Physical Review Letters*, 124(11):117205, 2020.

[182] Anders Andrae and Tomas Edler. On Global Electricity Usage of Communication Technology: Trends to 2030. *Challenges*, 6(1):117–157, 4 2015.

[183] Jorge Puebla, Junyeon Kim, Kouta Kondou, and Yoshichika Otani. Spintronic devices for energy-efficient data storage and energy harvesting. *Communications Materials*, 1(1):24, 12 2020.

[184] S. Sangiao, J. M. De Teresa, L. Morellon, I. Lucas, M. C. Martinez-Velarte, and M. Viret. Control of the spin to charge conversion using the inverse Rashba-Edelstein effect. *Applied Physics Letters*, 106(17):1–5, 2015.

[185] X. R. Wang. Anomalous spin Hall and inverse spin Hall effects in magnetic systems. *Communications Physics*, 4(1), 2021.

[186] B. F. Miao, S. Y. Huang, D. Qu, and C. L. Chien. Inverse Spin Hall Effect in a Ferromagnetic Metal. *Physical Review Letters*, 111(6):066602, 8 2013.

[187] S. D. Ganichev, E. L. Ivchenko, V. V. Bel'kov, S. A. Tarasenko, M. Sollinger, D. Weiss, W. Wegscheider, and W. Prettl. Spin-galvanic effect. *Nature*, 417(6885):153–156, 5 2002.

[188] Dai Tian, Yufan Li, D. Qu, Xiaofeng Jin, and C. L. Chien. Separation of spin Seebeck effect and anomalous Nernst effect in Co/Cu/YIG. *Applied Physics Letters*, 106(21):1–5, 2015.

[189] T. C. Chuang, P. L. Su, P. H. Wu, and S. Y. Huang. Enhancement of the anomalous Nernst effect in ferromagnetic thin films. *Physical Review B*, 96(17):1–5, 2017.

[190] M. Lakshmanan. The fascinating world of the Landau–Lifshitz–Gilbert equation: an overview. *Philosophical Transactions of the Royal Society A: Mathematical, Physical and Engineering Sciences*, 369(1939):1280–1300, 3 2011.

[191] T.L. Gilbert. Classics in Magnetics A Phenomenological Theory of Damping in Ferromagnetic Materials. *IEEE Transactions on Magnetics*, 40(6):3443–3449, 11 2004.

[192] A. Brataas, Y. Tserkovnyak, G. E. W. Bauer, and P. J. Kelly. *Spin pumping and spin transfer*, volume 1. Oxford University Press, 12 2017.

[193] R. H. Silsbee, A. Janossy, and P. Monod. Coupling between ferromagnetic and conduction-spin-resonance modes at a ferromagnetic—normal-metal interface. *Physical Review B*, 19(9):4382–4399, 5 1979.

[194] Yongbing Xu, David D. Awschalom, and Junsaku Nitta. *Handbook of Spintronics*. Springer Netherlands, Dordrecht, 2014.

[195] Diogo Castro Vaz. *Spin-to-charge current conversion in SrTiO3-based two-dimensional electron gases*. PhD thesis, Sorbonne Université École, 2020.

[196] Paul Noel. *Dynamical spin injection and spin to charge current conversion in oxide-based Rashba interfaces and topological insulators*. PhD thesis, Grenoble University, 2020.

[197] Junren Shi, Ping Zhang, Di Xiao, and Qian Niu. Proper Definition of Spin Current in Spin-Orbit Coupled Systems. *Physical Review Letters*, 96(7):076604, 2 2006.

[198] Z. An, F. Q. Liu, Y. Lin, and C. Liu. The universal definition of spin current. *Scientific Reports*, 2:1–6, 2012.

[199] Franz Dominik Czeschka. *Spin Currents in Metallic Nanostructures*. PhD thesis, Technische Universität München, 2011.

[200] S. Y. Huang, D. Qu, T. C. Chuang, C. C. Chiang, W. Lin, and C. L. Chien. Pure spin current phenomena. *Applied Physics Letters*, 117(19), 2020.

[201] Jack Bass and William P. Pratt. Spin-diffusion lengths in metals and alloys, and spin-flipping at metal/metal interfaces: an experimentalist's critical review. *Journal of Physics: Condensed Matter*, 19(18):183201, 5 2007.

[202] R. J. Elliott. Theory of the Effect of Spin-Orbit Coupling on Magnetic Resonance in Some Semiconductors. *Physical Review*, 96(2):266–279, 10 1954.

[203] M M Glazov and E L Ivchenko. D'yakonov-Perel' spin relaxation controlled by electron-electron scattering, 2003.

[204] E. H. Hall. On a New Action of the Magnet on Electric Currents. *American Journal of Mathematics*, 2(3):287, 9 1879.

[205] E.H. Hall. XVIII. On the "Rotational Coefficient" in nickel and cobalt. *The London, Edinburgh, and Dublin Philosophical Magazine and Journal of Science*, 12(74):157–172, 9 1881.

[206] Emerson M. Pugh and T. W. Lippert. Hall e.m.f. and Intensity of Magnetization. *Physical Review*, 42(5):709–713, 12 1932.

[207] Emerson M. Pugh and Norman Rostoker. Hall Effect in Ferromagnetic Materials. *Reviews of Modern Physics*, 25(1):151–157, 1 1953.

[208] Naoto Nagaosa, Jairo Sinova, Shigeki Onoda, A. H. MacDonald, and N. P. Ong. Anomalous Hall effect. *Reviews of Modern Physics*, 82(2):1539–1592, 5 2010.

[209] Robert Karplus and J. M. Luttinger. Hall effect in ferromagnetics. *Physical Review*, 95(5):1154–1160, 9 1954.

[210] N. P. ONG and WEI-LI LEE. GEOMETRY AND THE ANOMALOUS HALL EFFECT IN FERROMAGNETS. *Foundations of Quantum Mechanics in the Light of New Technology*, 3:121–126, 6 2006.

[211] Jairo Sinova, Sergio O. Valenzuela, J. Wunderlich, C. H. Back, and T. Jungwirth. Spin Hall effects. *Reviews of Modern Physics*, 87(4):1213–1260, 10 2015.

[212] M.I. Dyakonov and V.I. Perel. Current-induced spin orientation of electrons in semiconductors. *Physics Letters A*, 35(6):459–460, 7 1971.

[213] Yaroslav Tserkovnyak, Arne Brataas, and Gerrit E.W. Bauer. Spin pumping and magnetization dynamics in metallic multilayers. *Physical Review B - Condensed Matter and Materials Physics*, 66(22):1–10, 2002.

[214] D. Qu, S. Y. Huang, B. F. Miao, S. X. Huang, and C. L. Chien. Self-consistent determination of spin Hall angles in selected 5d metals by thermal spin injection. *Physical Review B*, 89(14):140407, 4 2014.

[215] H. Nakayama, M. Althammer, Y. T. Chen, K. Uchida, Y. Kajiwara, D. Kikuchi, T. Ohtani, S. Geprägs, M. Opel, S. Takahashi, R. Gross, G. E.W. Bauer, S. T.B. Goennenwein, and E. Saitoh. Spin Hall Magnetoresistance Induced by a Nonequilibrium Proximity Effect. *Physical Review Letters*, 110(20):1–5, 2013.

[216] Luqiao Liu, Takahiro Moriyama, D. C. Ralph, and R. A. Buhrman. Spin-torque ferromagnetic resonance induced by the spin Hall effect. *Physical Review Letters*, 106(3):1–4, 2011.

[217] I. A. Nechaev, M. F. Jensen, E. D.L. Rienks, V. M. Silkin, P. M. Echenique, E. V. Chulkov, and Ph Hofmann. Hole dynamics in a two-dimensional spin-orbit coupled electron system: Theoretical and experimental study of the Au(111) surface state. *Physical Review B - Condensed Matter and Materials Physics*, 80(11):1–4, 2009.

[218] A.G. Aronov and Yu. B. Lyanda-Geller. Nuclear electric resonance and orientation of carrier spins by an electric field. *Soviet Journal of Experimental and Theoretical Physics Letters*, 50:431, 1989.

[219] J. C.Rojas Sánchez, L. Vila, G. Desfonds, S. Gambarelli, J. P. Attané, J. M. De Teresa, C. Magén, and A. Fert. Spin-to-charge conversion using Rashba coupling at the interface between non-magnetic materials. *Nature Communications*, 4:1–7, 2013.

[220] K. Uchida, S. Takahashi, K. Harii, J. Ieda, W. Koshibae, K. Ando, S. Maekawa, and E. Saitoh. Observation of the spin Seebeck effect. *Nature*, 455(7214):778–781, 10 2008.

[221] A. v. Ettingshausen and W. Nernst. Ueber das Auftreten electromotorischer Kräfte in Metallplatten, welche von einem Wärmestrome durchflossen werden und sich im magnetischen Felde befinden. *Annalen der Physik und Chemie*, 265(10):343–347, 1886.

[222] Gerrit E. W. Bauer, Eiji Saitoh, and Bart J. van Wees. Spin caloritronics. *Nature Materials*, 11(5):391–399, 5 2012.

[223] D. Qu, S. Y. Huang, and C. L. Chien. Inverse spin Hall effect in Cr: Independence of antiferromagnetic ordering. *Physical Review B*, 92(2):020418, 7 2015.

[224] Hiroto Adachi, Ken Ichi Uchida, Eiji Saitoh, and Sadamichi Maekawa. Theory of the spin Seebeck effect. *Reports on Progress in Physics*, 76(3), 2013.

[225] A. Slachter, F. L. Bakker, J. P. Adam, and B. J. Van Wees. Thermally driven spin injection from a ferromagnet into a non-magnetic metal. *Nature Physics*, 6(11):879–882, 2010.

[226] A. Bose and Ashwin A. Tulapurkar. Recent advances in the spin Nernst effect. *Journal of Magnetism and Magnetic Materials*, 491(June):165526, 2019.

[227] Yuya Sakuraba. Potential of thermoelectric power generation using anomalous Nernst effect in magnetic materials. *Scripta Materialia*, 111:29–32, 1 2016.

[228] Shu Guang Cheng, Yanxia Xing, Qing Feng Sun, and X. C. Xie. Spin Nernst effect and Nernst effect in two-dimensional electron systems. *Physical Review B - Condensed Matter and Materials Physics*, 78(4):1–5, 2008.

[229] A. Bose, S. Bhuktare, H. Singh, S. Dutta, V. G. Achanta, and A. A. Tulapurkar. Direct detection of spin Nernst effect in platinum. *Applied Physics Letters*, 112(16), 2018.

[230] Peng Sheng, Yuya Sakuraba, Yong Chang Lau, Saburo Takahashi, Seiji Mitani, and Masamitsu Hayashi. The spin Nernst effect in tungsten. *Science Advances*, 3(11):1–8, 2017.

[231] Ken Ichi Uchida, Tatsumi Nonaka, Takeru Ota, and Eiji Saitoh. Longitudinal spin-Seebeck effect in sintered polycrystalline (Mn,Zn) Fe2 O4. *Applied Physics Letters*, 97(26):3–5, 2010.

[232] Jinhui Shen, Zheng Feng, Pengchao Xu, Dazhi Hou, Yang Gao, and Xiaofeng Jin. Spin-to-Charge Conversion in Ag/Bi Bilayer Revisited. *Physical Review Letters*, 126(19):197201, 5 2021.

[233] Zheng Feng, Hongsong Qiu, Dacheng Wang, Caihong Zhang, Song Sun, Biaobing Jin, and Wei Tan. Spintronic terahertz emitter. *Journal of Applied Physics*, 129(1):010901, 1 2021.

[234] Matthias B. Jungfleisch, Qi Zhang, Wei Zhang, John E. Pearson, Richard D. Schaller, Haidan Wen, and Axel Hoffmann. Control of Terahertz Emission by Ultrafast Spin-Charge Current Conversion at Rashba Interfaces. *Physical Review Letters*, 120(20):207207, 2018.

[235] Qi Zhang, Ziyan Luo, Hong Li, Yumeng Yang, Xinhai Zhang, and Yihong Wu. Terahertz Emission from Anomalous Hall Effect in a Single-Layer Ferromagnet. *Physical Review Applied*, 12(5):054027, 11 2019.

[236] M Battiato, K Carva, and P M Oppeneer. Superdiffusive spin transport as a mechanism of ultrafast demagnetization. *Physical Review Letters*, 105(2), 2010.

[237] Alexey Melnikov, Ilya Razdolski, Tim O Wehling, Evangelos Th Papaioannou, Vladimir Roddatis, Paul Fumagalli, Oleg Aktsipetrov, Alexander I Lichtenstein, and Uwe Bovensiepen. Ultrafast transport of laser-excited spin-polarized carriers in Au/Fe/MgO(001). *Physical Review Letters*, 107(7), 2011.

[238] T H Dang, J Hawecker, E Rongione, G. Baez Flores, D. Q. To, J. C. Rojas-Sanchez, H. Nong, J. Mangeney, J. Tignon, F. Godel, S. Collin, P. Seneor, M. Bibes, A. Fert, M. Anane, J. M. George, L. Vila, M. Cosset-Cheneau, D. Dolfi, R. Lebrun, P. Bortolotti, K. Belashchenko, S. Dhillon, and H. Jaffrès. Ultrafast spin-currents and charge conversion at 3 d-5 d interfaces probed by time-domain terahertz spectroscopy. *Applied Physics Reviews*, 7(4):41409, 2020.

[239] Jacques Hawecker, Thi Huong Dang, Enzo Rongione, James Boust, Sophie Collin, Jean Marie George, Henri Jean Drouhin, Yannis Laplace, Romain Grasset, Jingwei Dong, Juliette Mangeney, Jerome Tignon, Henri Jaffrès, Luca Perfetti, and Sukhdeep Dhillon. Spin Injection

Efficiency at Metallic Interfaces Probed by THz Emission Spectroscopy. *Advanced Optical Materials*, 9(17), 9 2021.

[240] Dennis M Nenno, Rolf Binder, and Hans Christian Schneider. Simulation of Hot-Carrier Dynamics and Terahertz Emission in Laser-Excited Metallic Bilayers. *Physical Review Applied*, 11(5):54083, 2019.

[241] Wen Tian Lu, Yawen Zhao, Marco Battiato, Yizheng Wu, and Zhe Yuan. Interface reflectivity of a superdiffusive spin current in ultrafast demagnetization and terahertz emission. *Physical Review B*, 101(1):14435, 2020.

[242] T. Seifert, S. Jaiswal, U. Martens, J. Hannegan, L. Braun, P. Maldonado, F. Freimuth, A. Kronenberg, J. Henrizi, I. Radu, E. Beaurepaire, Y. Mokrousov, P. M. Oppeneer, M. Jourdan, G. Jakob, D. Turchinovich, L. M. Hayden, M. Wolf, M. Münzenberg, M. Kläui, and T. Kampfrath. Efficient metallic spintronic emitters of ultrabroadband terahertz radiation. *Nature Photonics*, 10(7):483–488, 2016.

[243] G. Li, R. V. Mikhaylovskiy, K. A. Grishunin, J. D. Costa, Th Rasing, and A. V. Kimel. Laser induced THz emission from femtosecond photocurrents in Co/ZnO/Pt and Co/Cu/Pt multilayers. *Journal of Physics D: Applied Physics*, 51(13), 2018.

[244] Hui Zhang, Zheng Feng, Jine Zhang, He Bai, Huaiwen Yang, Jianwang Cai, Weisheng Zhao, Wei Tan, Fengxia Hu, Baogen Shen, and Jirong Sun. Laser pulse induced efficient terahertz emission from Co/Al heterostructures. *Physical Review B*, 102(2):1–7, 7 2020.

[245] Dewang Yang, Jianhui Liang, Chao Zhou, Lu Sun, Ronger Zheng, Shengnian Luo, Yizheng Wu, and Jingbo Qi. Powerful and Tunable THz Emitters Based on the Fe/Pt Magnetic Heterostructure. *Advanced Optical Materials*, 4(12):1944–1949, 12 2016.

[246] Y. Sasaki, K. Z. Suzuki, and S. Mizukami. Annealing effect on laser pulse-induced THz wave emission in Ta/CoFeB/MgO films. *Applied Physics Letters*, 111(10):1–6, 2017.

[247] Yuta Sasaki, Yukiko Takahashi, and Shinya Kasai. Laser-induced terahertz emission in Co 2 MnSi/Pt structure. *Applied Physics Express*, 13(9):093003, 9 2020.

[248] G. Li, R. Medapalli, R. V. Mikhaylovskiy, F. E. Spada, Th Rasing, E. E. Fullerton, and A. V. Kimel. THz emission from Co/Pt bilayers with varied roughness, crystal structure, and interface intermixing. *Physical Review Materials*, 3(8):1–11, 2019.

[249] M. Matthiesen, D. Afanasiev, J. R. Hortensius, T. C. van Thiel, R. Medapalli, E. E. Fullerton, and A. D. Caviglia. Temperature dependent inverse spin Hall effect in Co/Pt spintronic emitters. *Applied Physics Letters*, 116(21):212405, 5 2020.

[250] H. S. Qiu, K. Kato, K. Hirota, N. Sarukura, M. Yoshimura, and M. Nakajima. Layer thickness dependence of the terahertz emission based on spin current in ferromagnetic heterostructures. *Optics Express*, 26(12):15247, 6 2018.

[251] Garik Torosyan, Sascha Keller, Laura Scheuer, René Beigang, and Evangelos Th Papaioannou. Optimized Spintronic Terahertz Emitters Based on Epitaxial Grown Fe/Pt Layer Structures. *Scientific Reports*, 8(1):1–9, 2018.

[252] Dennis M. Nenno, Laura Scheuer, Dominik Sokoluk, Sascha Keller, Garik Torosyan, Alexander Brodyanski, Jörg Lösch, Marco Battiato, Marco Rahm, Rolf H. Binder, Hans C. Schneider, René Beigang, and Evangelos Th. Papaioannou. Modification of spintronic terahertz emitter performance through defect engineering. *Scientific Reports*, 9(1):13348, 12 2019.

[253] Tom S. Seifert, Samridh Jaiswal, Joseph Barker, Sebastian T. Weber, Ilya Razdolski, Joel Cramer, Oliver Gueckstock, Sebastian F. Maehrlein, Lukas Nadvornik, Shun Watanabe, Chiara Ciccarelli, Alexey Melnikov, Gerhard Jakob, Markus Münzenberg, Sebastian T.B. Goennenwein, Georg Woltersdorf, Baerbel Rethfeld, Piet W. Brouwer, Martin Wolf, Mathias Kläui, and Tobias Kampfrath. Femtosecond formation dynamics of the spin Seebeck effect revealed by terahertz spectroscopy. *Nature Communications*, 9(1):1–11, 2018.

[254] Qi Zhang, Yumeng Yang, Ziyan Luo, Yanjun Xu, Rongxiang Nie, Xinhai Zhang, and Yihong Wu. Terahertz Emission from an Exchange-Coupled Synthetic Antiferromagnet. *Physical Review Applied*, 13(5):1, 2020.

[255] C. Baldasseroni, G. K. Pálsson, C. Bordel, S. Valencia, A. A. Unal, F. Kronast, S. Nemsak, C. S. Fadley, J. A. Borchers, B. B. Maranville, and F. Hellman. Effect of capping material on interfacial ferromagnetism in FeRh thin films. *Journal of Applied Physics*, 115(4):1–9, 2014.

[256] Xiaocui Han, Hong Cui, Bo Liu, Cunling Tian, Junzhong Wang, Hong Chen, and Hongkuan Yuan. Effects of overlayer capping and lattice strain on perpendicular magnetic anisotropy of TM|FePt|MgO heterostructures. *Scientific Reports*, 8(1):1–12, 2018.

[257] Eric Vetter, Melike Biliroglu, Dovletgeldi Seyitliyev, Pramod Reddy, Ronny Kirste, Zlatko Sitar, Ramón Collazo, Kenan Gundogdu, and Dali Sun. Observation of carrier concentration dependent spintronic terahertz emission from n -GaN/NiFe heterostructures. *Applied Physics Letters*, 117(9), 2020.

[258] C. Zhou, Y. P. Liu, Z. Wang, S. J. Ma, M. W. Jia, R. Q. Wu, L. Zhou, W. Zhang, M. K. Liu, Y. Z. Wu, and J. Qi. Broadband Terahertz Generation via the Interface Inverse Rashba-Edelstein Effect. *Physical Review Letters*, 121(8):1–6, 2018.

[259] E. Beaurepaire, G. M. Turner, S. M. Harrel, M. C. Beard, J. Y. Bigot, and C. A. Schmuttenmaer. Coherent terahertz emission from ferromagnetic films excited by femtosecond laser pulses. *Applied Physics Letters*, 84(18):3465–3467, 2004.

[260] Wentao Zhang, Pablo Maldonado, Zuanming Jin, Tom S. Seifert, Jacek Arabski, Guy Schmerber, Eric Beaurepaire, Mischa Bonn, Tobias Kampfrath, Peter M. Oppeneer, and Dmitry Turchinovich. Ultrafast terahertz magnetometry. *Nature Communications*, 11(1), 2020.

[261] T. J. Huisman, R. V. Mikhaylovskiy, J. D. Costa, F. Freimuth, E. Paz, J. Ventura, P. P. Freitas, S. Blügel, Y. Mokrousov, T. Rasing, and A. V. Kimel. Femtosecond control of electric currents in metallic ferromagnetic heterostructures. *Nature Nanotechnology*, 11(5):455–458, 2016.

[262] T. J. Huisman, C. Ciccarelli, A. Tsukamoto, R. V. Mikhaylovskiy, Th Rasing, and A. V. Kimel. Spin-photo-currents generated by femtosecond laser pulses in a ferrimagnetic GdFeCo/Pt bilayer. *Applied Physics Letters*, 110(7), 2017.

[263] Zhaoliang Liao, Matthew Brahlek, Jong Mok Ok, Lauren Nuckols, Yogesh Sharma, Qiyang Lu, Yanwen Zhang, and Ho Nyung Lee. Pulsed-laser epitaxy of topological insulator Bi 2 Te 3 thin films. *APL Materials*, 7(4):041101, 4 2019.

[264] Evangelos Th Papaioannou, Garik Torosyan, Sascha Keller, Laura Scheuer, Marco Battiato, Valynn Katrine Mag-Usara, Johannes L'Huillier, Masahiko Tani, and Rene Beigang. Efficient Terahertz Generation Using Fe/Pt Spintronic Emitters Pumped at Different Wavelengths. *IEEE Transactions on Magnetics*, 54(11), 2018.

[265] René Beigang, Evangelos Papaioannou, Laura Scheuer, Sascha Keller, Garik Torosyan, Marco Rahm, Dominik Sokoluk, Miezel Talara, Yoshinori Oda, Hideaki Kitahara, Jessica Afalla, Valynn K. Mag-usara, and Masahiko Tani. Efficient terahertz generation using Fe/Pt spintronic emitters pumped at different wavelengths. In Laurence P. Sadwick and Tianxin Yang, editors, *Terahertz, RF, Millimeter, and Submillimeter-Wave Technology and Applications XII*, page 23. SPIE, 3 2019.

[266] D. J. Hilton, R. D. Averitt, C. A. Meserole, G. L. Fisher, D. J. Funk, and A. J. Taylor. Terahertz spectroscopy of ultrafast demagnetization in ferromagnetic iron. In *Quantum Electronics and Laser Science Conference (QELS)*, volume 1, pages 347–349. IEEE, 2005.

[267] Lin Huang, Sang-Hyuk Hyuk Lee, Seongheun Dae Seon-Dae Kim, Je-Ho Ho Shim, Hee Jun Shin, Seongheun Dae Seon-Dae Kim, Jaehun Park, Seung-Young Young Park, Yeon Suk Choi, Hyun-Joong Joong Kim, Jung-Il Il Hong, Dong-Hyun Hyun Eon Kim, and Dong-Hyun Hyun Eon Kim. Universal field-tunable terahertz emission by ultrafast photoinduced demagnetization in Fe, Ni, and Co ferromagnetic films. *Scientific Reports*, 10(1):15843, 12 2020.

[268] Lin Huang, Ji-Wan Wan Kim, Sang-Hyuk Hyuk Lee, Seongheun Dae Seon-Dae Kim, Van Manh Tien, Kiran Prakash Shinde, Je-Ho Ho Shim, Yooleemi Shin, Hee Jun Shin, Seongheun Dae Seon-Dae Kim, Jaehun Park, Seung-Young Young Park, Yeon Suk Choi, Hyun-Joong Joong Kim, Jung-Il Il Hong, Dong-Hyun Hyun Eon Kim, and Dong-Hyun Hyun Eon Kim. Direct observation of terahertz emission from ultrafast spin dynamics in thick ferromagnetic films. *Applied Physics Letters*, 115(14):142404, 9 2019.

[269] Tom S. Seifert, Ulrike Martens, Florin Radu, Mirkow Ribow, Marco Berritta, Lukáš Nádvorník, Ronald Starke, Tomas Jungwirth, Martin Wolf, Ilie Radu, Markus Münzenberg, Peter M. Oppeneer, Georg Woltersdorf, and Tobias Kampfrath. Frequency-Independent Terahertz Anomalous Hall Effect in DyCo5, Co32Fe68, and Gd27Fe73 Thin Films from DC to 40 THz. *Advanced Materials*, 33(14), 2021.

[270] T. Seifert, S. Jaiswal, M. Sajadi, G. Jakob, S. Winnerl, M. Wolf, M. Kläui, and T. Kampfrath. Ultrabroadband single-cycle terahertz pulses with peak fields of 300 kV cm-1 from a metallic spintronic emitter. *Applied Physics Letters*, 110(25), 2017.

[271] Ryunosuke Takahashi, Yoshiki Tani, Hirotaka Abe, Minato Yamasaki, Ikumi Suzuki, Daisuke Kan, Yuichi Shimakawa, and Hiroki Wadati. Ultrafast demagnetization in NiCo2O4 thin films probed by time-resolved microscopy. *Applied Physics Letters*, 119(10), 2021.

[272] Wei He, Tao Zhu, Xiang Qun Zhang, Hai Tao Yang, and Zhao Hua Cheng. Ultrafast demagnetization enhancement in CoFeB/MgO/CoFeB magnetic tunneling junction driven by spin tunneling current. *Scientific Reports*, 3:1–5, 2013.

[273] A Eschenlohr, L Persichetti, T Kachel, M Gabureac, P Gambardella, and C Stamm. Spin currents during ultrafast demagnetization of ferromagnetic bilayers. *Journal of Physics Condensed Matter*, 29(38):384002, 9 2017.

[274] Ute Bierbrauer, Sebastian T Weber, David Schummer, Moritz Barkowski, Anna Katharina Mahro, Stefan Mathias, Hans Christian Schneider, Benjamin Stadtmüller, Martin Aeschlimann, and Baerbel Rethfeld. Ultrafast magnetization dynamics in Nickel: Impact of pump photon energy. *Journal of Physics Condensed Matter*, 29(24):244002, 6 2017.

[275] Vincent Cardin, Tadas Balciunas, Katherine Légaré, Andrius Baltuska, Heide Ibrahim, Emmanuelle Jal, Boris Vodungbo, Nicolas Jaouen, Charles Varin, Jan Lüning, and François

Légaré. Wavelength scaling of ultrafast demagnetization in Co/Pt multilayers. *Physical Review B*, 101(5):1–6, 2 2020.

[276] A. L. Chekhov, Y. Behovits, J. J. F. Heitz, C. Denker, D. A. Reiss, M. Wolf, M. Weinelt, P. W. Brouwer, M. Münzenberg, and T. Kampfrath. Ultrafast Demagnetization of Iron Induced by Optical versus Terahertz Pulses. *Physical Review X*, 11(4):41055, 2021.

[277] K V Shanavas. Theoretical study of the cubic Rashba effect at the SrTiO 3 (001) surfaces. *Physical Review B*, 93(4), 2016.

[278] Talieh S. Ghiasi, Alexey A. Kaverzin, Patrick J. Blah, and Bart J. Van Wees. Charge-to-Spin Conversion by the Rashba-Edelstein Effect in Two-Dimensional van der Waals Heterostructures up to Room Temperature. *Nano Letters*, 19(9):5959–5966, 2019.

[279] J. Holanda, O. Alves Santos, R. O. Cunha, J. B.S. Mendes, R. L. Rodríguez-Suárez, A. Azevedo, and S. M. Rezende. Longitudinal spin Seebeck effect in permalloy separated from the anomalous Nernst effect: Theory and experiment. *Physical Review B*, 95(21):1–8, 2017.

[280] B. Dieny and M. Chshiev. Perpendicular magnetic anisotropy at transition metal/oxide interfaces and applications. *Reviews of Modern Physics*, 89(2):025008, 6 2017.

[281] H.-S. Rhie, H. A. Dürr, and W. Eberhardt. Femtosecond Electron and Spin Dynamics in Ni/W(110) Films. *Physical Review Letters*, 90(24):247201, 6 2003.

[282] Vivek Unikandanunni, F. Rigoni, Matthias C. Hoffmann, Paolo Vavassori, Sergei Urazhdin, and Stefano Bonetti. Ultrafast electron dynamics in platinum and gold thin films driven by optical and terahertz fields. *Applied Physics Letters*, 120(2):021601, 1 2022.

[283] Xinan Liang, Xuewu Xu, Ruitao Zheng, Zhiming Abel Lum, and Jinjun Qiu. Optical constant of CoFeB thin film measured with the interference enhancement method. *Applied Optics*, 54(7):1557, 3 2015.

[284] Yang Wu, Mehrdad Elyasi, Xuepeng Qiu, Mengji Chen, Yang Liu, Lin Ke, and Hyunsoo Yang. High-Performance THz Emitters Based on Ferromagnetic/Nonmagnetic Heterostructures. *Advanced Materials*, 29(4):1603031, 1 2017.

[285] Rick Astley and Stock Aitken Waterman. The one last peculiar reference-link for particularly attentive readers: https://youtu.be/dQw4w9WgXcQ. *The Unknown Journal*, 228(15):1, 2022.

DOCTORAT MATIERE BRETAGNE MOLECULES LOIRE ET MATERIAUX

Le Mans Université

Titre : Sonde et contrôle des phonons cohérents et de la conversion spin-charge dans les nanostructures à l'aide d'impulsions lumineuses ultrarapides dans le visible et le THz

Mot clés : Spectroscopie térahertz, pompe-sonde, phonons, conversion spin/charge

Résumé : L'étude du couplage ultrarapide entre les électrons, les phonons et les spins demeure un enjeu majeur en physique de l'état condensé. Ces recherches doivent à terme répondre à divers défis posés par les technologiques très haute cadence.

La première partie de cette thèse est l'étude expérimentale de la génération de phonons cohérents avec des impulsions ultra-brèves térahertz et proche infrarouge dans des nanofilms de Cr, Al et de Bi_2Te_3. Grâce à une comparaison quantitative de ces deux types d'excitation, nous montrons de manière inédite que le processus de génération de phonons acoustiques par térahertz est principalement induit par la contrainte thermoélastique (effet Joule ultra-rapide).

Dans un deuxième temps, nous montrons aussi que l'impulsion térahertz peut exciter des modes actifs Raman par des processus non-linéaires optiques et phononiques.

La troisième réalisation de cette thèse est le contrôle par excitation optique ultra-rapide de la conversion spin/charge dans des bicouches nanométriques magnétiques à fort couplage spin-orbite. En particulier, nous discutons de l'effet Edelstein inverse ultra-rapide dans les hétérostructures CoFeB/MgO. Nous montrons qu'il est sensible à l'énergie des photons de pompe, ce qui ouvre des perspectives excitantes pour les émetteurs spintroniques ultra-rapides.

Title: Probing and controlling coherent-phonon and spin-charge conversion in nanostructures with ultrafast visible and THz light pulses

Keywords: Terahertz spectroscopy, pump-probe, phonons, spin/charge conversion

Abstract: The study of ultrafast coupling between electrons, phonons, and spins remains a major challenge in condensed state physics. This research must ultimately respond to various challenges posed by very high-frequency technologies.

The first part of this thesis is the experimental investigation of the coherent phonon generation with terahertz and near-infrared ultra-short pulses in nanofilms of Cr, Al, and Bi_2Te_3. By comparing two distinct excitation processes, we unprecedentedly show that the mechanism of acoustic phonon generation with terahertz is mainly driven by thermoelastic stress (ultrafast Joule effect).

As the next step, we also show that the terahertz pulse can excite Raman active modes through non-linear photonic and phononic processes.

The third achievement of this thesis is the picosecond control of the spin-to-charge conversion driven by the strong spin-orbit coupling in magnetic nanometric bilayers. In particular, we discuss the ultrafast inverse Edelstein effect in CoFeB/MgO heterostructures. We show that it is sensitive to the pump photon energy, which opens exciting perspectives of ultrafast spintronics emitters.